

Award Number: W81XWH-11-1-0493

TITLE: Development of Magnetic Resonance Imaging Biomarkers for Traumatic Brain Injury

PRINCIPAL INVESTIGATOR: E. Mark Haacke, Ph.D.

CONTRACTING ORGANIZATION: Wayne State University, Detroit, MI 48201

REPORT DATE: September 2014

TYPE OF REPORT: Final Addendum

PREPARED FOR: U.S. Army Medical Research and Materiel Command  
Fort Detrick, Maryland 21702-5012

DISTRIBUTION STATEMENT:

Approved for public release; distribution unlimited

The views, opinions and/or findings contained in this report are those of the author(s) and should not be construed as an official Department of the Army position, policy or decision unless so designated by other documentation.

# REPORT DOCUMENTATION PAGE

*Form Approved  
OMB No. 0704-0188*

Public reporting burden for this collection of information is estimated to average 1 hour per response, including the time for reviewing instructions, searching existing data sources, gathering and maintaining the data needed, and completing and reviewing this collection of information. Send comments regarding this burden estimate or any other aspect of this collection of information, including suggestions for reducing this burden to Department of Defense, Washington Headquarters Services, Directorate for Information Operations and Reports (0704-0188), 1215 Jefferson Davis Highway, Suite 1204, Arlington, VA 22202-4302. Respondents should be aware that notwithstanding any other provision of law, no person shall be subject to any penalty for failing to comply with a collection of information if it does not display a currently valid OMB control number. PLEASE DO NOT RETURN YOUR FORM TO THE ABOVE ADDRESS.

<b>1. REPORT DATE</b> September 2014			<b>2. REPORT TYPE</b> Final Addendum		<b>3. DATES COVERED</b> 2 June 2011 - 1 June 2014	
<b>4. TITLE AND SUBTITLE</b> Development of Magnetic Resonance Imaging Biomarkers for Traumatic Brain Injury			<b>5a. CONTRACT NUMBER</b> W81XWH-11-1-0493			
			<b>5b. GRANT NUMBER</b> W81XWH-11-1-0493			
			<b>5c. PROGRAM ELEMENT NUMBER</b>			
<b>6. AUTHOR(S)</b> E. Mark Haacke, Ph.D. (Principal Investigator), Zhifeng Kou, Ph.D. (co-PI)  E-Mail: nmrimaging@aol.com			<b>5d. PROJECT NUMBER</b>			
			<b>5e. TASK NUMBER</b>			
			<b>5f. WORK UNIT NUMBER</b>			
<b>7. PERFORMING ORGANIZATION NAME(S) AND ADDRESS(ES)</b> Wayne State University, Inc Michael Anderson 5700 Cass Ave. Suite 4900 Detroit, MI 48202-3692					<b>8. PERFORMING ORGANIZATION REPORT NUMBER</b>	
<b>9. SPONSORING / MONITORING AGENCY NAME(S) AND ADDRESS(ES)</b> U.S. Army Medical Research and Materiel Command Fort Detrick, Maryland 21702-5012					<b>10. SPONSOR/MONITOR'S ACRONYM(S)</b>	
					<b>11. SPONSOR/MONITOR'S REPORT NUMBER(S)</b>	
<b>12. DISTRIBUTION / AVAILABILITY STATEMENT</b> Approved for Public Release; Distribution Unlimited						
<b>13. SUPPLEMENTARY NOTES</b>						
<b>14. ABSTRACT</b>  The purpose of this research program was to develop an imaging-based protocol to improve diagnosis and outcome prediction of mild traumatic brain injury (mTBI). In our technical program, we developed susceptibility weighted imaging and mapping (SWIM) as a means to quantify cerebral hemorrhage and venous blood oxygenation. By translating this work into mTBI patients, along with other imaging techniques, we made significant achievements. First, we demonstrated that these new advanced MRI methods complement conventional imaging methods in their ability to detect mTBI in the acute setting. Second, susceptibility weighted imaging and mapping (SWIM) are able to delineate venous structures and microbleeds making it possible to quantify and monitor evolution of pathological changes. And third, we have combined SWIM with other advanced imaging techniques, including diffusion tensor imaging, functional MRI, and perfusion imaging, to improve the detection of mTBI. The significance of this work to date is that we are now able to find evidence of damage in mTBI where that has heretofore been difficult with conventional MRI. Finally, we have developed SWIM as a tool for clinical TBI detection and quantification.						
<b>15. SUBJECT TERMS</b> none provided						
<b>16. SECURITY CLASSIFICATION OF:</b>			<b>17. LIMITATION OF ABSTRACT</b> UU	<b>18. NUMBER OF PAGES</b> 130	<b>19a. NAME OF RESPONSIBLE PERSON</b> USAMRMC	
<b>a. REPORT</b> U	<b>b. ABSTRACT</b> U	<b>c. THIS PAGE</b> U			<b>19b. TELEPHONE NUMBER (include area code)</b>	

## **Table of Contents**

	<u>Page</u>
<b>Introduction.....</b>	<b>3</b>
<b>Body.....</b>	<b>4</b>
<b>Key Research Accomplishments.....</b>	<b>15</b>
<b>Reportable Outcomes.....</b>	<b>15</b>
<b>Conclusion.....</b>	<b>18</b>
<b>References.....</b>	<b>18</b>
<b>Appendices.....</b>	<b>20</b>

## INTRODUCTION

**Background:** Traumatic brain injury (TBI) has been labeled as a “signature wound” in the anti-terrorism wars in Iraq and Afghanistan. 15% - 25% of surveyed returning service members have been reported to have possible long-term mild traumatic brain injury (mTBI) or concussion. In the civilian sector, the prolonged neurocognitive and functional symptoms following mTBI affects over 1.2 million Americans annually. However, our understanding of the neuropathology of mTBI and its recovery process is still very limited due to the lack of sensitive clinical and diagnostic tools. First, current TBI classification scales are mainly based on results from computed tomography (CT) scans of moderate to severe TBI patients, and thus can hardly be applied to mTBI cases. Secondly, current laboratory biological markers, clinical CT and conventional magnetic resonance imaging (MRI) are either insensitive or not specific to the subtle abnormalities in mTBI and poorly predict patient’s long-term outcome. It is in urgent need of developing a set of advanced MR imaging biomarkers that can: i) be sensitive enough to differentiate mTBI patient population from normal healthy subjects, ii) have the potential for outcome prediction; and iii) assist in management of mTBI patients in acute settings.

**Objective/Hypothesis:** The overall goal of the current research is to develop imaging-based biomarkers to improve diagnosis and outcome prediction of mTBI. Advanced MRI techniques reveal many more details than conventional imaging. For example, susceptibility weighted imaging (SWI) and susceptibility mapping (SWIM) can detect and quantify temporal reduction of hemorrhagic lesions associated with mTBI patients’ functional outcome and diffusion tensor imaging (DTI) can detect axonal injury at the acute stage and possible changes over time. As the next generation of SWI developed in our lab, SWIM will be used to quantify iron in microbleeds and oxygen saturation in major veins throughout the brain. Our central hypothesis is that axonal injury (measured by DTI) and vascular damage (detected as hemorrhagic lesions by SWI/SWIM) are important pathologies in mTBI that are associated with patients’ neurocognitive and clinical symptoms in their recovery.

**Study Design:** The original project was designed for a two-phase study. Phase I — “Technical Development,” was to develop our susceptibility weighted imaging and mapping (SWIM) for quantitative measurement of traumatic hemorrhage and venous blood oxygenation as well as to recruit a relatively small cohort of mTBI patients and controls. Phase II — “Clinical Application,” is to apply the developed SWIM technique, along with diffusion tensor imaging (DTI), into a relatively large number of mTBI patients. Our work was funded for Phase I, Technical Development. To date, 40 adult mTBI patients were screened and enrolled at the acute stage (within 24 hours after injury) from the emergency department of our local Level-One Trauma Center. Both up-to-60-minute MRI scan and neuropsychological/clinical assessment was conducted in mTBI patients. In the subacute (1 month) and chronic (6 months) stages after injury, the patients were brought back to repeat both the MRI scans and neurocognitive evaluations. Age/gender/education-matched healthy controls will be recruited and followed up using the same imaging and neuropsychological protocol of evaluation.

**Specific Aims:** **Specific Aim 1** was to assess whether the advanced MRI data (SWI and DTI) acquired acutely (within 24 hours after injury) are more sensitive than conventional imaging (CT and cMRI) in detecting mTBI. **Specific Aim 2** was to determine at what time point after the injury (i.e., acute, subacute and chronic) these advanced MR techniques can differentiate mTBI patients from healthy controls. **Specific Aim 3** was to use susceptibility weighted imaging and mapping (SWIM), our next generation of SWI technique, to quantify the amount of iron in microbleeds, to monitor any changes (evolution) of the microbleed over time and to monitor oxygen saturation compared to normal volunteers. And **Specific Aim 4** was to determine which MRI indices have statistically significant associations with neurocognitive outcome in mTBI patients over all time points.

## BODY

**Technical Development:** We have developed SWIM as a means to quantify hemorrhagic blood and venous blood oxygenation (1-3). For the clinical study, we collected 40 mTBI patients at the acute stage (within 24 hours after injury) and 40 demographically matched controls. Below is a summary of our progress report in support of each aim.

**Development of SWI/SWIM:** We successfully developed the SWIM technique to quantify iron and blood oxygenation of the brain (2) (see Figure 1). We validated the susceptibility measure in both an iron phantom and a cadaver brain (4). We made technical improvements of the SWIM technique by removing various artifacts (3). As a result, we were able to differentiate hemorrhagic bleeds from veins. We quantified the partial volume effect of veins with different diameters for an improved correction of venous blood oxygenation. In addition, we further improved our SWI sequence to acquire both angiography and venography data at the same time to have a global picture of both the arterial and venous systems (5, 6). At the end of the Phase I study, we have gained significant experience with SWIM in this area which can be shared with the military and civilian research groups promoting TBI imaging methods (7).

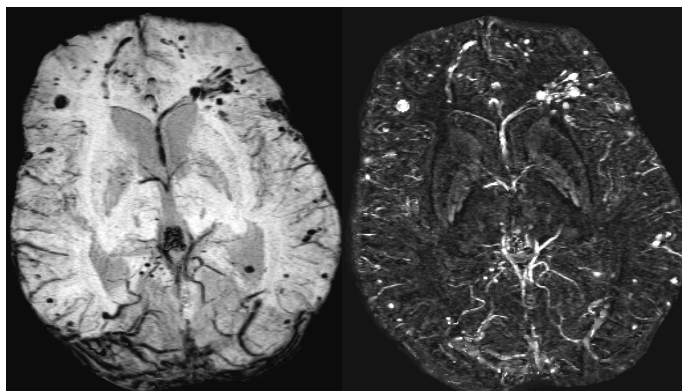


**Figure 1:** The image on the left is a state-of-the-art SWI image from a 3T scanner. The image on the right is the SWIM data which can be used to quantitatively differentiate basal ganglia, microbleeds and veins.

**Validation of susceptibility measurement of iron content:** We further validated our SWIM estimation of iron content in human cadaveric brain with multiple sclerosis by using X-ray fluorescence (XRF) imaging and inductively coupled plasma mass spectrometry (ICPMS) (see Figure 2) (4). The relationship between susceptibility and ferritin iron was estimated at  $1.10 \pm 0.08$  ppb susceptibility per  $\mu\text{g}$  iron/g wet tissue, similar to that of iron in fixed (frozen/thawed) cadaveric brain and previously published data from unfixed brains. We conclude that magnetic susceptibility can provide a direct and reliable quantitative measurement of iron content and that it can be used clinically in brain regions with high iron content (4).

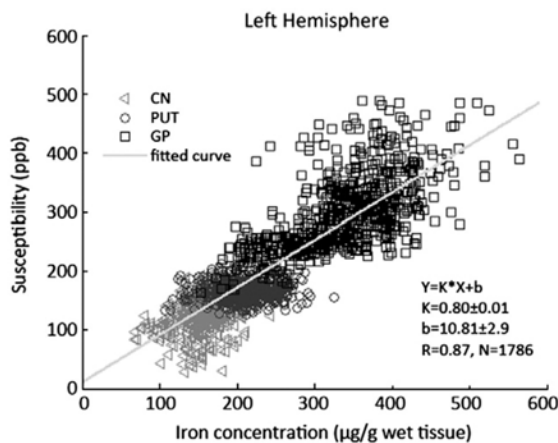


**Figure 2:** Correlation between susceptibility and XRF imaging of iron measurements for data points taken from left hemisphere of a cadaveric brain with multiple sclerosis.  $R = 0.87$ .

Iterative SWIM: We developed an advanced form of susceptibility mapping, which we refer to as “Iterative SWIM”, to reduce the artifacts caused by the ill-posed behavior of the inverse filter (3). These artifacts are particularly severe for subjects with microbleeds that have a very high susceptibility. An example is shown below in Figure 3 (3). Note that microbleeds are surrounded by black ring artifacts with the usual quantitative susceptibility mapping methods (indicated by arrows in Fig. 1c) and that these are significantly reduced using iterative SWIM (Fig. 1d). These artifacts can cause misinterpretation of the images (i.e., the presence of false structures). Removing this systematic error helps improve the accuracy and diagnosis of CMB detection in TBI.

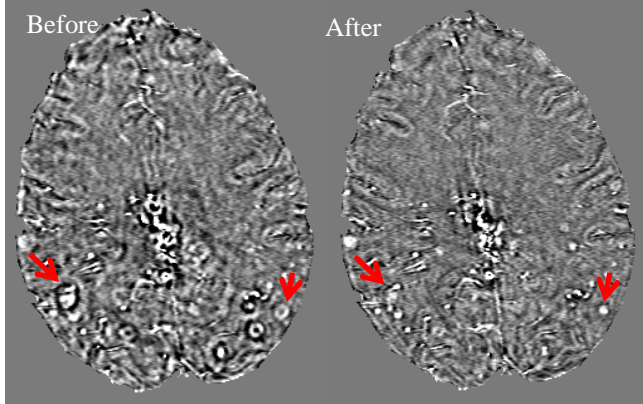


**Figure 3:** Comparison of susceptibility map from conventional SWIM (left) and iterative SWIM (right). As can be seen, black ring artifacts associated with microbleeds permeate the image in (left) and are significantly reduced in (right), which shows higher image quality with better SNR and better microbleed detection.

Improved background phase removal using variable high-pass filtering: The background field induces aliasing and low spatial frequency artifacts in the phase images. In the past it has been most commonly removed using homodyne high-pass filtering. This easy-to-apply filter is effective in removing the background phase but it also causes signal loss to the local field variation in larger objects. Even though this is less of a problem for veins, which are usually small in size and have relatively high spatial frequency, it leads to an under-estimation of the susceptibility for larger structures such as the basal ganglia. It also prevents an unbiased estimate of the oxygen saturation level. To solve this problem, we applied a variable high-pass filter which is weaker in the central part of the brain and stronger near the edge of the brain. In this way, the low spatial frequency signal of the bigger deep grey matter structures is preserved, while the background phase, which is mainly induced by the air-tissue interfaces, is removed. By using the variable high pass filter, the contrast in the veins is enhanced, as is the contrast in the globus pallidus. As a result, the variable high pass filter provides a much better estimate of the iron content in the tissue. This could be useful in quantification of venous blood oxygenation. See Figure 4.

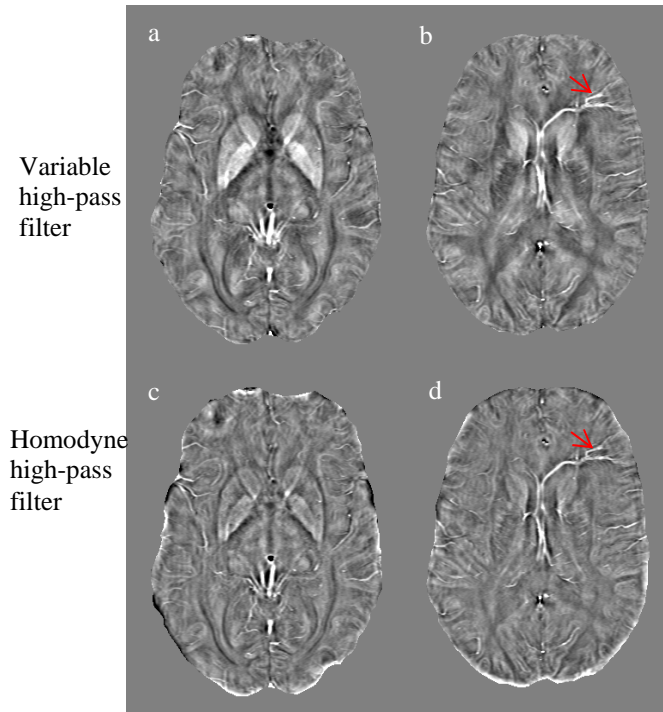


**Figure 4 (above):** The processed susceptibility maps. The susceptibility maps in a) and b) are generated using the phase processed with the variable high-pass filter, while c) and d) are generated using the homodyne high-pass filtered phase images. The red arrows indicate the damaged medullary vein. Note that in a) and b) the contrast even in the veins is enhanced in this case as is the contrast in the globus pallidus so that one obtains a much better estimate of the iron content in the tissue.

Concurrent Acquisition of MR Angiography (MRA) and Venography (MRV): To have a complete examination of both arterial and venous systems of the brain, we have developed a dual echo SWI technique that will provide the ability to acquire both SWI/SWIM and MRA images at the same time (5, 6). This is not the ordinary double echo sequence but a fully flow compensated double echo sequence so no interference from arteries takes place (see Figure 5) (5).

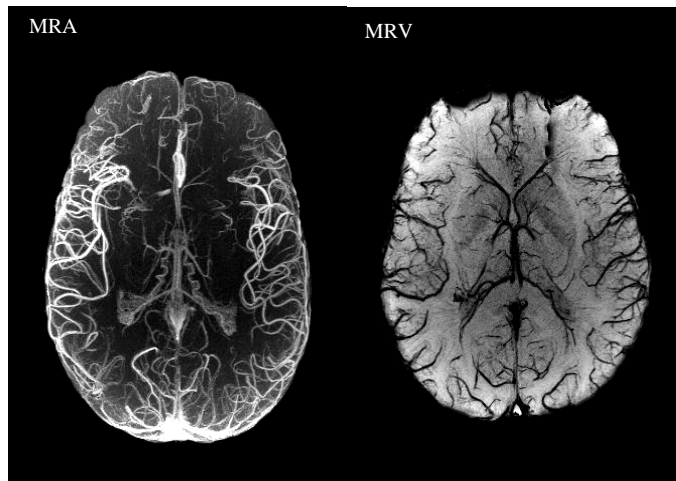


**Figure 5:** The double echo SWI sequence makes it possible to acquire both arteries and veins at the same time. The rephased/dephased version of the double echo SWI could generate angiography (MRA) with all the arteries demonstrated. The image on the right is the venography (MRV) in usual SWI generated in the second echo.

Differentiating hemorrhage from veins: Based on our technical development in SWIM, we were able to apply it to TBI patients to semi-automatically differentiate microbleeds from major veins, which is a challenge in everyday radiological diagnosis. From their histogram, it can clearly show that the microbleeds have much higher susceptibility than major veins (see Figure 6). By using threshold of 200ppb, we will be able to semi-automatically differentiate bleed form veins with both sensitivity and specificity of 92%.

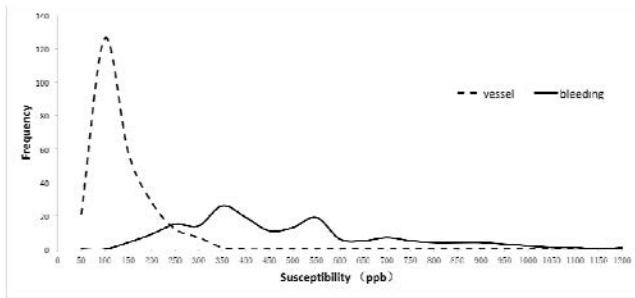


**Figure 6:** Susceptibility histograms of major veins (dotted line) and hemorrhages (solid line). The venous histogram is significantly shifted to the left compared to that of the hemorrhagic component showing the relatively lower susceptibility of the veins. The two histograms cross over at 200 ppb, which serves as a threshold to differentiate hemorrhage from the veins.

Correction of partial volume effects for blood oxygenation estimation: Due to partial volume effect of the different sizes of veins, they may show different susceptibility values. We have further determined the correlation between venous size and its susceptibility values, which will be used as a correction factor in our further blood oxygenation quantification (See Figure 7).

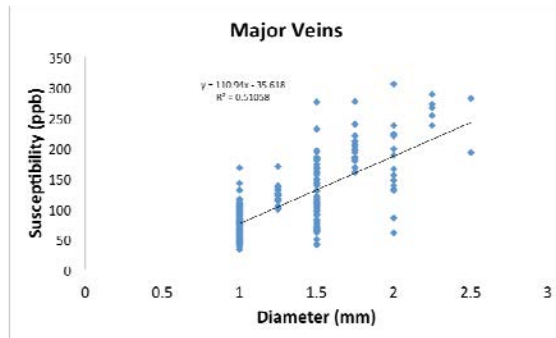


**Figure 7:** Correlation of venous blood susceptibility and diameter due to partial volume effect.

## Clinical Investigation

As the clinical arm of the Phase I study, we have successfully enrolled 44 mTBI patients from the emergency department (within 24 hours after injury) and 45 demographically matched controls. Patients were being followed up at 1 month and 6 months after injury (8). Controls repeated the study at 1 month after first visit. We have implemented our SWIM technical improvements into the clinical protocol and made significant advances for each specific aim set forth for both Phases I and II. The following preliminary data were laid out according to each aim.

To assess whether the advanced MRI is more sensitive than CT and conventional MRI in mTBI detection: SWI detected 6 out of 40 cases with hemorrhages. Of these, 4 had positive CT findings. Our MRI data showed that all mTBI patients with positive CT have parenchymal injury, though CT only detected extra-axial injury. This

finding explains the reason why CT-positive mTBI patients tend to have prolonged symptoms as compared to CT-negative mTBI patients. In the follow-up study of these patients in the subacute stage, SWI detected a decrease of hemorrhagic lesion load over time. Our DTI data demonstrated that DTI can detect lesions that are invisible on conventional MRI (9).

**Imaging the Progression of Brain Pathology:** There is very limited data regarding imaging findings of pathological changes over time in mTBI patients. Recently, two studies revealed the possible normalization of DTI FA over time after injury (10, 11). In a longitudinal, prospective study of 42 severely injured adults (12), our collaborating center at LLUMC indicated the time course of N-acetyl aspartate (NAA) changes following injury. In addition, they also performed a follow-up analysis of SWI lesions in 25 patients ranging in age from 16 to 80 years (mean=26) imaged within 2-23 days (mean=6) of injury (12). They found the total number of lesions decreased by 41.2% over time. The greatest percentage of decrease in lesion number/volume occurred after 30 days from injury. SWI can be used to follow the evolution of traumatic brain hemorrhages, which can be useful in patient management. *These findings provide a rationale for comparing imaging findings at acute and later time points in our proposal to reveal the pathological changes of the brain after mild TBI and its association with patients' neurocognitive outcome.*

**Initial Attempt to Classify TBI using SWI:** Our group also made the first attempt to develop an SWI classification scheme to predict moderate to severe TBI patients' outcome measured by Glasgow Outcome Score (GOS) (13, 14). SWI data were collected in 63 moderate to severe TBI patients with conventional MRI data between 1 to 30 days after injury along and CT on the first day of injury. In this classification scheme, different types of injuries (diffuse vs. focal or both) along with different levels of injury severity (severe, moderate and mild in diffuse injury; and lesion size in focal lesions) in 15 different brain regions were assigned with different weighting factors. The total score from these weighting factors was used as the SWI score for each patient. The SWI scores were then compared with the GCS and GOS scores. The scatter plot between SWI imaging scores and long term outcome is shown in Figure 8. This plot reveals that there was no overlap in SWI scores between the group of patients with favorable outcomes (GOS of 5) and the group of patients with unfavorable outcomes (GOS less than 5). In particular, an SWI score of 8 could be used as a threshold value to predict whether the patients will have a favorable or unfavorable outcome, while the initial or discharge GCS failed to distinguish outcomes.

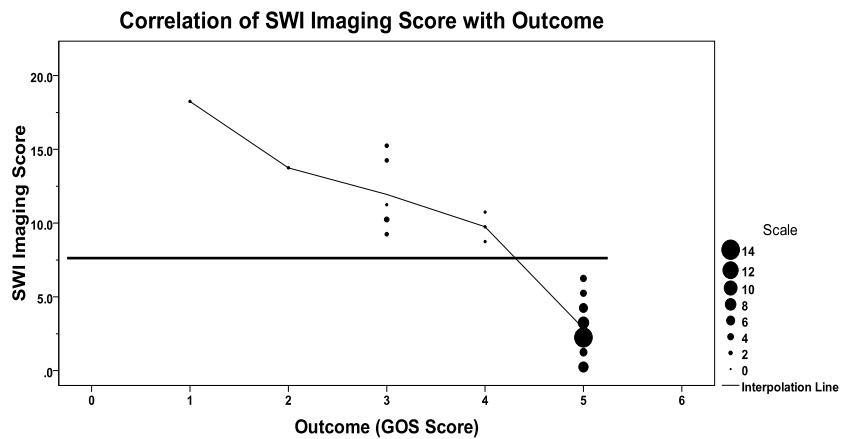


**Figure 8 (Above):** Correlation of SWI score with outcome (GOS score). Notice there is no overlap of the SWI score between the favorable outcomes and unfavorable outcomes (horizontal line). The points above the threshold of 8 represent all 15 of the poor outcome patients.

Quantifying venous blood oxygenation. We are also the first group using SWIM to quantify venous blood oxygenation in TBI patients. Our data in mTBI demonstrate a decreased venous blood susceptibility, which suggests increased blood oxygenation in left thalamostriatal vein and right basal vein (See Figure 9).

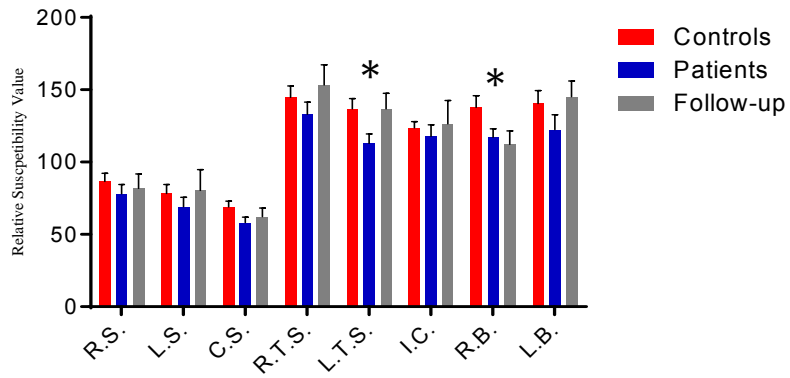


**Figure 9:** Mean susceptibility values and standard error in major veins. \* indicates statistically significant difference. R.S.: Right Septum, L.S.: Left Septum, C.S.: Central Septum, R.T.S.: Right Thalamostriate, L.T.S.: Left Thalamostriate I.C.: Internal Cerebral Vein, R.B.: Right Basal Vein of Rosenthal L.B.: Left Basal Vein of Rosenthal.

#### To determine mTBI hemodynamic profile and its relationship with functional network disturbance.

We performed extensive analysis of rsfcMRI data. Our independent component analysis (ICA) indicates decreased connectivity within the default mode network (DMN) in patients as compared to controls. Specifically, the functional connectivity between the precuneus, posterior cingulate cortex (PCC), and frontal lobe shows significant decreases in the patient group, and these differences are consistent with different group ICA analysis by using our permutation validation analysis (Figure 10) (15). Additionally, our seed region analysis showed increased inter-network connectivity. By using PCC as a seed region, a 2-sample t-test showed significantly higher correlations with several regions of the frontal lobe in patients than controls, including the dorsolateral prefrontal cortex, Brodmann area (BA) 9, and adjoining voxels in BA 8 and the anterior cingulate cortex (BA 32) (see Figure 11). These regions belong to other brain networks instead of the DMN. Similarly, by choosing the precuneus, thalamus, and hippocampus as seed regions, the results also show decreased intra-network connectivity and increased inter-network connectivity (15, 16).

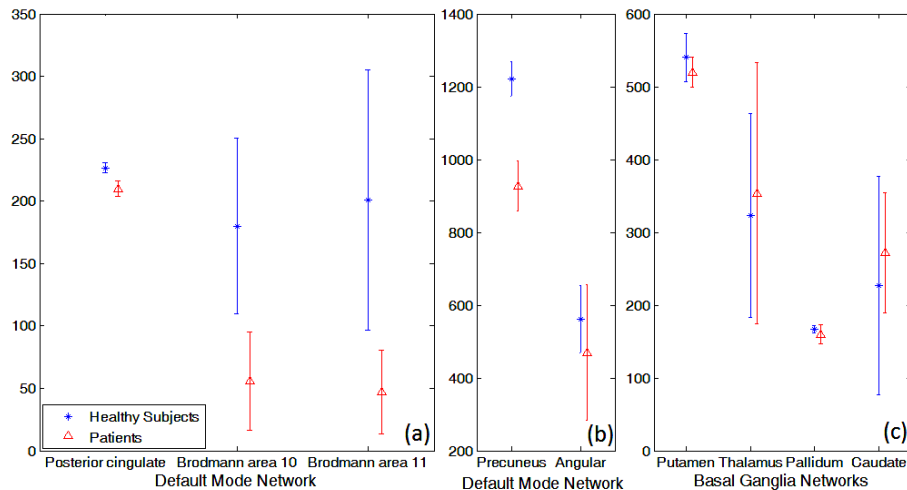


**Figure 10 (Above):** Cross validation results: Number of associated voxels to the resting state networks: The default mode network shows a difference between two groups in the posterior cingulate cortex (a), and precuneus (b), while the Basal ganglia network (c) does not show any significant difference. Error bar is one standard deviation beyond the mean.

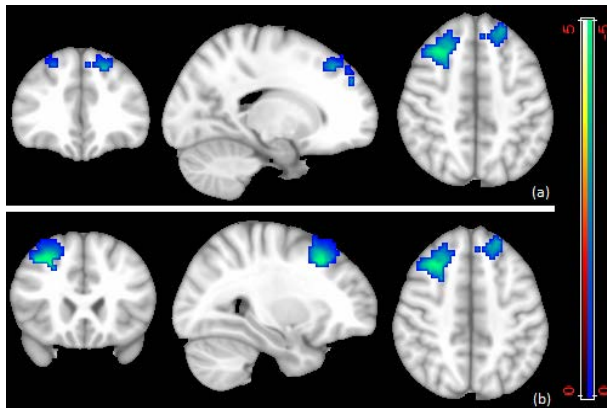


**Figure 11 (Above):** Two-sample t-test ( $p=0.01$ ) for the posterior cingulate cortex (PCC) correlation map (using PCC as seed region): The cold color labels the region that has more correlation with the posterior cingulate in the patients than in controls. Two levels show to highlight the two areas.

To investigate the hemodynamic underpinnings, we also performed perfusion imaging analysis with arterial spin labeling (ASL) data in the same patient population. We found increases in regional CBF (rCBF) in the left striatum and in the frontal and occipital lobes in patients as compared to controls ( $p = 0.01, 0.03, 0.028$ , respectively). See Figure 12. This result is also in agreement with our SWIM data, which shows increases in oxygenation of the venous system in the same patients as in Specific Aim 2. Taken together, our hemodynamic data show an early elevated CBF as a potential compensatory mechanism. However, it is still unknown to what extent this hemodynamic response correlates with patients' rsfcMRI data.

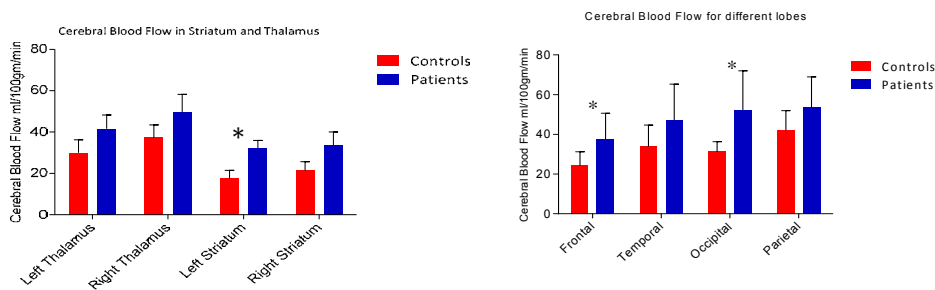


**Figure 12 (Above):** Perfusion analysis of mTBI at the acute stage using ASL shows increased cerebral blood flow (CBF) in several regions of the brain at the acute stage in comparison with controls (\*  $p<0.05$ ), including the left striatum and frontal and occipital lobes. This suggests that increased CBF results in the increased blood oxygenation in venous system as shown in SWIM data in the same patient population.

**Neuropsychological Studies in TBI:** Over the past 15 years, our collaborating research team at WSU has published extensively in the areas of functional outcome following TBI, psychometrics, and neurobehavioral instrument development. We have investigated the impact of focal frontal lesions on community re-integration, examined the relationship between NP functioning and the level of caregiver supervision needed following TBI, developed models to predict return-to-work following TBI using NP tests scores collected acutely, used executive function measures to predict functional outcome and social integration, determined NP predictors of motor vehicle driving following TBI, and identified different subtypes of verbal learning and memory deficits

following TBI. We have examined the capacity of the GCS and Revised Trauma Score to predict functional outcome following TBI. We have precisely defined the “dose-response” relationship in TBI with regard to initial injury severity and NP impairment and have examined the long-term NP outcome following TBI.

We have published a series of studies that have provided normative data and psychometric analyses of many NP tests used in TBI samples, including the Visual Form Discrimination Test, Warrington Recognition Memory Test, California Verbal Learning Test, Wisconsin Card Sorting Test and Visual Object and Space Perception Battery. Our collaborating team was the first to identify psychometric difficulties with the Wechsler Memory Scale – III via confirmatory factor analysis (17, 18). We were first to use Bayesian model averaging in the detection of malingered neurocognitive disorder (19). We have developed validity indicators for several NP tests to determine whether a test score may be invalid due to an examinee’s failure to provide sufficient effort to complete the test.

Our preliminary data on mTBI demonstrated significant reductions in patients’ memory, attention and executive functions at the acute stage. Though they tend to recover at the subacute stage, a significant percentage of the patients still have neurocognitive problems (see Figure 13 as an example). Our further imaging correlation with patients neurocognitive data demonstrated that the DTI lesion load is negatively correlated with patients memory (see Figure 14) (9). This also further suggests the superiority of DTI over cMRI for the detection of microstructural lesions, in support of Aim 1.

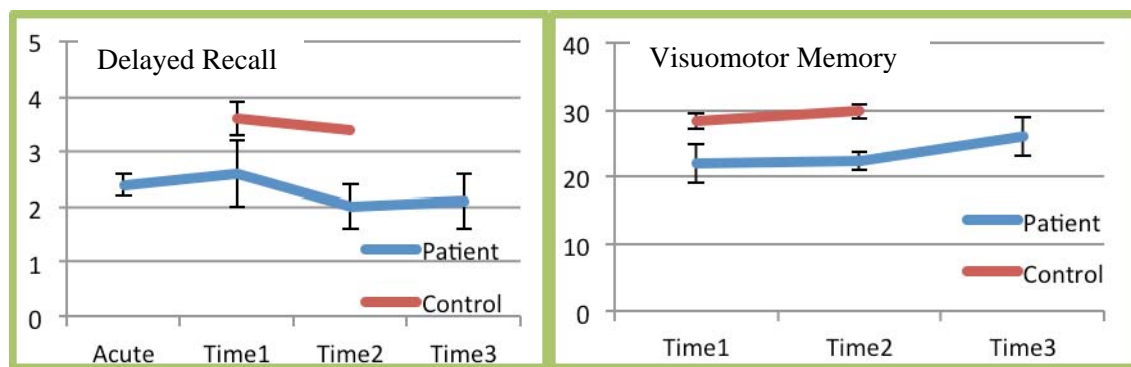


**Figure 13 (Up):** Memory deficit and recovery pattern after mTBI (n=36) over different time points. Time1-within 3 days, Time2-one month, and Time3-6 month. Left: SAC delayed recall; Right: Brief Visuomotor Memory Test-Revised for visual memory test, total recall.

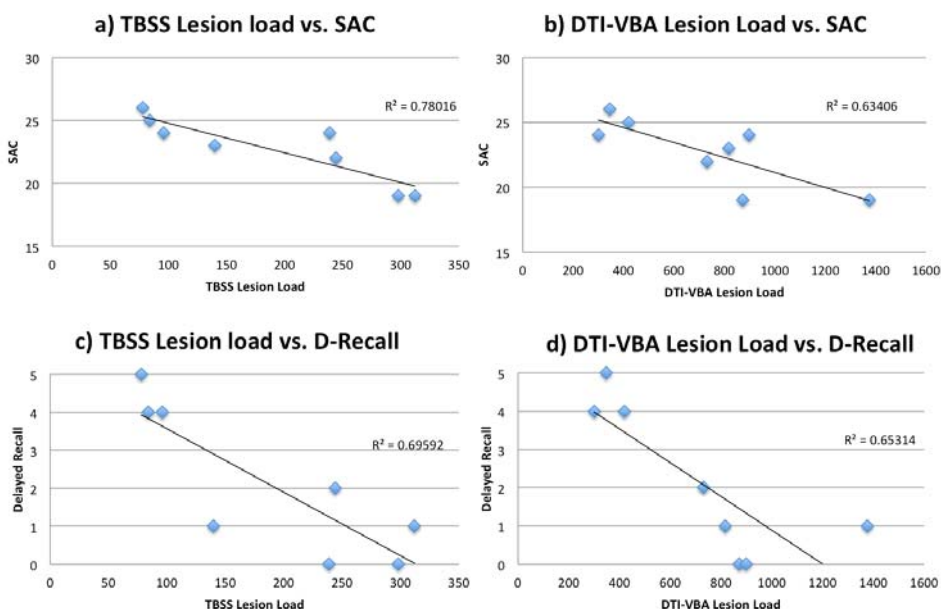


**Figure 14:** Correlations between DTI lesion load and patients' neurocognitive data. As demonstrated in the figures, DTI lesion load (both TBSS and VBA data) are significantly correlated with patients' overall SAC score and delayed recall. R squared values are shown on each figure for linear regression.

**Correlation MR imaging data with blood biomarker data:** In addition to MR imaging, we also collected serum blood sample in a subset of patients and, for the first time, demonstrated the relationship between serum blood biomarkers and MRI findings. Our data demonstrated that a) serum blood biomarkers, including UCH-L1 and GFAP, significantly increased in mTBI (Figure 15), and b) GFAP levels are significantly higher in patients with intracranial bleeding than those without bleeding (Figure 16). This finding has never been reported before. It implies that a blood biomarker might be able to serve as a screening tool for MRI in the acute stage.

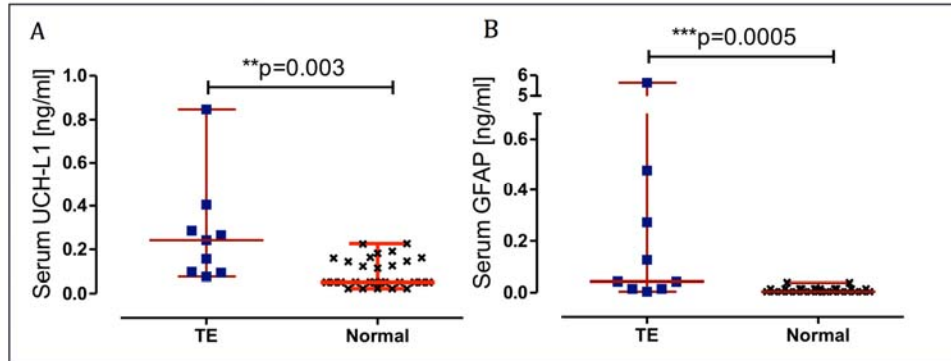


**Figure 15: Serum biomarker levels elevated in mTBI at the acute stage.** As shown above, mTBI patients' UCH-L1 and GFAP levels at the acute stage are significantly higher than demographically matched controls.

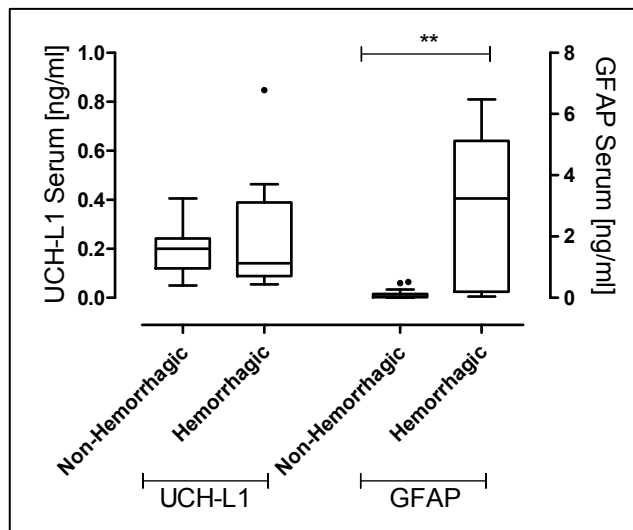


**Figure 16: Box-and-whisker plots demonstrating UCH-L1 and GFAP concentrations** in patients with ventricular hemorrhages and hemorrhagic contusions and in patients with non-hemorrhagic lesions. The black horizontal line in each box represents the median, with the boxes representing the interquartile range. Significant differences are indicated \* ( $P < 0.05$ ) or \*\* ( $P < 0.01$ ) (Mann–Whitney U-test).

## Connectome-scale Assessment of Brain Connectivity after mTBI

In addition to analysis of specific white matter tracts or certainly functional networks, we also adopted a novel analytical approach for DTI and fMRI analysis, called dense individualized and common connectivity-based cortical landmarks (DICCCOL). Instead of co-registering each individual subject onto a normalized template to define each functional network, which overlooks the individual variations, DICCCOL approach defines 358 individualized functional region of interests (ROIs) or network nodes for each subject and also consistent across the group. Our DICCCOL analysis of acute state mTBI identified 41 discrepant functional nodes among total 358 nodes. The emanating white matter fibers from these 41 discrepant nodes are significantly different between mTBI patients and controls, which is likely caused by the brain injury. As shown in Figures 17 and 18, the structural connectivity changes are cross the whole brain, involving almost all of the major white matter tracts.

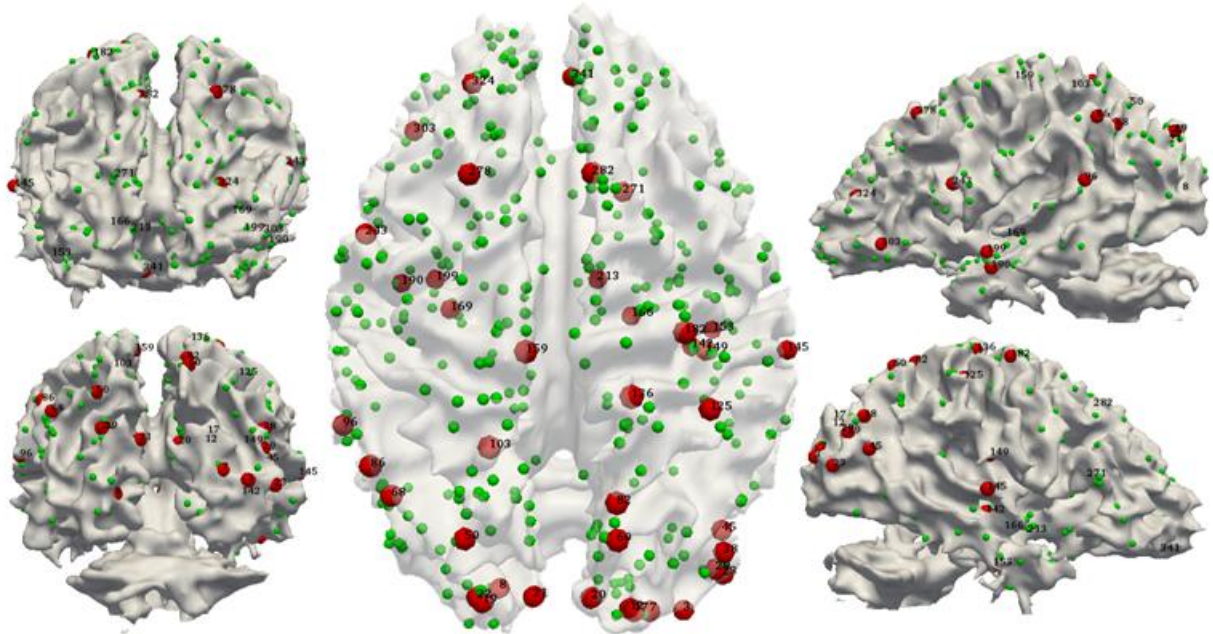


**Figure 17:** Visualization of location of discrepant nodes (landmarks) (red sphere) and the common nodes (landmarks) (green sphere) on cortical surface. IDs of discrepant nodes are labeled. Discrepant nodes are those landmarks from which emanating white matter fibers showing group difference between mTBI patients and controls.

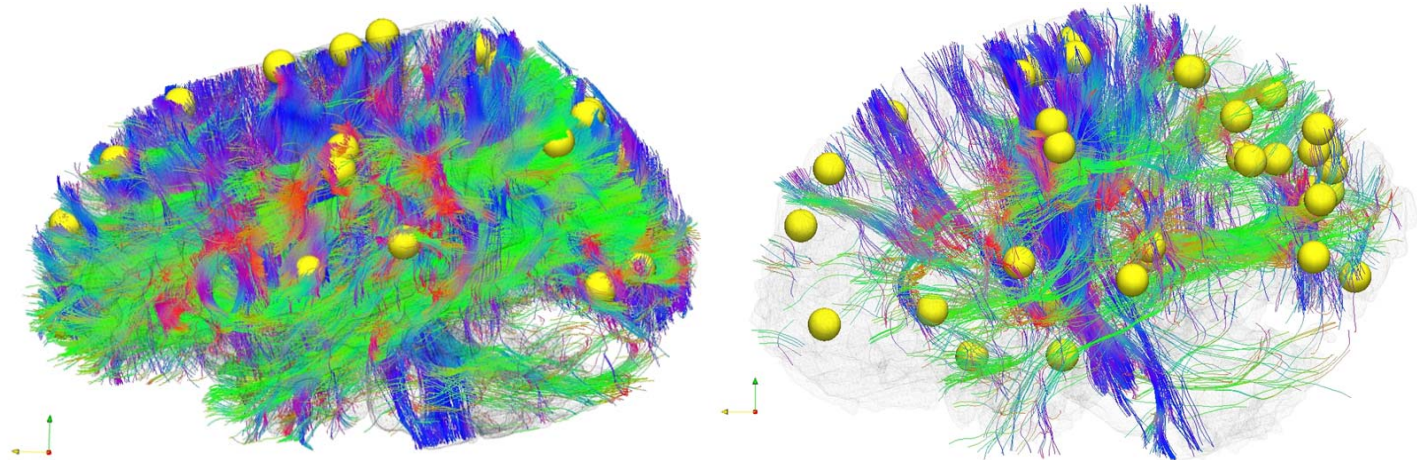


**Figure 18:** Comparison of white matter fibers emanating from discrepant nodes between a healthy control (left) and a mTBI patient (right), both are randomly chosen. The yellow bubbles are the discrepant functional

landmarks. As shown in the figure, the mTBI patient's white matter tracts are significantly affected by the injury at the whole brain level.

We performed functional connectivity analysis of those 317 common functional nodes. We identified 60 functional connectivity networks as the most distinctive and discriminative features of our data to differentiate patients from healthy control subjects, and labeled them connectomic signatures. As shown in Figure 18, in addition to structural changes over the whole brain, functional connectivity changes of the brain in the resting state are at a large scale across the whole brain. Our work represents the first connectome-scale analysis of TBI.

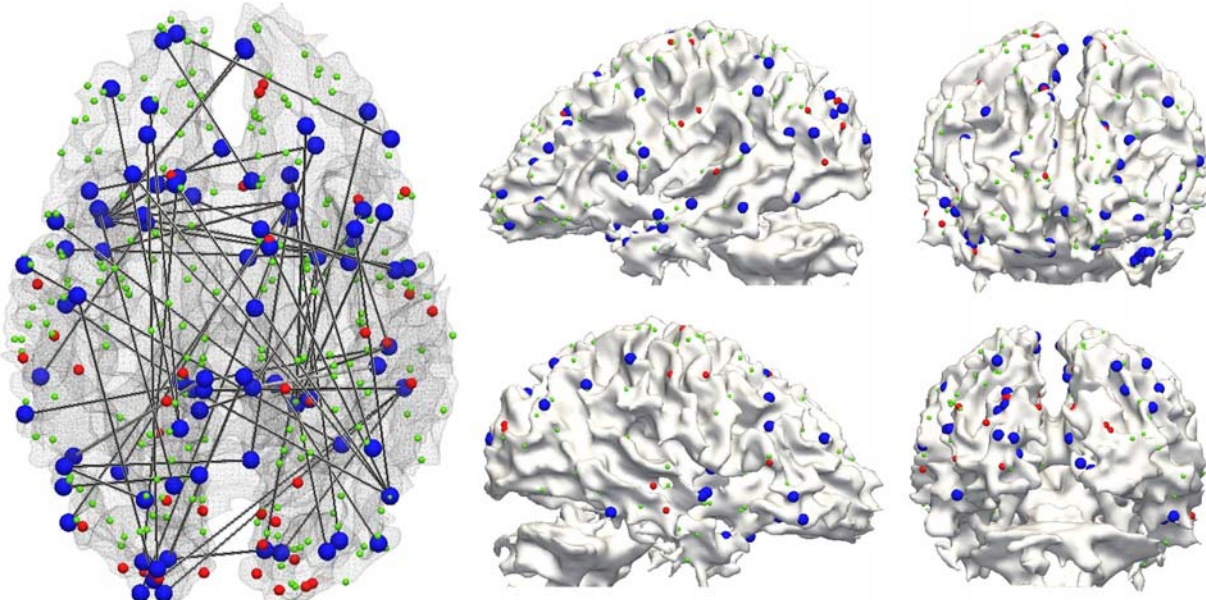


**Figure 19:** Visualization of discriminative functional connectivities at resting state (gray lines) between mTBI patients and normal controls and the location of related functional landmarks. The landmarks were represented by color-coded spheres (blue: common landmarks with discriminative functional connectivities; red: discrepant landmarks with discriminative structural connectivity; green: rest common DICCCOLs without showing discriminative functional connectivity).

## Summary of Work

Our data demonstrated that we have successfully accomplished Phase I study, Technical Development, for SWIM and related pilot data collection. We have made significant advances in the development of the SWIM technique. Further application into clinical studies suggest that 1) advanced MRI improves detection of mTBI over CT and cMRI (9, 20); 2) SWIM can quantify traumatic hemorrhage and blood oxygen saturation. In some cases, mTBI patients have demonstrated abnormal venous blood oxygen saturation at the acute stage, which tends to return to normal levels over time (1, 2); 3) traumatic hemorrhagic is related with the changes in serum blood biomarker elevations, particularly GFAP increase, in mTBI patients; 4) mTBI induces both cerebral hemodynamic disturbance and functional network disruptions (15); 5) DTI lesion load accounts for mTBI neurocognitive symptoms at the acute stage (9); and 6) brain injury in both structural connectivity and functional connectivity are at connectome scale. Of particular note, the investigation of cerebral hemodynamics and functional networks as well as serum blood biomarkers were not in the original plan. ***This work exceeds what was promised in content in the original proposal.***

Meanwhile, **our Aims were originally planned for a two-phase study in a large number of patients.** To fully achieve these aims set forth for two phases, it is critical to continue the Phase II Clinical Application.

## KEY RESEARCH ACCOMPLISHMENTS

The following accomplishments have been made in the past two years:

- Developed SWIM technical for traumatic hemorrhage quantification and venous blood oxygenation measurement.
- Validated the susceptibility measurement of irons in hemorrhage.
- Quantified the susceptibility difference between hemorrhage and venous blood oxygenation.
- Recruited and followed up an initial cohort of patients and controls. We have recruited 44 mTBI patients from the emergency department and followed them up at the 1 month and 6 months after injury for both imaging and neuropsychological assessment.
- Applied SWIM technique into mTBI. Our data demonstrated that in addition to small hemorrhages in a small fraction of patients, mTBI also demonstrated venous blood oxygenation changes at the acute stage and then returned back to normal at the subacute stage.
- Integrated other advanced imaging techniques, including DTI, perfusion, and fMRI, for mTBI detection and outcome prediction. Our data suggest that, in addition to an increased cerebral blood flow as an early response to brain concussion, mTBI patients show demonstrated white matter injury, measured by DTI lesion load, and changes of functional connectivity. DTI lesion load is negatively correlated with mTBI neurocognitive performance at the acute stage.
- Combined serum blood biomarker with advanced MRI for an improved detection and outcome prediction. Our data demonstrated that GFAP levels significantly increased in intracranial hemorrhage cases. This implies serum blood biomarker might be used as a screening tool for MRI identification of traumatic hemorrhages.
- Disseminated our findings regularly to the TBI neuroscience community and the military.

## REPORTABLE OUTCOMES

### Papers and book chapters:

- 1) S. Liu, J. Neelavalli, Y.-C. N. Cheng, J. Tang, and E. M. Haacke, *Quantitative susceptibility mapping of small objects using volume constraints*, Magn. Reson. in Med., vol. 69, no. 3, pp. 716-723, 2013.
- 2) J. Tang, S. Liu, J. Neelavalli, Y.-C. N. Cheng, S. Buch, and E. M. Haacke, *Improving susceptibility mapping using a threshold-based k-space/image domain iterative reconstruction approach*, Magn. Reson. in Med., vol. 69, no. 5, pp. 1396-1407, 2013.
- 3) W. Zheng, H. Nichol, YC Cheng, EM Haacke. *Measuring iron in the brain using quantitative susceptibility mapping and X-ray fluorescence imaging*. [Neuroimage](#), Sep;78:68-74, 2013.
- 4) Zhifeng Kou, Ramtilak Gattu, Firas Kobeissy, Robert Welch, Brian O'Neil, John Woodard, Sayed Imran Ayaz, Andrew Kulek, Robert Kas'shamoun, Valerie Mika, Conor Zuk, Francesco Tomasello, Stefania Mondello. *Combining Biochemical and Imaging Markers to Improve Diagnosis and Characterization of Mild Traumatic Brain Injury in the Acute Setting: Results from a Pilot Study*. PLoS One. 2013 Nov 19;8(11):e80296. doi: 10.1371/journal.pone.0080296.
- 5) Zhifeng Kou, Pamela VandeVord. *Traumatic White Matter Injury and Glial Activation*. GLIA, invited review. In press.

- 6) Zhifeng Kou, Armin Iraji. *Imaging Brain Plasticity after Trauma*. Neural Regeneration Research. 9(7): 693-700. 2014.
- 7) Zhifeng Kou and E Mark Haacke. *Neuroimaging of Mild Traumatic Brain Injury*, in *Concussions in Athletics: From Brain to Behavior*. Edited by Semyon M. Slobounov and Wayne Sebastianelli. Springer, 2013.
- 8) Benson RR, Gattu R, Sewick B, Kou Z, Zakariah N, Cavanaugh JM, Haacke EM. *Detection of hemorrhagic and axonal pathology in mild traumatic brain injury using advanced MRI: implications for neurorehabilitation*. NeuroRehabilitation. 2012;31(3):261-79. doi: 10.3233/NRE-2012-0795.
- 9) Feng W, Neelavalli J, Haacke EM. *Catalytic multiecho phase unwrapping scheme (CAMPUS) in multiecho gradient echo imaging: Removing phase wraps on a voxel-by-voxel basis*. Magn Reson Med. 70(1):117-26, 2013.
- 10) Y. Ye, J. Hu, D. Wu, E.M. Haacke., *Noncontrast-enhanced magnetic resonance angiography and venography imaging with enhanced angiography*. J Magn Reson Imaging, 2013. 38(6): p. 1539-48.
- 11) Ye, Y., J. Hu, and E.M. Haacke, *Robust selective signal suppression using binomial off-resonant rectangular (BORR) pulses*. J Magn Reson Imaging, 2014. 39(1): p. 195-202.
- 12) E.M. Haacke, W. Raza, W. Bo and Z. Kou. *The Presence of Venous Damage and Microbleeds in Traumatic Brain Injury and the Potential Future Role of Angiographic and Perfusion Magnetic Resonance Imaging in Cerebral Blood Flow, Metabolism, and Head Trauma: The Pathotrajectory of Traumatic Brain Injury*, Chapter 4, editors C. W. Kreipke and J. A. Rafols, Springer, 2012.
- 13) Sagar Buch, MS<sup>1</sup>, Yu-Chung Norman Cheng, Ph.D.<sup>2</sup>, Jaladhar Neelavalli, Ph.D.<sup>2</sup>, E. Mark Haacke, Ph.D.<sup>1-3</sup> *Susceptibility Mapping of Air, Bone and Calcium in the Brain using Short Echo Times. Conditionally accepted in MRM, 2014.*
- 14) Armin Iraji, Robert Welch, Brian O'Neil, Randall Benson, Syed Imran Ayaz, Andrew Kulek, E Mark Haacke, Zhifeng Kou. Resting State Functional Connectivity in Mild Traumatic Brain Injury in the Acute Setting. In submission.
- 15) Armin Iraji, Hanbo Chen, Robert Welch, Brian O'Neil, E Mark Haacke, Tianming Liu, Zhifeng Kou. Connectome-scale assessment of mild traumatic brain injury at the acute stage. In submission.
- 16) Jun Liu, Shuang Xia, Robin Hanks, Changya Peng, E Mark Haacke, Zhifeng Kou. *Susceptibility Weighted Imaging and Mapping of Small Hemorrhages after Traumatic Brain Injury*. In submission.

## **Presentations:**

Our group has given numerous presentations in national and international meetings. These include:

### *Student oral presentations:*

Hardik Doshi, *Cerebral Hemodynamic Changes in Mild Traumatic Brain Injury at the Acute Stage*. Feb 7. 2014. San Francisco, California.

Hardik Doshi, *Hemorrhagic Lesions Based on Venous and Arterial Damage and its Clinical Correlation in Traumatic Brain Injury*. Feb 7. 2014. San Francisco, California.

Hardik Doshi, *Volumetric analysis of cingulum in retired NFL players: Its relationship with NFL experience and subjects' cognitive and functional performance*. 2014 Annual Conference of International Society for Magnetic Resonance in Medicine. May, Milan, Italy.

Meeting Poster:

Jie Yang, Zhifeng Kou, Robert Dean Welch, Randall Benson, Ramtilak Gattu, Valerie Mika, and E. Mark Haacke. Neuroimaging biomarkers of mild traumatic brain injury (mTBI) and its recovery: A preliminary study in acute setting 30pm. 21st Annual ISMRM Salt Lake City, 2013. Electronic poster 3561.

Invitations to speak for Prof. Haacke and Prof. Kou

Human Brain Mapping Society, SWIM, June 29th, 2011, Quebec City, Canada, Prof. Haacke.

NABIS Meeting, Brain Trauma, September 15th, 2011, New Orleans, Louisiana, Prof. Kou.

Wayne State University, TBI Workshop, New venous concepts in TBI, November 18, 2011, Detroit, Prof. Haacke

Wayne State University, TBI Workshop, Mild TBI, November 18, 2011, Detroit, Prof. Kou.

Henry Ford Hospital. The role of the vasculature in neurodegenerative disease with a focus on TBI and CCSVI. January 5th, 2012, Detroit, Prof. Haacke.

The Society for Cardiovascular Magnetic Resonance. CCSVI: Abnormal Venous Flow and Neurodegenerative Disease. ) American Society of Functional Neuroradiology (ASFNR) 6th Annual Scientific Meeting. March 7th, 2012. Orlando, FL, USA, SWI, oxygen saturation and TBI, Prof. Haacke

19th Annual Audiology Conference at the VA Hospital in Johnson City, Tennessee, on June 21st, 2012, Susceptibility weighted imaging and TBI, Prof. Haacke

2012 Annual National Neurotrauma Symposium, Phoenix, AZ. Susceptibility weighted imaging and mapping in traumatic brain injury. Prof. Haacke and Prof. Kou.

Penn State University Brain Concussion Workshop, 2012. Neuroimaging of mild traumatic brain injury at the acute stage, Prof. Kou

10th Annual Society for Brain Mapping and Therapy, Baltimore, 2013, Development of MRI Biomarkers for Improved Diagnosis of TBI, Prof. Haacke and Prof. Kou.

ISNVD, San Francisco, February 7-9, Marines Memorial Club and Hotel, special session on TBI and venous abnormalities, organized by Prof. Haacke.

4th Annual Meeting of International Society for Neural Vascular Diseases. Feb 7. 2014. San Francisco, California. The Role of Imaging and Venous Abnormalities in Traumatic Brain Injury, Prof. Kou.

**Grants, Honors and Awards**

A major award (Seed Grant Award) was received by Dr. Zhifeng Kou from the International Society for Magnetic Resonance in Medicine (ISMRM) to investigate the relationship between MR imaging and blood biomarkers in acute detection and outcome prediction of mTBI.

Zhifeng Kou won the prestigious Charles Hayes award from the North American Brain Injury Society (NABIS) in 2011.

Zhifeng Kou, Session Chair and Moderator for Next Generation Imaging session, 2012 National Neurotrauma Symposium meeting.

Zhifeng Kou, Session Chair and Moderator for Clinical Study session, 2014 National Neurotrauma Symposium meeting.

### List of Personnel Receiving Pay from this Research Effort:

Syed Ayaz, Anamika Chaudhary, E. Mark Haacke, Jiani Hu, Robert Kas-Shamoun, Yashwanth Katkuri, Zhifeng Kou, Zahid Latif, Andria Norman, Brian O'Neil, Annalise Rahman, Craig Thomas, Robert Welch, John Woodard, Bo Wu, Yang Xuan and Yongquan Ye.

## CONCLUSION

During the last two years we have made significant progress in SWIM technical development and its clinical application. We have developed SWIM technique to quantify traumatic hemorrhage over time and venous blood oxygenation. SWIM technique has the potential to quantify the recovery of brain injury. Our data also demonstrated that advanced MRI, including DTI, fMRI and perfusion, can improve the detection of microstructural, functional, and physiological aspects of the brain injury. Our data suggest that SWIM, along with other advanced MRI techniques, should be incorporated into clinical radiology practice to improve the detection of brain injury on daily basis. Meanwhile, a continuous collection of more clinical cases will certain help make more meaningful conclusions in mTBI outcome prediction.

## REFERENCES

1. Kou Z, Doshi H, Yang J, Gattu R, Mika V, Ma G, Benson RR, Welch RD, Woodard J, Millis S, Haacke EM, in *Annual Conference of International Society for Magnetic Resonance in Medicine*. (Melbourne, Australia, 2012).
2. Haacke EM, Tang J, Neelavalli J, Cheng YCN, Susceptibility Mapping as a Means to Visualize Veins and Quantify Oxygen Saturation *JMRI* **32**, 663 (2010).
3. L. S. Tang J, Neelavalli J, Cheng Y.C.N, Buch S, Haacke EM, Improving Susceptibility Mapping Using a Threshold-Based K-Space/Image Domain Iterative Reconstruction Approach. *Magn Reson Med In press*, (2012).
4. N. H. Zheng W, Liu S, Cheng YC, Haacke EM, Measuring iron in the brain using quantitative susceptibility mapping and X-ray fluorescence imaging. *NeuroImage* **78**, 68 (2013).
5. H. J. Ye Y, Wu D, Haacke EM, Noncontrast-enhanced magnetic resonance angiography and venography imaging with enhanced angiography. *JMRI* **38**, 1539 (2013).
6. Y. Y. Haacke EM, The role of susceptibility weighted imaging in functional MRI. *Neuroimage* **62**, 923 (2012).
7. E. M. Haacke, J. Tang, J. Neelavalli, Y. C. Cheng, Susceptibility mapping as a means to visualize veins and quantify oxygen saturation. *Journal of magnetic resonance imaging : JMRI* **32**, 663 (Sep, 2010).
8. Zhifeng Kou, Randall Benson, Valerie Mika, Ramtilak Gattu, LynnMarie Mango, Robert Welch, Scott Millis & E Mark Haacke, Advanced Magnetic Resonance Imaging of Mild Traumatic Brain Injury in Emergency Settings. *Brain Inj* **24**, 197 (2010).
9. Kou Z *et al.*, Combining Biochemical and Imaging Markers to Improve Diagnosis and Characterization of Mild Traumatic Brain Injury in the Acute Setting: Results from a Pilot Study. *PLoS ONE* **8**, e80296 (2013).
10. Mayer AR *et al.*, A prospective diffusion tensor imaging study in mild traumatic brain injury. *Neurology* **74**, 643 (2010).
11. Rutgers DR *et al.*, Diffusion tensor imaging characteristics of the corpus callosum in mild, moderate, and severe traumatic brain injury. *AJNR Am J Neuroradiol* **29**, 1730 (2008).

12. Kou Z, Wu Z, Tong KA, Holshouser BA, Benson RR, Hu J, Haacke EM, The Role of Advanced Magnetic Resonance Imaging Findings as Biomarkers of Traumatic Brain Injury *Journal of Head Trauma Rehabilitation* **In press**, (2010).
13. Zhen Wu, McMaster University (2009).
14. Wu Z, Li S, Lei J, An D, Haacke EM, Evaluation of traumatic subarachnoid hemorrhage using susceptibility weighted imaging comparing with CT. *Journal of magnetic resonance imaging* **In Press**, (2010).
15. Iraji A, Mika V, Yang J, Rahman A, Ma G, Welch RD, Benson RR, Millis S, Soltanian-Zadeh H, Haacke EM, and Kou EM, in *Annual Conference of International Society for Magnetic Resonance in Medicine*. (Salt Lake City, Utah, 2013).
16. Kou Z, Iraji A, Imaging brain plasticity after trauma. *Neural Regeneration Research* **9**, 693 (2014).
17. R. A. Hanks, L. J. Rapport, S. R. Millis, S. A. Deshpande, Measures of executive functioning as predictors of functional ability and social integration in a rehabilitation sample. *Archives of Physical Medicine & Rehabilitation* **80**, 1030 (Sep, 1999).
18. L. Price, D. Tulsky, S. Millis, L. Weiss, Redefining the factor structure of the Wechsler Memory Scale-III: confirmatory factor analysis with cross-validation. *J Clin Exp Neuropsychol* **24**, 574 (Aug, 2002).
19. S. R. Millis, C. T. Volinsky, Assessment of response bias in mild head injury: beyond malingering tests. *J Clin Exp Neuropsychol* **23**, 809 (Dec, 2001).
20. Kou Z, VandeVord PJ, Traumatic White Matter Injury and Glial Activation. *Glia* **In press**, (2014).

## **APPENDICES (PUBLICATIONS)**

# Traumatic White Matter Injury and Glial Activation: From Basic Science to Clinics

Zhifeng Kou<sup>1,2</sup> and Pamela J. VandeVord<sup>3,4</sup>

An improved understanding and characterization of glial activation and its relationship with white matter injury will likely serve as a novel treatment target to curb post injury inflammation and promote axonal remyelination after brain trauma. Traumatic brain injury (TBI) is a significant public healthcare burden and a leading cause of death and disability in the United States. Particularly, traumatic white matter (WM) injury or traumatic axonal injury has been reported as being associated with patients' poor outcomes. However, there is very limited data reporting the importance of glial activation after TBI and its interaction with WM injury. This article presents a systematic review of traumatic WM injury and the associated glial activation, from basic science to clinical diagnosis and prognosis, from advanced neuroimaging perspective. It concludes that there is a disconnection between WM injury research and the essential role of glia which serve to restore a healthy environment for axonal regeneration following WM injury. Particularly, there is a significant lack of non-invasive means to characterize the complex pathophysiology of WM injury and glial activation in both animal models and in humans. An improved understanding and characterization of the relationship between glia and WM injury will likely serve as a novel treatment target to curb post injury inflammation and promote axonal remyelination.

GLIA 2014;00:000–000

**Key words:** traumatic brain injury, traumatic axonal injury, diffuse axonal injury, glial activation, neuroinflammation, microglia, astrocyte, biomarkers, magnetic resonance imaging, neuroimaging, diffusion tensor imaging

## Introduction

Traumatic brain injury (TBI) is a significant public healthcare burden in the United States and worldwide. Each year, 1.7 million Americans suffer from a TBI (Faul et al., 2010; Kay, 1993; National Institutes of Health, 1999), with major causes including motor vehicle crash (MVC) accidents, falls, assaults, and sports. TBI has been referred to as "a silent epidemic" (Goldstein, 1990). After TBI, the cognitive, physical, and emotional symptoms and disabilities significantly impact the patients' quality of life and their family members. Currently 5.3 million Americans live in the shadow of TBI-related long-term disability (Thurman et al., 1999). The direct and indirect cost of TBI in the United States was around \$60 billion per year (Finkelstein et al., 2006). Traditionally, TBI has been classified into three categories of severity using Glasgow Coma Scale (GCS) score: mild (GCS 13–15), moderate (9–12), and severe (8 or below) (Teasdale and Jennett, 1974). Among

them, mild TBI (mTBI) accounts for the majority of the TBI cases (CDC, 2003).

Despite its name of "mild," the consequences of mTBI are not mild at all (CDC, 2003). It has been recognized that TBI is not a single event or single disease entity, but has a heterogeneous spectrum of pathophysiology and has progressive and complex consequences (Maas et al., 2007; Saatman et al., 2008). The underpinning pathophysiology involves hemorrhage, axonal shear injury, ischemic/hypoxic injury, and glial injury and reactivity (Maas et al., 2007), and can be classified pathoanatomically as either focal injury or diffuse injury. Focal injury or focal contusion tends to occur on the cortical surface of inferior frontal and temporal lobes and the inferior part of the cerebellum, where the surface of the basal frontal and temporal cortices impact or sweep across rigid inner table of the skull, sphenoid wing, and petrous ridges, leading to hemorrhagic contusion. However, focal injury patients have the potential for more favorable outcomes as

View this article online at [wileyonlinelibrary.com](http://wileyonlinelibrary.com). DOI: 10.1002/glia.22690

Published online Month 00, 2014 in Wiley Online Library ([wileyonlinelibrary.com](http://wileyonlinelibrary.com)). Received Oct 29, 2013, Accepted for publication Apr 23, 2014.

Address correspondence to Zhifeng Kou, Department of Biomedical Engineering, Wayne State University, Detroit, Michigan 48201, USA. E-mail: zhifeng\_kou@wayne.edu or Pamela J. VandeVord, School of Biomedical Engineering and Sciences, Virginia Tech University, Blacksburg, Virginia 24061, USA. E-mail: pvord@vt.edu

From the <sup>1</sup>Department of Biomedical Engineering, Wayne State University, Detroit, Michigan; <sup>2</sup>Department of Radiology, Wayne State University, Detroit, Michigan;

<sup>3</sup>School of Biomedical Engineering and Sciences, Virginia Tech University, Blacksburg, Virginia; <sup>4</sup>Salem VA Medical Center, Research & Development Service, Salem, Virginia.



compared with diffuse injury patients. Diffuse axonal injury (DAI), also called traumatic axonal injury (TAI), is more devastating and tends to result in long-term neurocognitive sequelae (Gennarelli, 1993). As the name implies, DAI or TAI manifests as multi-focal injury in clinical evidence. Major WM tracts, including subcortical WM, corpus callosum (CC), internal capsule, brain stem, and sometimes cerebellar, are the main locations susceptible to TAI (Adams et al., 1989; Grossman and Yousem, 2003). Mounting evidence suggests that even mTBI has diffuse manner of WM injury (Blumbergs et al., 1994), especially in MVC, due to the rotational motion or angular acceleration of the head *versus* neck during vehicle impact, which causes the shearing and stretching injury of brain WM (Adams et al., 1982, 1989).

Despite its clinical and social impact, DAI is very difficult to detect in the clinical setting. Because axonal damage occurs at the microscale level, it is technically challenging to diagnosis and study these injury events. Most DAI cases, especially in mTBI, have normal findings in conventional neuroimaging, including computed tomography (CT) and magnetic resonance imaging (MRI), although recent advances in MRI have improved detection of WM injury and patients' outcome prediction. Additionally, tremendous efforts in basic science have been invested to understand the cellular and molecular mechanisms of axonal injury. Although both basic and clinical research have made significant advancements, further studies are necessary to fill the translational gap.

To advance clinical patient care, it is important to understand the cellular injury mechanisms for effective diagnosis and treatment targets. The brain is a complex organ principally composed of neurons and glial cells. Although the number of neurons varies from one brain region to another, it is accepted that neurons make up less than 25% of the cells in the brain, yet are responsible for information processing and control of bodily functions. Astrocytes, which make up 30–65% of glial cells in the brain, are multifunctional cells whose roles range from homeostatic, information processing, and response to central nervous system (CNS) injury (Buffo et al., 2010). Microglia compose approximately 10% of total glial cells in the brain and function as the immune cell of the CNS, arriving first at the site of injury to initiate the inflammatory cascade (Parekkadan et al., 2008). Lastly, oligodendrocytes provide support to axons to produce the myelin sheath, which has several functions such as insulating axons. Myelin is 80% lipid and 20% protein and covers 99% of the axon surface. There is a high density of Na and K channels which allows for preserving the efficient conduction of action potentials down the axons (Poliak and Peles, 2003). These cells all work together to maintain a physiological homeostasis and functionality. The significance of glial cells to the CNS function and plasticity has only been noticed relatively recently;

over the last 25 years, glial cells have been demonstrated to be more than structural components of the brain. It has become clear that glial cells are intimately involved in the complexities of neural network system. Moreover, the importance of glia in TAI has come to the forefront in discussions to improve axonal regeneration and functional recovery. When the architecture of myelinated fibers becomes disrupted from injurious forces, the glial response to the primary injury and can be the deciding factor for axonal regeneration.

This article reviews the most recent advances in WM injury, from the advanced imaging perspective, with an emphasis on the relationship between glial injury and WM injury from basic science to clinical studies. Considering that both WM injury and glial activation could be different in immature and aged brains, the article mainly focuses on adult TBI. In the end, it highlights major gaps in the field and points to potential directions of investigation.

## Basic Science

### Traumatic Axonal Injury at Cellular Level

Axonal injury is a common pathological feature of TBI. Axons are known to be highly susceptible to mechanical forces produced during TBI and their viscoelastic properties lead to increased damage with high rate deformations. It has been thought that axonal disruption mainly occurs in primary injury (Adams et al., 1982; Gennarelli et al., 1982; Strich, 1961), and is caused by the stretching and shearing forces and strains at the moment of a direct impact. A number of studies have demonstrated that rapid stretching of axons induces axonal cytoskeleton impairment (Bain and Meaney, 2000; Tang-Schomer et al., 2010). Recent studies have branched into both experimental and computational models which serve to determine a threshold for various types of mechanical forces on axons (Hampton et al., 2013; Magdeian et al., 2012; Peter and Mofrad, 2012). Mounting evidence suggests that, except during severe impact which causes a significant portion of axons severed directly, most TAI is a temporal progression that starts from axonal impairment to final axonal disconnection to form the axonal retraction balls and neuronal death (Maxwell et al., 1993, 1997; Povlishock et al., 1983).

Although the exact mechanism of primary injury from the initial insult is still under investigation, several molecular cascades are known to be triggered by the acute deformation injury [see Stys (2005) and Büki and Povlishock (2006) for comprehensive reviews of general axonal injury mechanisms] (Büki and Povlishock, 2006; Stys, 2005). Briefly, the biomechanical stretching or shearing forces during impact will result in an impaired morphology and physiology in axons. This includes increased axolemmal membrane permeability through a mechanoporation mechanism (Pettus et al., 1994;

Pettus and Povlishock, 1996). Failure of the ion-pumping ATPases appears to be a primary event which includes the impairment of the Na-K ATPase, promoting ionic imbalance within the axon as  $\text{Na}^+$  enters and  $\text{K}^+$  is lost. Activation of  $\text{Na}^+$  channels triggers the voltage sensitive  $\text{Ca}^{2+}$  channels (Wolf et al., 2001), resulting in an increase of intracellular  $\text{Ca}^{2+}$  as storage units within the axon (endoplasmic reticulum) fail as a consequence of the energy depletion. Elevated levels of intracellular  $\text{Ca}^{2+}$  initiate calpain-mediated spectrin proteolysis (CMSP) (Roberts-Lewis et al., 1994; Siman et al., 1984). Spectrin provides cytoskeletal support of axon structure, so irreversibly cleavage in the CMSP process can destroy the cytoskeleton. Indeed, the CMSP cascade of processes includes spectrin compartmentalization (Büki et al., 1999), neural filament compaction (NFC) (Lee et al., 1987; Maxwell et al., 1997; Okonkwo et al., 1998), microtubular loss, and local mitochondrial swelling (Büki et al., 1999). As a result of CMSP, the affected axons will have impaired axoplasma transport and swelling, and some segments will have loosened myelin sheaths with pathologic formation of a periaxolemmal space (Büki et al., 1999). Finally, due to excessive sequestration of  $\text{Ca}^{2+}$ , the opened mitochondrial membrane permeability transition pore will further damage the local mitochondria (Büki and Povlishock, 2006).

The pathological increase of  $\text{Na}^+$  and  $\text{Ca}^{2+}$  within the axoplasm leads to collapse of several other transporters, most notably the Na-dependent glutamate transport, initiating the release of glutamate from the axon and glial cells. The high levels of extracellular glutamate lead to an overstimulation of voltage-gated channels leading to further ionic disruption within the axon and contributing to conduction abnormalities. The injured axons will lead to a destroyed ionic homeostasis environment (Büki and Povlishock, 2006). Another devastating consequence of mitochondrial swelling is the release of pro-apoptotic substances (Krajewski et al., 1999; Mancini et al., 1998; Susin et al., 1999) that lead to activation of the caspase death cascade (Cai et al., 1998; Montal, 1998; Susin et al., 1998, 1999). The caspase death cascade will eventually lead to irreversible structural proteolysis to the injured axons and ultimate disconnection (Bal-Price and Brown, 2001; Borutaite et al., 1999; Büki and Povlishock, 2006). The continuous supply of cellular organelles in proximal axonal segment will accumulate at the disconnected end of axons to form axonal retraction balls, which can be detected by both silver staining and an immunochemical technique beta-APP as a hall marker of axonal disruption. The proximal segment will eventually undergo atrophy and lead to cell death (Büki and Povlishock, 2006), while the distal segments of disconnected axon undergo Wallerian degeneration over weeks to months in human (Büki and Povlishock, 2006). Evidence also suggests that the amount of degenerated

nerve terminals downstream far exceeds the number of actually injured axons, which implies a diffuse deafferentation and provides possibility of neuronal plasticity in recovery process (Phillips et al., 1994; Phillips and Reeves, 2001).

This complex cascade of molecular events following TAI has been and continues to be the target of therapeutic strategies to protect the axons from degeneration. Although the intra-axonal cascades are ongoing, it is clear that surrounding glial cells play a key role in maintain a healthy environment for axons following TAI. Local astrocytes and microglia release a number of different molecules which contribute to neuronal survival, axonal preservation, and regeneration. Although the knowledge about the precise role glia play in TAI is still unknown, several protective factors have been identified which promoted axonal repair and functional recovery.

### **The Role of Glial Cells in Normal Brain Condition and Its Relationship with WM Injury**

**Astrocyte Behavior in Normal and Injured WM Tissue.** Astrocytes function to not only provide mechanical support the mature neuronal circuits but also provide growth cues to neurons during axonal regeneration, buffer neurotransmitters (specifically glutamate) and ions released during neuronal signaling, help control the chemical environment of the neurons, transfer nutrients across the blood brain barrier, and modulate the firing activity of neurons (Fitch and Silver, 2008; Negi et al., 2010; Polikov et al., 2005). Astrocytes are a major source of extracellular matrix (ECM) proteins and adhesion molecules such as laminin, fibronectin, cytactin, and nerve cell adhesion molecule (N-CAM) (Miller and Peppas, 1985). They produce growth factors to regulate the morphology, proliferation, differentiation, and survival of neuronal subpopulations *in vivo* and *in vitro* (Oberheim et al., 2012). Astrocytes contain ion channels for  $\text{K}^+$ ,  $\text{Na}^+$ ,  $\text{Cl}^-$ ,  $\text{HCO}_3^-$ , and  $\text{Ca}^{2+}$ . Most WM astrocytes are considered to be fibrous in appearance and have long processes which establish perivascular endfeet and extensions that contact axons at the nodes of Ranvier (Matute, 2010). They are critical for synaptogenesis and play an important role in synapse maintenance (Pfrieger, 2009a, 2009b, 2010). Understanding how astrocytes contribute to WM health is relevant to the development of therapeutic targets for clinical management of WM injury (Colangelo et al., 2012).

Astrocytes become activated (termed reactive gliosis) in reaction to CNS injury (Buffo et al., 2010). Moreover, astrocytes are responsible for blockading damaged areas after injury from the healthy brain tissue (Fitch and Silver, 2008; Nimmerjahn, 2009). Astrocytic activation occurs through a mechanism of hypertrophy and an upregulation of intermediate filaments such as glial fibrillary acidic protein (GFAP) and vimentin (Buffo et al., 2010; Gervasi et al., 2008; Seker



et al., 2010). Classically, reactive astrocytes form locally at the site of injury but are thought to migrate from distant sites (Seker et al., 2010; Squire et al., 2012; Turner et al., 1999). However, astrocyte migration historically has been determined from postmortem studies. New *in vivo* evidence has questioned whether astrocyte migration is occurring or if selective proliferation at the injury site is occurring (Bardehle et al., 2013). Studies have shown a variety of cytokines involved with either the initiation or modulation of reactive astrogliosis (Farina et al., 2007; John et al., 2003; Liberto et al., 2004; Rao et al., 2012). These cytokines include interleukin-1beta (IL-1 $\beta$ ), tumor necrosis factor alpha (TNF $\alpha$ ), and transforming growth factor beta 1 (TGF $\beta$ 1), of which astrocytes express receptors and result in an astrocytic reactive response. Astrocyte-derived cytokines such as IL-1 $\beta$  and TNF $\alpha$  are considered to promote neurotoxicity whereas TGF $\beta$ 1 is neuro-protective (Farina et al., 2007; John et al., 2003; Liberto et al., 2004; Rao et al., 2012).

**Microglial Behavior in Normal and Injured WM Tissue.** Microglia are termed the resident macrophages of the CNS. Like astrocytes, they are dispersed throughout the brain and occupy a specific territorial domain. Microglia have small somata and multiple fine processes that assist them in surveying the environment (Nimmerjahn et al., 2005). Microglia continuously migrate and sample their local environment, and they are the first cells at the site of injury. They work to promote neuroplasticity and axonal regeneration, in addition to the monitoring and pruning of synapses. The function of a potent microglial response and the release of cytokines following TBI remain controversial, as effects may be neuroprotective, neuroregenerative, or neurodegenerative.

Under pathological conditions, microglia rapidly respond and become activated (activated microglia). Activated microglia undergo essential morphological changes from a branched phenotype to active amoeboid cells (Aihara et al., 1995). Moreover, there is an upregulation of a variety of membrane receptors which include those which support phagocytosis. Microglia protect neurons by migrating to the site of injury surrounding damaged or dead cells. They clear debris from the area such as myelin, as myelin debris can act as a rate-limiting factor in the process of remyelination, hamper axon regeneration, and stimulate inflammatory responses (Kotter et al., 2011). They are also known to release neurotrophic factors such as nerve growth factor (NGF), brain-derived neurotrophic factor (BDNF), and neurotrophin-3 (NT-3) which aid in neuronal growth and survival (Parekkadan et al., 2008). Microglia also have detrimental effects, although, including secretion of various cytotoxic and neurotoxic factors that can lead to neuronal death (Streit et al., 2004). They release pro-inflammatory factors such as cyto-

kines and react to injury by secreting proteolytic enzymes to help degrade ECM and cellular debris (Fitch and Silver, 2008; Polikov et al., 2005). These pro-inflammatory cytokines include IL-1 $\alpha$ , IL-1 $\beta$ , IL-6, and TNF $\alpha$ , and the chemo-kine monocyte chemoattractant protein-1 (MCP-1) used in the recruitment of macrophages and additional microglial activation (Parekkadan et al., 2008). IL-1 specifically promotes microglial proliferation, activation of astrocytes, and is known to be upregulated following axonal injury. Microglia also secrete excitatory amino acids, such as glutamate, reactive oxygen intermediates, such as hydrogen peroxide, and reactive nitrogen intermediates, such as nitric oxide. Increasing evidence has demonstrated that microglial activation is a key component of neuropathology that occurs following single and repetitive brain injuries (Smith, 2013). Understanding the acute microglial response following injury may provide clues to improving chronic functional outcomes.

**Oligodendrocyte Behavior in Normal and Injured WM Tissue.** The central function of oligodendrocytes is to produce the myelin sheaths that surround CNS axons. Each oligodendrocyte may branch to form myelin on many axons within the surrounding tissue. Oligodendrocytes and their precursor cells (OPCs) are distributed throughout both gray and white matter of the CNS. They can provide trophic factors by the production of glial cell line-derived neurotrophic factor (GDNF), BDNF, and insulin-like growth factor-1 (IGF-1) (Dougherty et al., 2000; Du and Dreyfus, 2002). Oligodendrocytes have extremely high metabolic rates which are required to properly myelinate axons. As such, they consume large amounts of oxygen and ATP (McTigue and Tripathi, 2008), which makes them highly susceptible to the molecular consequences of tissue damage. Glutamate and other neurotransmitters triggering Ca<sup>2+</sup> signaling have a major role in both normal oligodendrocyte development and oligodendrocyte injury in WM disorders. Oligodendrocytes are known to undergo programmed cell death when exposed to excitotoxic damage, oxidative stress, and effects of specific cytokines and their death causes demyelination, impairment of axonal conduction, and ultimately axon death.

In response to WM injury, oligodendrocyte loss can occur from TAI events which lead to hypoxia and lack of metabolic requirements such as oxidative stress and mitochondrial injury, or as a result of exposure to inflammatory cytokines found in the environment. To promote axonal regeneration, OPCs become activated, undergoing proliferation, migration to the site of damage, and differentiation into mature myelinating oligodendrocytes. In both clinical injuries and experimental models, newly formed oligodendrocytes have been shown to replace the damaged myelin sheath in a process known as remyelination. When injuries cause a

significant loss of myelin, permanent loss of the myelin sheath can lead to functional deficits and irreversible axonal degeneration. Understanding the mechanism by which oligodendrocytes may support axon survival following injury is a current topic for the development of novel therapeutic avenues.

### **Glial Response to Traumatic Brain Injury**

When TBI occurs, quiescent glia of multiple types become rapidly activated in a process termed “reactive gliosis.” This process involves activated microglia initiating and sustaining astrocitic activation through the production and release of inflammatory mediators that in turn act on surrounding glia and neurons. This acute inflammatory process following the initial insult can function to regulate both degenerative and reparative events in the injured and recovering brain. This neuroinflammation, a term which only recently has been widely accepted and used, sensitizes neurons and facilitates the degeneration process (Mrak and Griffin, 2005; Streit et al., 2004). Glial activation causes morphological and functional changes within the cells which effect the neural–glial and glial–glial interactions. This response can cause dysfunction of synaptic connections, imbalances of neurotransmitter homeostasis, and potential axonal degeneration and neuronal death (Bal-Price and Brown, 2001). Because of the recent highlight of sport and military concussions, the concept of chronic neuroinflammation and WM injury has been discussed within the context of TBI. Historically, chronic neuroinflammation had been associated with neurological diseases, such as multiple sclerosis, instead of injury (Kutzenigg and Lassmann, 2014). However, several reports are linking single and repeated TBI events to chronic WM outcomes associated with neuroinflammation. Neuropathology in pre-clinical and clinical studies has provided evidence that glial cells are a central component to the chronic WM degenerative process (Glushakova et al., 2014; Mouzon et al., 2014; Sajja et al., 2014).

**Impact-Related TBI.** Experimental evidence that associates neuroinflammation with traumatic WM injury and chronic degeneration has been growing. Oligodendrocyte injury and related myelin loss have been reported following fluid percussion injury in rats, where studies have demonstrated a significant loss of mature oligodendrocytes and myelin for up to 21 days following injury (Flygt et al., 2013; Lotocki et al., 2011). This oligodendrocyte vulnerability may influence the ongoing inflammatory process. Several TBI rodent models have reported long-term activation of astrocytes and microglia as a consequence from a single impact event. Activated microglia contained myelin debris 4 weeks following injury (Kelley et al., 2007), and studies in mice have demonstrated that microglia play an important role in the pathogenesis of TAI

within the CC both acutely and chronically (Jacobowitz et al., 2012; Venkatesan et al., 2010). Using p38 $\alpha$  MAPK knockout mice, cytokine signaling pathways in microglia were found to inhibit chronic microglial activation, linking microglia activation to secondary neuropathologic sequelae after TBI (Bachstetter et al., 2013). Another study inducing sensorimotor cortex injury in rodents focused on deciphering the molecular mechanisms controlling the CNS glial reactivity to degeneration of axons in a CNS pathway (Basiri and Doucette, 2010) and found that microglial reactivity always preceded that of astrocytes by at least 1 week. A study on non-human primates demonstrated that microglia remain reactive at the site of WM injury for at least 12 months following TBI (Nagamoto-Combs et al., 2007). Repeated TBI models have also elucidated the role of glial activation in WM injury. Using a repetitive mild or “concussive” TBI mouse model, reactive microglia were observed to be located surrounding injured axons of several WM tracts and remained up to 7 weeks following injuries (Shitaka et al., 2011). Additional studies have used anti-inflammatory agents to demonstrate that reducing inflammation after repeated mild brain injury in rats leads to improved behavioral outcomes (d’Avila et al., 2012; Kabadi et al., 2012; Shultz et al., 2013).

**Blast-Related TBI.** The role of neuroinflammation as a chronic pathology with the military population suffering from blast exposure and TBI is a recent topic of investigation. A significant number of these individuals are presenting with clinical symptoms of neurodegenerative diseases and cognitive decline (Gavett et al., 2010). To further complicate the scenario, combat personnel can be and have been exposed to repeated concussions which could lead to the long-term sequelae (Elder et al., 2010). Clinical research indicates that TBI is associated with various cognitive deficits in memory, problem solving skills, and attention (Belanger et al., 2009, 2010; Hoge et al., 2008). Many individuals have delayed onset of these symptoms, which is one of the major issues associated with the diagnosis of those affected by TBI (Cawley and Mokadam, 2010; Kochanek et al., 2009).

Limited experimental research has been conducted focusing on the association between neuroinflammation and WM injury. Neuroinflammation has been commonly reported as an acute pathological response to blast (Leung et al., 2008). Some early studies identified both astrocytes and microglia as being key components in the neuropathology found after blast (Kaur et al., 1995, 1997a, 1997b). More recently, specific inflammatory markers have been found in animals exposed to blast (Ahlers et al., 2012; Dalle Lucca et al., 2012; Koliatsos et al., 2011; Readnower et al., 2010; Sajja et al., 2012a, 2012b, 2013; Vandevord et al., 2012). A significant up-regulation of mRNA and protein expressions of

**TABLE 1: Available Techniques Sensitive to White Matter and Glial Injury**

Imaging technique	Imaging target	Pros	Cons
PET	Specific glial activations	High sensitivity and specificity to glial injury	Use of radioactive tracers; short half life of radiotracer
FLAIR	Glial scar (gliosis)	Low sensitivity	Low-specificity
DTI	WM injury	High sensitivity	Low-specificity
DKI	Astrogliosis	High sensitivity	Low-specificity
DBSI	Whiter matter injury and glial infiltration	High sensitivity	Non-specific to what type of glial response

Note: PET-positron emission tomography, FLAIR-fluid attenuated inversion recovery, DTI-diffusion tensor imaging, DKI-diffusion kurtosis imaging, and DBSI-diffusion basis spectrum imaging.

pro-inflammatory mediators, such as interferon- $\gamma$  (IFN- $\gamma$ ) and MCP-1, have been found in the hippocampus of rats exposed to blast (Cho et al., 2013b). However, the link between neuroinflammation and axonal injury has not yet been established.

### **Imaging Characterization of WM Injury and Glial Reactivation**

Recent decades witnessed tremendous advancement of neuroimaging techniques, including MRI. Among advanced MRI techniques, diffusion tensor imaging (DTI) might be the most widely used technique with high sensitivity to WM injury. Several other techniques are also reported to be sensitive to glial injury as well. Table 1 summarizes the pros and cons of several imaging techniques.

**Diffusion Tensor Imaging.** Diffusion sequences are sensitive to TAI secondary to stretch and shear forces. DTI measures the bulk motion of water molecular diffusion in biological tissues (Le Bihan et al., 2001). It is most useful when tissues are anisotropic, that is, when diffusion is not equivalent in all directions, such as in skeletal muscle or axons in WM of the CNS (Le Bihan et al., 2001). The apparent diffusion coefficient (ADC) and fractional anisotropy (FA) (Conturo et al., 1996; Shimony et al., 1999) are two parameters derived from DTI that have been extensively studied in TBI. ADC is an estimate of the average magnitude of water movement in a voxel (regardless of direction), while FA is an index of the directional non-uniformity, or anisotropy, of water diffusion within a voxel (Le Bihan et al., 2001).

FA in WM is high when well myelinated axonal fibers are oriented in parallel within a voxel and low when fibers bundles are crossing (Alexander, 2005; Tuch et al., 2002) or have been damaged (Le Bihan et al., 2001). When axons are injured, as in acceleration/deceleration injuries (such as MVCs), diffusion anisotropy typically decreases (Kou et al.,

2010; Niogi and Mukherjee, 2010). Theoretically, loss of diffusion anisotropy could be the result of a number of axonal changes after injury (Song et al., 2002, 2003, 2005), including: (1) increased permeability of the axonal membrane, causing an increase in radial diffusivity; (2) swelling of axons and/or derangement of axonal cytoskeletal structure, causing reduced axial (longitudinal) diffusivity; (3) degeneration or demyelination in the chronic stage, causing increased radial diffusivity; and (4) loss of axons in the chronic stage, resulting in a more isotropic diffusivity. In contrast, other causes of FA increase after injury include: (1) cytotoxic edema, which decreases the extra cellular space and reduces radial diffusivity (Jiang et al., 2011; Lundbaek and Hansen, 1992; Sykova et al., 1994); (2) loss of crossing fibers; and (3) axonal regeneration and plasticity (Jiang et al., 2011). As DTI FA fails in crossing fiber areas, an alternative diffusion measure to FA is Shannon's entropy (Shannon, 1997), which has been reported to be more sensitive to axonal density rather than axonal orientation (Fozouni et al., 2013). This aids in distinguishing axonal remodeling after injury, in which fibers reorganize in different orientations (fiber crossing) (Fozouni et al., 2013).

In contrast, ADC, FA, and directionally selective diffusivities (longitudinal and radial components of diffusion) can help to better characterize brain injury pathologies. It has long been accepted that cytotoxic edema results in increased ADC and vasogenic edema causes a reduction in ADC (Unterberg et al., 2004). Song et al. was the first to use DTI directional diffusivity to characterize axonal pathology in mouse models of white matter injury (Song et al., 2002), reporting that decreased axial diffusivity is associated with axonal injury and dysfunction, and increased radial diffusivity is associated with myelin injury (Song et al., 2002, 2003, 2005).

**DTI Findings in Animal Work.** Despite its hypothetical explanation of DTI signature, there are very limited histological studies to reveal axonal and glial signature underneath the

abnormal DTI findings in TBI research. Mac Donald performed the validation of DTI findings in a controlled cortical injury (CCI) mouse model induced with moderate to severe TAI (Mac Donald et al., 2007a, 2007b). In the ipsilateral pericontusional region, they found the reduction of axial diffusivity, but no change of radial diffusivity, as well as a negative correlation between relative anisotropy (RA) (similar to FA) to the density of beta-APP immunohistochemical staining at the acute stage (within 24 h after injury) (Mac Donald et al., 2007b). This suggests that axonal disruption and breakdown of axonal cytoskeleton structure are the major pathology of TAI at the acute stage (Mac Donald et al., 2007b). Over 4 weeks after injury, the RA remains decreased with axial diffusivity “pseudo-normalized” and radial diffusivity increased, confirmed by histology of demyelination, edema, neurofilament compaction as well as axonal disruption (Mac Donald et al., 2007a). Furthermore, they also reported reactive astrogliosis since 4 days after injury and microglial activation at 4 weeks after injury (Mac Donald et al., 2007a). Taken together, their work depicts a systematic picture of temporal progression of axonal injury pathologies in association with DTI parameter changes, suggesting that changes of different directional diffusivities could represent different stages of the injury (Mac Donald et al., 2007a). The same group also conducted DTI imaging of a repetitive mild head injury model in mice. At 7 days after injury, they reported reduced axial and mean diffusivity as well as the strong correlation between reduced RA and silver staining, which is in line with their previous findings (Bennett et al., 2012). They also reported microglial activation at 7 days after injury (Bennett et al., 2012). However, it is still not certain to what extent microglial activation affects the DTI parameter changes, and the DTI parameters still cannot differentiate different pathophysiologies at the same stage.

Meanwhile, DTI offers macro-level measurement of overall WM effect of both axonal injury and glial activations. It has never been the case of pure WM injury after TBI. As reported by Johnson et al, inflammation and WM degeneration could persist for years after a single TBI (Johnson et al., 2013). Figure 1 shows the co-existence of microglial activation and axonal demyelination in CC among three patients who survived from TBI and later died of other causes (Johnson et al., 2013). The imaging measures, particularly DTI, use the bulk movement of water molecules in the injured WM environment as a surrogate marker of WM injury. This makes it sensitive to WM injury, but not specific to its underlying pathophysiology due to the abundance of water molecule in both axons and glial cells.

**Contribution of Astrogliosis to DTI Signature.** Budde et al. (2011) performed both *in vivo* and *ex vivo* DTI study of TBI in a rat CCI model to quantify the contribution of astrogliosis

to DTI findings at subacute to chronic stage. They reported an increase in FA in peri-lesion cortical area with axial (longitudinal) diffusivity increase but no change in radial (perpendicular) diffusivity; and a decrease in FA in peri-lesion WM (CC) with increased radial (perpendicular) diffusivity but no change of axial (longitudinal) diffusivity. Instead of directly correlating DTI finding with histology, they applied 2D-Fourier Transform to quantify the anisotropy of histology images so that they could correlate histology FA with DTI FA. They report that gliosis, as detected by GFAP immunohistochemistry, is correlated with increased cortical anisotropy; in contrast, WM demyelination (detected by myelin basic protein) is correlated with reduced WM FA (Budde et al., 2011). Taken together, their data show that reactive astrogliosis is the major contributor to the gray matter DTI finding and demyelination is the major contributor to the WM DTI finding at the subacute to chronic stages. This is also in the same line as Mac Donald’s work (Mac Donald et al., 2007a). Further, Budde et al. showed that the astrogliosis also affects DTI fiber tractography, suggesting that data leading to spurious conclusions of fiber crossing in lesioned gray matter may be caused by the glial activation instead of fiber reorganization (Budde et al., 2011).

**Diffusion Kurtosis Imaging of Astrogliosis.** One limitation of DTI model is a simplified assumption of a Gaussian distribution of water molecule diffusion. In reality, biological tissue is far more complex and many structures, including various types of cells and their membranes, could restrict water diffusion, and cause the decay of the diffusion signal to substantially deviate from its Gaussian distribution (Karger, 1985). This excess deviation from its Gaussian behavior, in return, could be used as a measure of a tissue’s degree of structure (Jensen et al., 2005; Jensen and Helpern, 2010). Especially when high *b*-values are used and the diffusion gradients are programmed to probe restricted diffusion in small molecular structure, the signal decay substantially deviates from Gaussian distribution (Fig. 2). As a model free approach, diffusion kurtosis imaging (DKI) measures the non-Gaussian distribution of the water molecular diffusion by estimating the deviation of water signal decay at high *b* values from its linear estimate in the DTI model (Jensen et al., 2005; Jensen and Helpern, 2010). This deviation can potentially reveal more information about brain tissue microstructure changes in normal conditions like moving from adolescence to adulthood (Falangola et al., 2008), which features increased myelination and cell packing density, and in pathological conditions like tumor (Falangola et al., 2013; Raab et al., 2010), ischemia stroke (Jensen et al., 2011), neurodegenerative diseases (Falangola et al., 2013), multiple sclerosis (Raz et al., 2013), and TBI (Jiang et al., 2011).

After injury, astrocyte proliferation and disrupted astrocyte domains as well as microglial activation make the brain

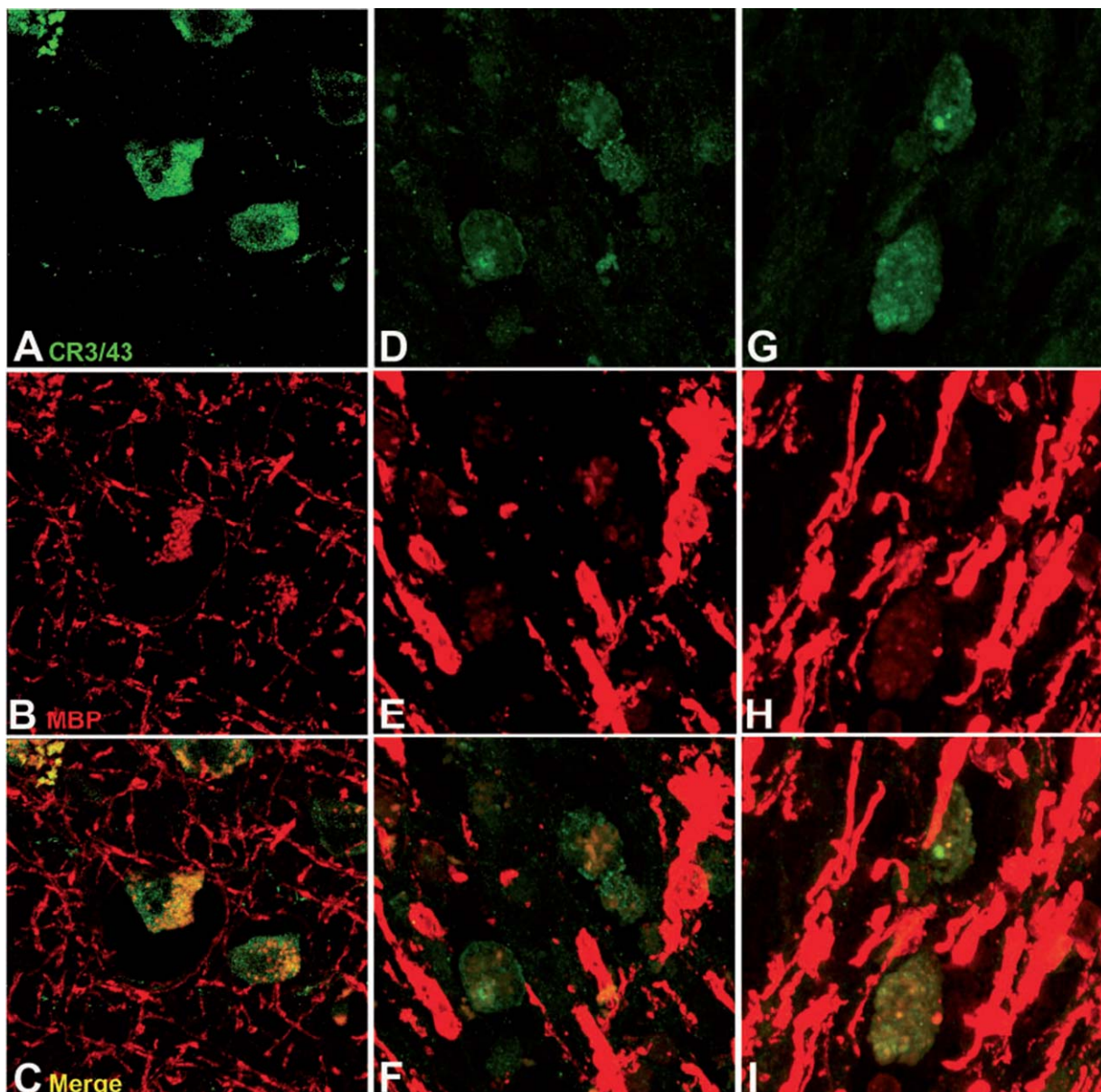


**FIGURE 1:** Representative images showing co-existence of microglial activation (CR3/43 labeling, green color) and demyelination (myelin basic protein labeling, red color) in the CC following survival from TBI. (A–C) A 67-year-old male 8 months following TBI caused by a fall. (D–F) A 44-year-old female 2 years post-TBI caused by a fall. (G–I) A 37-year-old male 4 years post-TBI caused by a fall. Note the co-localization of myelin basic protein immunoreactivity within CR3/43 reactive cells, indicating the co-existence of both white matter injury and microglial activation. Reproduced with permission from Johnson et al. (2013) and Oxford University Press.

microstructure more complicated and likely results in increased kurtosis (Sofroniew and Vinters, 2010). Zhuo et al. reported the use DKI to detect astrogliosis, validated by GFAP staining, in a rat CCI model (Zhuo et al., 2012). They reported an increase of Mean Kurtosis (MK) over baseline in association with increased reactive GFAP staining at the contra-lateral cortex at 7 days after injury, in which DTI failed to detect any changes over baseline (Zhuo et al., 2012). This suggests the potential use of DKI in detection of astroglial reactivity (see Fig. 3 as an example). However, in recent

clinical studies, Grossman et al. reported decreased, instead of increased, MK in mild TBI patients in comparison with controls and a correlation between MK in thalamus region and mTBI patients' neurocognitive status (Grossman et al., 2012, 2013). The seeming contradiction between animal models and clinical study suggests a far more complicated pathology spectrum than just glial activation in TBI. Despite its progress over DTI in the detection of glial response and microstructural changes, DKI still lacks specificity in identifying the underlying pathology.

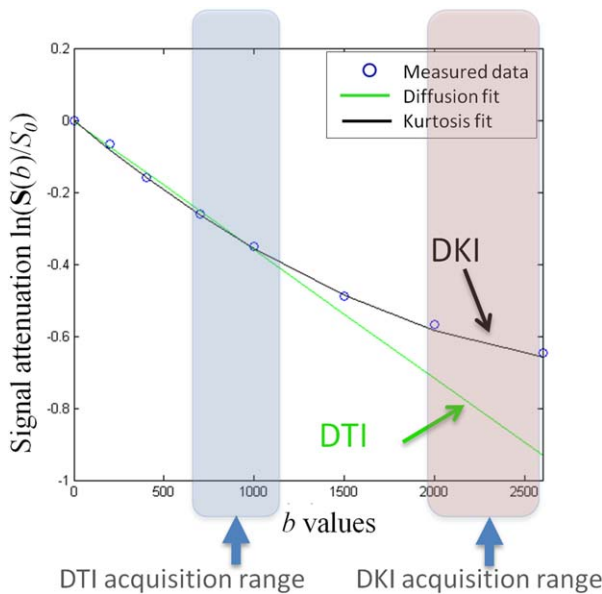


**FIGURE 2:** Comparison of DTI and DKI fitting models in a diffusion weighted imaging dataset obtained from the CC of rat brain using various  $b$ -values. For DTI, the logarithm of diffusion weighted signal intensity as a function of the  $b$ -value fits to a straight line for small  $b$ -values, up to  $1,000 \text{ s/mm}^2$ . When the  $b$ -values exceed  $1,000 \text{ s/mm}^2$ , the data fits the DKI model much better than the DTI model. Reproduced with permission from Zhuo et al. (2012) and Neuroimage Journal.

**Diffusion Basis Spectrum Imaging.** The complex pathologies in WM injury, including increased membrane permeability, derangement of axonal cytoskeleton, axonal swelling, loosened myelin sheaths, and even demyelination, all lead to changes of DTI diffusivities and FA. In addition, glial reactivation and edema, including both vasogenic and cytotoxic edema, also contribute to the changes of DTI FA, axial, or radial diffusivity (Anderson et al., 2000; Kuroiwa et al., 2009). To make it worse, the crossing fibers (Wheeler-Kingshott and Cercignani, 2009) and partial volume effects caused by CSF or gray matter (Karampinos et al., 2008) also cause DTI FA decreases. As a gross measure, DTI cannot effectively differentiate these underneath pathologies. Characterization of the pathology will likely shed light on potential treatment plans. A novel technique, diffusion basis spectrum imaging (DBSI), holds promise in this direction (Wang et al., 2011b). It considers the diffusion-weighted MR signal as a linear combination of multiple anisotropic and a spectrum of isotropic diffusion tensors. Among them, myelinated and unmyelinated axons are considered as anisotropic, and edema and glial cell infiltration due to inflammation or gliosis as isotropic. In addition, vasogenic edema and CSF have non-restricted water diffusion and have been recognized to result in elevated ADC (Kuroiwa et al., 2009; Naismith et al., 2010; Pasternak et al., 2009), while increased cellularity (astroglial or microglial infiltration) has restricted isotropic diffusion and likely result in

decreased ADC (Anderson et al., 2000). Using a certain data acquisition scheme as determined in a gradient table, DBSI could differentiate these anisotropic and isotropic signals (Wang et al., 2011b) (Fig. 4). As a result, after separating the isotropic contribution, the axial and radial diffusivities on DBSI are better correlated with the axonal injury or demyelination on histology data that DTI failed to detect. Furthermore, the separation of the isotropic effects also results in an improved reconstruction of crossing fibers with more correct angles (Wang et al., 2011b) over diffusion spectrum imaging, which is a popular fiber tracking algorithm (Wedgeen et al., 2005). For the isotropic part, the DBSI-derived cell ratio (restricted diffusion ratio) is significantly correlated with the density of cell infiltration measured in histology (Wang et al., 2011b). To date, DBSI might be the most promising MRI technique for characterizing brain injury pathology, including both axonal injury and glial activation. The interplay between inflammation and neurodegeneration at chronic stage is one area in particular which would benefit from such distinctions; being able to identify increased cellularity, as seen in neuroinflammation, from axonal loss or axonal swelling would be valuable in understanding the pathophysiology. This would be enormously informative in examining the changes in white matter tracts that occur over time after TBI. However, DBSI was originally developed for neuroinflammatory diseases like multiple sclerosis, and its potential in TBI research is yet to be fully investigated.

## Clinical Studies

Advances in basic science have tremendously enhanced our understanding of the pathophysiology of TAI and glial activation. Although clinical study has far less means than basic science to characterize the underlying pathology, advanced neuroimaging has allowed researchers to gain more insights into TAI for an improved detection of TBI and prediction of TBI patients' long-term neurologic and neuropsychological outcome. In diagnostic radiology, TAI is classified as hemorrhagic or non-hemorrhage, based on multi-focal hyper-intensities on fluid attenuated inversion recovery (FLAIR) image, edema on T2-weighted images or hemorrhage on T2-weighted gradient recalled echo (GRE) images (Grossman and Yousem, 2003). Because focal hemorrhagic lesions at major WM tracts were usually associated with microscopic diffuse axonal damage (Adams et al., 1982, 1989), these focal lesions have become clinical diagnostic markers of DAI/TAI. Hemorrhages are mostly seen at the junction of gray matter and white matter (GM/WM), the CC, and in the dorso-rostral quadrant of the brain stem (Grossman and Yousem, 2003). Susceptibility weighted imaging (SWI) is the most sensitive technique to detect hemorrhagic focal lesions (Haacke et al., 2004), and it has been reported three to six

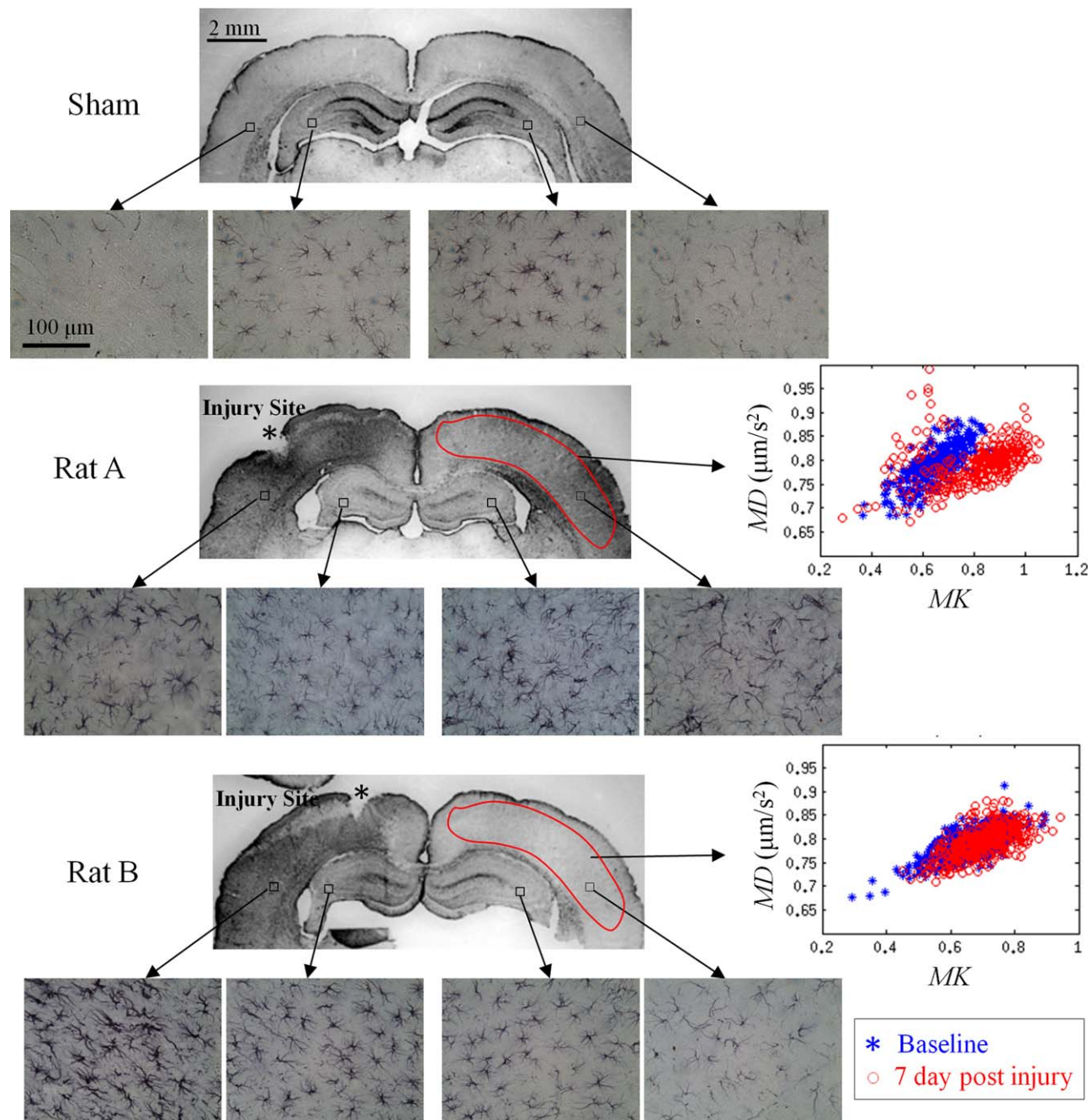


**FIGURE 3:** Comparison of immunohistochemical stains using glial fibrillary acidic protein (GFAP) in two representative CCI exposed rats (Rats A and B) at 7 days post-injury and a sham rat. In addition to increased GFAP immunoreactivity at the site of the injury, Rat A also expressed significantly elevated GFAP compared with Rat B in the contralateral cortex. Scattered plots are the mean Kurtosis (MK) versus mean diffusivity (MD) from the contralateral cortex of both rats. The GFAP stains ( $\times 40$  magnification) are shown from the ipsilateral cortex, hippocampus and contralateral hippocampus, cortex of each rat. Increased MK was associated with increased GFAP staining as in the case of Rat A while it remained the same among rats that did not show elevated GFAP staining as in the case of Rat B. However, no changes are seen in MD for Rat A between the baseline and 7 days post-injury despite an increase in MK. Reproduced from Zhuo et al. (2012) with permission.

times more sensitive to hemorrhage than gradient recalled echo (GRE) sequence, which is the clinical standard of hemorrhage (Tong et al., 2003). Higher lesion load has been reported being associated with unfavorable outcome after TBI

(Tong et al., 2004). Meanwhile, most DAI cases are non-hemorrhagic (Grossman and Yousem, 2003), in which cases DTI is the most widely used techniques for DAI detection and outcome prediction (Kou et al., 2010).

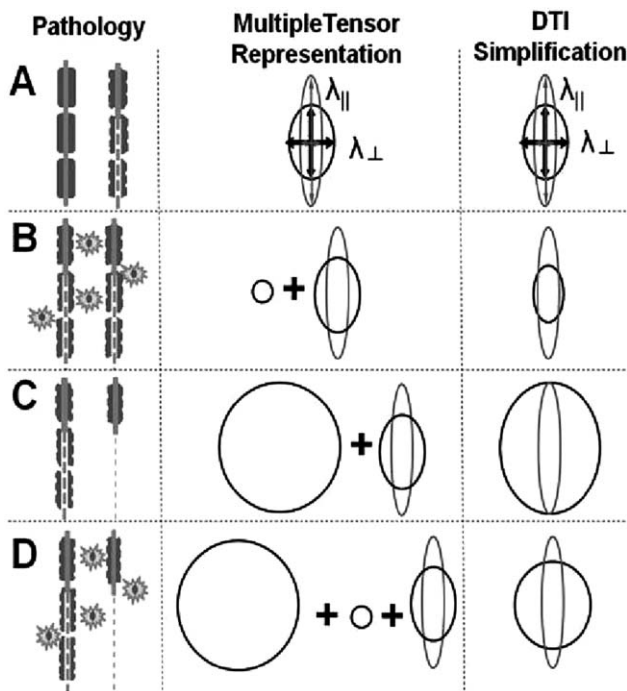


**FIGURE 4:** Schematic view of different white matter pathologies associated with multiple tensor representation and DTI simplification. Gray ellipsoid represents the diffusion tensor profile for normal myelinated white matter with axial diffusivity greater than radial diffusivity. Black drawings represent the diffusion profiles for multiple tensor representation or DTI simplification: (A) co-existing axonal and myelin injury of coherent pure myelinated axons; (B) axonal and myelin injury with cell infiltration; (C) axonal and myelin injury with axonal loss; and (D) axonal and myelin injury, cell infiltration, or proliferation and axonal loss. Reproduced with permission from Wang et al. (2011b) and Oxford University Press.

#### Temporal Progression of DTI Signature in TBI Patients

**Findings in Moderate to Severe TBI.** Similar to animal data showing a temporal progression of axonal injury, measured as changes of DTI parameters (Mac Donald et al., 2007a), clinical studies of TBI patients at different stages also report different DTI findings, suggesting a temporal progression of TBI pathology. All DTI studies of moderate to severe TBI patients (Benson et al., 2007; Kou et al., 2008; Levin et al., 2008; Newcombe et al., 2007) and subacute/chronic mTBI patients (Inglese et al., 2005; Jang et al., 2013; Kraus et al., 2007; Niogi et al., 2008a, 2008b; Rutgers et al., 2008; Wozniak et al., 2007) report FA decreases and/or ADC increase in major WM tracts that are correlated with clinical or neuropsychological measures in different degrees, interpreted as axonal injury and edema. Adnan et al. (2013) prospectively scanned 29 moderate to severe TBI patients at two time points: 5 months and 29 months after injury. They reported that the loss of WM continues in fornix, part of the memory network, in moderate and severe TBI patients even after the

acute neurological effects of TBI have resolved (Adnan et al., 2013). Similarly, Wang et al. did a DTI tractography study of 28 patients, mostly severe TBI, scanning them at both acute and chronic stages (Wang et al., 2011a). They reported that WM tract change over time was correlated with patients' long-term outcome (Wang et al., 2011a). This correlates with autopsy data that shows microglial activation continuing years after injury (Johnson et al., 2013).

**DTI Findings on Mild TBI.** In contrast to DTI studies of moderate to severe TBI, there are seemingly contradictory findings in mild TBI in the acute stage (within 1 week after injury) in the literature. Chu et al. (2010) and Wilde et al. (2008) (Wu et al., 2010) scanned 10–12 adolescents with mTBI within 6 days of injury and reported increased FA, reduced ADC, and reduced radial (perpendicular axis) diffusivity in WM regions and left thalamus. Similarly, Bazarian et al. (2007) studied six mTBI patients within 72 h of injury and reported increased FA in the posterior CC and reduced ADC in the anterior limb of the internal capsule (IC). Additionally, Mayer et al. (2010) studied 22 mTBI patients within 12 days of injury and reported increased FA and reduced radial diffusivity in the CC and left hemisphere tracts.

However, Inglese et al. (2005) found reduced FA in the splenium of CC and posterior limb of IC in 20 mTBI patients imaged up to 10 days after injury (mean = 4 days). In the same line, Arfanakis et al. (2002) studied a handful of mTBI patients at the acute stage and reported decreased FA in major WM tracts. Furthermore, Lipton et al. (2012) reported bi-directional changes (both increases and decreases) of FA in chronic mTBI patients. Bazarian et al. (2012) studied nine high school athletes with diagnosed concussion or multiple sub-concussive blows and also reported bi-directional changes of FA at chronic stages. Most recently, Kou et al. also reported bi-directional changes of FA at the hyperacute stage (within 24 h after injury) in mTBI patients with the increased FA as the dominant abnormality over reduced FA (Kou et al., 2013).

These seemingly conflicting results may make sense in the context of multiple simultaneous processes. One explanation of increased FA is cytotoxic edema (Wilde et al., 2008), particularly astrocyte swelling, because astrocytes are more susceptible to pathological swelling than neurons or axons (Liang et al., 2007). In animal models of stroke, astrocyte swelling initiates within 30 min of injury and results in an average reduction of extracellular space from the normal 20% down to 10% (Lundbaek and Hansen, 1992; Sykova et al., 1994). The shunted extracellular space will result in reduced axial diffusivity and increased FA in WM fiber tracts. Supported by the animal data that astrogliosis is associated with an increased FA in gray matter area (Budde et al.,



2011; Zhuo et al., 2012), the clinical studies suggest that astroglial activation could also be a significant pathology in mTBI patients at the acute stage that lead to increased FA. The bi-directional changes of FA may suggest the co-existence of both axonal injury (impaired axonal transportation and/or demyelination) and astroglial activation. All this evidence further demonstrates the heterogeneity of mTBI pathology at this stage and the necessity of developing new techniques that could better characterize both axonal injury and glial response.

**What do we Know and we do not Know.** It is clear that (a) TBI pathologies in human patients progress temporally; (b) glial cells likely play an important role during this progression; and (c) even at the same stage, the pathology may be heterogeneous across different populations. However, the underlying pathophysiology of this temporal progression is still not clear, due to the lack of necessary non-invasive imaging tools. Particularly, the role of glial reactivity in neuroprotection and repair at the acute and subacute stage as well as the role of neuroinflammation at the chronic stage are still unknown in clinical studies. Delineation of these roles could likely provide novel treatment target for TBI patients at different stages.

### **Mapping White Matter Injury with Higher Level Neurocognitive Deficits**

In clinical imaging, one important issue is to predict TBI patients' outcome at the early stage so that clinicians can institute proactive treatment or management plans, potentially including patients' family members preparing in advance for long term care, both financially and logistically. In moderate to severe TBI, the neurocognitive sequelae could easily last for years and even be lifelong in some patients. Among them, four major domains have been shown being widely existed in TBI patients: attention deficits, memory problems, deficits in speed of information processing, and deficits in executive functions. The most widely used neurologic outcome measure is Glasgow Outcome Scale score (GOS) or extended GOS (GOSE) (Wilson et al., 1998). In mild TBI, memory and attention deficits are major complaints (Dikmen et al., 1986a, 1986b; Levin et al., 1987; Macciocchi et al., 1996), in addition to a constellation of their post concussive symptoms (CDC, 2003). However, the pathophysiological underpinning of these functional, neurocognitive, physical, and emotional symptoms/deficits are still not well understood. It has been thought that disruption of certain functional and structural brain networks can account for the patients' symptoms (Kou et al., 2010; Niogi and Mukherjee, 2010). Major WM tracts, including the CC, the major tract that connects the two hemispheres; cingulum; long associa-

tion fibers, including superior and inferior longitudinal fasciculus; and WM structure in frontal and temporal lobes are well studied.

**Predicting Moderate to Severe TBI Outcome.** In moderate to severe TBI, Galanaud et al. performed a multicenter DTI study of 105 TBI patients at the subacute stage (Galanaud et al., 2012). They reported that DTI has a sensitivity of 64% and specificity of 95% for the prediction of patients' unfavorable outcome, measured as GOSE (Galanaud et al., 2012). Most recently, Spitz et al. studied 68 mild to severe TBI patients at the chronic stage (Spitz et al., 2013). They reported a significantly decreased FA in moderate to severe TBI patients and a trend of decreased FA in mild TBI. Decreased FA of major WM tracts has been shown to be strongly associated with patients' speed of information processing and executive abilities (Spitz et al., 2013). Arentz et al. (2014) studied 12 chronic TBI patients, ranging from complicated mild, moderate to severe severity, and reported decreased FA in the CC, in correlation with patients' impaired performance, both in terms of cognitive tasks and reaction time.

**Predicting mTBI Outcome.** As most mTBI patients have normal structural findings, outcome prediction of mTBI could be more challenging. It has been reported that damage to different WM tracts were related with patients' specific neurocognitive symptoms (Kou et al., 2012; Niogi and Mukherjee, 2010). Figure 5 summarizes the reported literature regarding functional mapping of structural WM abnormality with corresponding neurocognitive impairment in mTBI.

**Frontal WM Injury.** Damage to the frontal WM has been reported to be associated with impaired executive function and attention. Lipton et al. (2009) studied 20 acute to subacute patients and reported that reduced FA in WM of dorsolateral prefrontal cortex (DLPFC) is correlated with worse executive function. Niogi et al. (2008a, 2008b) reported that reduced FA in the left anterior corona radiata correlates with attention control in chronic mild TBI patients.

**Temporal WM and Cingulate Bundle Injury.** Injury at the temporal WM tracts or cingulum bundle may cause memory problems. Niogi et al. reported that reduced FA in the uncinate fasciculus correlated with memory performance (Niogi et al., 2008a, 2008b). Wu et al. (2010) reported that the FA of the left cingulum bundle correlated with delayed recall. Baek et al. (2013) performed a diffusion tractography study of chronic TBI patients and reported that the integrity of the basal forebrain and cingulum are associated with patients' overall cognition and memory. Similarly, Treble et al. (2013) performed diffusion tensor tractography study of 74 pediatric

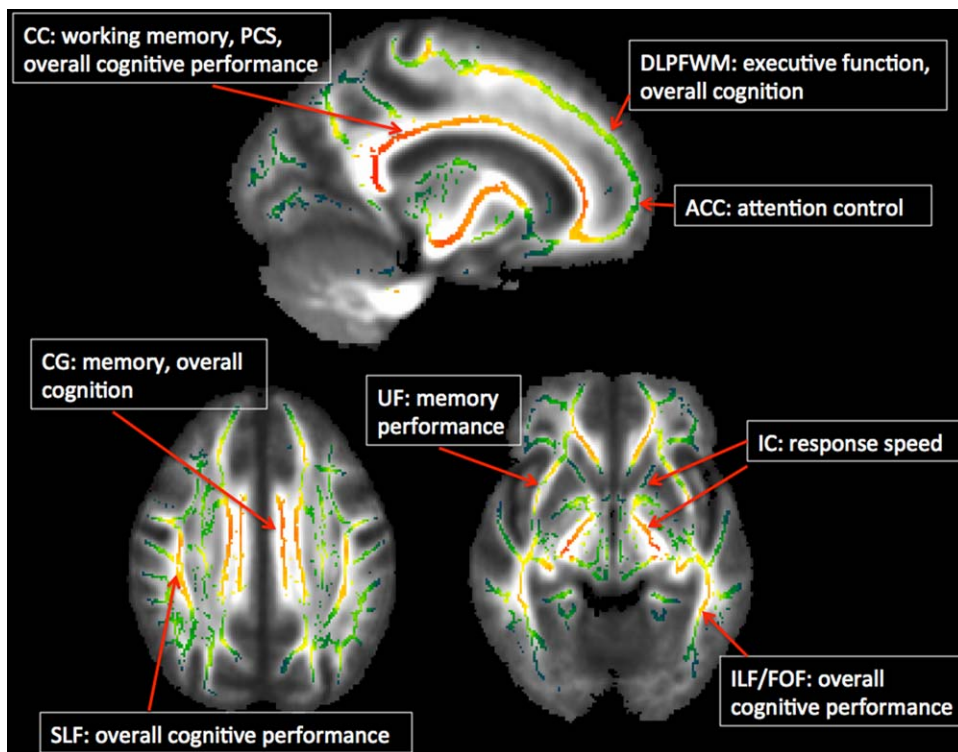


**FIGURE 5:** Summary of reported functional mapping with structural WM damage in mild TBI patients. Acronyms: ACC—anterior corona radiata, DLPFWM—dorsal lateral prefrontal white matter, CC—corpus callosum, CG—cingulum, SLF—superior longitudinal fasciculus, UF—uncinate fasciculus, IC—internal capsule, ILF—inferior longitudinal fasciculus, and FOF—fronto-occipital fasciculus.

TBI patients and suggested that reduced microstructural integrity of the CC, particularly in subregions connecting parietal and temporal cortices, may act as a neuropathological mechanism contributing to long-term working memory deficits (Treble et al., 2013).

**Corpus Callosum Injury.** As the largest WM fiber bundle in the brain that bridges left and right hemispheres, the CC is highly susceptible to injury during rotational motion of the brain in the sagittal and coronal planes, striking the falx cerebri and tentorium cerebri (Blumbergs, 1997). Injury of the callosal fibers has been reported to be associated with post concussion symptom (PCS) scores in mTBI. Wilde et al. (2008) studied 10 adolescent mTBI patients in the acute stage and reported that increased FA and reduced ADC and mean diffusivity (MD) in the CC is correlated with patients' PCS score. Bazarian et al. (2007) studied six mild TBI patients in the acute stage and reported a lower mean trace in the left anterior interior capsule and a higher FA in the posterior CC. FA values correlated with patients' 72 h PCS score and visual motor speed and impulse control.

**Injury at Whole Brain Level.** Because of the complex biomechanical scenario during impact, which can vary across individuals, the injury locations could vary individually. Instead of looking at injury at certain specific locations, an assessment

of whole brain lesion could be more meaningful for prediction of patients' outcome. The overall burden or extent of WM injury is associated with both speed of information processing and overall functional outcome. Niogi et al. (2008a, 2008b) studied 34 subacute to chronic mTBI patients and reported that FA was decreased in several WM regions, including anterior corona radiata, uncinate fasciculus, CC genu, and cingulum bundle. They demonstrated that the number of damaged WM regions is correlated with patients' reaction time. Miles et al. (2008) studied 17 mTBI patients at the acute stage and followed them up to 6 months after injury. They reported that, at the acute stage, the increased MD in centra semiovale, the genu, and splenium of CC and the posterior limb of the internal capsule tended to correlate with patients' response speed at 6 months after injury. Regarding the overall outcome, Messé et al. (2011) divided mTBI patients into two outcome groups: poor outcome *versus* good outcome. Poor outcome patients showed significantly higher mean diffusivity values than both controls and good outcome patients in the corpus callosum, the right anterior thalamic radiations and the superior longitudinal fasciculus, the inferior longitudinal fasciculus, and the fronto-occipital fasciculus. Most recently, Kou et al. studied mTBI at the hyperacute stage (within 24 h after injury) and reported that the volume of clusters with abnormally increased FA in

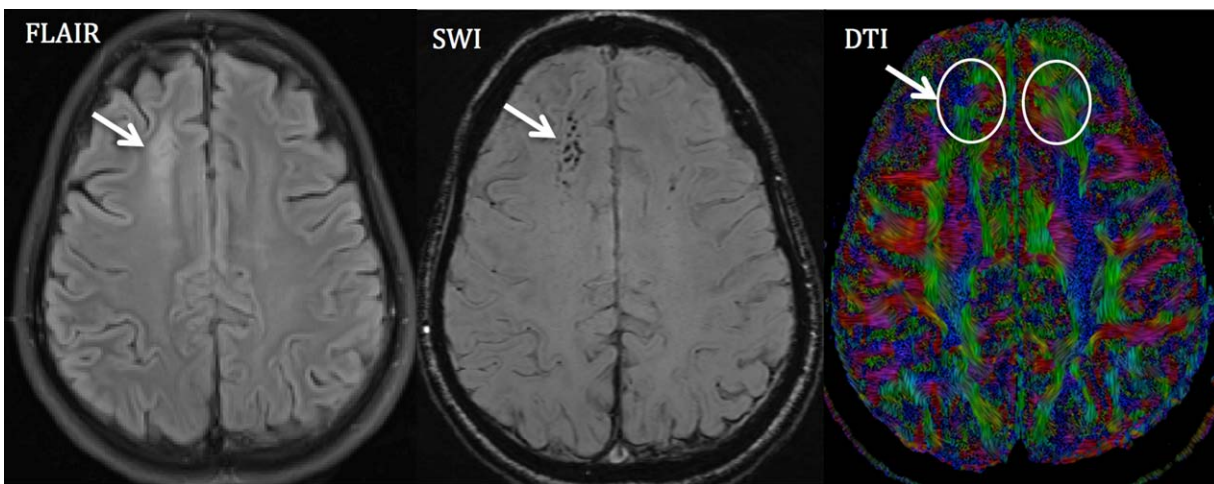


**FIGURE 6:** White matter injury and glial activation in a chronic TBI case. FLAIR image demonstrates a foci of hyper-intensity in right anterior corona radiata, suggesting gliosis (see arrow). SWI image shows the co-existence of small hemorrhages at the same location (see arrow). DTI color-encoded directional diffusivity map demonstrates asymmetry of contralateral locations (see arrow). As opposed to pure axonal injury, the altered directional diffusivity of DTI map is a gross indicator of potential gliosis, hemorrhage, and axonal injury at the same foci.

comparison with controls is correlated with patients' delayed recall at this stage.

**What do we Know and we do not Know.** It is known that brain injury affects multiple WM tracts and that the mapping of certain brain regions to some specific neurocognitive domain may not approach the ideal. Instead, the brain performs tasks by recruiting certain neural networks. It is still not clear of the brain injury at network level, particularly at the large scale network or connectome level. Irimia reported a whole brain connectomics approach in three TBI patients in this direction (Irimia et al., 2012). However, its value is still yet to be proved in a large number of patients. Further, how the alterations of both structural and functional networks account for patients' neurocognitive performance is still unknown. Furthermore, at different stages, it is still not known how glial reactivity affects patients' high level neurocognitive performance.

#### Detecting Glial Activation in TAI Patients

Despite promising progress in DTI characterization of TAI, it is still a gross biomarker of overall effect of WM pathology after injury. It still cannot effectively detect glial activation. Indeed, autopsy studies of human TBI patients have suggested that neuroinflammation is persistent following TBI and can be associated with chronic deficits. Using immunohistochemistry techniques, TBI cases with survival times of less than 12 months or with survival times from 12 months up to 22 years were found to have elevated microglial activity maintained with time following injury (Gentleman et al., 2004). Another study found ongoing inflammation in the CC up to 18 years following TBI. Fur-

thermore, the inflammatory cells were associated with increased axonal pathology and marked thinning of the CC (Johnson et al., 2013). In addition to DTI, the hyperintensity on FLAIR imaging is also a conventional diagnostic biomarker of WM injury (Grossman and Yousem, 2003). It represents the water content due to edema at the acute stage or gliosis at later stage (glial scar) in the sheared or stretched lesion area in WM tracts. It has been reported that FLAIR lesion load is correlated with DAI patients' outcomes (Marquez de la Plata et al., 2007). This data indicated that TBI is capable of inducing chronic neuroinflammation which facilitates MW degradation. Together with animal model work, these studies provide evidence that inhibitors of microglial activation following injury could be highly beneficial in reducing chronic outcomes.

Meanwhile, like DTI technique, FLAIR hyperintensity is not specific to glial activation, either. It is also quite common to see the co-existence of FLAIR hyperintensities and DTI FA abnormalities. As shown in Fig. 6 in a chronic TBI case, the hyperintensity on FLAIR image is likely due to gliosis, which co-exists with the micro-hemorrhages on SWI images. The non-symmetry of DTI fiber tractography on the same region does not represent the orientation change of WM tracts. Instead, it is caused by the change of water diffusivities due to the existence of gliosis and paramagnetic hemorrhagic blood product.

**Positron emission tomography (PET) Molecular Imaging.** Another way to detect glial activation in TBI patients is PET molecular imaging. Because activated microglia express translocator protein receptors (TSPO) and are the primary source of TSPO expression in neuroinflammation (Banati et al.,

1997), these receptors can be exploited to image activated microglia using positron emission tomography (PET) with a suitable radiotracer bound to a ligand specific for the TSPO receptors (Venneti et al., 2006). The PET tracer (R)-<sup>11</sup>C-PK11195 (PK), or 1-(2-chlorophenyl)-N-methyl-N-(1-methylpropyl)-3-isoquinoline carboxamide, is one such specific ligand for TSPO. Several studies have shown increased PK binding in a wide variety of neurological diseases characterized by underlying activated microglial neuroinflammation, reviewed in Cagnin et al. (2002, 2007) and Venneti et al. (2006). To date, only a couple of studies have been performed using PK PET in a handful of TBI patients. Folkersma et al. found increased cerebral PK uptake and glutamate release in a rat model of TBI (Folkersma et al., 2011b). Subsequently, the same group studied eight patients with moderate to severe TBI and seven demographically matched controls (Folkersma et al., 2011a). They reported increased binding of PK throughout the whole brain in TBI patients 6 months after the injury. In another study, Ramlackhansingh et al. (2011) evaluated 10 patients with moderate to severe TBI and 15 controls and found that PK binding was significantly increased in the thalamus, putamen, occipital cortices, and posterior limb of the internal capsules, suggesting microglial activated neuroinflammation in TBI patients up to 17 years after injury. However, they did not find increased PK binding at the original site of focal brain injury identified by structural MRI, and PK binding was not found to be correlated with either the time since injury or the extent of structural damage on MRI. They suggested that TBI can trigger a chronic inflammatory response, particularly in sub-cortical regions, protracted over a long period of time. Taken together, these PET studies suggest that neuroinflammation could persist for a long time after injury in moderate to severe TBI, although existing data are very limited and rather preliminary.

Further, there are several other unresolved issues that can be addressed with PET, including delineation of the extent and temporal progression of neuroinflammatory changes after TBI, its relationship with neurodegeneration at chronic stage, and its predictive value of patients' neurocognitive outcome. Presently, confirmation of microglial activation cannot be obtained with any other standard radiological or biochemical techniques, except for direct histopathological examination of brain tissues, a procedure which is quite invasive and possible only post-mortem. These novel techniques can help in developing novel therapeutic intervention. They can also help in selecting or categorizing such patients for possible anti-inflammatory treatment, evaluation of treatment response and subsequent follow-up. Furthermore, it is still unknown whether PK ligand is sensitive to the microglial activation in mild TBI. This is of particular importance in

chronic mTBI patients, so-called "miserable minorities," who suffer prolonged symptoms after injury (Ruff et al., 1996), because confirmation of neuroinflammation could provide a novel treatment target at the chronic stage. Indeed, a recent animal study of mTBI suggests that glial activation and BBB impairment could last at least 18 days after mTBI, with no further time points assessed (Perez-Polo et al., 2013). Further investigation with the PK ligand is warranted in chronic mTBI patients.

Not surprisingly, PET imaging, using PK or similar tracers, has some technical issues. Arterial input function is usually required for exact quantification, which is not always possible to obtain. A reference tissue model has been proposed as a solution with use of clustering analysis to get the value of reference region, as a surrogate for input function. This could be a problem in case of diffuse brain injury patients, where a "normal" reference region is difficult to define. Further, PK brain uptake can increase with age, which could be a confounding factor in data analysis and interpretation, particularly in cases of longitudinal follow-up (Kumar et al., 2012). Therefore, in these cases PK brain dynamics will have to be taken into consideration and adjusted for. Another limitation of PK PET imaging is the limited availability of these scanners compared with MRI or CT and the short half-life (about 20 min) of radioactive tracer (<sup>11</sup>C-labeled PK ligand), necessitating an on-site cyclotron and likely preventing its wide spread use in routine clinical practice.

**Combinational use of Imaging and Blood Biomarkers.** Another potential solution to characterize glial activation and WM injury is the combinational use of both glia-specific blood protein biomarkers and imaging techniques. Table 2 summarizes a panel of protein biomarkers that are both sensitive and specific to certain types of glial activation. By combining it with advanced imaging, which offers high resolution anatomical information, researchers might be able to probe the in-depth response of glial cells along with WM structural injury and even vascular damage of the brain. Kou et al. were the first group to investigate in this direction by a combinational use of advanced MRI and serum blood biomarkers (Kou et al., 2013). They reported elevated GFAP and UCH-L1 protein biomarkers at the acute stage in mTBI patients in comparison with controls. GFAP in particular was significantly elevated in patients with hemorrhage on SWI images (Kou et al., 2013). Figure 7 presents a sample mild TBI case to show activation of astrocytes (GFAP) along with small hemorrhages on SWI and WM injury on DTI images. This finding suggests that blood protein biomarkers could be potentially used as a screening tool for positive MRI findings,

**TABLE 2: Candidate Blood Biomarkers for Neuroinflammation and Axonal Injury**

Biomarker	Specificity	Localization	Function	TBI experimental	TBI clinical
S100 $\beta$	Astroglia	Cytoplasm, extracellular secretion	Intracellular signaling, pKC phosphorylation	Hardemark et al. (1989); Rothoerl et al. (2000)	Begaz et al. (2006); Bellander et al. (2011); Gonzlez-Mao (2011, #371); Haqqani et al. (2007); Pleines et al. (2001); Townend et al. (2006); Zurek and Fedora (2012)
GFAP	Astroglia	Cytoskeleton	Structural protein	Pineda et al. (2004); Sajja et al. (2012a, 2012b); Woertgen et al. (2002)	Liu et al. (2010); Vos et al. (2010); Zurek and Fedora (2012)
IL-1 $\beta$	Glia	Serum, cell receptors	Inflammatory process	Kinoshita et al. (2002); Sajja et al. (2012b)	Zurek and Fedora (2012)
IL-6	Glia	Serum, cell receptors	Inflammatory process	Sajja et al. (2012b); Zurek and Fedora (2012)	Stein et al. (2011b); Zurek and Fedora (2012)
IL-8	Glia	Serum, cell receptors	Inflammatory process	N/A	Stein et al. (2011b); Zurek and Fedora (2012)
TNF- $\alpha$	Activated macrophages	Serum, cell receptors	Inflammatory process	Vitarbo et al. (2004)	Hayakata et al. (2004); Stein et al. (2011a)
IFN- $\gamma$	Activated macrophages	Serum, cell receptors	Inflammatory process	Cho et al. (2013a)	Frugier et al. (2010)
MCP1	Activated monocytes	Serum, cell receptors	Inflammatory process	Cho et al. (2013a)	Ho et al. (2012)
pNF-H	Neuron	Cytoskeleton, axon	Structural integrity	Anderson et al. (2008); Petzold (2005)	Siman et al. (2009); Zurek and Fedora (2012)
NF-H	Neuron	Cytoskeleton, axon	Structural integrity	Park et al. (2007)	Haqqani et al. (2007)
MBP	Oligodendrocytes	White matter, axon	Myelination	Liu et al. (2010)	Berger (2006); Svetlov et al. (2010)
Alpha II—Spectrin SBPs	Neuron	Cytoskeleton, axon	Structural integrity	Pike et al. (2001)	Stein et al. (2011a)
	Neuron	Cytoskeleton, axon	Serum	Newcomb et al. (1997); Ringger et al. (2004)	Stein et al. (2011b)
Tau and p-Tau	Neuron	Cytoskeleton, axon	Structural integrity	Hawkins et al. (2013)	Tsitsopoulos and Marklund (2013)

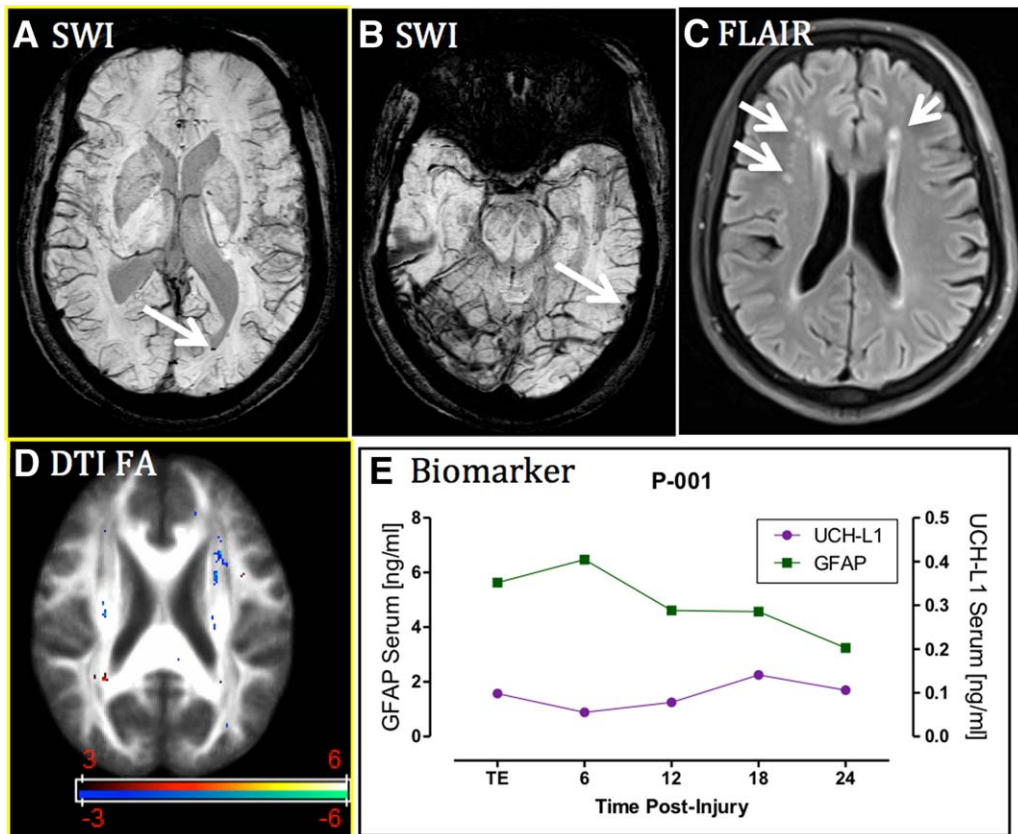


**FIGURE 7:** MRI and biomarker profile in a mTBI patient with intraventricular hemorrhage missed by CT. Panels (A) and (B) are SWI images at different locations of the brain showing intraventricular blood and left lingual gyrus blood product (see arrows); panel (C) is a FLAIR image showing non-specific WM hyperintensities (see arrows); panel (D) is a DTI FA map showing the co-existence of voxels with increased and decreased FA measures (red color indicates decreased FA and blue color indicates increased FA in comparison with controls,  $t > 3$  for t-test); and panel (E) shows a blood biomarker temporal profile, which exhibits extraordinarily high GFAP levels over time in comparison with controls. Despite being missed by CT, the injury was still detected by both blood biomarker and MRI. Image adapted with permission from Kou et al. (2013) and PLoS ONE.

which could be very useful in clinical diagnosis of intracranial bleeding in the acute setting (Kou et al., 2013).

### Future Directions

Overall, there are clear shortages in several areas. First, the relationship between glial activation and WM injury in both basic science and clinical studies, particularly the role of glia following axonal injury, degeneration, and possible regeneration, requires more research. Glial cells are fundamental for controlling WM health. When injury occurs, glial cells are crucial in responding to repair the environment to promote neuronal survival, axonal preservation, and regeneration. Furthermore, TAI is often accompanied by demyelination and oligodendrocytes damage. Decades of pathological and physiological studies have focused on neurons when describing brain injury cascades, but it is becoming increasingly evident that glial cells play an irreplaceable part in brain homeostasis and repair. Acute neuroinflammation is characterized by widespread astrogliosis and microglial response to brain injury, and while glial cells play a necessary role to protect neurons after

injury, their activities have also been linked to neurodegeneration and cognitive decline. A comprehensive investigation of the potential relationship between traumatic WM injury and glial injury will likely shed the light to TBI patients' identification, management, and treatment.

A detailed understanding of how glial cells contribute to axonal recovery or degeneration following traumatic injury currently lacking. Historically, preclinical experimental models of TAI have focused on *in vitro* cell culture models which contain only single cell types, with several studies on axonal injury limited by their use of only cultured neurons (Chung et al., 2005; Kilinc et al., 2008; Mesfin et al., 2012; Skotak et al., 2012; Smith, 2009; Staal et al., 2009; Tang-Schomer et al., 2010; von Reyn et al., 2012). Although these models have provided exceptional data on TAI threshold, the lack of inclusion of glia inhibits gaining accurate knowledge on recovery following injury. Similarly, with glial injury and activation cell culture experiments, studies have focused on single cell types (Kane et al., 2012; Ralay Ranaivo et al., 2011; VandeVord et al., 2008; Wanner, 2012). Mixed cell cultures and



organotypic brain tissue slices will be most helpful in elucidating how glial cells contribute to WM degeneration and repair following injury.

Second, How this glio-axonal interaction could serve as a target for novel treatment, which should be reflected as both structural plasticity or neural restoration at microscopic level and neurocognitive improvement at higher functional level also warrants further research. Promising data from TBI animal models and other neurological disorders, including stroke and multiple sclerosis, have demonstrated the potential roles of neurorestorative agents, for example, thymosin $\beta$ 4 (T $\beta$ 4) and erythropoietin (EPO), to promote oligodendrogenesis and axonal remodeling (Morris et al., 2010, 2012; Xiong et al., 2011; Zhang et al., 2009b, 2010) and of bone marrow stromal cells to facilitate axonal sprouting and remyelination (increased of OPC cells) in the cortical ischemic boundary zone and CC (Shen et al., 2006; Zhang et al., 2005, 2009a), among others. Collectively, they reported an improvement in animal neurological or behavioral functioning. However, there is still a paucity of data on the use of glial activation as a beneficial target to promote anti-inflammation, re-myelination, and neural restoration in TBI. Particularly, how these treatment schemes could be translated into human TBI patients to improve their neurocognitive performance still needs extensive investigation.

And finally, but not of least importance, the development of novel imaging and molecular biomarkers to quantitatively assess and characterize the glial response and axonal injury requires further research. Not only in identification of biomarkers that can reveal either the stage of recovery or level of neurodegeneration but also in development and validation, which would be remarkably beneficial in diagnosis, and eventually, rehabilitation strategies for our civilian and veteran TBI populations. The current limited number of imaging indices are far from enough to characterize the complexity and heterogeneity of TBI pathophysiology. Novel imaging techniques need to be further developed to identify WM injury, neuroinflammation, and astrogliosis across different stages. A recent study reported that veterans with a history of mTBI could not be differentiated from those without TBI at the acute stage (Jorge et al., 2012). However, several years after the trauma, veterans with a history of mTBI were found to have abnormal DTI results, highlighting the importance of identifying injury at the acute stage so that treatment can be provided to prevent further degeneration. In addition, a combinational use of both molecular biomarkers and advanced imaging could also serve as a feasible solution for human TBI investigation. To date, this is still a wide-open field of investigation.

In summary, glial activation is initiated from the beginning of traumatic white matter injury and can continue for

several years afterward. This chronic pathology may explain why white matter injury patients tend to suffer continued brain atrophy and degeneration and neurocognitive decline over the long run. Investigation into the role of glial activation in association with white matter injury has the potential to provide novel treatment targets for inhibition of neuroinflammation and for axonal regeneration. Development of advanced neuroimaging techniques and novel molecular biomarkers which correlate with this glial response will likely help to characterize the pathophysiological processes, as well as help translate the glial activation-targeted treatment in basic science to an improved neurocognitive performance in human patients.

## Acknowledgment

Grant sponsor: International Society for Magnetic Resonance in Medicine Seed Grant (PI: Zhifeng Kou); Grant sponsor: Department of Defense; Grant number: W81XWH-11-1-0493

The authors sincerely thank Dr. Shen-Kwei Victor Song for proof reading the DBSI description, Dr. Jiachen Zhuo for proof reading DKI description, Dr. Ajay Kumar for revising PET molecular imaging description, and Natalie Wiseman for proof reading the whole manuscript. The authors also thank anonymous reviewers for their time.

## References

- Adams JH, Doyle D, Ford I, Gennarelli TA, Graham DI, McLellan DR. 1989. Diffuse axonal injury in head injury: Definition, diagnosis and grading. *Histopathology* 15:49–59.
- Adams JH, Graham DI, Murray LS, Scott G. 1982. Diffuse axonal injury due to nonmissile head injury in humans: An analysis of 45 cases. *Ann Neurol* 12: 557–563.
- Adnan A, Crawley A, Mikulis D, Moscovitch M, Colella B, Green R. 2013. Moderate-severe traumatic brain injury causes delayed loss of white matter integrity: Evidence of fornix deterioration in the chronic stage of injury. *Brain Inj* 27:1415–1422.
- Ahlers ST, Vasserman-Stokes E, Shaughness MC, Hall AA, Shear DA, Chavko M, McCarron RM, Stone JR. 2012. Assessment of the effects of acute and repeated exposure to blast overpressure in rodents: Toward a greater understanding of blast and the potential ramifications for injury in humans exposed to blast. *Front Neurol* 3:32.
- Aihara N, Hall JJ, Pitts LH, Fukuda K, Noble LJ. 1995. Altered immunoexpression of microglia and macrophages after mild head injury. *J Neurotrauma* 12:53–63.
- Alexander DC. 2005. Multiple-fiber reconstruction algorithms for diffusion MRI. *Ann NY Acad Sci* 1064:113–133.
- Anderson AW, Xie J, Pizzonia J, Bronen RA, Spencer DD, Gore JC. 2000. Effects of cell volume fraction changes on apparent diffusion in human cells. *Magn Reson Imaging* 18:689–695.
- Anderson KJ, Scheff SW, Miller KM, Roberts KN, Gilmer LK, Yang C, Shaw G. 2008. The phosphorylated axonal form of the neurofilament subunit NF-H (pNF-H) as a blood biomarker of traumatic brain injury. *J Neurotrauma* 25:1079–1085.
- Arenth PM, Russell KC, Scanlon JM, Kessler LJ, Ricker JH. 2014. Corpus callosum integrity and neuropsychological performance after traumatic brain injury: A diffusion tensor imaging study. *J Head Trauma Rehabil* 29:E1–E10.

- Arfanakis K, Haughton VM, Carew JD, Rogers BP, Dempsey RJ, Meyerand M. 2002. Diffusion tensor MR imaging in diffuse axonal injury. *Am J Neuroradiol* 23:794–802.
- Bachstetter AD, Rowe RK, Kaneko M, Goulding D, Lifshitz J, Van Eldik LJ. 2013. The p38alpha MAPK regulates microglial responsiveness to diffuse traumatic brain injury. *J Neurosci* 33:6143–6153.
- Baek SO, Kim OL, Kim SH, Kim MS, Son SM, Cho YW, Jang SH. 2013. Relation between cingulum injury and cognition in chronic patients with traumatic brain injury; diffusion tensor tractography study. *NeuroRehabilitation* 33:465–471.
- Bain AC, Meaney DF. 2000. Tissue-level thresholds for axonal damage in an experimental model of central nervous system white matter injury. *J Biomech Eng* 122:615–622.
- Bal-Price A, Brown GC. 2001. Inflammatory neurodegeneration mediated by nitric oxide from activated glia-inhibiting neuronal respiration, causing glutamate release and excitotoxicity. *J Neurosci* 21:6480–6491.
- Banati RB, Myers R, Kreutzberg GW. 1997. PK ('peripheral benzodiazepine')—Binding sites in the CNS indicate early and discrete brain lesions: Microautoradiographic detection of [3H]PK11195 binding to activated microglia. *J Neurocytol* 26:77–82.
- Bardehle S, Krüger M, Buggenthin F, Schwausch J, Ninkovic J, Clevers H, Snippert HJ, Theis FJ, Meyer-Luehmann M, Bechmann I, Dimou L, Götz M. 2013. Live imaging of astrocyte responses to acute injury reveals selective juxtavascular proliferation. *Nat Neurosci* 16:580–586.
- Basiri M, Doucette R. 2010. Sensorimotor cortex aspiration: A model for studying Wallerian degeneration-induced glial reactivity along the entire length of a single CNS axonal pathway. *Brain Res Bull* 81:43–52.
- Bazarian JJ, Zhong J, Blyth B, Zhu T, Kavcic V, Peterson D. 2007. Diffusion tensor imaging detects clinically important axonal damage after mild traumatic brain injury: A pilot study. *J Neurotrauma* 24:1447–1459.
- Bazarian JJ, Zhu T, Blyth B, Borrino A, Zhong J. 2012. Subject-specific changes in brain white matter on diffusion tensor imaging after sports-related concussion. *Magn Reson Imaging* 30:171–180.
- Begaz T, Kyriacou DN, Segal J, Bazarian JJ. 2006. Serum biochemical markers for post-concussion syndrome in patients with mild traumatic brain injury. *J Neurotrauma* 23:1201–1210.
- Belanger HG, Kretzmer T, Vanderploeg RD, French LM. 2010. Symptom complaints following combat-related traumatic brain injury: Relationship to traumatic brain injury severity and posttraumatic stress disorder. *J Int Neuropsychol Soc* 16:194–199.
- Belanger HG, Kretzmer T, Yoash-Gantz R, Pickett T, Tupler LA. 2009. Cognitive sequelae of blast-related versus other mechanisms of brain trauma. *J Int Neuropsychol Soc* 15:1–8.
- Bellander BM, Olafsson IH, Ghatal PH, Bro Skejo HP, Hansson LO, Wanecik M, Svensson MA. 2011. Secondary insults following traumatic brain injury enhance complement activation in the human brain and release of the tissue damage marker S100B. *Acta Neurochir (Wien)* 153:90–100.
- Bennett RE, Mac Donald CL, Brody DL. 2012. Diffusion tensor imaging detects axonal injury in a mouse model of repetitive closed-skull traumatic brain injury. *Neurosci Lett* 513:160–165.
- Benson RR, Meda SA, Vasudevan S, Kou Z, Govindarajan KA, Hanks RA, Millis SR, Makki M, Latif Z, Coplin W, Meythaler J, Haacke EM. 2007. Global white matter analysis of diffusion tensor images is predictive of injury severity in TBI. *J Neurotrauma* 24:446–459.
- Berger RP. 2006. The use of serum biomarkers to predict outcome after traumatic brain injury in adults and children. *J Head Trauma Rehabil* 21:315–333.
- Blumbergs PC. 1997. Pathology. In: Reilly P, Bullock R, editors. *Head injury*. London: Chapman & Hill. p 39–70.
- Blumbergs PC, Scott G, Manavis J, Wainwright H, Simpson DA, McLean AJ. 1994. Staining of amyloid precursor protein to study axonal damage in mild head injury. *Lancet* 344:1055–1056.
- Butoraitis V, Morkuniene R, Brown GC. 1999. Release of cytochrome c from heart mitochondria is induced by high Ca<sup>2+</sup> and peroxynitrite and is responsible for Ca(2+)-induced inhibition of substrate oxidation. *Biochim Biophys Acta* 1453:41–48.
- Budde MD, Janes L, Gold E, Turtzo LC, Frank JA. 2011. The contribution of gliosis to diffusion tensor anisotropy and tractography following traumatic brain injury: Validation in the rat using Fourier analysis of stained tissue sections. *Brain* 134:2248–2260.
- Buffo A, Rolando C, Ceruti S. 2010. Astrocytes in the damaged brain: Molecular and cellular insights into their reactive response and healing potential. *Biochem Pharmacol* 79:77–89.
- Bükü A, Povlishock JT. 2006. All roads lead to disconnection?—Traumatic axonal injury revisited. *Acta Neurochir (Wien)* 148:181–193.
- Bükü A, Siman R, Trojanowski JQ, Povlishock JT. 1999. The role of calpain-mediated spectrin proteolysis in traumatically induced axonal injury. *J Neuropathol Exp Neurol* 58:365–375.
- Cagnin A, Gerhard A, Banati RB. 2002. The concept of in vivo imaging of neuroinflammation with [11C](R)-PK11195 PET. *Ernst Schering Res Found Workshop* 179–191.
- Cagnin A, Kassiou M, Meikle SR, Banati RB. 2007. Positron emission tomography imaging of neuroinflammation. *Neurotherapeutics* 4:443–452.
- Cai J, Yang J, Jones DP. 1998. Mitochondrial control of apoptosis: The role of cytochrome c. *Biochim Biophys Acta* 1366:139–149.
- Cawley PJ, Mokadam NA. 2010. Delayed complications from exposure to improvised explosive devices. *Ann Intern Med* 153:278–279.
- CDC. 2003. Report to Congress on Mild Traumatic brain injury in the United States: Steps to Prevent a Serious Public Health Problem. Atlanta (GA): Centers for Disease Control and Prevention, National Center for Injury Prevention and Control.
- Cho HJ, Sajja VS, Vandevord PJ, Lee YW. 2013a. Blast induces oxidative stress, inflammation, neuronal loss and subsequent short-term memory impairment in rats. *Neuroscience* 253C:9–20.
- Cho HJ, Sajja VS, Vandevord PJ, Lee YW. 2013b. Blast induces oxidative stress, inflammation, neuronal loss and subsequent short-term memory impairment in rats. *Neuroscience* 253:9–20.
- Chu Z, Wilde EA, Hunter JV, McCauley SR, Bigler ED, Troyanskaya M, Yallampalli R, Chia JM, Levin HS. 2010. Voxel-based analysis of diffusion tensor imaging in mild traumatic brain injury in adolescents. *AJNR Am J Neuroradiol* 31:340–346.
- Chung RS, McCormack GH, King AE, West AK, Vickers JC. 2005. Glutamate induces rapid loss of axonal neurofilament proteins from cortical neurons in vitro. *Exp Neurol* 193:481–488.
- Colangelo AM, Cirillo G, Lavitrano ML, Alberghina L, Papa M. 2012. Targeting reactive astrogliosis by novel biotechnological strategies. *Biotechnol Adv* 30:261–271.
- Conturo TE, McKinstry RC, Akbudak E, Robinson BH. 1996. Encoding of anisotropic diffusion with tetrahedral gradients: A general mathematical diffusion formalism and experimental results. *Magn Reson Med* 35:399–412.
- d'Avila JC, Lam TI, Bingham D, Shi J, Won SJ, Kauppinen TM, Massa S, Liu J, Swanson RA. 2012. Microglial activation induced by brain trauma is suppressed by post-injury treatment with a PARP inhibitor. *J Neuroinflammation* 9:31.
- Dalle Lucca JJ, Chavko M, Dubick MA, Adeeb S, Falabella MJ, Slack JL, McCarron R, Li Y. 2012. Blast-induced moderate neurotrauma (BINT) elicits early complement activation and tumor necrosis factor alpha (TNF $\alpha$ ) release in a rat brain. *J Neurol Sci* 318:146–154.
- Dikmen S, McLean A Jr, Temkin NR, Wyler AR. 1986a. Neuropsychologic outcome at one-month postinjury. *Arch Phys Med Rehabil* 67:507–513.
- Dikmen S, McLean A, Temkin N. 1986b. Neuropsychological and psychosocial consequences of minor head injury. *J Neurol Neurosurg Psychiatry* 49: 1227–1232.
- Dougherty KD, Dreyfus CF, Black IB. 2000. Brain-derived neurotrophic factor in astrocytes, oligodendrocytes, and microglia/macrophages after spinal cord injury. *Neurobiol Dis* 7:574–585.



- Du Y, Dreyfus CF. 2002. Oligodendrocytes as providers of growth factors. *J Neurosci Res* 68:647–654.
- Elder GA, Mitsis EM, Ahlers ST, Cristian A. 2010. Blast-induced mild traumatic brain injury. *Psychiatr Clin North Am* 33:757–781.
- Falangola MF, Jensen JH, Tabesh A, Hu C, Deardorff RL, Babb JS, Ferris S, Helpern JA. 2013. Non-Gaussian diffusion MRI assessment of brain microstructure in mild cognitive impairment and Alzheimer's disease. *Magn Reson Imaging* 31:840–846.
- Falangola MF, Jensen JH, Babb JS, Hu C, Castellanos FX, Di Martino A, Ferris SH, Helpern JA. 2008. Age-related non-Gaussian diffusion patterns in the prefrontal brain. *J Magn Reson Imaging* 28:1345–1350.
- Farina C, Aloisi F, Meini E. 2007. Astrocytes are active players in cerebral innate immunity. *Trends Immunol* 28:138–145.
- Faul M, Xu L, Wald MM, Coronado VG. 2010. Traumatic brain injury in the United States: Emergency department visits, hospitalizations, and deaths. Atlanta (GA): Centers for Disease Control and Prevention, National Center for Injury Prevention and Control.
- Finkelstein E, Corso P, Miller T. 2006. The incidence and economic burden of injuries in the United States. New York, NY: Oxford University Press.
- Fitch MT, Silver J. 2008. CNS injury, glial scars, and inflammation: Inhibitory extracellular matrices and regeneration failure. *Exp Neurol* 209:294–301.
- Flygt J, Djupsjö A, Lenne F, Marklund N. 2013. Myelin loss and oligodendrocyte pathology in white matter tracts following traumatic brain injury in the rat. *Eur J Neurosci* 38:2153–2165.
- Folkersma H, Boellaard R, Yaqub M, Kloet RW, Windhorst AD, Lammertsma AA, Vandertop WP, van Berckel BN. 2011a. Widespread and prolonged increase in (R)-(11)C-PK11195 binding after traumatic brain injury. *J Nucl Med* 52:1235–1239.
- Folkersma H, Foster Dingley JC, van Berckel BN, Rozemuller A, Boellaard R, Huisman MC, Lammertsma AA, Vandertop WP, Molthoff CF. 2011b. Increased cerebral (R)-(11)C-PK11195 uptake and glutamate release in a rat model of traumatic brain injury: A longitudinal pilot study. *J Neuroinflammation* 8:67.
- Fozouni N, Chopp M, Nejad-Davarani SP, Zhang ZG, Lehman NL, Gu S, Ueno Y, Lu M, Ding G, Li L, Hu J, Bagher-Ebadian H, Hearshen D, Jiang Q. 2013. Characterizing brain structures and remodeling after TBI based on information content, diffusion entropy. *PLoS One* 8:e76343.
- Frugier T, Morganti-Kossmann MC, O'Reilly D, McLean CA. 2010. In situ detection of inflammatory mediators in post mortem human brain tissue after traumatic injury. *J Neurotrauma* 27:497–507.
- Galanaud D, Perlberg V, Gupta R, Stevens RD, Sanchez P, Tollard E, de Champfleur NM, Dinkel J, Faivre S, Soto-Ares G, Veber B, Cottenceau V, Masson F, Tourdias T, Andre E, Audibert G, Schmitt E, Ibarrola D, Dailler F, Vanhaudenhuyse A, Tshibanda L, Payen JF, Le Bas JF, Krainik A, Bruder N, Girard N, Laureys S, Benali H, Puybasset L; Neuro Imaging for Coma Emergence and Recovery Consortium. 2012. Assessment of white matter injury and outcome in severe brain trauma: A prospective multicenter cohort. *Anesthesiology* 117:1300–1310.
- Gavett BE, Stern RA, Cantu RC, Nowinski CJ, McKee AC. 2010. Mild traumatic brain injury: A risk factor for neurodegeneration. *Alzheimers Res Ther* 2:18.
- Gennarelli TA. 1993. Mechanisms of brain injury. *J Emerg Med* 11:5–11.
- Gennarelli TA, Thibault LE, Adams JH, Graham DL, Thompson CJ, Marcincin RP. 1982. Diffuse axonal injury and traumatic coma in the primate. *Ann Neurol* 12:564–574.
- Gentleman SM, Leclercq PD, Moyes L, Graham DL, Smith C, Griffin WS, Nicoll JA. 2004. Long-term intracerebral inflammatory response after traumatic brain injury. *Forensic Sci Int* 146:97–104.
- Gervasi NM, Kwok JC, Fawcett JW. 2008. Role of extracellular factors in axon regeneration in the CNS: Implications for therapy. *Regen Med* 3:907–923.
- Glushakova O, Johnson D, Hayes RL. 2014. Delayed increases in microvascular pathology following experimental traumatic brain injury are associated with prolonged inflammation, blood brain barrier disruption and progressive white matter damage. *J Neurotrauma*. Feb 24 [Epub ahead of print].
- Goldstein M. 1990. Traumatic brain injury: A silent epidemic [editorial]. *Ann Neurol* 27:327.
- González-Mao MC, Repáraz-Andrade A, Del Campo-Pérez V, Alvarez-García E, Vara-Perez C, Andrade-Olivé MA. 2011. Model predicting survival/exodus after traumatic brain injury: biomarker S100B 24h. *Clin Lab* 57:587–597.
- Grossman EJ, Ge Y, Jensen JH, Babb JS, Miles L, Reaume J, Silver JM, Grossman RI, Inglesse M. 2012. Thalamus and cognitive impairment in mild traumatic brain injury: A diffusional kurtosis imaging study. *J Neurotrauma* 29:2318–2327.
- Grossman EJ, Jensen JH, Babb JS, Chen Q, Tabesh A, Fieremans E, Xia D, Inglesse M, Grossman RI. 2013. Cognitive impairment in mild traumatic brain injury: A longitudinal diffusional kurtosis and perfusion imaging study. *AJR Am J Neuroradiol* 34:951–957.
- Grossman RI, Yousem DM. 2003. *Neuroradiology*. Philadelphia, PA: Mosby.
- Haacke EM, Xu Y, Cheng Y-CN, Reichenbach JR. 2004. Susceptibility weighted imaging (SWI). *Magn Reson Med* 52:612–618.
- Hampton CE, Thorpe CN, Sholar CA. 2013. A novel bridge wire model of blast traumatic brain injury—Biomed 2013. *Biomed Sci Instrum* 49:312–319.
- Haqqani AS, Hutchison JS, Ward R, Stanimirovic DB. 2007. Biomarkers and diagnosis; protein biomarkers in serum of pediatric patients with severe traumatic brain injury identified by ICAT-LC-MS/MS. *J Neurotrauma* 24:54–74.
- Hardemark HG, Ericsson N, Kotwica Z, Rundstrom G, Mendel-Hartwig I, Olsson Y, Pahlman S, Persson L. 1989. S-100 protein and neuron-specific enolase in CSF after experimental traumatic or focal ischemic brain damage. *J Neurosurg* 71:727–731.
- Hawkins BE, Krishnamurthy S, Castillo-Carranza DL, Sengupta U, Prough DS, Jackson GR, DeWitt DS, Kayed R. 2013. Rapid accumulation of endogenous tau oligomers in a rat model of traumatic brain injury: Possible link between traumatic brain injury and sporadic tauopathies. *J Biol Chem* 288:17042–17050.
- Hayakata T, Shiozaki T, Tasaki O, Ikegawa H, Inoue Y, Toshiyuki F, Hosotubo H, Kieko F, Yamashita T, Tanaka H, Shimazu T, Sugimoto H. 2004. Changes in CSF S100B and cytokine concentrations in early-phase severe traumatic brain injury. *Shock* 22:102–107.
- Ho L, Zhao W, Dams-O'Connor K, Tang CY, Gordon W, Peskind ER, Yemul S, Haroutunian V, Pasinetti GM. 2012. Elevated plasma MCP-1 concentration following traumatic brain injury as a potential "predisposition" factor associated with an increased risk for subsequent development of Alzheimer's disease. *J Alzheimers Dis* 31:301–313.
- Hoge CW, McGurk D, Thomas JL, Cox AL, Engel CC, Castro CA. 2008. Mild traumatic brain injury in U.S. Soldiers returning from Iraq. *N Engl J Med* 358:453–463.
- Inglesse M, Makani S, Johnson G, Cohen BA, Silver JA, Gonon O, Grossman RI. 2005. Diffuse axonal injury in mild traumatic brain injury: A diffusion tensor imaging study. *J Neurosurg* 103:298–303.
- Irimia A, Chambers MC, Torgerson CM, Filippou M, Hovda DA, Alger JR, Gerig G, Toga AW, Vespa PM, Kikinis R, Van Horn JD. 2012. Patient-tailored connectomics visualization for the assessment of white matter atrophy in traumatic brain injury. *Front Neurol* 3:10.
- Jacobowitz DM, Cole JT, McDaniel DP, Pollard HB, Watson WD. 2012. Microglia activation along the corticospinal tract following traumatic brain injury in the rat: A neuroanatomical study. *Brain Res* 1465:80–89.
- Jang SH, Kim SH, Kim OR, Byun WM, Kim MS, Seo JP, Chang MC. 2013. Cingulum injury in patients with diffuse axonal injury: A diffusion tensor imaging study. *Neurosci Lett* 543:47–51.
- Jensen JH, Falangola MF, Hu C, Tabesh A, Rapalino O, Lo C, Helpern JA. 2011. Preliminary observations of increased diffusional kurtosis in human brain following recent cerebral infarction. *NMR Biomed* 24:452–457.
- Jensen JH, Helpern JA, Ramani A, Lu H, Kaczynski K. 2005. Diffusional kurtosis imaging: The quantification of non-Gaussian water diffusion by means of magnetic resonance imaging. *Magn Res Med* 53:1432–1440.

- Jensen JH, Helpern JA. 2010. MRI quantification of non-Gaussian water diffusion by kurtosis analysis. *NMR Biomed* 23:689–710.
- Jiang Q, Qu C, Chopp M, Ding GL, Davarani SP, Helpern JA, Jensen JH, Zhang ZG, Li L, Lu M, Kaplan D, Hu J, Shen Y, Kou Z, Li Q, Wang S, Mahmood A. 2011. MRI evaluation of axonal reorganization after bone marrow stromal cell treatment of traumatic brain injury. *NMR Biomed* 24:1119–1128.
- John GR, Lee SC, Brosnan CF. 2003. Cytokines: Powerful regulators of glial cell activation. *Neuroscientist* 9:10–22.
- Johnson VE, Stewart JE, Begbie FD, Trojanowski JQ, Smith DH, Stewart W. 2013. Inflammation and white matter degeneration persist for years after a single traumatic brain injury. *Brain* 136:28–42.
- Johnson VE, Stewart JE, Begbie FD, Trojanowski JQ, Smith DH, Stewart W. 2013. Inflammation and white matter degeneration persist for years after a single traumatic brain injury. *Brain* 136:28–42.
- Jorge RE, Acion L, White T, Tordesillas-Gutierrez D, Pierson R, Crespo-Facorro B, Magnotta VA. 2012. White matter abnormalities in veterans with mild traumatic brain injury. *Am J Psychiatry* 169:1284–1291.
- Kabadi SV, Stoica BA, Byrnes KR, Hanscom M, Loane DJ, Faden AI. 2012. Selective CDK inhibitor limits neuroinflammation and progressive neurodegeneration after brain trauma. *J Cereb Blood Flow Metab* 32:137–149.
- Kane MJ, Angoa-Perez M, Francescutti DM, Sykes CE, Briggs DL, Leung LY, VandeVord PJ, Kuhn DM. 2012. Altered gene expression in cultured microglia in response to simulated blast overpressure: Possible role of pulse duration. *Neurosci Lett* 522:47–51.
- Karampinos DC, Van AT, Olivero WC, Georgiadis JG, Sutton BP. 2008. High resolution reduced-FOV diffusion tensor imaging of the human pons with multi-shot variable density spiral at 3T. *Conf Proc IEEE Eng Med Biol Soc* 2008:5761–5764.
- Karger J. 1985. NMR self-diffusion studies in heterogeneous systems. *Adv Colloid Interface Sci* 23:129–148.
- Kaur C, Singh J, Lim MK, Ng BL, Ling EA. 1997a. Macrophages/microglia as ‘sensors’ of injury in the pineal gland of rats following a non-penetrative blast. *Neurosci Res* 27:317–322.
- Kaur C, Singh J, Lim MK, Ng BL, Yap EP, Ling EA. 1995. The response of neurons and microglia to blast injury in the rat brain. *Neuropathol Appl Neuropatol* 21:369–377.
- Kaur C, Singh J, Lim MK, Ng BL, Yap EP, Ling EA. 1997b. Ultrastructural changes of macroglial cells in the rat brain following an exposure to a non-penetrative blast. *Ann Acad Med Singapore* 26:27–29.
- Kay T. 1993. Neuropsychological treatment of mild traumatic brain injury. *J Head Trauma Rehabil* 8:74–85.
- Kelley BJ, Lifshitz J, Povlishock JT. 2007. Neuroinflammatory responses after experimental diffuse traumatic brain injury. *J Neuropathol Exp Neurol* 66:989–1001.
- Kilinc D, Gallo G, Barbee KA. 2008. Mechanically-induced membrane poration causes axonal beading and localized cytoskeletal damage. *Exp Neurol* 212:422–430.
- Kinoshita K, Chatzipanteli IK, Vitarbo E, Truettner JS, Alonso OF, Dietrich WD. 2002. Interleukin-1beta messenger ribonucleic acid and protein levels after fluid-percussion brain injury in rats: Importance of injury severity and brain temperature. *Neurosurgery* 51:195–203; discussion 203.
- Kochanek PM, Bauman RA, Long JB, Dixon CR, Jenkins LW. 2009. A critical problem begging for new insight and new therapies. *J Neurotrauma* 26:813–814.
- Koliatsos VE, Cernak I, Xu L, Song Y, Savonenko A, Crain BJ, Eberhart CG, Frangakis CE, Melnikova T, Kim H, Lee D. 2011. A mouse model of blast injury to brain: Initial pathological, neuropathological, and behavioral characterization. *J Neuropathol Exp Neurol* 70:399–416.
- Kotter MR, Stadelmann C, Hartung HP. 2011. Enhancing remyelination in disease—can we wrap it up? *Brain* 134(Pt 7):1882–1900.
- Kou Z, Benson RR, Haacke EM. 2012. Magnetic resonance imaging biomarkers of mild traumatic brain injury. In: Dambinova SEA, editor. *Biomarkers for traumatic brain injury*. Royal Society of Chemistry, London, United Kingdom.
- Kou Z, Gattu R, Kobeissy F, Welch RD, O’Neil B, Woodard JL, Ayaz SI, Kulek A, Kas-Shamoun R, Mika V, Zuk C, Tomasello F, Mondello S. 2013. Combining biochemical and imaging markers to improve diagnosis and characterization of mild traumatic brain injury in the acute setting: Results from a pilot study. *PLoS One* 8(11):e80296.
- Kou Z, Gattu R, Benson RR, Raz N, Haacke EM. 2008. Region of interest analysis of DTI FA histogram differentiates mild traumatic brain injury from controls. *Proceedings of Annual Conference for International Society for Magnetic Resonance in Medicine*, Toronto, Canada.
- Kou Z, Wu Z, Tong KA, Holshouser B, Benson RR, Hu J, Haacke EM. 2010. The role of advanced MR imaging findings as biomarkers of traumatic brain injury. *J Head Trauma Rehabil* 25:267–282.
- Krajewski S, Krajewska M, Ellerby LM, Welsh K, Xie Z, Deveraux QL, Salvesen GS, Bredesen DE, Rosenthal RE, Fiskum G, Reed JC. 1999. Release of caspase-9 from mitochondria during neuronal apoptosis and cerebral ischemia. *Proc Natl Acad Sci USA* 96:5752–5757.
- Kraus MF, Susmaras T, Caughlin BP, Walker CJ, Sweeney JA, DM L. 2007. White matter integrity and cognition in chronic traumatic brain injury: A diffusion tensor imaging study. *Brain* 130:2508–2519.
- Kumar A, Muzik O, Shandal V, Chugani D, Chakraborty P, Chugani HT. 2012. Evaluation of age-related changes in translocator protein (TSPO) in human brain using <sup>(11)C</sup>-[R]-PK11195 PET. *J Neuroinflammation* 9:232.
- Kuroiwa T, Nagaoka T, Ueki M, Yamada I, Miyasaka N, Akimoto H, Ichinose S, Okeda R, Hirakawa K. 2009. Correlations between the apparent diffusion coefficient, water content, and ultrastructure after induction of vasogenic brain edema in cats. *J Neurosurg* 90:499–503.
- Kutzeligg A, Lassmann H. 2014. Pathology of multiple sclerosis and related inflammatory demyelinating diseases. *Handb Clin Neurol* 122:15–58.
- Le Bihan D, Mangin JF, Poupon C, Clark CA, Pappata S, Molko N, Chabriat H. 2001. Diffusion tensor imaging: Concepts and applications. *JMRI* 13:534–546.
- Lee VM, Carden MJ, Schlaepfer WW, Trojanowski JQ. 1987. Monoclonal antibodies distinguish several differentially phosphorylated states of the two largest rat neurofilament subunits (NF-H and NF-M) and demonstrate their existence in the normal nervous system of adult rats. *J Neurosci* 7:3474–3488.
- Leung LY, VandeVord PJ, Dal Cengio AL, Bir C, Yang KH, King AI. 2008. Blast related neurotrauma: A review of cellular injury. *Mol Cell Biomech* 5:155–168.
- Levin HS, Wilde EA, Chu Z, Yallampalli R, Hanten GR, Li X, Chia J, Vasquez AC, Hunter JV. 2008. Diffusion tensor imaging in relation to cognitive and functional outcome of traumatic brain injury in children. *J Head Trauma Rehabil* 23:197–208.
- Levin HS, Mattis S, Ruff RM, Eisenberg HM, Marshall LF, Tabaddor K, High WM, Frankowski RF. 1987. Neurobehavioral outcome following minor head injury: A three-center study. *J Neurosurg* 66:234–243.
- Liang D, Bhatta S, Gerzanich V, Simard JM. 2007. Cytotoxic edema: Mechanisms of pathological cell swelling. *Neurosurg Focus* 22:E2.
- Liberto CM, Albrecht PJ, Herx LM, Yong VW, Levison SW. 2004. Pro-regenerative properties of cytokine-activated astrocytes. *J Neurochem* 89:1092–1100.
- Lipton ML, Gulko E, Zimmerman ME, Friedman BW, Kim M, Gellella E, Gold T, Shifteh K, Ardekani BA, Branch CA. 2009. Diffusion-tensor imaging implicates prefrontal axonal injury in executive function impairment following very mild traumatic brain injury. *Radiology* 252:816–824.
- Lipton ML, Kim N, Park YK, Hulkower MB, Gardin TM, Shifteh K, Kim M, Zimmerman ME, Lipton RB, Branch CA. 2012. Robust detection of traumatic axonal injury in individual mild traumatic brain injury patients: Intersubject variation, change over time and bidirectional changes in anisotropy. *Brain Imaging Behav* 6:329–342.
- Liu MC, Akinyi L, Scharf D, Mo J, Larner SF, Muller U, Oli MW, Zheng W, Kobeissy F, Papa L, Lu XC, Dave JR, Tortella FC, Hayes RL, Wang KK. 2010.



- Ubiquitin C-terminal hydrolase-L1 as a biomarker for ischemic and traumatic brain injury in rats. *Eur J Neurosci* 31:722–732.
- Lotocki G, de Rivero Vaccari JP, Alonso O, Molano JS, Nixon R, Safavi P, Dietrich WD, Bramlett HM. 2011. Oligodendrocyte vulnerability following traumatic brain injury in rats. *Neurosci Lett*. 499:143–148.
- Lundbaek JA, Hansen AJ. 1992. Brain interstitial volume fraction and tortuosity in anoxia. Evaluation of the ion-selective micro-electrode method. *Acta Physiol Scand* 146:473–484.
- Maas AIR, Marmarou A, Murry GD, Teasdale GM, Steyerberg EW. 2007. Prognosis and clinical trial design in traumatic brain injury: The IMPACT study. *J Neurotrauma* 24:232–238.
- Mac Donald CL, Dikranian K, Bayly P, Holtzman D, Brody D. 2007a. Diffusion tensor imaging reliably detects experimental traumatic axonal injury and indicates approximate time of injury. *J Neurosci* 27:11869–11876.
- Mac Donald CL, Dikranian K, Song SK, Bayly PV, Holtzman DM, Brody DL. 2007b. Detection of traumatic axonal injury with diffusion tensor imaging in a mouse model of traumatic brain injury. *Exp Neurol* 205:116–131.
- Macciocchi SN, Barth JT, Alves W, Rimel RW, Jane JA. 1996. Neuropsychological functioning and recovery after mild head injury in collegiate athletes. *Neurosurgery* 39:510–514.
- Magdesian MH, Sanchez FS, Lopez M, Thostrup P, Durisic N, Belkaid W, Liazoghi D, Grutter P, Colman DR. 2012. Atomic force microscopy reveals important differences in axonal resistance to injury. *Biophys J* 103:405–414.
- Mancini M, Nicholson DW, Roy S, Thornberry NA, Peterson EP, Casciola-Rosen LA, Rosen A. 1998. The caspase-3 precursor has a cytosolic and mitochondrial distribution: Implications for apoptotic signaling. *J Cell Biol* 140:1485–1495.
- Marquez de la Plata C, Ardelean A, Koovakkattu D, Srinivasan P, Miller A, Phuong V, Harper C, Moore C, Whittemore A, Madden C, Diaz-Arrastia R, Devous M Sr. 2007. Magnetic resonance imaging of diffuse axonal injury: Quantitative assessment of white matter lesion volume. *J Neurotrauma* 24:591–598.
- Matute C. 2010. Calcium dyshomeostasis in white matter pathology. *Cell Calcium* 47:150–157.
- Maxwell WL, Povlishock JT, Graham DL. 1997. A mechanistic analysis of non-disruptive axonal injury: A review. *J Neurotrauma* 14:419–440.
- Maxwell WL, Watt C, Graham DL, Gennarelli TA. 1993. Ultrastructural evidence of axonal shearing as a result of lateral acceleration of the head in non-human primates. *Acta Neuropathol (Berl)* 86:136–144.
- Mayer AR, Ling J, Mannell MV, Gasparovic C, Phillips JP, Doezeema D, Reichard R, Yeo RA. 2010. A prospective diffusion tensor imaging study in mild traumatic brain injury. *Neurology* 74:643–650.
- McTigue DM, Tripathi RB. 2008. The life, death, and replacement of oligodendrocytes in the adult CNS. *J Neurochem* 107:1–19.
- Mesfin MN, von Reyn CR, Mott RE, Putt ME, Meaney DF. 2012. In vitro stretch injury induces time- and severity-dependent alterations of STEP phosphorylation and proteolysis in neurons. *J Neurotrauma* 29:1982–1998.
- Messé A, Caplain S, Paradot G, Garrigue D, Mineo JF, Soto Ares G, Dureux D, Vignaud F, Rozec G, Desal H, Pélegrini-Issac M, Montreuil M, Benali H, Lehéricy S. 2011. Diffusion tensor imaging and white matter lesions at the subacute stage in mild traumatic brain injury with persistent neurobehavioral impairment. *Hum Brain Mapp* 32:999–1011.
- Miles L, Grossman RI, Johnson G, Babb JS, Diller L, Inglese M. 2008. Short-term DTI predictors of cognitive dysfunction in mild traumatic brain injury. *Brain Inj* 22:115–122.
- Miller DR, Peppas NA. 1985. The use of ellipsometry to study adsorption on hydrogels. *Biomaterials* 6:33–40.
- Montal M. 1998. Mitochondria, glutamate neurotoxicity and the death cascade. *Biochim Biophys Acta* 1366:113–126.
- Morris DC, Chopp M, Zhang L, Lu M, Zhang ZG. 2010. Thymosin beta4 improves functional neurological outcome in a rat model of embolic stroke. *Neuroscience* 169:674–682.
- Morris DC, Zhang ZG, Zhang J, Xiong Y, Zhang L, Chopp M. 2012. Treatment of neurological injury with thymosin  $\beta$ 4. *Ann N Y Acad Sci* 1269:110–116.
- Mouzon BC, Bachmeier C, Ferro A, Ojo JO, Crynen G, Acker CM, Davies P, Mullan M, Stewart W, Crawford F. 2014. Chronic neuropathological and neurobehavioral changes in a repetitive mild traumatic brain injury model. *Ann Neurol* 75:241–254.
- Mrak RE, Griffin WS. 2005. Glia and their cytokines in progression of neurodegeneration. *Neurobiol Aging* 26:349–354.
- Nagamoto-Combs K, McNeal DW, Morecraft RJ, Combs CK. 2007. Prolonged microgliosis in the rhesus monkey central nervous system after traumatic brain injury. *J Neurotrauma* 24:1719–1742.
- Naismith RT, Xu J, Tutlam NT, Scully PT, Trinkaus K, Snyder AZ, Song SK, Cross AH. 2010. Increased diffusivity in acute multiple sclerosis lesions predicts risk of black hole. *Neurology* 74:1694–1701.
- National Institutes of Health. 1999. NIH consensus development panel on rehabilitation of persons with traumatic brain injury. *JAMA* 282:974–983.
- Negi S, Bhandari R, Rieth L, Solzbacher F. 2010. In vitro comparison of sputtered iridium oxide and platinum-coated neural implantable microelectrode arrays. *Biomed Mater* 5:15007.
- Newcomb JK, Kampfl A, Posmantur RM, Zhao X, Pike BR, Liu SJ, Clifton GL, Hayes RL. 1997. Immunohistochemical study of calpain-mediated breakdown products to alpha-spectrin following controlled cortical impact injury in the rat. *J Neurotrauma* 14:369–383.
- Newcombe VF, Williams GB, Nortje J, Bradley PG, Harding SG, Smielewski P, Coles JP, Maiya B, Gillard JH, Hutchinson PJ, Pickard JD, Carpenter TA, Menon DK. 2007. Analysis of acute traumatic axonal injury using diffusion tensor imaging. *Br J Neurosurg* 21:340–348.
- Nimmerjahn A. 2009. Astrocytes going live: Advances and challenges. *J Physiol* 587:1639–1647.
- Nimmerjahn A, Kirchhoff F, Helmchen F. 2005. Resting microglial cells are highly dynamic surveillants of brain parenchyma in vivo. *Science* 308:1314–1318.
- Niogi SN, Mukherjee P. 2010. Diffusion tensor imaging of mild traumatic brain injury. *J Head Trauma Rehabil* 25:241–255.
- Niogi SN, Mukherjee P, Ghajar J, Johnson C, Kolster RA, Sarkar R, Lee H, Meeker M, Zimmerman RD, Manley GT, McCandliss BD. 2008a. Extent of microstructural white matter injury in postconcussive syndrome correlates with impaired cognitive reaction time: A 3T diffusion tensor imaging study of mild traumatic brain injury. *AJNR Am J Neuroradiol* 29:967–973.
- Niogi SN, Mukherjee P, Ghajar J, Johnson CE, Kolster R, Lee H, Suh M, Zimmerman RD, Manley GT, McCandliss BD. 2008b. Structural dissociation of attentional control and memory in adults with and without mild traumatic brain injury. *Brain* 131:3209–3221.
- Oberheim NA, Goldman SA, Nedergaard M. 2012. Heterogeneity of astrocytic form and function. *Methods Mol Biol* 814:23–45.
- Okonkwo DO, Pettus EH, Moroi J, Povlishock JT. 1998. Alteration of the neurofilament sidearm and its relation to neurofilament compaction occurring with traumatic axonal injury. *Brain Res* 784:1–6.
- Parekkadan B, Berdichevsky Y, Irimia D, Leeder A, Yarmush G, Toner M, Levine JB, Yarmush ML. 2008. Cell-cell interaction modulates neuroectodermal specification of embryonic stem cells. *Neurosci Lett* 438:190–195.
- Park E, Liu E, Shek M, Park A, Baker AJ. 2007. Heavy neurofilament accumulation and alpha-spectrin degradation accompany cerebellar white matter functional deficits following forebrain fluid percussion injury. *Exp Neurol* 204:49–57.
- Pasternak O, Sochen N, Gur Y, Intrator N, Assaf Y. 2009. Free water elimination and mapping from diffusion MRI. *Magn Res Med* 62:717–730.
- Perez-Polo JR, Rea HC, Johnson KM, Parsley MA, Unabia GC, Xu G, Infante SK, Dewitt DS, Hulsebosch CE. 2013. Inflammatory consequences in a rodent model of mild traumatic brain injury. *J Neurotrauma* 30:727–740.
- Peter SJ, Mofrad MR. 2012. Computational modeling of axonal microtubule bundles under tension. *Biophys J* 102:749–757.

- Pettus EH, Christman CW, Giebel ML, Povlishock JT. 1994. Traumatically induced altered membrane permeability: Its relationship to traumatically induced reactive axonal change. *J Neurotrauma* 11:507–522.
- Pettus EH, Povlishock JT. 1996. Characterization of a distinct set of intra-axonal ultrastructural changes associated with traumatically induced alteration in axolemmal permeability. *Brain Res* 722:1–11.
- Petzold A. 2005. Neurofilament phosphoforms: Surrogate markers for axonal injury, degeneration and loss. *J Neurol Sci* 233:183–198.
- Pfrieger FW. 2009a. Letter from the guest editor: The relevance of cell adhesion for synapse-glia interactions. *Cell Adh Migr* 3:27–28.
- Pfrieger FW. 2009b. Roles of glial cells in synapse development. *Cell Mol Life Sci* 66:2037–2047.
- Pfrieger FW. 2010. Role of glial cells in the formation and maintenance of synapses. *Brain Res Rev* 63:39–46.
- Phillips LL, Lyeth BG, Hamm RJ, Povlishock JT. 1994. Combined fluid percussion brain injury and entorhinal cortical lesion: A model for assessing the interaction between neuroexcitation and deafferentation. *J Neurotrauma* 11:641–656.
- Phillips LL, Reeves TM. 2001. Interactive pathology following traumatic brain injury modifies hippocampal plasticity. *Restor Neurol Neurosci* 19:213–235.
- Pike BR, Flint J, Dutta S, Johnson E, Wang KK, Hayes RL. 2001. Accumulation of non-erythroid alpha II-spectrin and calpain-cleaved alpha II-spectrin breakdown products in cerebrospinal fluid after traumatic brain injury in rats. *J Neurochem* 78:1297–1306.
- Pineda JA, Wang KK, Hayes RL. 2004. Biomarkers of proteolytic damage following traumatic brain injury. *Brain Pathol* 14:202–209.
- Pleines UE, Morganti-Kossmann MC, Rancan M, Joller H, Trentz O, Kossmann T. 2001. S-100 beta reflects the extent of injury and outcome, whereas neuronal specific enolase is a better indicator of neuroinflammation in patients with severe traumatic brain injury. *J Neurotrauma* 18:491–498.
- Poliak S, Peles E. 2003. The local differentiation of myelinated axons at nodes of Ranvier. *Nat Rev Neurosci* 4:968–980.
- Polikov VS, Tesco PA, Reichert WM. 2005. Response of brain tissue to chronically implanted neural electrodes. *J Neurosci Methods* 148:1–18.
- Povlishock JT, Becker DP, Cheng CL, Vaughan GW. 1983. Axonal change in minor head injury. *J Neuropathol Exp Neurol* 42:225–242.
- Raab P, Hattingen E, Franz K, Zanella FE, Lanfermann H. 2010. Cerebral gliomas: Diffusional kurtosis imaging analysis of microstructural differences. *Radiology* 254:876–881.
- Ralay Ranaivo H, Zurich SM, Choi N, Hodge JN, Wainwright MS. 2011. Mild stretch-induced injury increases susceptibility to interleukin-1beta-induced release of matrix metalloproteinase-9 from astrocytes. *J Neurotrauma* 28:1757–1766.
- Ramlackhansingh AF, Brooks DJ, Greenwood RJ, Bose SK, Turkheimer FE, Kinnunen KM, Gentleman S, Heckemann RA, Gunanayagam K, Gelosa G, Sharp DJ. 2011. Inflammation after trauma: Microglial activation and traumatic brain injury. *Ann Neurol* 70:374–383.
- Rao JS, Kellom M, Kim HW, Rapoport SI, Reese EA. 2012. Neuroinflammation and synaptic loss. *Neurochem Res* 37:903–910.
- Raz E, Bester M, Sigmund EE, Tabesh A, Babb JS, Jaggi H, Helpert J, Mitnick RJ, Inglesse M. 2013. A better characterization of spinal cord damage in multiple sclerosis: A diffusional kurtosis imaging study. *AJNR Am J Neuroradiol* 34:1846–1852.
- Readnower RD, Chavko M, Adeeb S, Conroy MD, Pauly JR, McCarron RM, Sullivan PG. 2010. Increase in blood-brain barrier permeability, oxidative stress, and activated microglia in a rat model of blast-induced traumatic brain injury. *J Neurosci Res* 88:3530–3539.
- Ringger NC, O'Steen BE, Brabham JG, Silver X, Pineda J, Wang KK, Hayes RL, Papa L. 2004. A novel marker for traumatic brain injury: CSF alphah-spectrin breakdown product levels. *J Neurotrauma* 21:1443–1456.
- Roberts-Lewis JM, Savage MJ, Marcy VR, Pinsker LR, Siman R. 1994. Immunolocalization of calpain I-mediated spectrin degradation to vulnerable neurons in the ischemic gerbil brain. *J Neurosci* 14:3934–3944.
- Rothoerl RD, Brawanski A, Woertgen C. 2000. S-100B protein serum levels after controlled cortical impact injury in the rat. *Acta Neurochir (Wien)* 142:199–203.
- Ruff RM, Camenzuli LF, Mueller J. 1996. Miserable minority: Emotional risk factors that influence the outcome of mild traumatic brain injury. *Brain Inj* 10: 551–556.
- Rutgers DR, Fillard P, Paradot G, Tadié M, Lasjaunias P, Ducreux D. 2008. Diffusion tensor imaging characteristics of the corpus callosum in mild, moderate, and severe traumatic brain injury. *AJNR Am J Neuroradiol* 29:1730–1735.
- Saatman KE, Duhaime AC, Bullock Ross, Maas AIR, Valadka A, Manley GT, members wstaap. 2008. Classification of traumatic brain injury for targeted therapies. *J Neurotrauma* 25:719–738.
- Sajja VS, Perrine SA, Ghodoussi F, Hall CS, Galloway MP, Vandevord PJ. 2014. Blast neurotrauma impairs working memory and disrupts prefrontal myo-inositol levels in rats. *Mol Cell Neurosci* 59C:119–126.
- Sajja VS, Galloway M, Ghodoussi F, Kepsel A, VandeVord P. 2013. Effects of blast-induced neurotrauma on the nucleus accumbens. *J Neurosci Res* 91:593–601.
- Sajja VS, Galloway MP, Ghodoussi F, Thiruthalinathan D, Kepsel A, Hay K, Bir CA, Vandevord PJ. 2012a. Blast-induced neurotrauma leads to neurochemical changes and neuronal degeneration in the rat hippocampus. *NMR Biomed* 25:1331–1339.
- Sajja VS, Tenn C, McLaws LJ, Vandevord PJ. 2012b. A temporal evaluation of cytokines in rats after blast exposure. *Biomed Sci Instrum* 48:374–379.
- Seker E, Berdichevsky Y, Begley MR, Reed ML, Staley KJ, Yarmush ML. 2010. The fabrication of low-impedance nanoporous gold multiple-electrode arrays for neural electrophysiology studies. *Nanotechnology* 21:125504.
- Shannon CE. 1997. The mathematical theory of communication. 1963. *MD Comput* 14:306–317.
- Shen LH, Li Y, Chen J, Zhang J, Vanguri P, Borneman J, Chopp M. 2006. Intracarotid transplantation of bone marrow stromal cells increases axon-myelin remodeling after stroke. *Neuroscience* 137:393–399.
- Shimony JS, McKinstry RC, Akbudak E, Aronovitz JA, Snyder AZ, Lori NF, Cull TS, Conturo TE. 1999. Quantitative diffusion-tensor anisotropy brain MR imaging: Normative human data and anatomic analysis. *Radiology* 212:770–784.
- Shitaka Y, Tran HT, Bennett RE, Sanchez L, Levy MA, Dikranian K, Brody DL. 2011. Repetitive closed-skull traumatic brain injury in mice causes persistent multifocal axonal injury and microglial reactivity. *J Neuropathol Exp Neurol* 70:551–567.
- Shultz SR, Bao F, Weaver LC, Cain DP, Brown A. 2013. Treatment with an anti-CD11d integrin antibody reduces neuroinflammation and improves outcome in a rat model of repeated concussion. *J Neuroinflammation* 10:26.
- Siman R, Baudry M, Lynch G. 1984. Brain fodrin: Substrate for calpain I, an endogenous calcium-activated protease. *Proc Natl Acad Sci USA* 81:3572–3576.
- Siman R, Toraskar N, Dang A, McNeil E, McGarvey M, Plaum J, Maloney E, Grady MS. 2009. A panel of neuron-enriched proteins as markers for traumatic brain injury in humans. *J Neurotrauma* 26:1867–1877.
- Skotak M, Wang F, Chandra N. 2012. An in vitro injury model for SH-SY5Y neuroblastoma cells: Effect of strain and strain rate. *J Neurosci Methods* 205: 159–168.
- Smith C. 2013. Review: The long-term consequences of microglial activation following acute traumatic brain injury. *Neuropathol Appl Neurobiol* 39:35–44.
- Smith DH. 2009. Stretch growth of integrated axon tracts: Extremes and exploitations. *Prog Neurobiol* 89:231–239.
- Sofroniew MV, Vinters HV. 2010. Astrocytes: Biology and pathology. *Acta Neuropathol* 119:7–35.
- Song SK, Sun SW, Ju WK, Lin SJ, Cross AH, Neufeld AH. 2003. Diffusion tensor imaging detects and differentiates axon and myelin degeneration in mouse optic nerve after retinal ischemia. *Neuroimage* 20:1714–1722.
- Song SK, Sun SW, Ramsbottom MJ, Chang C, Russell J, Cross AH. 2002. Dysmyelination revealed through MRI as increased radial (but unchanged axial) diffusion of water. *Neuroimage* 17:1429–1436.



- Song SK, Yoshino J, Le TQ, Lin SJ, Sun SW, Cross AH, Armstrong RC. 2005. Demyelination increases radial diffusivity in corpus callosum of mouse brain. *Neuroimage* 26:132–140.
- Spitz G, Maller JJ, O'Sullivan R, Ponsford JL. 2013. White matter integrity following traumatic brain injury: The association with severity of injury and cognitive functioning. *Brain Topogr* 26:648–660.
- Squire L, Berg D, Bloom FE, du Lac S, Ghosh A, Spitzer NC. 2012. Fundamental neuroscience. Academic Press, Waltham, MA, USA; 4th ed.
- Staal JA, Dickson TC, Chung RS, Vickers JC. 2009. Disruption of the ubiquitin proteasome system following axonal stretch injury accelerates progression to secondary axotomy. *J Neurotrauma* 26:781–788.
- Stein DM, Kufera JA, Lindell A, Murdock KR, Menaker J, Bochicchio GV, Aarabi B, Scalea TM. 2011a. Association of CSF biomarkers and secondary insults following severe traumatic brain injury. *Neurocrit Care* 14:200–207.
- Stein DM, Lindell A, Murdock KR, Kufera JA, Menaker J, Keledjian K, Bochicchio GV, Aarabi B, Scalea TM. 2011b. Relationship of serum and cerebrospinal fluid biomarkers with intracranial hypertension and cerebral hypoperfusion after severe traumatic brain injury. *J Trauma* 70:1096–1103.
- Streit WJ, Mrak RE, Griffin WS. 2004. Microglia and neuroinflammation: A pathological perspective. *J Neuroinflammation* 1:14.
- Strich SJ. 1961. Shearing of nerve fibers as a cause of brain damage due to head injury: A pathological study of twenty cases. *Lancet* 2:443–448.
- Stys PK. 2005. General mechanisms of axonal damage and its prevention. *J Neurol Sci* 233:3–13.
- Susin SA, Lorenzo HK, Zamzami N, Marzo I, Snow BE, Brothers GM, Mangion J, Jacicot E, Costantini P, Loeffler M, Larochette N, Goodlett DR, Aebersold R, Siderovski DP, Penninger JM, Kroemer G. 1999. Molecular characterization of mitochondrial apoptosis-inducing factor. *Nature* 397:441–446.
- Susin SA, Zamzami N, Kroemer G. 1998. Mitochondria as regulators of apoptosis: Doubt no more. *Biochim Biophys Acta* 1366:151–165.
- Svetlov SI, Prima V, Kirk DR, Gutierrez H, Curley KC, Hayes RL, Wang KK. 2010. Morphologic and biochemical characterization of brain injury in a model of controlled blast overpressure exposure. *J Trauma* 69:795–804.
- Sykova E, Svoboda J, Polak J, Chvátal A. 1994. Extracellular volume fraction and diffusion characteristics during progressive ischemia and terminal anoxia in the spinal cord of the rat. *J Cereb Blood Flow Metab* 14:301–311.
- Tang-Schomer MD, Patel AR, Baas PW, Smith DH. 2010. Mechanical breaking of microtubules in axons during dynamic stretch injury underlies delayed elasticity, microtubule disassembly, and axon degeneration. *FASEB J* 24:1401–1410.
- Teasdale G, Jennett B. 1974. Assessment of coma and impaired consciousness: A practical scale. *Lancet* 2:81–84.
- Thurman D, Alverson C, Dunn K, Guerrero J, Snieszek J. 1999. Traumatic brain injury in the United States: A public health perspective. *J Head Trauma Rehabil* 14:602–615.
- Tong KA, Ashwal S, Holshouser BA, Nickerson JP, Wall CJ, Shutter LA, Osterdock RJ, Haacke EM, Kido D. 2004. Diffuse axonal injury in children: Clinical correlation with hemorrhagic lesions. *Ann Neurol* 56:36–50.
- Tong KA, Ashwal S, Holshouser BA, Shutter LA, Herigault G, Haacke EM, Kido D. 2003. Hemorrhagic shearing lesions in children and adolescents with posttraumatic diffuse axonal injury: Improved detection and initial results. *Radiology* 27:332–339.
- Townend W, Dibble C, Abid K, Vail A, Sherwood R, Lecky F. 2006. Rapid elimination of protein S-100B from serum after minor head trauma. *J Neurotrauma* 23:149–155.
- Treble A, Hasan KM, Iftikhar A, Stuebing KK, Kramer LA, Cox CS Jr, Swank PR, Ewing-Cobbs L. 2013. Working memory and corpus callosum microstructural integrity after pediatric traumatic brain injury: A diffusion tensor tractography study. *J Neurotrauma* 30:1609–1619.
- Tsitsopoulos PP, Marklund N. 2013. Amyloid-beta peptides and tau protein as biomarkers in cerebrospinal and interstitial fluid following traumatic brain injury: A review of experimental and clinical studies. *Front Neurol* 4:79.
- Tuch DS, Reese TG, Wiegell MR, Makris N, Belliveau JW, Wedeen VJ. 2002. High angular resolution diffusion imaging reveals intravoxel white matter fiber heterogeneity. *Magn Res Med* 48:577–582.
- Turner JN, Shain W, Szarowski DH, Andersen M, Martins S, Isaacson M, Craighead H. 1999. Cerebral astrocyte response to micromachined silicon implants. *Exp Neurol* 156:33–49.
- Unterberg AW, Stover J, Kress B, Kiening KL. 2004. Edema and brain trauma. *Neuroscience* 129:1021–1029.
- Vandevord PJ, Bolander R, Sajja VS, Hay K, Bir CA. 2012. Mild neurotrauma indicates a range-specific pressure response to low level shock wave exposure. *Ann Biomed Eng* 40:227–236.
- Vandevord PJ, Leung LY, Hardy W, Mason M, Yang KH, King AI. 2008. Up-regulation of reactivity and survival genes in astrocytes after exposure to short duration overpressure. *Neurosci Lett* 434:247–252.
- Venkatesan C, Chrzaszcz M, Choi N, Wainwright MS. 2010. Chronic upregulation of activated microglia immunoreactive for galectin-3/Mac-2 and nerve growth factor following diffuse axonal injury. *J Neuroinflammation* 7:32.
- Venneti S, Lopresti BJ, Wiley CA. 2006. The peripheral benzodiazepine receptor (Translocator protein 18kDa) in microglia: From pathology to imaging. *Prog Neurobiol* 80:308–322.
- Vitarbo EA, Chatzipanteli K, Kinoshita K, Truettner JS, Alonso OF, Dietrich WD. 2004. Tumor necrosis factor alpha expression and protein levels after fluid percussion injury in rats: The effect of injury severity and brain temperature. *Neurosurgery* 55:416–424; discussion 424–425.
- von Reyn CR, Mott RE, Siman R, Smith DH, Meaney DF. 2012. Mechanisms of calpain mediated proteolysis of voltage gated sodium channel alpha-subunits following in vitro dynamic stretch injury. *J Neurochem* 121:793–805.
- Vos PE, Jacobs B, Andriessen TM, Lamers KJ, Borm GF, Beems T, Edwards M, Rosmalen CF, Vissers JL. 2010. GFAP and S100B are biomarkers of traumatic brain injury: An observational cohort study. *Neurology* 75:1786–1793.
- Wang JY, Bakhadirov K, Abdi H, Devous MD Sr, Marquez de la Plata CD, Moore C, Madden CJ, Diaz-Arrastia R. 2011a. Longitudinal changes of structural connectivity in traumatic axonal injury. *Neurology* 77:818–826.
- Wang Y, Wang Q, Haldar JP, Yeh FC, Xie M, Sun P, Tu TW, Trinkaus K, Klein RS, Cross AH, Song SK. 2011b. Quantification of increased cellularity during inflammatory demyelination. *Brain* 134:3590–3601.
- Wanner IB. 2012. An in vitro trauma model to study rodent and human astrocyte reactivity. *Methods Mol Biol* 814:189–219.
- Wedeen VJ, Hagmann P, Tseng WY, Reese TG, Weisskoff RM. 2005. Mapping complex tissue architecture with diffusion spectrum magnetic resonance imaging. *Magn Res Med* 54:1377–1386.
- Wheeler-Kingshott CA, Cercignani M. 2009. About "axial" and "radial" diffusivities. *Magn Res Med* 61:1255–1260.
- Wilde EA, McCauley SR, Hunter JV, Bigler ED, Chu Z, Wang ZJ, Hanten GR, Troyanskaya M, Yallampalli R, Li X, Chia J, Levin HS. 2008. Diffusion tensor imaging of acute mild traumatic brain injury in adolescents. *Neurology* 70:948–955.
- Wilson JT, Pettigrew LE, Teasdale GM. 1998. Structured interviews for the Glasgow Outcome Scale and the extended Glasgow Outcome Scale: Guidelines for their use. *J Neurotrauma* 15:573–585.
- Woertgen C, Rothoerl RD, Wiesmann M, Missler U, Brawanski A. 2002. Glial and neuronal serum markers after controlled cortical impact injury in the rat. *Acta Neurochir Suppl* 81:205–207.
- Wolf JA, Stys PK, Lusardi T, Meaney D, Smith DH. 2001. Traumatic axonal injury induces calcium influx modulated by tetrodotoxin-sensitive sodium channels. *J Neurosci* 21:1923–1930.
- Wozniak JR, Krach L, Ward E, Mueller BA, Muetzel R, Schnoebel S, Kiragu A, Lim KO. 2007. Neurocognitive and neuroimaging correlates of pediatric traumatic brain injury: A diffusion tensor imaging(DTI) study. *Arch Clin Neuropsychol* 22:555–568.

Kou and VandeVord: Traumatic White Matter Injury and Glial Activation

- Wu TC, Wilde EA, Bigler ED, Yallampalli R, McCauley SR, Troyanskaya M, Chu Z, Li X, Hanten G, Hunter JV, Levin HS. 2010. Evaluating the relationship between memory functioning and cingulum bundles in acute mild traumatic brain injury using diffusion tensor imaging. *J Neurotrauma* 27:303–307.
- Xiong Y, Mahmood A, Meng Y, Zhang Y, Zhang ZG, Morris DC, Chopp M. 2011. Treatment of traumatic brain injury with thymosin  $\beta_4$  in rats. *J Neurosurg* 114:102–115.
- Zhang J, Li Y, Chen J, Cui Y, Lu M, Elias SB, Mitchell JB, Hammill L, Vanguri P, Chopp M. 2005. Human bone marrow stromal cell treatment improves neurological functional recovery in EAE mice. *Exp Neurol* 195:16–26.
- Zhang J, Li Y, Zhang ZG, Lu M, Borneman J, Buller B, Savant-Bhonsale S, Elias SB, Chopp M. 2009a. Bone marrow stromal cells increase oligodendrogenesis after stroke. *J Cereb Blood Flow Metab* 29:1166–1174.
- Zhang J, Zhang ZG, Morris D, Li Y, Roberts C, Elias SB, Chopp M. 2009b. Neurological functional recovery after thymosin beta4 treatment in mice with experimental auto encephalomyelitis. *Neuroscience* 164:1887–1893.
- Zhang L, Chopp M, Zhang RL, Wang L, Zhang J, Wang Y, Toh Y, Santra M, Lu M, Zhang ZG. 2010. Erythropoietin amplifies stroke-induced oligodendrogenesis in the rat. *PLoS One* 5:e11016.
- Zhuo J, Xu S, Proctor JL, Mullins RJ, Simon JZ, Fiskum G, Gullapalli RP. 2012. Diffusion kurtosis as an in vivo imaging marker for reactive astrogliosis in traumatic brain injury. *NeuroImage* 59:467–477.
- Zurek J, Fedora M. 2012. The usefulness of S100B, NSE, GFAP, NF-H, secretagogin and Hsp70 as a predictive biomarker of outcome in children with traumatic brain injury. *Acta Neurochir (Wien)* 154:93–103; discussion 103.



# NIH Public Access

## Author Manuscript

*Magn Reson Med.* Author manuscript; available in PMC 2014 May 01.

Published in final edited form as:

*Magn Reson Med.* 2013 May ; 69(5): 1396–1407. doi:10.1002/mrm.24384.

## Improving Susceptibility Mapping Using a Threshold-Based K-space/Image Domain Iterative Reconstruction Approach

J. Tang<sup>1</sup>, S. Liu<sup>1</sup>, J. Neelavalli<sup>2</sup>, Y.C.N. Cheng<sup>2</sup>, S. Buch<sup>1</sup>, and E. M. Haacke<sup>1,2,3</sup>

<sup>1</sup>McMaster University, Hamilton, Ontario, Canada

<sup>2</sup>Wayne State University, Detroit, Michigan, USA

<sup>3</sup>The MRI Institute for Biomedical Research, Detroit, Michigan, USA

### Abstract

To improve susceptibility quantification, a threshold-based k-space/image domain iterative approach that uses geometric information from the susceptibility map itself as a constraint to overcome the ill-posed nature of the inverse filter is introduced. Simulations were used to study the accuracy of the method and its robustness in the presence of noise. *In vivo* data was processed and analyzed using this method. Both simulations and *in vivo* results show that most streaking artifacts inside the susceptibility map caused by the ill-defined inverse filter were suppressed by the iterative approach. In simulated data, the bias toward lower mean susceptibility values inside vessels has been shown to decrease from around 10% to 2% when choosing an appropriate threshold value for the proposed iterative method. Typically, three iterations are sufficient for this approach to converge and this process takes less than 30 seconds to process a  $512 \times 512 \times 256$  dataset. This iterative method improves quantification of susceptibility inside vessels and reduces streaking artifacts throughout the brain for data collected from a single-orientation acquisition. This approach has been applied to vessels alone as well as to vessels and other structures with lower susceptibility to generate whole brain susceptibility maps with significantly reduced streaking artifacts.

### Keywords

oxygen saturation; susceptibility mapping; susceptibility weighted imaging

### INTRODUCTION

Susceptibility weighted imaging (SWI) using phase information has become an important clinical tool [1–3]. However, the use of phase information itself has stimulated great interest both as a source of contrast [4–6] and a source for producing susceptibility maps (SM) [7–24]. The impetus for solving the inverse problem from magnetic field perturbation came from the work described in Deville et al. [25]. This was noted by Marques and Bowtell in 2005 [26]. Salomir et al. [27] were the first group to utilize this concept in MRI. Unfortunately, this inverse process is ill-posed and requires a regularization procedure to estimate the susceptibility map. There are a variety of approaches to tackle this problem [7–24]. One unique method uses a multiple orientation data acquisition to remove the singularities [17]. Constrained regularizations [14,20,22,23] have shown good overall results, but they require longer reconstruction times and assumptions about the contrast in or

Corresponding author: E. Mark Haacke, PhD, Department of Radiology, Wayne State University, 3990 John R Street, Detroit MI 48201., nmrimage@aol.com.

near the object to be detected. Threshold-based, single-orientation regularization methods (TBSO) [11,15,18,24] provide the least acquisition time and the shortest computational time to calculate SM. However, their calculated SMs lead to underestimated susceptibility values ( $\Delta\chi$ ) and display severe streaking artifacts especially around structures with large  $\Delta\chi$ , such as veins or parts of the basal ganglia.

Based on TBSO approaches, we propose an iterative method to overcome the singularities in the inverse filter and produce improved accuracy for susceptibility mapping. In this approach, we iteratively replace k-space values of the susceptibility maps,  $\chi(k)$ , near the singularities to obtain an almost artifact free SM,  $\chi(r)$ . The k-space values used for substitutions are estimated using structural information from the masked version of  $\chi(r)$ . Simulations using 2D cylinders and full brain 3D models were performed to examine the efficacy of this iterative approach. High resolution human data are also evaluated.

## MATERIALS AND METHODS

Briefly, the expression for the susceptibility distribution [26,27] derived from the phase data can be written as (for a right handed system[28]):

$$\chi(r)=FT^{-1}\left[\frac{1}{g(k)} \bullet FT\left[\frac{\Phi(r)}{-\gamma B_0 TE}\right]\right] \quad [1]$$

where,

$$g(k)=\frac{1}{3}-\frac{k_z^2}{k_x^2+k_y^2+k_z^2} \quad [2]$$

and  $\Phi(r)$  is the phase distribution, TE is the echo time,  $\gamma$  is the gyromagnetic ratio for hydrogen protons,  $B_0$  is the main field strength,  $k_x$ ,  $k_y$  and  $k_z$  are coordinates in k-space, and  $g(k)$  is the Green's function or filter. Clearly, the analytic inverse filter  $g^{-1}(k) = 1/g(k)$ , is ill-posed when  $g(k)$  is equal or close to zero, i.e., points on or near two conical surfaces in k-space at the magic angles of  $54.7^\circ$  and  $125.3^\circ$  from the  $B_0$  axis. This ill-posedness leads to severe artifacts (including severe streaking) in  $\chi(k)$  and noise amplification [29]. Thus, for a proper pixel-by-pixel reconstruction of  $\chi(r)$ , recovering the correct values of  $\chi(k)$  near the region of singularities is critical.

### K-space Iterative Approach

If the shapes of the structures of interest are known, then one can use this information in the SM to create a more accurate k-space of said SM in the conical region. The structure of the vessels is obtained directly from the first pass susceptibility map  $\chi_{i=0}(r)$ . The detailed steps of the iterative method are discussed below and shown in Fig. 1.

- Step-1** An initial estimate of the SM,  $\chi_{i=0}(r)$ , is obtained by applying a regularized version of the threshold-based inverse filter,  $g_{reg}^{-1}(k)$  [18], in Eq.[1] using the suggested threshold value,  $thr=0.1$ . The subscript “i” denotes the SM after the  $i^{th}$  iteration (“i=0” denotes the initial step before doing the iterative method and  $i=1$  for the first iteration).
- Step-2** The geometry of the structures of interest is extracted from  $\chi_{i=0}(r)$  using a binary vessel mask, i.e. outside the veins, the signal in the mask is set to zero, and inside it is set to 1. Since streaking artifacts associated with veins in the SM are usually outside the vessels, after multiplying the  $\chi_i(r)$  map by the

mask, little streaking remains in the SM. This leads to  $\chi_{vm, i}(r)$  as shown in part (b) of Fig.1. Vessel mask generation will be addressed in the next section.

- Step-3**  $\chi_{vm, i}(k)$  is obtained by Fourier transformation of  $\chi_{vm, i}(r)$  (part (c) in Fig. 1).
- Step-4** The pre-defined ill-posed region of k-space in  $\chi_{vm, i}(k)$  is extracted (part (d) in Fig. 1). These extracted k-space data are denoted by  $\chi_{vm, cone, i}(k)$ . The size of  $\chi_{vm, cone, i}(k)$  is decided by a threshold value,  $a$ , which is assigned to  $g(k)$ . For the matrix size  $512 \times 512 \times 512$ , the percentages of the cone region in k-space for a given  $a$ , are 2.4% ( $a=0.01$ ), 24.1% ( $a=0.1$ ), 47.1% ( $a=0.2$ ) and 70.6% ( $a=0.3$ ), respectively. When  $a$  increases, the size of  $\chi_{vm, cone, i}(k)$  increases too and if  $a$  is increased too much then most of the original information will be lost.
- Step-5** Data from  $\chi_{vm, cone, i}(k)$  and  $\chi_{i=0}(k)$  (part (e) in Fig. 1) are merged. This means part of  $\chi_{i=0}(k)$  has been replaced by  $\chi_{vm, cone, i}(k)$ . The merged data are denoted by  $\chi'_{merged, i}(k)$  (part (f) in Fig. 1).
- Step-6** Inverse Fourier transformation of  $\chi'_{merged, i}(k)$  gives the improved SM,  $\chi_{i+1}(r)$  (part (g) in Fig. 1).
- Step-7**  $\chi_i(r)$  in step-1 is replaced by  $\chi_{i+1}(r)$  from step-6 and the algorithm is repeated until

$$\sqrt{\sum [(\chi_i(r) - \chi_{i+1}(r))^2]} / N < \varepsilon \quad [3]$$

where  $N$  is the number of pixels in  $\chi_i(r)$  and  $\varepsilon$  is the tolerance value (chosen here to be 0.004ppm).

### Binary Vessel Mask Generation

The binary vessel mask was generated using thresholding from the  $\chi(r)$  map itself. The detailed steps are discussed below and shown in Fig. 2.

- Step-1** A threshold,  $th_1$ , is applied to  $\chi_{i=0}(r)$  to create an initial binary vessel mask,  $M_0$ . The pixels whose susceptibility values are lower than  $th_1$  will be set to zero while those greater than or equal to  $th_1$  will be set to unity. In this study, a relatively low susceptibility of 0.07 ppm is used for  $th_1$  to capture most vessels. However, this choice of threshold inevitably includes other brain structures in  $M_0$  that have high susceptibility.
- Step-2** A morphological operation i.e., a closing operation is performed to fill in holes in  $M_0$  to generate an updated mask  $M_1$ .
- Step-3** A median filter is applied to remove noise in  $M_1$  and create  $M_2$ .
- Step-4** False positive data points from  $M_2$  are removed as follows: First, the  $\chi(r)$  map is Mipped over 5 slices centered about the slice of interest to better obtain contiguous vessel information, as seen in  $\chi_{MIP}(r)$ . Second, another threshold,  $th_2 = 0.25$  ppm, is performed on  $\chi_{MIP}(r)$  to create a new  $\chi_{MIP\_vm}(r)$  and binary mask  $M_P$ , which only contains predominantly vessels. Here, 0.25 ppm was chosen to isolate the major vessels in the MIP image. Third, each slice from  $M_2$  is compared with  $M_P$  on a pixel by pixel basis to create  $M_3$ . If a data point from  $M_2$  does not appear on  $M_P$ , this data point will be treated as a false positive and removed from  $M_2$ . This process can be equally well applied to extract other tissues by choosing appropriate values for  $th_1$  and  $th_2$ .

## 2D Cylinder Simulations

Simulation of a two dimensional cylinder and its induced phase was first performed using a  $8192 \times 8192$  matrix. A lower resolution complex image was then obtained by taking the Fourier transform of this matrix and applying an inverse Fourier transform of the central  $512 \times 512$  matrix in k-space. This procedure is to simulate Gibbs ringing effects caused by finite sampling which we usually see in conventionally required MR data sets. Gibbs ringing comes from discontinuities in both the magnitude and phase images. To avoid Gibbs ringing from magnitude discontinuities, we used a magnitude image with a uniform signal of unity. A large sized object of 32 pixels was chosen to avoid major partial volume effects. All phase simulations were performed using a forward method [8,26,27,32] with  $B_0 = 3\text{T}$ ,  $\Delta\chi = 0.45\text{ ppm}$  in SI units,  $TE = 5\text{ ms}$ , and the cylinder perpendicular to the main magnetic field. The susceptibility value of  $0.45\text{ ppm}$  represents venous blood when the hematocrit ( $Hct$ ) = 0.44,  $\Delta\chi_{do} = 4\pi \cdot 0.27\text{ ppm}$  [30] and the oxygen saturation level = 70%, where  $\Delta\chi_{do}$  is the susceptibility difference between fully deoxygenated and fully oxygenated blood [31]. A relatively small echo time was chosen to avoid phase aliasing that can affect the estimated susceptibility values.

**Selection of a TBSO Method to Generate the  $\chi_{i=0}(r)$  Map**—Threshold based single-orientation (TBSO) methods [11, 15, 18, 24] use a truncated  $g(k)$  to solve the singularity problem in the inverse filter  $g^{-1}(k)$  when  $g(k)$  is less than a predetermined threshold value,  $thr$ . When  $g(k) < thr$ ,  $g^{-1}(k)$  is either set to zero [11, 24]; or to  $1/thr$  [15]; or set to  $g^{-1}(k) = 1/thr$  first and then  $g^{-1}(k)$  is brought smoothly to zero as  $k$  approaches  $k_{zo}$ . This smoothing is accomplished by multiplying  $g^{-1}(k)$  by  $\alpha^2(k_z)$  with  $\alpha(k_z) = (k_z - k_{zo})/|k_{zthr} - k_{zo}|$  where  $k_z$  is the z component of that particular point in k-space,  $k_{zo}$  is the point at which the function  $g^{-1}(k)$  becomes undefined, and  $k_{zthr}$  is the  $k_z$  coordinate value where  $|g(k)| = thr$  [18].

SMs using the methods in ref. [11,15,18] were calculated based on Eq. 1 using the 2D cylindrical model. Eq.1 is also valid to use for the simulated 2D cylinder phase to calculate SM since the 2D version is a special case of a 3D study with 1 slice and our actual study model is essentially an infinite cylinder perpendicular to the main field. Streaking artifacts are obvious in all three SMs (figures are not shown). The calculated mean susceptibility values inside the cylinder are around  $0.40 \pm 0.01\text{ ppm}$  for all SMs. The background noise levels, (i.e., standard deviation of the susceptibility values) measured from a region outside the streaking artifact in SM using ref. [18] are around 1/2 to 2/3 of the background noise levels in SMs using ref. [11,15] using  $thr = 0.06, 0.07$  and  $0.1$ , which are the optimal threshold values suggested in [11, 12, 18]. Given this result, the method [18] was chosen to generate a  $\chi_{i=0}(r)$  map.

**Finding an Optimal Threshold Value**—To find the optimal threshold, a series of  $\chi(r)$  maps were reconstructed by the iterative method using threshold values  $a$  of  $0.01, 0.03, 0.07, 0.1, 0.15, 0.2, 0.25$  and  $0.3$ . The larger this threshold, the closer the final estimate for  $\chi(r)$  will be to  $\chi_{vm}(r)$ . The optimal threshold value was found by comparing the accuracy of the estimated susceptibility values as well as the effects on reducing streaking artifacts in the reconstructed  $\chi(r)$  maps. To study the effect of noise in  $\chi(r)$  maps due to the noise in phase images, complex datasets for cylinders of diameter 2, 4, 8, 32 voxels, respectively, were simulated with Gaussian noise added to both real and imaginary channels. Noise was added in the complex images to simulate an  $\text{SNR}_{\text{magnitude}}$  of  $40:1, 20:1, 10:1$  and  $5:1$  in the magnitude images. Since  $\sigma_{\text{phase}} = 1/\text{SNR}_{\text{magnitude}}$ , this corresponds to  $\sigma_{\text{phase}} = 0.025, 0.05, 0.1$  and  $0.2$  radians.

To estimate the improvement in the SM by the iterative method, we used a root mean squared error (RMSE) to measure streaking artifacts outside the cylinder. Background noise

in the SM is measured in a region away from all major sources of streaking artifacts to compare to the noise measured in the phase image (i.e., so we can correlate noise in the phase with the expected noise enhancement from the inversion process).

**Effect of High-Pass Filter**—The effect of high-pass (HP) filtering the phase data on the  $\chi(r)$  map generated by the iterative method was also studied. Phase images of a cylindrical geometry with diameters of 2, 4, 8, 16, 32, and 64 voxels were simulated. Homodyne HP filters [33] with a 2D hanning filter (full width at half-maximum, FWHM = 4, 8, 16, and 32 pixels) were applied on these phase images in both in-plane directions. SM reconstructions were stopped based on the criteria in step 7 of the iterative process.

### Three Dimensional Brain Model Simulations

To address the potential of the iterative technique to improve the SM of general structures such as the basal ganglia, a 3D model of the brain was created including the: red nucleus (RN), substantia nigra (SN), crus cerebri (CC), thalamus (TH), caudate nucleus (CN), putamen (PUT), globus pallidus (GP), grey matter (GM), white matter (WM), cerebrospinal fluid (CSF) and the major vessels [34]. The structures in the 3D brain model were extracted from two human 3D T1 weighted and T2 weighted data sets. Basal ganglia and vessels are from one person; grey matter and white matter are from the other person's data set. Since all structures are from *in vivo* human data sets, this brain model represents realistic shapes and positions of the structures in the brain. Susceptibility values in parts per million (ppm) for the structures SN, RN, PUT and GP, were taken from ref. [12] and others were from measuring the mean susceptibility value in a particular region from SMs using ref. [18] from *in vivo* human data: RN = 0.13, SN = 0.16, CC = -0.03, TH = 0.01, CN = 0.06, PUT = 0.09, GP = 0.18, vessels = 0.45, GM = 0.02, CSF = -0.014 and WM=0. All structures were set inside a  $512 \times 512 \times 256$  matrix of zeros. The phase of the 3D brain model was created by applying the forward method [8,26,27,32] to the 3D brain model with different susceptibility distributions using the imaging parameters: TE = 5ms and  $B_0 = 3T$ . A comparison between the phase maps from this brain model and a real data set is shown in Fig.3. To match the imaging parameters of the real data set,  $B_0=3T$  and TE=18ms were applied for the results presented in Fig.3. Except for Fig.3, all other figures in the paper associated with the 3D brain were simulated by using TE=5ms.

### In Vivo MR Data Collection and Processing

A standard high-resolution 3D gradient echo SWI sequence was used for data acquisition. A transverse 0.5 mm isotropic resolution brain dataset was collected at 3T from a 23-year-old healthy volunteer. The sequence parameters were: TR = 26 ms, flip angle =  $15^\circ$ , read bandwidth = 121 Hz/pixel, TE = 14.3 ms, 192 slices, and a matrix size of  $512 \times 368$ . To reconstruct  $\chi_{i=0}(r)$  with minimal artifacts, the following steps were carried out:

1. The unwanted background phase variations were removed using either: a) a homodyne HP filter (FWHM = 16 pixels) [33] or b) Prelude in FSL [35] to unwrap the phase, followed by the process of Sophisticated Harmonic Artifact Reduction for Phase data (SHARP) [36] with a filter radius of 6 pixels. To reduce artifacts in the calculated SMs, regions with the highest phase deviations due to air/tissue interfaces were removed manually from the HP filtered phase images and the phase in those regions were set to be zero.
2. A complex threshold approach [37] was used to separate the brain from the skull.
3. The phase image with an original matrix size of  $512 \times 368 \times 192$  was zero filled to  $512 \times 512 \times 256$  to increase the field-of-view and to avoid streaking artifacts caused by the edge of brain to alias back to the reconstructed SM.

4. The regularized inverse filter,  $g_{\text{reg}}^{-1}(k)$  [18] was applied to obtain  $\chi_{i=0}(r)$ , followed by the iterative process using  $a = 0.1$ . For *in vivo* data, the iterative program was terminated at the third iterative step.

## RESULTS

### Selection of threshold level based on simulations

To find the optimal threshold value, SMs were reconstructed using  $a = 0.01, 0.03, 0.07, 0.1, 0.15, 0.2, 0.25$  and  $0.3$ , respectively, with different noise levels (Fig. 4). The streaking artifacts shown in  $\chi_{i=0}(r)$  (the first column in Fig. 4a) have been significantly reduced by the iterative method and fall below the noise level when  $a \geq 0.1$ . Also, when  $a \geq 0.1$ , the mean susceptibility value inside the cylinder was found to increase to  $0.44\text{ppm}$  when the diameter of the cylinder was larger than 8 pixels (Fig. 4b) and this trend is independent of the object size and the noise in the phase image. The optimal result in terms of obtaining the true susceptibility value was with a threshold of  $0.1$ . Fig. 4c shows a plot of RMSE of the susceptibility values from the whole region outside the 32-pixel cylinder using different  $a$ . The RMSE of the susceptibility values decreases as  $a$  increases. Therefore, for vessels, a value of  $0.3$  would be the optimal value. However, a large threshold value means replacing more original k-space with the k-space only consisting of vessel information which will reduce the signals from other brain structures and blur these structures. Since the SM using  $a = 0.1$  already reveals the optimal susceptibility value for the vessels and an acceptable RMSE, it is appropriate to choose  $0.1$  for more general application to study the entire brain.

Fig. 4a compares the converged  $\chi_{i=b}(r)$  map with the  $\chi_{i=0}(r)$  map, where  $b$  is the iterative step required to reach convergence. In this data,  $b = 2$  when  $a = 0.01$  and  $0.03$ ,  $b = 3$  when  $a = 0.07, 0.1$  and  $0.15$  and  $b = 4$  when  $a = 0.2, 0.25$  and  $0.3$  for  $\sigma_{\text{phase}} = 0$ . When  $\sigma_{\text{phase}}$  increases, more iterative steps were required to reach convergence. For instance, the maximum iterative step number is 9 when  $\sigma_{\text{phase}} = 0.2$  radians. Using a noise level of  $0.025$  radians in the phase image as an example,  $g_{\text{reg}}^{-1}(k)$  [18] leads to a susceptibility noise of roughly  $0.025\text{ ppm}$  in the  $\chi_{i=0}(r)$  map. The iterative approach leads to a slight decrease in background noise,  $0.021\text{ ppm}$ , in  $\chi_{i=3}(r)$  map when  $a = 0.1$ . The background noise was measured in a region outside the streaking artifact indicated by the black circle in Fig. 4a. The overall decrease in RMSE in the background (Fig. 4c) is a consequence of both a decrease in streaking artifacts and a reduction in thermal noise contribution.

### Selection of the Optimal Iterative Step

The inverse process [18] was applied to the dipole field in Fig. 5a to give the  $\chi_{i=0}(r)$  map shown in Fig. 5b; prominent streaking artifacts are evident in this image. Streaking artifacts are significantly reduced at each step of the iterative method quickly reaching convergence (Figs. 5c to 5e). The largest improvement is seen in the first iterative step, which is verified by Fig. 5f, showing the difference between Fig. 5c ( $\chi_{i=1}(r)$  map) and Fig. 5b ( $\chi_{i=0}(r)$  map). After the second iteration, we can see some minor streaking reductions (Fig. 5g, the difference between the  $\chi_{i=1}(r)$  map and  $\chi_{i=2}(r)$  map). The mean susceptibility value approaches  $0.44\text{ppm}$  in a single step. Similar results (not shown) are also obtained when the iterative method is run with different aspect ratios between the in-plane resolution and the through plane resolution (such as 1:2 and 1:4). The iterative results always lead to higher final susceptibility values compared to the initial value in  $\chi_{i=0}(r)$ . Finally, even when an HP filter is applied, up to a 10% increase in the susceptibility is realized (Fig. 5i). Large vessels benefit from a HP filter (FWMH = 4 pixels) and small vessels up to 8 pixels can still benefit from a HP filter (FWMH = 16 pixels).

## Effect of the Iterative Approach on Surrounding Brain Tissues in the 3D Brain Model

**a) SM Reconstruction using a vessel mask only**—Figs. 6a and 6d represent  $\chi_{i=0}(r)$ , without noise and with 0.025 radians of noise in phase images. Fig. 6f is the vessel map. Streaking artifacts (delineated by the black arrows) are obvious in Figs. 6a and 6d and completely disappeared in the  $\chi_{i=3}(r)$  maps (Figs. 6b and 6e) using  $a = 0.1$ . Fig. 6c is the  $\chi_{i=3}(r)$  map using  $a = 0.2$ . As can be seen, when  $a$  increases, the iterative method still works for vessels, but brain tissues become more blurred. Fig. 7a plots the mean susceptibility values inside the vessel (vein of Galen), GP, SN, RN, PUT and CN from  $\chi_{i=3}(r)$  maps generated by using  $a=0.1, 0.15, 0.2, 0.25$  and  $0.3$ , respectively. The susceptibility value in the brain model and  $\chi_{i=0}(r)$  map are also provided in the plot as references. Generally, the susceptibility values of brain tissues except vessels decrease as  $a$  increases while, for vessels, the susceptibility value is 0.41ppm in the  $\chi_{i=0}(r)$  map and is increased to 0.45ppm in the  $\chi_{i=3}(r)$  maps.

**b) SM Reconstruction using a mask including vessels and brain structures**—The iterative method is not limited to improving SM from just vessels; it can also be applied to the entire brain. Figure 6g shows a coronal view of the  $\chi_{i=0}(r)$  map for the brain model. The  $\chi_{i=3}(r)$  map using a mask keeping all major structures (GP, SN, RN, PUT, CN) and vessels is shown in Fig. 6h. In practice, this is equivalent to setting thresholds in the  $\chi_{i=0}(r)$  map to be greater than 0.009ppm to extract all these high susceptibility structures from the  $\chi_{i=0}(r)$  map to create the mask. Fig. 6h reveals that streaking artifacts associated with veins as well as all major structures have been reduced. Fig. 6i shows the difference between Fig. 6g and 6h. In addition, streaking artifacts sometimes cause the appearance of “false” structures. For instance, there is no internal capsule (IC) included in the model (Fig. 6l), yet we see an IC like structure in the  $\chi_{i=0}(r)$  map (Fig. 6j) (indicated by a dashed white arrow in Figs. 6j to 6l). The iterative method removes the streaking artifacts and the “false” IC (Fig. 6k). Fig. 7b shows susceptibility values in each structure in the brain model for  $\chi_{i=0}(r)$  and  $\chi_{i=3}(r)$  when the mask includes vessels and all major structures. The underestimated susceptibility values of all major structures and vessels in the  $\chi_{i=0}(r)$  map have been recovered by the iterative method in the  $\chi_{i=3}(r)$  map.

## Effect of Errors in the Vessel Map

Accurately extracting vessels from  $\chi_{i=0}(r)$  is critical for the iterative method. Figs. 8b–8d and the corresponding enlarged views (Figs. 8f–8h) from the rectangular region indicated in Fig. 8a, show the  $\chi_{i=3}(r)$  maps using an accurate (Fig. 8j), a dilated (Fig. 8k) and an eroded (Fig. 8l) vessel map to show the effect of errors in the vessel mask on the  $\chi_{i=3}(r)$  map. The dilated and eroded vessel maps were generated using Matlab functions based on a 3-by-3 square structuring element object. The susceptibility values measured from a vein indicated by the white arrow in Fig. 8e are  $0.40 \pm 0.03$ ppm (Fig. 8e),  $0.45 \pm 0.03$ ppm (Fig. 8f),  $0.45 \pm 0.03$ ppm (Fig. 8g) and  $0.40 \pm 0.07$ ppm (Fig. 8h), respectively. The iterative method still works if the vessel is slightly enlarged but does little to change the original  $\chi_{i=0}(r)$  map if the vessels are too small or absent in the mask. As we just discussed, streaking artifacts produced “false” vessels indicated by the dashed black arrow in Fig. 8e since these vessels are not in the model (Fig. 8i). These false vessels disappeared in Fig. 8f.

## Results from the In Vivo Dataset

In the *in vivo* example, we compare the differences between SHARP (Figs. 9a to 9d) and a homodyne HP filter (FWHM = 16 pixels) (Figs. 9e to 9h). Compared to the transverse view, streaking artifacts are more obvious in the sagittal or coronal view. Fig. 9a shows the  $\chi_{i=0}(r)$  map with severe streaking artifacts. The streaking artifacts were significantly reduced in the  $\chi_{i=3}(r)$  map (Fig. 9b) using  $a = 0.1$ . The streaking artifacts associated with the superior

sagittal sinus vein (indicated by two black arrows in Fig. 9a) were significantly decreased in Figs. 9b and 9d. The subtracted image (Fig. 9c), Fig. 9a minus Fig. 9b, reveals the removed streaking artifacts. These streaking artifacts are one of the reasons why the  $\chi_{i=0}(r)$  maps appear noisy. In the  $\chi_{i=3}(r)$  map, the reduction in streaking artifacts from individual veins leads to a decrease of noise therefore an increased SNR of veins. If veins are the only interest, even a threshold of 0.2 can work reasonably well (Fig. 9d). Two relatively big veins, V1 and V2, indicated by the white dashed and white solid arrows, respectively, in Fig. 9b, were chosen to measure the susceptibility values. Results are provided in Table 1. The susceptibility values of these two veins have been improved by roughly 16% by the iterative method. The standard deviation of the susceptibility values measured from a uniform region inside the white matter decreased from 0.042 ppm in  $\chi_{i=0}(r)$  map to 0.035 ppm and 0.023 ppm in the  $\chi_{i=3}(r)$  map with  $a = 0.1$  and  $0.2$ , respectively. The baseline susceptibilities of the major structures are higher with SHARP than with the HP filter. The iterative method works for brain structures also when the structure is included in the mask. For instance, the mean susceptibility values of the GP and SN have been increased from  $0.155 \pm 0.058$  ppm and  $0.162 \pm 0.067$  ppm in the  $\chi_{i=0}(r)$  map to  $0.163 \pm 0.070$  ppm and  $0.186 \pm 0.083$  ppm in the  $\chi_{i=3}(r)$  map, from the dataset processed using SHARP. The result after HP filtering (Fig. 9e) shows more edge artifacts indicated by the left arrow in Fig. 9e. Much of this error was reduced by the iterative method (Fig. 9f). It seems that the iterative method compensated for the worse first guess (Fig. 9e) and ended up with almost the same result (Figs. 9f and 9h) as having started with SHARP (Fig. 9b and 9d) from the image perspective. Since a small sized HP filter cannot remove rapid phase wrapping at air-tissue interfaces; we had to cut out the region near the sinuses in the phase images.

## DISCUSSION

In this article, a threshold-based k-space/image domain iterative approach has been presented. Simulations and *in vivo* results show that the ill-posed problems of streaking artifacts and biases in the estimates of susceptibilities can be significantly reduced. The replacement of the  $\chi(k)$  values near the singularities by  $\chi_{vm}(k)$ , which is obtained from the geometric information from the  $\chi(r)$  map itself, obviates many of the current problems seen in the TBSO methods. Since  $\chi_{vm}(r)$  contains little streaking artifacts itself, the values used inside the thresholded regions in  $\chi(k)$  now contain no artifact either. In this sense, we obtain an almost perfect k-space without bad data points in the region of singularities. This explains why this method converges quickly and the major improvement is in the first iterative step (Fig. 5).

The proposed iterative approach is different from the other threshold based methods [11,15,18,19,24] which fill a pre-defined conical region using a constant, zero or  $1/thr$  threshold [11, 15, 24] or the first-order derivative of  $g^{-1}(k)$  [19]. The iterative method uses full geometry information from the SM (vessels or pre-defined structures and not edge information) to iteratively change k-space values in the conical region using the forward model. This is also quite different than other currently proposed solutions [9, 12, 20, 22]. Even though spatial priors such as gradients of the magnitude are used [9, 12, 20, 22], in those methods, the meaningful values of the singularity regions in k-space are obtained through solving the complex cost function problem. However, the iterative method uses priors not from the magnitude image but from the SM. The missing data in the singularity regions are obtained through iterating back and forth between the SMs and their k-space. The advantage of cost function approaches is that they do not need to pre-define the singularity region in k-space which is solved by the optimization process automatically (although the optimization process itself is usually quite time-consuming). On the other hand, the iterative method is the most time-efficient. It is fast enough to reconstruct SMs for

a  $512 \times 512 \times 256$  data set using an Intel Core i7 CPU 3.4GHz processor in less than 30 seconds, since in practice usually 3 iterations are good enough to generate decent results.

The threshold value also plays a key role. A threshold value of 0.1 is a reasonable choice since a lower threshold value leads to an increase in noise and a higher threshold value leads to a blurring of the object (Fig. 6c, Figs. 9d and 9h).

It is known that the ill-posedness of the inverse filter will increase the noise level from the phase to the SM. Based on both simulations and real data, we find that there is a factor of 4 increase in noise in the SM relative to the original phase data. This result and the fact that at  $B_0 = 3\text{T}$ ,  $\text{TE} = 5\text{ms}$  and  $\sigma_{\chi_{i=0}(r)} = 0.025\text{ppm}$ , makes it possible to write the white noise error in  $\chi_{i=0}(r)$  as  $0.025 \cdot 4 \cdot (3/B_0) \cdot (5/\text{TE})$  in ppm. White noise error in  $\chi_{i=3}(r)$  will be less than this value since the iterative method will decrease noise in SM.

The iterative method can be used to remove streaking artifacts associated with not only vessels but also other brain structures as well. Fig. 6h shows a reduction in artifacts associated specifically with iron-rich regions such as the GP and CN.

Accurately extracting vessels from the  $\chi_{i=0}(r)$  map is critical for the iterative method (Fig. 8). In this study, vessels were segmented directly from the SM (Fig. 2). It may also possible to segment veins from original magnitude images [9,12,20,22], phase images and/or SWI images. Extraction of accurate anatomic information from phase data sometimes is difficult since phase is orientation dependent and phase changes are generally nonlocal. SWI images work better for an anisotropic dataset rather than an isotropic dataset since phase cancellation is needed to highlight vessel information. Therefore, we may consider combining SMs with magnitude images, phase images and/or SWI images together to segment the veins, since different types of images can compensate for missing information.

The iterative method appears to help even in the presence of non-isotropic resolution with partial volume effects and to a minor degree when an HP filter is applied. A smaller sized HP filter would be better, since a larger HP filter will significantly underestimate the susceptibility value (Table 1). SHARP gave us better results compared with the HP filter (FWHM=16 pixels) (Fig. 9), but SHARP requires phase unwrapping which can be time consuming and is noise dependent [19]. From this perspective, an HP filter has the advantage since it does not need unwrapped phase. If the forward modeling approach of Neelavalli et al [38] can be used to reduce air/tissue interface fields, then it may be possible to use a small size HP filter (FWHM=8 pixels) which may provide similar results to SHARP.

Severe streaking artifacts associated with structures having high susceptibility values such as veins can lead to major changes in the appearance of the brain structures with low susceptibility. Practically, the susceptibility of the veins is a factor of 2.5 to 20 times higher than other structures in the brain. Therefore, even a 10% streaking effect can overwhelm the information in the rest of the brain and create false appearing structures as in (Fig. 6j) and in (Fig. 8e). The reduction of these artifacts makes a dramatic difference in the ability to properly extract the susceptibility of other tissues.

In conclusion, both simulations and human studies have demonstrated that the proposed iterative approach can dramatically reduce streaking artifacts and improve the accuracy of susceptibility quantification inside the structures of interest such as veins or other brain tissues. Given its fast processing time, it should be possible to expand its use into more daily clinical practice. With the improved accuracy of the susceptibility values inside veins, this method could be used potentially to improve quantification of venous oxygen saturation [18].

## Acknowledgments

This work is partially supported by National Institutes of Health, NHLBI R01HL062983-A4; NHLBI R21 HL108230-A2 and DoD grant W81XWH-11-1-0493.

## References

1. Haacke EM, Mittal S, Wu Z, Neelavalli J, Cheng YC. Susceptibility-weighted imaging: technical aspects and clinical applications, part 1. *AJNR Am J Neuroradiol*. 2009; 30:19–30. [PubMed: 19039041]
2. Mittal S, Wu Z, Neelavalli J, Haacke EM. Susceptibility-weighted imaging: technical aspects and clinical applications, part 2. *AJNR Am J Neuroradiol*. 2009; 30:232–52. [PubMed: 19131406]
3. Haacke, EM.; Reichenbach, JR. *Susceptibility Weighted Imaging in MRI: Basic Concepts and Clinical Applications*. New Jersey: John Wiley & Sons, Hoboken; 2011.
4. Duyn JH, van Gelderen P, Li TQ, de Zwart JA, Koretsky AP, Fukunaga M. High-field MRI of brain cortical substructure based on signal phase. *Proc Natl Acad Sci U S A*. 2007; 104:11796–11801. [PubMed: 17586684]
5. Haacke EM, Lai S, Yablonskiy DA, Lin W. In-vivo validation of the BOLD mechanism: a review of signal changes in gradient-echo functional MRI in the presence of flow. *International Journal of Imaging Systems and Technology*. 1995; 6:153–163.
6. Rauscher A, Sedlacik J, Barth M, Mentzel HJ, Reichenbach JR. Magnetic susceptibility-weighted MR phase imaging of the human brain. *AJNR Am J Neuroradiol*. 2005; 26:736–42. [PubMed: 15814914]
7. Haacke EM, Cheng NY, House MJ, Liu Q, Neelavalli J, Ogg RJ, Khan A, Ayaz M, Kirsch W, Obenaus A. Imaging iron stores in the brain using magnetic resonance imaging. *Magn Reson Imaging*. 2005; 23:1–25. [PubMed: 15733784]
8. Koch KM, Papademetris X, Rothman DL, de Graaf RA. Rapid calculations of susceptibility-induced magnetostatic field perturbations for in vivo magnetic resonance. *Phys Med Biol*. 2006; 51:6381–6402. [PubMed: 17148824]
9. de Rochefort L, Brown R, Prince MR, Wang Y. Quantitative MR susceptibility mapping using piece-wise constant regularized inversion of the magnetic field. *Magn Reson Med*. 2008; 60:1003–1009. [PubMed: 18816834]
10. Cheng YC, Neelavalli J, Haacke EM. Limitations of calculating field distributions and magnetic susceptibilities in MRI using a Fourier based method. *Phys Med Biol*. 2009; 54:1169–1189. [PubMed: 19182322]
11. Wharton S, Schafer A, Bowtell R. Susceptibility mapping in the human brain using threshold-based k-space division. *Magn Reson Med*. 2010; 63:1292–1304. [PubMed: 20432300]
12. Wharton S, Bowtell R. Whole-brain susceptibility mapping at high field: a comparison of multiple- and single-orientation methods. *Neuroimage*. 2010; 53:515–525. [PubMed: 20615474]
13. Schweser F, Deistung A, Lehr BW, Reichenbach JR. Differentiation between diamagnetic and paramagnetic cerebral lesions based on magnetic susceptibility mapping. *Med Phys*. 2010; 37:5165–5178. [PubMed: 21089750]
14. Kressler B, de Rochefort L, Liu T, Spincemaille P, Jiang Q, Wang Y. Nonlinear regularization for per voxel estimation of magnetic susceptibility distributions from MRI field maps. *IEEE Trans Med Imaging*. 2010; 29:273–281. [PubMed: 19502123]
15. Shmueli K, de Zwart JA, van Gelderen P, Li TQ, Dodd SJ, Duyn JH. Magnetic susceptibility mapping of brain tissue in vivo using MRI phase data. *Magn Reson Med*. 2009; 62:1510–1522. [PubMed: 19859937]
16. Schafer A, Wharton S, Gowland P, Bowtell R. Using magnetic field simulation to study susceptibility-related phase contrast in gradient echo MRI. *Neuroimage*. 2009; 48:126–137. [PubMed: 19520176]
17. Liu T, Spincemaille P, de Rochefort L, Kressler B, Wang Y. Calculation of susceptibility through multiple orientation sampling (COSMOS): a method for conditioning the inverse problem from

- measured magnetic field map to susceptibility source image in MRI. *Magn Reson Med.* 2009; 61:196–204. [PubMed: 19097205]
- 18. Haacke EM, Tang J, Neelavalli J, Cheng YC. Susceptibility mapping as a means to visualize veins and quantify oxygen saturation. *J Magn Reson Imaging.* 2010; 32:663–676. [PubMed: 20815065]
  - 19. Li W, Wu B, Liu C. Quantitative susceptibility mapping of human brain reflects spatial variation in tissue composition. *NeuroImage.* 2011; 55:1645–1656. [PubMed: 21224002]
  - 20. Liu T, Liu J, de Rochefort L, Spincemaille P, Khalidov I, Ledoux JR, Wang Y. Morphology enabled dipole inversion (MEDI) from a single-angle acquisition: Comparison with COSMOS in human brain imaging. *Magn Reson Med.* 2011; 66:777–783. [PubMed: 21465541]
  - 21. Li L, Leigh JS. Quantifying arbitrary magnetic susceptibility distributions with MR. *Magn Reson Med.* 2004; 51:1077–1082. [PubMed: 15122694]
  - 22. de Rochefort L, Liu T, Kressler B, Liu J, Spincemaille P, Lebon V, Wu J, Wang Y. Quantitative susceptibility map reconstruction from MR phase data using bayesian regularization: validation and application to brain imaging. *Magn Reson Med.* 2010; 63:194–206. [PubMed: 19953507]
  - 23. Li Y, Xu N, Fitzpatrick JM, Morgan VL, Pickens DR, Dawant BM. Accounting for signal loss due to dephasing in the correction of distortions in gradient-echo EPI via nonrigid registration. *IEEE Trans Med Imaging.* 2007; 12:1698–1707. [PubMed: 18092739]
  - 24. Grabner G, Trattnig S, Barth M. Filtered deconvolution of a simulated and an in vivo phase model of the human brain. *J Magn Reson Imaging.* 2010; 32:289–297. [PubMed: 20677253]
  - 25. Deville G, Bernier M, Delrieux J. NMR multiple echoes observed in solid  $^{3}\text{He}$ . *Phys Rev B.* 1979; 19:5666–5688.
  - 26. Marques JP, Bowtell R. Application of a Fourier-based method for rapid calculation of field inhomogeneity due to spatial variation of magnetic susceptibility. *Concepts Magn Reson B Magn Reson Eng.* 2005; 25B:65–78.
  - 27. Salomir R, De Senneville BD, Moonen CTW. A fast calculation method for magnetic field inhomogeneity due to an arbitrary distribution of bulk susceptibility. *Concepts Magn Reson B Magn Reson Eng.* 2003; 19B:26–34.
  - 28. Hagberg GE, Welch EB, Greiser A. The sign convention for phase values on different vendor systems: definition and implications for susceptibility weighted imaging. *Magn Reson Imaging.* 2010; 28:297–300. [PubMed: 19699598]
  - 29. Demmel JW. Applied numerical linear algebra. Berkeley, CA: SIAM; 1997. Perturbation theory for the least squares problem; p. 117–118.
  - 30. Spees WM, Yablonskiy DA, Oswood MC, Ackerman JJ. Water proton MR properties of human blood at 1. 5 Tesla: magnetic susceptibility, T(1), T(2), T\*(2), and non-Lorentzian signal behavior. *Magn Reson Med.* 2001; 45:533–542. [PubMed: 11283978]
  - 31. Haacke, EM.; Brown, RW.; Thomson, MR.; Venkatesan, R. Physical Principles and Sequence Design. New York: John Wiley & Sons; 1999. Magnetic Resonance Imaging; p. 766
  - 32. Hoffman RE. Measurement of magnetic susceptibility and calculation of shape factor of NMR samples. *J Magn Reson.* 2006; 178:237–247. [PubMed: 16253530]
  - 33. Reichenbach JR, Venkatesan R, Schillinger DJ, Kido DK, Haacke EM. Small vessels in the human brain: MR venography with deoxyhemoglobin as an intrinsic contrast agent. *Radiology.* 1997; 204:272–277. [PubMed: 9205259]
  - 34. Buch, S.; Liu, S.; Neelavalli, J.; Haacke, EM. Simulated 3D brain model to study the phase behavior of brain structures. Proceedings of the 20th Annual Meeting of ISMRM; Melbourne, Australia. 2012. p. 2332
  - 35. Smith SM. Fast robust automated brain extraction. *Hum Brain Map.* 2002; 17:143–155.
  - 36. Schweser F, Deistung A, Lehr BW, Reichenbach JR. Quantitative imaging of intrinsic magnetic tissue properties using MRI signal phase: an approach to in vivo brain iron metabolism? *Neuroimage.* 2011; 54:2789–2807. [PubMed: 21040794]
  - 37. Pandian DS, Ciulla C, Haacke EM, Jiang J, Ayaz M. Complex threshold method for identifying pixels that contain predominantly noise in magnetic resonance images. *J Magn Reson Imaging.* 2008; 28:727–735. [PubMed: 18777533]

38. Neelavalli J, Cheng YCN, Jiang J, Haacke EM. Removing background phase variations in susceptibility weighted imaging using a fast, forward-field calculation. *J Magn Reson Imaging*. 2009; 29:937–948. [PubMed: 19306433]

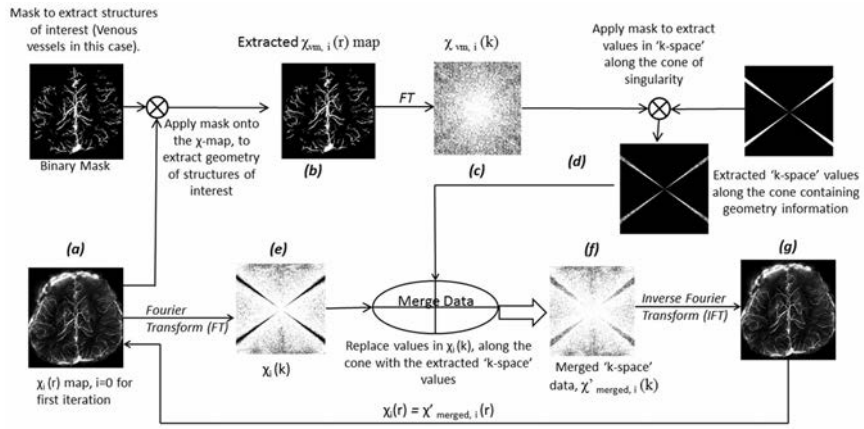
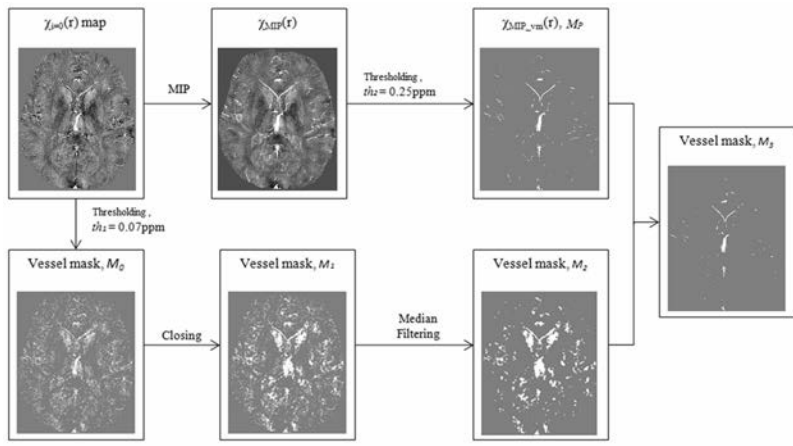
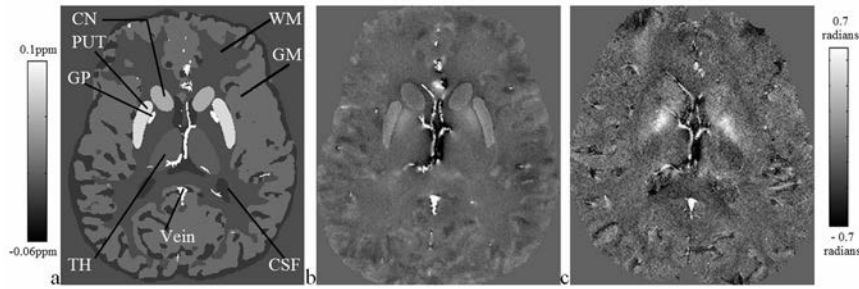
**Figure 1.**

Illustration of the iterative reconstruction algorithm to obtain artifact free  $\chi(r)$  maps.



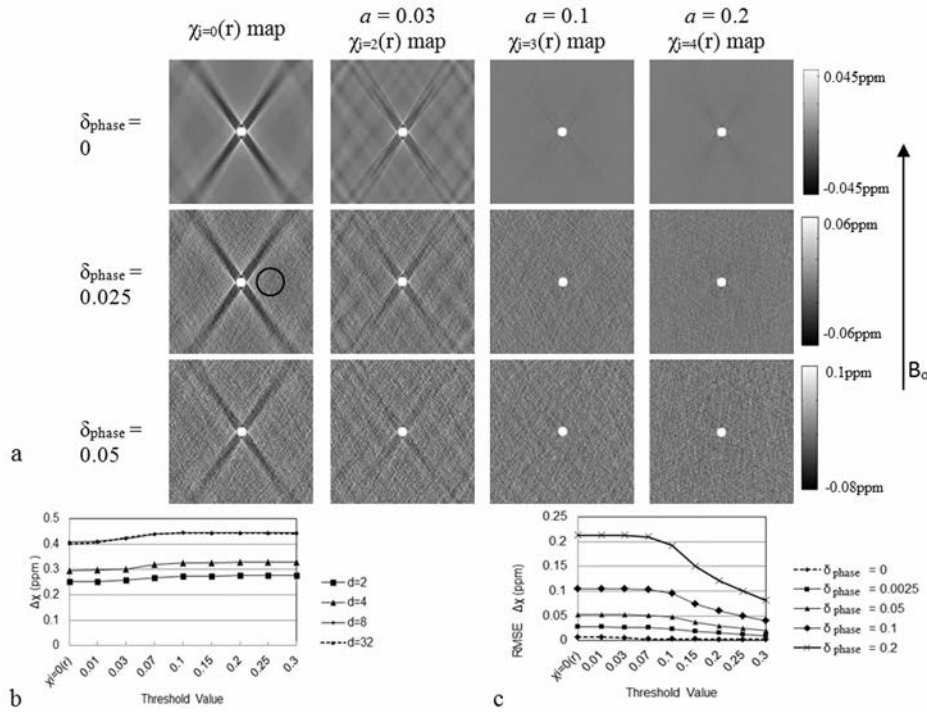
**Figure 2.**

Illustration of the binary vessel mask generation process.

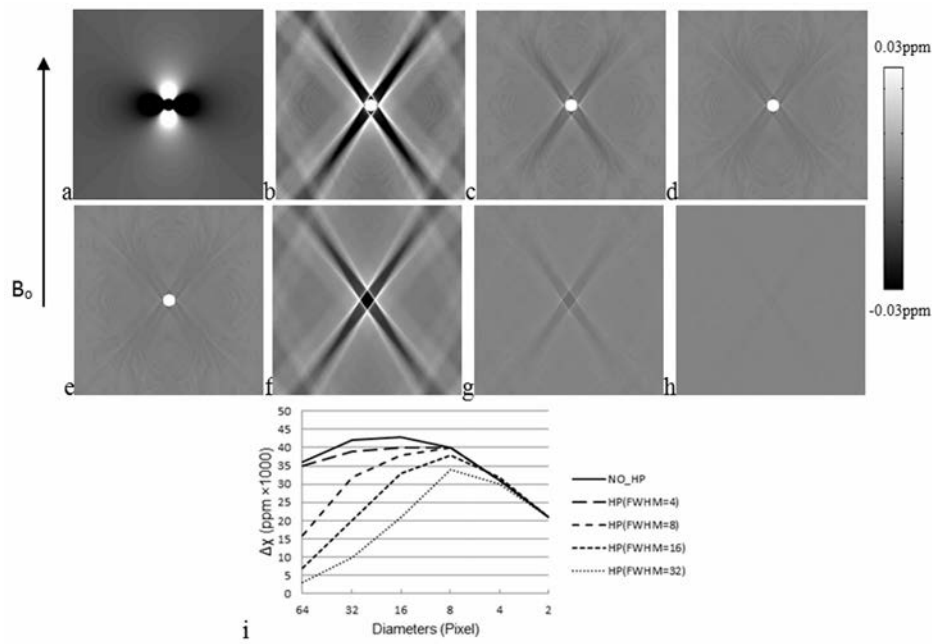


**Figure 3.**

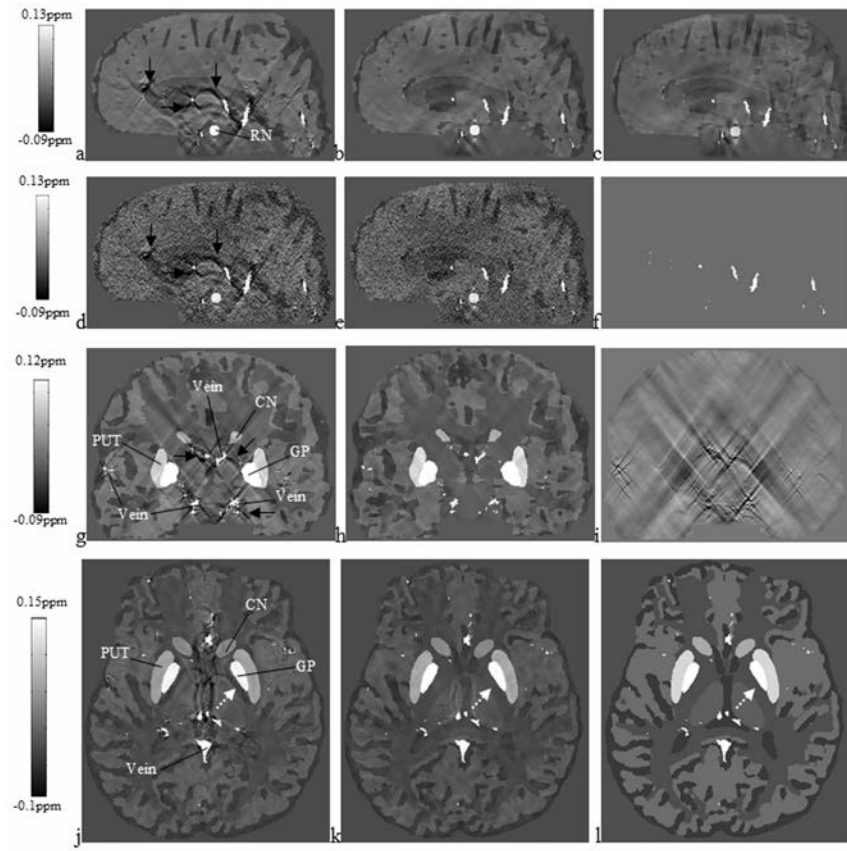
a) A transverse view of the 3D brain model. b) The simulated phase map from the model using parameters:  $B_0=3\text{T}$  and  $\text{TE}=18\text{ms}$  which are consistent with imaging parameters in the real data c). Images b) and c) have the same window level setting.

**Figure 4.**

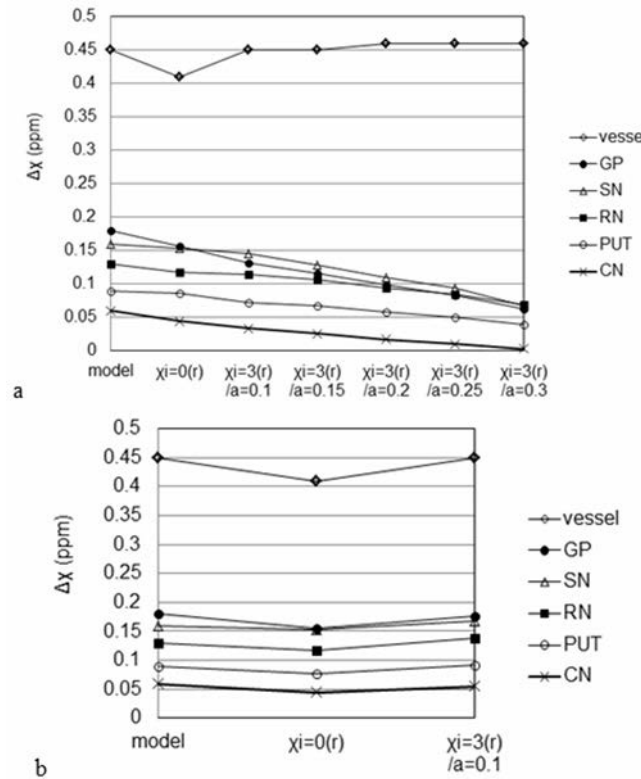
Simulations showing the comparison of the calculated susceptibility distributions for a cylinder perpendicular to  $B_o$  at different threshold values (a) applied to  $g(k)$  as well as the initial  $\chi_{i=0}(r)$  map. The direction of  $B_o$  is indicated by a black long arrow. The susceptibility,  $\Delta\chi$ , inside the cylinder is 0.45 ppm. a) The comparison of the converged  $\chi_{i=b}(r)$  map with the  $\chi_{i=0}(r)$  map for a diameter of 32-pixel cylinder, where  $b$  is the iterative step required to reach convergence. In this data,  $b = 2$  when  $a = 0.03$ ,  $b = 3$  when  $a = 0.1$  and  $b = 4$  when  $a = 0.2$  when  $\sigma_{\text{phase}} = 0$ . The top row of images shows simulations with no phase noise. The second and the third row show simulations with added phase noises  $\sigma_{\text{phase}} = 0.025$  and  $0.05$  radians, respectively. The first column of images show initial  $\chi_{i=0}(r)$  maps for reference. b) The variation of the mean calculated susceptibility inside the cylinder with different threshold value,  $a$ , for diameter ( $d$ ) = 2, 4, 8 and 32 pixels cylinders. The mean susceptibility value is independent of the noise level; therefore, only mean values from  $\sigma_{\text{phase}} = 0$  were provided. c) The variation of the RMSE of the susceptibility values outside the cylinder as a function of the threshold value,  $a$ , and the noise level. The  $d=32$  pixels cylinder was used to generate (c).

**Figure 5.**

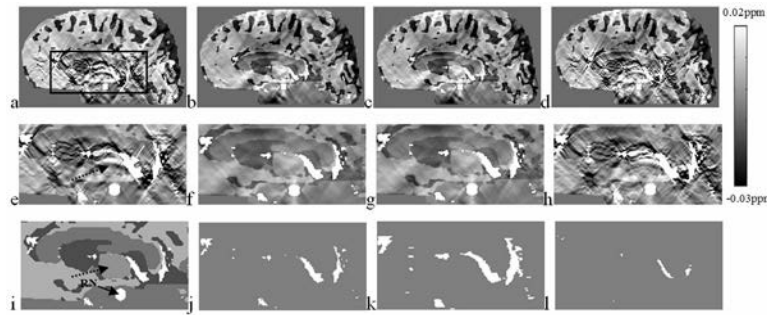
a) Phase images from a cylinder with a diameter of 32 pixels are simulated with:  $\Delta\chi=0.45\text{ppm}$ ,  $B_0=3\text{T}$  and  $\text{TE}=5\text{ms}$ . The cylinder is perpendicular to the main field. No thermal noise was added in these images. b) The initial  $\chi_{i=0}(r)$  map. c) The SM from the first iteration,  $\chi_{i=1}(r)$  map, d)  $\chi_{i=2}(r)$  map and e)  $\chi_{i=3}(r)$  map using threshold value  $a = 0.1$ . The SM has converged at  $\chi_{i=3}(r)$  map. The streaking artifacts are reduced as the number of iterative steps increases. f) The difference image of c) subtracted from b) illustrates that the streaking artifacts were reduced by the iterative procedure and the largest improvement happens in this first iterative step. g) The difference image of the  $\chi_{i=1}(r)$  map subtracted from the  $\chi_{i=2}(r)$  map indicates that the streaking artifacts were further reduced by the second iterative step. h) The difference image of  $\chi_{i=2}(r)$  map subtracted from  $\chi_{i=3}(r)$  map shows much less improvement at the third iterative step. Thus it indicates a convergence of the iterative procedure. All images were set to the same window level setting for direct comparisons and for enhancing the presence of the streaking and the remnant error. i) The effect of the iterative approach on the changes in susceptibility values from HP filtered phase images. Differences between the values in iterative and non-iterative susceptibility map reconstruction (i.e.  $\chi_{\text{converged}}(r) - \chi_{i=0}(r)$ ) from HP filtered phase images are plotted for different filter sizes (FWHM = 4, 8, 16 and 32 pixels) are shown here. Applying an HP filter leads to an underestimation of  $\Delta\chi$  [18]. The iterative approach helps to improve the accuracy of the estimated susceptibility values.

**Figure 6.**

Results before and after the iterative method using a region of interest map which consists of either only vessels or specific brain structures (in this case the basal ganglia) plus vessels. a) The initial  $\chi_{i=0}(r)$  map without noise added in the original simulated images. b)  $\chi_{i=3}(r)$  map of (a) using threshold value  $a=0.1$ . c) Similar to (b),  $a=0.2$ . d) The initial  $\chi_{i=0}(r)$  map with noise added in original images, resulting a standard deviation of 0.025 radian in phase images. e)  $\chi_{i=3}(r)$  map of (d) using  $a=0.1$ . f) The associated vessel map. g) The  $\chi_{i=0}(r)$  map in the coronal plane as a reference. The streaking artifacts are clearly shown in every structure. h) The  $\chi_{i=3}(r)$  maps created by using a region of interest map which consists GP, SN, RN, PUT, CN and vessels. i) The difference image of (g) and (h). j) The initial  $\chi_{i=0}(r)$  map in the transverse plane has “false” internal capsule (IC) (pointed by an arrow) around GP; k) The  $\chi_{i=3}(r)$  map shows no “IC.” This matches the originally simulated model (l). No noises were added to images from (g) to (l).

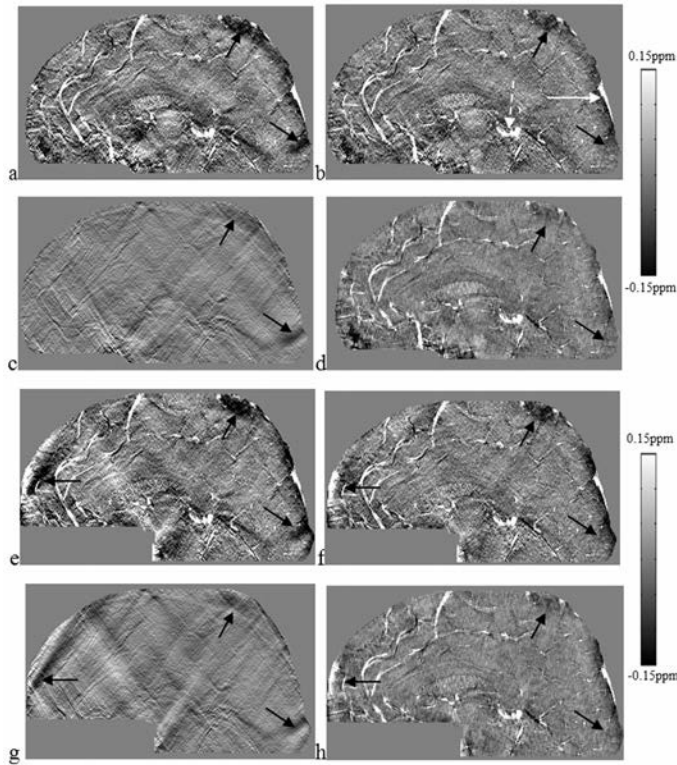
**Figure 7.**

The plots of mean susceptibility values inside the vessel (vein of Galen), GP, SN, RN, PUT and CN from  $\chi_{i=3}(r)$  maps. The first two data points of each curve is the value inside each structure from the brain model and the  $\chi_{i=0}(r)$  map, respectively. a)  $\chi_{i=3}(r)$  maps generated by applying a region of interest map which consists only vessels using  $a=0.1, 0.15, 0.2, 0.25$  and  $0.3$ , respectively. b)  $\chi_{i=3}(r)$  maps generated by applying a region of interest map which consists the GP, SN, RN, PUT, CN and vessels using  $a=0.1$ .



**Figure 8.**

Comparison of the reconstructed  $\chi_{i=3}(r)$  maps using j) accurate, k) dilated and l) eroded vessel maps. Their corresponding vessel maps and the enlarged views from the rectangular regions are provided in b) – d) and f) – h). a) and e) The initial  $\chi_{i=0}(r)$  maps and i) the original brain model as references. The circle in the midbrain in the  $\chi(r)$  maps represents the red nucleus (RN) and is indicated by a black arrow in i). Other hyper-intense regions in SMs are vessels.

**Figure 9.**

Comparisons of SMs using SHARP or a HP filter ( $\text{FWHM} = 16$  pixels) to remove the background field. The iterative method with  $a = 0.1$  and  $0.2$  is applied after the background is removed. a – d) and e – h) are results after the application of SHARP and the HP filter, respectively. a) and e) the initial  $\chi_{i=0}(r)$  maps. b) and f) The  $\chi_{i=3}(r)$  maps generated from the iterative method with  $a = 0.1$ . c) and g) The differences of images between (a) and (b), and between (e) and (f), respectively. These two images show the successful reduction of the streaking artifacts. d) and h) The  $\chi_{i=3}(r)$  maps generated from the iterative method with  $a = 0.2$ .

**Table 1**

$\Delta\chi$  measured *in vivo* in two veins in  $\chi_{i=0}(r)$  maps and  $\chi_{i=3}(r)$  maps with different threshold values

	$\chi_{i=0}(r)$ map	$\chi_{i=3}(r)$ map/a=0.1	$\chi_{i=3}(r)$ map/a=0.2
V1 (SHARP)	$0.32 \pm 0.07$	$0.37 \pm 0.08$	$0.38 \pm 0.09$
V1 (HP)	$0.24 \pm 0.05$	$0.28 \pm 0.06$	$0.28 \pm 0.06$
V2 (SHARP)	$0.35 \pm 0.04$	$0.40 \pm 0.05$	$0.41 \pm 0.05$
V2 (HP)	$0.25 \pm 0.05$	$0.31 \pm 0.06$	$0.30 \pm 0.06$

Mean and standard deviation for the susceptibility values (in ppm) of two veins processed using SHARP and a HP filter (FWHM = 16 pixels), respectively, were chosen from the 0.5 mm isotropic resolution data. V1 and V2 are shown in Fig. 9. The susceptibility values of these two veins have been slightly increased by the iterative method. There is not much variation of the susceptibility value with different threshold values.



● SPECIAL ISSUE

# Imaging brain plasticity after trauma

Zhifeng Kou<sup>1,2</sup>, Armin Iraji<sup>1</sup>

1 Department of Biomedical Engineering, Wayne State University, Detroit, MI, USA

2 Department of Radiology, Wayne State University, Detroit, MI, USA

## Abstract

**Corresponding author:**

Zhifeng Kou, Ph.D., Department of Biomedical Engineering, Wayne State University, Detroit, MI 48201, USA, zhifeng\_kou@wayne.edu.

**doi:**10.4103/1673-5374.131568

<http://www.nrronline.org/>

**Accepted:** 2014-04-10

The brain is highly plastic after stroke or epilepsy; however, there is a paucity of brain plasticity investigation after traumatic brain injury (TBI). This mini review summarizes the most recent evidence of brain plasticity in human TBI patients from the perspective of advanced magnetic resonance imaging. Similar to other forms of acquired brain injury, TBI patients also demonstrated both structural reorganization as well as functional compensation by the recruitment of other brain regions. However, the large scale brain network alterations after TBI are still unknown, and the field is still short of proper means on how to guide the choice of TBI rehabilitation or treatment plan to promote brain plasticity. The authors also point out the new direction of brain plasticity investigation.

**Key Words:** traumatic brain injury; brain plasticity; neuroplasticity; neuroimaging; magnetic resonance imaging; fMRI; diffusion tensor imaging

**Funding:** The work was supported by the Department of Defense, grant number W81X-WH-11-1-0493.

Kou Z, Iraji A. Imaging brain plasticity after trauma. *Neural Regen Res.* 2014;9(7):693-700.

## Introduction

Traumatic brain injury (TBI) is a significant public health care burden, with over 1.7 million incidents every year in the United States alone (Kay, 1993; National Institutes of Health, 1999). Currently, over 5.7 million Americans live in the shadow of TBI-induced disability (Kay, 1993; National Institutes of Health, 1999). Design of proper rehabilitation program is urgently needed to help them cope with TBI-induced challenges on daily basis. Evidence demonstrates that, even with damage in certain functional structures or networks, e.g., motor control and somatosensory networks, many patients can still pick up these functionalities during their recovery. This leads to the possibility that the brain could reorganize itself either through natural recovery or acquired training experience to cope with deficits.

More evidence also suggests a cumulative effect of brain injury, which may depend on changes in the baseline status of the brain at each injury. Most recently, the TRACK TBI study reported that TBI patients who had a previous head injury history, even just a brief loss of consciousness, tend to have worse outcomes than those without a history of brain injury (Dams-O'Connor et al., 2013). This evidence suggests that, after TBI, the brain does not return to its previous state. The neurocognitive recovery could be largely due to the brain remodeling to compensate for impaired function, called brain plasticity. In addition, the advent of advanced magnetic resonance imaging (MRI) techniques has significantly changed the view of our brain in both normal and pathological conditions. High resolution structural imaging

enables improved quantification of even small anatomical changes; diffusion tensor imaging (DTI) allows us to probe the brain's physiological conditions at microstructural level that is invisible on structural MRI; and functional MRI (fMRI) detects brain functional changes in response to external stimuli. The use of advanced MRI to detect brain plasticity has expanded drastically in cognitive neuroscience. From an imaging point of view, brain plasticity could be broken down into structural reorganization and functional compensation (Voss and Schiff, 2009).

Previously, Chen et al. (2010) gave a systematic review of brain plasticity after stroke. Dijkhuizen (2012) summarized recent DTI and fMRI findings of brain plasticity in animal stroke models. Kolb et al. (2010) summarized factors that influence cerebral plasticity in the normal and injured brain based on animal studies. Staudt (2010) gave insights into brain plasticity following early life brain injury (at the perinatal stage) from an imaging perspective. This mini-review adds to these efforts by summarizing the most recent imaging evidence of brain plasticity in TBI patients, from synaptic, microstructural, to functional network levels of the brain, particularly focusing on advanced MRI. At the end of the paper, the authors also point out the future directions for further investigation.

## Brain plasticity at the synaptic level

Brain plastic changes are age-, gender-, time-, experience-, and region-dependent (Chen et al., 2010; Kolb et al., 2010; Staudt, 2010). Among all regions, the cortex is the most

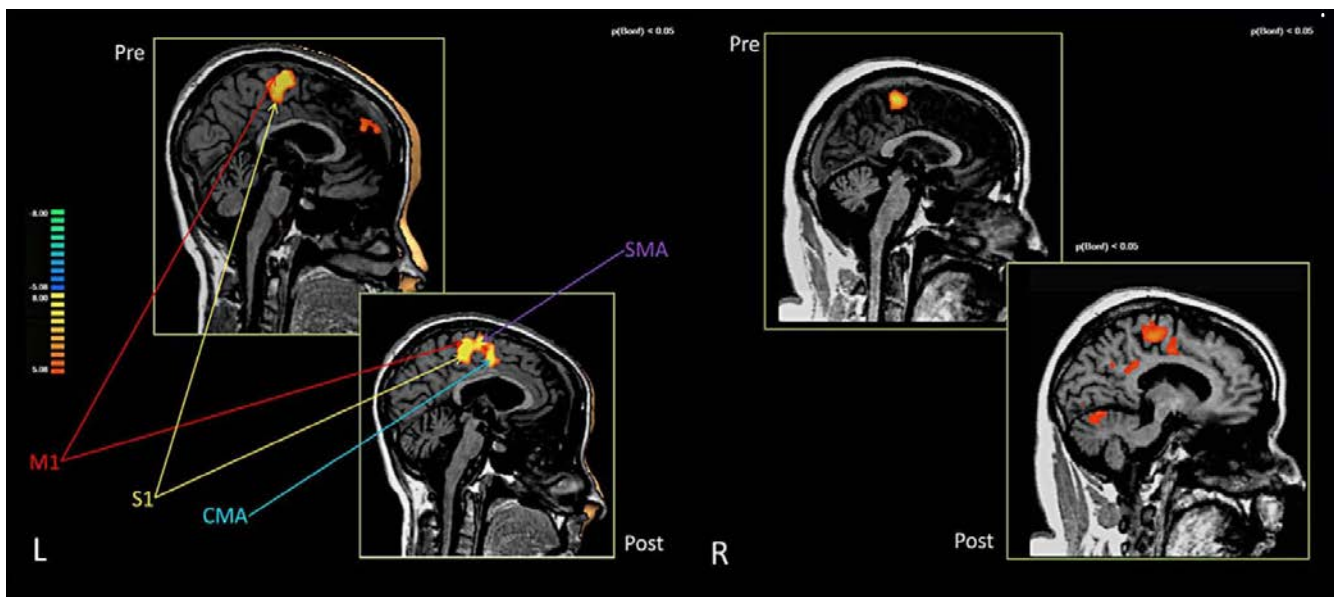


**Figure 1 Brain activations in the pre- and post-training conditions of two chronic traumatic brain injury patients receiving a combined robotic and cognitive training for rehabilitation.**

The highlighted warm areas designate signal intensity of brain activation. For the first patient at left side (L), combined training increased the recruitment of cingulate motor area and supplemental motor area in compensation of brain function. For the second case at right (R), combined training increased recruitment of more brain regions for compensation. M1: Primary motor cortex; S1: primary somatosensory cortex; CMA: cingulate motor area; SMA: supplemental motor area. Image courtesy Sacco et al. (2011) and Frontiers in Human Neurosciences.

widely reported as the most plastic region after injury. These plastic changes can be seen as reorganization in regions surrounding the damaged area and recruitment of new regions or use of alternative networks (Muñoz-Cespedes et al., 2001; Chen et al., 2010; Nishibe et al., 2010). In experimental animal models, extensive synaptic remodeling can be seen in the ipsilateral neocortex at the acute stage, as shown by a decrease in the density of pedunculated spines on apical dendrites (Campbell et al., 2012). Depending on the injury type, animals with focal injury show reinnervation of damaged tissue by surrounding tissue, and animals with diffuse injury show regenerative responses in damaged tissue areas at the acute stage (Hall and Lifshitz, 2010). At the chronic stage, there is a drag during neuroinflammatory microglial activation, which could be detrimental to brain recovery, along with continuous expression of plasticity-relevant proteins in promotion of cortical plasticity, including microtubule-associated protein-2 (MAP2) and synaptophysin (SYN) (Hall and Lifshitz, 2010; Jones et al., 2012; Morris et al., 2013).

Another important region of brain plasticity investigation is the striatum, including the thalamus. The thalamus serves as a relay station of somatosensory and motor function, and the striatum is full of dopaminergic neurotransmitters and plays an important role in motor control, motivation, arousal, cognition, and reward. Using fMRI, manganese-enhanced MRI and histological validation, Yu et al. (2012) demonstrated that thalamocortical inputs may represent a major site for adult plasticity, in contrast to the consensus that adult plasticity mainly occurs at cortico-cortical connections. Synaptic plasticity in the striatum is also linked to the activation of dopamine receptors with DARPP-32 as well as glutamatergic

transmission (Calabresi et al., 2000), and tyrosine hydroxylase serves to catalyze the formation of dopamine precursors (van Bregt et al., 2012). van Bregt et al. (2012) reported lasting alterations in dopamine metabolism in association with neuronal degeneration in the substantia nigra at the acute stage but no tyrosine hydroxylase change. At the chronic stage, 28 days after injury in rodent TBI models, both van Bregt et al. (2012) and Yan et al. (2007) reported alterations of tyrosine hydroxylase in the striatum as a compensatory mechanism to counteract dopamine deficiency after TBI.

Additionally, the hippocampus in particular has been an important region of interest for plasticity investigation in animal models, due to its theorized role in memory modulation, which are widely reported across different populations and can persist for long time. Early after TBI, at 24 hours, a substantial increase in spine density on dendrites bilaterally in CA1 and CA3 and the dorsal dentate gyrus could be seen, indicative of an increase in excitatory synapses (Campbell et al., 2012). Later, from the first week up to 2 months after injury, aberrant mossy fiber sprouting in the dentate gyrus at the ipsilateral side of brain injury can be seen, which is associated with spontaneous convulsive seizures (Hunt et al., 2009). Therefore, mossy fiber sprouting may play a role, along with neuron loss, neurogenesis, gliosis, and morphological changes that alter sensitivity to stimulation after TBI in animal models (Hunt et al., 2009).

### Brain plasticity at microstructural level

It has been reported that brain injury in early life, at the perinatal stage, can trigger structural and functional reorganization of the brain, which can be seen in both structural

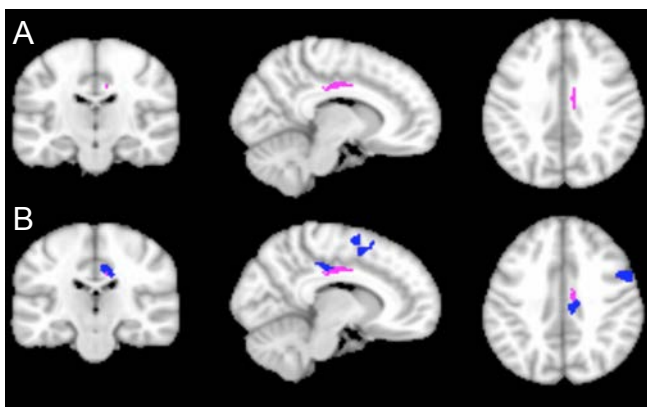


**Figure 2 Functional compensation for structural damage after traumatic brain injury.**

(A) Structural connectivity of white matter by using poster cingulate bundle as the seed region for probabilistic tractography analysis: The pink color shows the areas in which the patient group has lower connectivity (two sample  $t$ -test,  $P < 0.05$ ). (B) Overlay of functional connectivity onto DTI structural connectivity. The blue color shows the areas in which the patient group has higher functional connectivity by using posterior cingulate cortex as the seed region (two sample  $t$ -test,  $P < 0.005$ ). The figure clearly shows that the increased functional connectivity on resting state functional MRI (fMRI) tends to compensate for structural damage in the cingulate bundle in TBI patients. This demonstrates the complementary role of DTI and fMRI in delineating brain plasticity after TBI.

and functional MRI. Among structural MRI, DTI has been reported being sensitive to white matter (WM) injury at a microstructural level that is invisible on conventional MRI (Niogi et al., 2008a, 2008b).

Evidence of brain plasticity includes reorganizations of the motor system, somatosensory system, and language regions detected by structural T1, DTI tractography and task oriented fMRI (Staudt, 2010). In the early childhood, a patient who was born prematurely with serious injury on the arcuate fasciculus, the critical pathway for language processing, could still have preserved language and reading functions (Yeatman and Feldman, 2013). Instead, DTI tractography demonstrated intact ventral connections between the temporal and frontal lobes through the extreme capsule fiber system and uncinate fasciculus. This connection is likely to take over the language processing functionality as a compensational mechanism (Yeatman and Feldman, 2013). In adult brain injury patients, Yogarajah et al. (2010) conducted a DTI study of 46 epilepsy patients with anterior temporal lobe resection. They reported increased fractional anisotropy (FA) in the ventro-medial language network, in suggestion of structural reorganization in response to the resection (Yogarajah et al., 2010). In a case study of a patient suffering from tuberous meningitis at the age of 12 years, Jan et al. reported a new motor pathway posterior to the lesion in the midbrain and upper pons, evidenced by diffusion tensor tractography, task oriented fMRI, and transcranial magnetic stimulation (Ndode-Ekane et al., 2010). Laitinen et al. (2010) also reported increased fractional anisotropy in the hippocampal dentate gyrus in an animal model induced with status epilepticus, and the FA changes are correlated ( $P < 0.01$ )

with histologically verified axonal plasticity of myelinated and non-myelinated neuronal fibers. This evidence demonstrated that morphological structural is the foundation of brain plasticity. In case of injury at one location, other possible alternative routes must be intact to compensate the impaired function. Zhou et al. (2014) demonstrated that rats with partial corpus callosotomy can have restored functional connectivity between hemispheres at 28 days after injury, but rats with complete corpus callosotomy cannot, likely due to the compensation that occurred through the remaining interhemispheric axonal pathways. Their data suggest that axonal connections are the indispensable foundation for resting state functional connectivity.

## Brain plasticity at functional network level

### Task-oriented fMRI findings

fMRI is the most widely used modality to investigate brain functional network alternations in pathological conditions. Task-based fMRI is considered the gold standard for identifying corresponding functional activations. In a case study of two chronic TBI patients, Sacco et al. (2011) reported greater activation in the sensorimotor and supplementary motor cortices after a combined robotic and cognitive rehabilitation training, as well as enhanced functional connectivity within the motor network (Figure 1). Improvements in balance and, to a lesser extent, in gait outcomes were also found in these two patients. In another study of 20 patients at 1 month after mild TBI (mTBI) and 18 healthy controls, Chen et al. (2012) demonstrated that brain activation patterns differed between mTBI patients and controls in response to increasing working memory loads ( $P < 0.01$ , uncorrected). mTBI patients were impaired in their ability to increase activation in working memory circuitry under both moderate and high working memory load conditions in contrast with controls. However, mTBI patients showed cerebral plasticity, as evidenced by more activation in some areas outside and inside the working memory circuitry as compared with control subjects ( $P < 0.01$ , uncorrected). This work is in line with the earlier study by McAllister et al. (1999) on mTBI. In addition, Tivarus et al. (2012) reported the reorganization of language network to the right hemisphere after early left hemisphere injury by using task-based fMRI. In a study of a severe and persistent speech disorder, dysarthria, Morgan et al. (2013) reported functional reorganization involved over-recruitment of left-hemisphere motor regions for language processing. In contrast with these beneficial findings of brain plasticity, Hampshire et al. (2013) studied 13 retired National Football League players by using task-based fMRI. They reported that the players showed pronounced hyperactivation and hypoconnectivity of the dorsolateral frontal and frontopolar cortices. Critically, abnormal frontal lobe function was correlated with the self-reported number of times of the players' being removed from play due to head injury (Hampshire et al., 2013). This might be a direct evidence of pathological plasticity due to maladaptive recruitment of brain resources and activations.

### Resting state functional connectivity MRI (fcMRI) findings

Despite the popularity of task-based fMRI in mapping functional activations, it is not possible to use it to identify all functional networks of the brain. As a complement, resting state fcMRI is the most widely used technique in recent years to identify the brain network connectivity. Among all brain networks in the resting state, the “Default Mode Network” (DMN) is the most studied in mTBI (Mayer et al., 2011; Johnson et al., 2012; Stevens et al., 2012). The DMN is assumed to control passive mental activities in which individuals are awake and alert but do not specifically perform any “goal-directed task” (Broyd et al., 2009). The posterior cingulate cortex (PCC) and the medial prefrontal cortex (MPFC) are two important components of the DMN. PCC and MPFC are associated with self-referential and emotional processing, as well as semantic processing, and their activity is attenuated when attention to the “goal-directed task” increases (Gilbert et al., 2007). The DMN’s important role in several cognitive functions and its disruption in several neurocognitive disorders both highlight the importance of the DMN’s connections and possible alterations in its activity as a possible diagnostic marker of injury-related neural damage. In mTBI investigation, most studies demonstrated decreased functional connectivity among the regions of the default mode network (DMN) and increased connectivity of DMN regions with brain regions that belong to other functional networks, in suggestion of functional network remodeling of the brain after injury. Mayer et al. (2011) studied mTBI patients at the semi-acute stage (within 2 weeks after injury) by choosing the rostral anterior cingulate gyrus (rACC) as the seed region and demonstrated a reduction in connectivity within DMN for mTBI and an increase in connectivity within a task-related network (TRN) relative to matched controls. Similarly, Johnson et al. (2012) scanned sports athletes with mTBI at the sub-acute phase ( $10 \pm 2$  days). By using voxel-based and region of interest (ROI)-based analysis, they focused on DMN regions such as PCC, MPFC, the lateral parietal lobes, and the parahippocampal gyrus. They indicated that both the number and strength of connections decreased in the PCC and the lateral parietal cortices but increased in the medial prefrontal cortex following mTBI. With an independent component analysis (ICA) analysis, Stevens et al. (2012) explored different ICA components to find alterations between healthy subjects and mTBI patients who were scanned 61 days after injury. They found diminished functional connectivity in the DMN and many other networks in the patient group, such as the primary visual processing circuit, the motor system, the left-lateralized frontoparietal circuit, the dorsomedial circuit, the frontoparietal executive system, and the frontostriatal network. They found that the precuneus had greater connectivity with the default mode network, while the connectivity between the cingulate and the DMN was diminished.

In a severe TBI study, Nakamura et al. (2009) studied six TBI patients at 3 months and then followed them up at 6 months after injury. By using a graph theory-based analysis of whole brain networks, they reported reduced overall strength in connectivity and increased “small-worldness” of TBI pa-

tients at 3 months after injury. At 6 months after injury, these parameters tend to return back to normal level as healthy controls (Nakamura et al., 2009). Despite their obvious structural damage on conventional MRI in these severe TBI patients, their brain overall connectivity could still come back to normal level as controls at the chronic stage. This is another piece of direct evidence for brain plasticity after injury as an important determiner of recovery.

### Combining structural imaging with fcMRI

A combinational analysis of DTI (white matter structural damage) and fcMRI (functional network alternation) could offer more meaningful insights of the brain plasticity to cope with injury. We acquired MRI data in a preliminary dataset from 7 healthy controls ( $27.71 \pm 10.43$  years old) and 7 patients ( $33.57 \pm 8.44$  years old) with mTBI within 24 hours after injury. Both DTI probabilistic tractography and resting state fcMRI analysis have been performed to investigate the structural damage on DTI and functional alternatives on fcMRI. Our fcMRI analysis showed a decreased strength of connectivity within the DMN but an increased connectivity between posterior cingulate cortex (PCC) and other brain networks (especially supplementary motor cortex) in mTBI patients, which is consistent with our previous work and other studies. The DTI probabilistic tractography analysis also showed structural damage in the cingulate bundle. Statistical analysis on the fMRI functional connectivity map demonstrated significantly decreased connectivity in the angular gyrus ( $P = 0.0005$ ) with cluster size = 64, PCC ( $P = 0.005$ ), and orbitofrontal gyrus ( $P = 0.005$ ) (Figure 2). In other brain areas, such as in a big cluster in the supplementary motor cortex (Brodmann area 6), connectivity was significantly increased ( $P = 0.0005$ ) with cluster size = 116, which may be related to motor disabilities after injury. The PCC also showed higher connectivity with the middle cingulate gyrus in the patient group than in the control group. This region of high functional connectivity on fcMRI closely opposes a region of lower structural connectivity in DTI probabilistic measurements in the middle part of cingulum bundle in patients ( $P = 0.05$ ) (Figure 2). Our data represent the first report regarding the relationship between structural damage and functional response in mTBI at the hyperacute stage. It suggests that, along with structural damage in white matter tract after TBI, the brain is trying to recruit more neuronal resources to compensate for changes in functionalities.

### Brain plasticity at connectomic scale

Unlike stroke or epilepsy, in which the injury lesion tends to be restricted to a focal region, TBI pathology is much more heterogeneous and tends to have multi-focal lesions. One example is diffuse axonal injury, which always has more than one WM tract involved in TBI on DTI findings (Kou et al., 2010; Niogi and Mukherjee, 2010; Kou and VandeVord, 2014). Despite the plasticity findings in memory, sensorimotor and other functions, the extents of brain injury and responsive plasticity at a large scale brain network level or connectome level are still unknown. By using ICA analysis, Stevens et al.

(2012) identified the reduced connectivity in several brain networks and increased connectivity in other networks. However, ICA may not be the ideal approach to analyze whole brain connectivity: it is not clear which ICA network represents which brain function and using different numbers of components will result in different results. The combination of DTI, for the detection of structural damage, with fcMRI, for functional network identification, offers a unique opportunity to investigate the functional brain plasticity in response to structural damage over the whole brain. However, due to the lack of dense and corresponding cortical landmarks across individuals, the systematical alterations of functional connectivities in large-scale brain networks and the alteration of structural brain architecture in TBI brain are largely unknown. A newly developed data-driven strategy, called Dense Individualized and Common Connectivity-Based Cortical Landmarks (DICCCOL), might hold the promise in this avenue (Zhu et al., 2013a). It has been reported as being sensitive to brain network alterations at a connectomics level in mild cognitive impairment patients (Zhu et al., 2013b) as well as prenatal cocaine expose (PCE) patients (Li et al., 2013). It is based on the hypothesis that the common cortical architecture can be effectively represented by group-wise consistent structural fiber connections. Each DICCCOL node is a functional land marker on cortical area, defined by group-wise consistent white matter fiber connection patterns derived from DTI data (Zhu et al., 2013a). The analysis of PCE patients discovered informative functional connectomics signatures among consistent landmarks that distinctively differentiate PCE brains from their matched controls (Li et al., 2013). Taking it one step further, this approach could be used in TBI patients to detect their connectomics signature, including both structural deficit and functional connectivity remodeling.

## Brain plasticity as a treatment target

### Training promoted brain plasticity

It has been well recognized in both animal models and human studies that brain plasticity is experience dependent, even in adulthood (Chen et al., 2010; Kolb et al., 2010). The brain can be altered by a wide variety of experiences across the lifespan as summarized by Kolb et al. (2010). These include sensory and motor experience, e.g., sports training; psychomotor stimulus, e.g., drug use; and career related training experience. These changes can also be detected in modern MRI techniques. As an example, London taxi drivers tend to have increased hippocampal volumes with the length of their career, which is thought to be a result of navigating the streets of London on daily basis because of the hippocampus role in spatial navigation (Maguire et al., 2000). Another fMRI study of subjects who learned sequential finger movements demonstrated changes in the motor cortex, cerebellum and basal ganglia following the training (Ungerleider et al., 2002). Therefore, brain plasticity could be used as a treatment target even in TBI patients, by prescribing a method called training-induced recovery (Chen et al., 2010). Specific rehabilitation programs could

be designed to address certain deficit aspects of brain injury to stimulate the reorganization of functional brain regions. Advanced MRI, particularly fMRI, could play a significant role in assessing the treatment effect. Successful examples include language training in aphasia patients after stroke, which shows right-hemisphere activation shifted to left hemisphere activation at the chronic stage (Meinzer et al., 2007; Richter et al., 2008), and robot-based hand motor therapy, which promotes motor cortex activation and reorganization in chronic stroke patients (Luft et al., 2001; Takahashi et al., 2008).

Proactive neurorehabilitation, which targets specific impaired neurocognitive domain(s) in TBI patients, holds the promise of improving patients' recovery by stimulating brain remodeling of functional regions. Evidence also demonstrated that TBI patients who actively returned back to work that requires highly intellectual involvement tend have a favorable outcome. As a matter of fact, the highly intellectually involved work itself provides an ideal environment of neurorehabilitation that may promote brain reorganization. To date, its underlying brain plasticity mechanism is still yet to be investigated.

### The role of microglial activation

One important aspect of TBI at the chronic stage is the persistent microglial activated neuroinflammation, which may contradict the effort of treatment plans that promote brain plasticity. Recent positron emission tomography studies using <sup>11</sup>C-(R)-PK11195 (PK) tracer have demonstrated persistent microglial activation even 17 years after injury (Ramlackhansingh et al., 2011). This work is also confirmed in TBI animal model using PK binding (Folkersma et al., 2011). An autopsy study of brain injury patients also demonstrated that persistent microglial activation could be a major cause of progressive atrophy of the brain, indicating that one single brain injury can result in microglial activation persisting for decades (Ungerleider et al., 2002). However, we are still short of means to non-invasively quantify microglial activation in TBI patients (Kou and VandeVord, 2014). The field is still lacking in knowledge about the role of microglial activation and how it can negatively affect the efforts towards brain plasticity (Kou and VandeVord, 2014). As a matter of fact, the neuroscience community has been dramatically changing the view about the role of microglia in recent years (Eyo and Dailey, 2013). A recent systemic review reported on microglial activation and white matter injury, a potential treatment target (Kou and VandeVord, 2014). Under the notion of combinational therapy (Margulies et al., 2009), anti-inflammatory treatments may also need to be considered along with the brain plasticity stimulation plan to achieve better patient outcomes over the long run.

## The caveat

### Not all plasticity is good

Despite its overall beneficial role in brain functional compensation in the literature, not all brain plasticity is beneficial to the brain function (Chen et al., 2010; Kolb et al., 2010; Li et

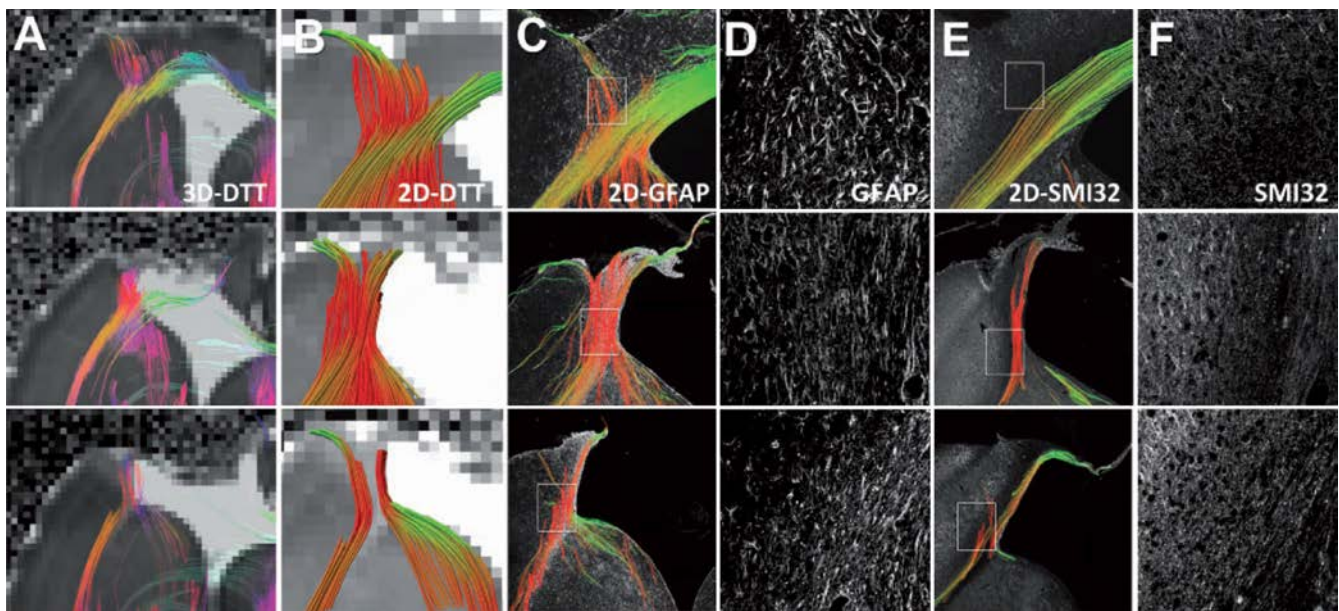


**Figure 3 Comparison of diffusion tensor tractography and histology-derived tractography demonstrates that the spurious fibers can be caused by reactive astrogliosis.**

Three representative controlled cortical impact animals are shown. (A) *Ex vivo* 3D diffusion tensor tractography (DTT) maps depict tracts propagating in and along the lesion periphery similar to those observed *in vivo*. (B) 2D diffusion tensor tractography was subsequently performed to allow direct comparison to the 2D histology-derived tractography. (C) 2D tractography maps from the glial fibrillary acidic protein (GFAP)-stained sections revealed similarities to the DTI-derived maps near the lesion border. (D) The coherent orientation of astrocytes is shown on confocal images from selected regions. (E) 2D tractography maps from the Sternberger monoclonal antibody (SMI) 32-stained sections revealed fewer, if any, tracts propagating into the cortex near the lesion periphery. (F) A loss of structural integrity is noted for both the injured white matter and grey matter along the lesion border. These three examples demonstrate spurious WM tracts that are actually caused by reactive astrogliosis instead of fiber reorganization during brain plasticity. Image reproduced with permission from Budde et al. (2011) and Brain journal.

al., 2014). Some plasticity can induce pathological conditions, or called pathological plasticity (Li et al., 2014). Examples include pathological pain (Baranauskas, 2001), pathological response to sickness (Raison et al., 2006), epilepsy (Teskey, 2001), schizophrenia (Black et al., 2004) and dementia (Mattson et al., 2001). One well-known example is that some drug treatments can cause maladaptive brain plasticity for drug addiction (Kolb et al., 2010). Another example is the mossy fiber sprouting and reorganization in hippocampus after TBI that may lead to epilepsy due to pathological firing of neurons and reduced synaptic inhibition in the region (Hunt et al., 2009). In addition, maladaptive changes during plasticity can have detrimental effects on the brain itself (Carey and Seitz, 2007; Chen et al., 2010) and interfere with regaining of normal functions (Murphy and Corbett, 2009). In stroke, recruitment of the contralateral region is compensatory in the early stage but may become maladaptive in later stages (Carey and Seitz, 2007; Chen et al., 2010). One challenge during pharmacological treatment or in the designing of rehabilitation programs for TBI patients is to minimize the side effects of treatment so that it will not induce maladaptive plastic changes that could actually interfere with recovery. Particular caution has to be taken during drug treatment to avoid maladaptive behavior of drug addiction (Kolb et al., 2010).

#### The spurious fibers may not be fibers

Another example is the spurious WM fibers after TBI on DTI either in contralateral or ipsilateral side of injury. It has been

recognized that reactive astroglial activation occurs in either ipsilateral or contralateral side of brain injury (Budde et al., 2011; Zhuo et al., 2012). In the DTI signature, the cellular infiltration of reactive astroglial cells will cause reduced radial diffusivity and increased FA, which is similar to neuronal regeneration or reorganization. DTI fiber tractography will show spurious WM fibers (Figure 3). As demonstrated by Budde et al. (2011), the spurious WM fibers on DTI tractography are caused by reactive astrocytes, as validated histologically, instead of axonal regeneration or reorganization. Particularly in neuroimaging of clinical patients, due to the lack of histological validation, caution should be taken before drawing any conclusion of axonal regeneration or reorganization after TBI, especially in cortical regions.

#### Summary

As the most important organ of human body, the brain is highly plastic even in the adulthood in response to external stimuli, either favorably or unfavorably. Damage to certain areas of brain can be compensated for, either structurally or functionally. Due to the heterogeneity and multi-focal nature of TBI, the brain network alterations in response to injury at a connectomic scale are still largely unknown. Further, the choice of pharmacological treatment plan and the design of proper rehabilitation programs hold the promise to stimulate functional brain plasticity for a favorable recovery. Methods to avoid pathological plasticity are an important area of investigation which can be strongly aided by the

use of advanced MRI.

**Acknowledgments:** The authors thank Ms. Natalie Wiseman, MD/PhD candidate, for her proof reading of the manuscript.

**Author contributions:** Kou Z was the main developer of this manuscript. Iraji A contributed literature review and data analysis in the manuscript. Both of these two authors approved the final version of this manuscript.

## References

- Baranauskas G (2001) Pain-induced plasticity in the spinal cord. In: Shaw CA, McEachern J, eds. *Toward a Theory of Neuroplasticity*. Philadelphia: PA: Psychology Press.
- Black JE, Kodish IM, Grossman AW, Klintsova AY, Orlovskaya D, Vostrikov V, Uranova N, Greenough WT (2004) Pathology of layer V pyramidal neurons in the prefrontal cortex of patients with schizophrenia. *Am J Psychiatry* 161:742-744.
- Broyd SJ, Demanuele C, Debener S, Helps SK, James CJ, Sonuga-Barke EJ (2009) Default-mode brain dysfunction in mental disorders: a systematic review. *Neurosci Biobehav Rev* 33:279-296.
- Budde MD, Janes L, Gold E, Turtzo LC, Frank JA (2011) The contribution of gliosis to diffusion tensor anisotropy and tractography following traumatic brain injury: validation in the rat using Fourier analysis of stained tissue sections. *Brain* 134: 2248-2260.
- Calabresi P, Gubellini P, Centonze D, Picconi B, Bernardi G, Chergui K, Svensson P, Fienberg AA, Greengard P (2000) Dopamine and cAMP-regulated phosphoprotein 32kDa controls both striatal long-term depression and long-term potentiation, opposing forms of synaptic plasticity. *J Neurosci* 20:8443-8451.
- Campbell JN, Register D, Churn SB (2012) Traumatic brain injury causes an FK506-sensitive loss and an overgrowth of dendritic spines in rat forebrain. *J Neurotrauma* 29:201-217.
- Carey LM, Seitz RJ (2007) Functional neuroimaging in stroke recovery and neurorehabilitation: conceptual issues and perspectives. *Int J Stroke* 2:245-264.
- Chen CJ, Wu CH, Liao YP, Hsu HL, Tseng YC, Liu HL, Chiu WT (2012) Working memory in patients with mild traumatic brain injury: functional MR imaging analysis. *Radiology* 264:844-851.
- Chen H, Epstein J, Stern E (2010) Neural plasticity after acquired brain injury: evidence from functional neuroimaging. *PM R* 2:S306-312.
- Dams-O'Connor K, Spielman L, Singh A, Gordon WA, Lingsma HF, Maas AI, Manley GT, Mukherjee P, Okonkwo DO, Puccio AM, Schnyer DM, Valadka AB, Yue JK, Yuh EL; Track-Tbi Investigators, Casey SS, Cooper SR, Cheong M, Hricik AJ, Knight EE, et al. (2013) The impact of previous traumatic brain injury on health and functioning: a TRACK-TBI study. *J Neurotrauma* 30:2014-2020.
- Dijkhuizen RM, van der Marel K, Otte WM, Hoff EI, van der Zijden JP, van der Toorn A, van Meer MP (2012) Functional MRI and diffusion tensor imaging of brain reorganization after experimental stroke. *Transl Stroke Res* 3:36-43.
- Eyo UB, Dailey ME (2013) Microglia: key elements in neural development, plasticity, and pathology. *J Neuroimmune Pharmacol* 8:494-509.
- Folkersma H, Foster Dingley JC, van Berkel BN, Rozemuller A, Boellaard R, Huisman MC, Lammertsma AA, Vandertop WP, Molthoff CF (2011) Increased cerebral (R)-[(11)C]PK11195 uptake and glutamate release in a rat model of traumatic brain injury: a longitudinal pilot study. *J Neuroinflammation* 8:67.
- Gilbert SJ, Dumontheil I, Simons JS, Frith CD, Burgess PW (2007) Comment on "Wanderingminds: The default network and stimulus-independent thought". *Science* 317:43.
- Hall KD, Lifshitz J (2010) Diffuse traumatic brain injury initially attenuates and later expands activation of the rat somatosensory whisker circuit concomitant with neuroplastic responses. *Brain Res* 1323:161-173.
- Hampshire A, MacDonald A, Owen AM (2013) Hypoconnectivity and hyperfrontality in retired American football players. *Sci Rep* doi:10.1038/srep02972.
- Hunt RF, Scheff SW, Smith BN (2009) Post traumatic epilepsy after controlled cortical impact injury in mice. *Exp Neurol* 215:243-252.
- Johnson B, Zhang K, Gay M, Horovitz S, Hallett M, Sebastianelli W, Slobounov S (2012) Alteration of brain default network in subacute phase of injury in concussed individuals: resting-state fMRI study. *Neuroimage* 59:511-518.
- Jones TA, Liput DJ, Maresh EL, Donlan N, Parikh TJ, Marlowe D, Kozlowski DA (2012) Use-dependent dendritic regrowth is limited after unilateral controlled cortical impact to the forelimb sensorimotor cortex. *J Neurotrauma* 29:1455-1468.
- Kay T (1993) Neuropsychological treatment of mild traumatic brain injury. *J Head Trauma Rehabil* 8:74-85.
- Kolb B, Teskey GC, Gibb R (2010) Factors influencing cerebral plasticity in the normal and injured brain. *Front Hum Neurosci* doi:10.3389/fnhum.2010.00204.
- Kou Z, VandeVord PJ (2014) Traumatic white matter injury and glial activation: Review. *Glia*: In press. DOI
- Kou Z, Wu Z, Tong KA, Holshouser B, Benson RR, Hu J, EM H (2010) The role of advanced MR imaging findings as biomarkers of traumatic brain injury. *J Head Trauma Rehabil* 25:267-282.
- Laitinen T, Sierra A, Pitkänen A, Gröhn O (2010) Diffusion tensor MRI of axonal plasticity in the rat hippocampus. *Neuroimage* 51:521-530.
- Li K, Zhu D, Guo L, Li Z, Lynch ME, Coles C, Hu X, Liu T (2013) Connectomics signatures of prenatal cocaine exposure affected adolescent brains. *Hum Brain Mapp* 34:2494-2510.
- Li N, Yang Y, Glover DP, Zhang J, Saraswati M, Robertson C, Pelled G (2014) Evidence for impaired plasticity after traumatic brain injury in the developing brain. *J Neurotrauma* 31:395-403.
- Luft AR, McCombe-Waller S, Whitall J, Forrester LW, Macko R, Sorkin JD, Schulz JB, Goldberg AP, Hanley DF (2001) Repetitive bilateral arm training and motor cortex activation in chronic stroke: a randomized controlled trial. *JAMA* 292:1853-1861.
- Maguire EA, Gadian DG, Johnsrude IS, Good CD, Ashburner J, Frackowiak RS, Frith CD (2000) Navigation-related structural change in the hippocampi of taxi drivers. *Proc Natl Acad Sci U S A* 97:4398-4403.
- Margulies S, Hicks R, Combination Therapies for Traumatic Brain Injury Workshop Leaders (2009) Combination therapies for traumatic brain injury: prospective considerations. *J Neurotrauma* 26:925-939.
- Mattson MP, Duan W, Chan SL, Guo Z (2001) Modification of brain aging and neurodegenerative disorders by genes, diet, and behavior. In: Shaw CA, McEachern J, eds. *Toward a Theory of Neuroplasticity*. Philadelphia, PA: Psychology Press.
- Mayer AR, Mannell MV, Ling J, Gasparovic C, Yeo RA (2011) Functional connectivity in mild traumatic brain injury. *Hum Brain Mapp* 32:1825-1835.
- McAllister TW, Saykin AJ, Flashman LA, Sparling MB, Johnson SC, Guerin SJ, Mamourian AC, Weaver JB, Yanofsky N (1999) Brain activation during working memory 1 month after mild traumatic brain injury: a functional MRI study. *Neurology* 53:1300-1308.
- Meinzer M, Elbert T, Djundja D, Taub E, Rockstroh B (2007) Extending the Constraint-Induced Movement Therapy (CIMT) approach to cognitive functions: Constraint-Induced Aphasia Therapy (CIAT) of chronic aphasia. *NeuroRehabilitation* 22:311-318.

- Morgan AT, Masterton R, Pigdon L, Connelly A, Liégeois FJ (2013) Functional magnetic resonance imaging of chronic dysarthric speech after childhood brain injury: reliance on a left-hemisphere compensatory network. *Brain* 136:646-657.
- Morris GP, Clark IA, Zinn R, Vissel B (2013) Microglia: a new frontier for synaptic plasticity, learning and memory, and neurodegenerative disease research. *Neurobiol Learn Mem* 105:40-53.
- Muñoz-Cespedes JM, Rios-Lago M, Paul N, Maestu F (2001) Functional neuroimaging studies of cognitive recovery after acquired brain damage in adults. *Neuropsychol Rev* 15:169-183.
- Murphy TH, Corbett D (2009) Plasticity during stroke recovery: from synapse to behaviour. *Nat Rev Neurosci* 10:861-872.
- Nakamura T, Hillary FG, Biswal BB (2009) Resting network plasticity following brain injury. *PLoS One* 4:e8220.
- National Institutes of Health (1999) NIH consensus development panel on rehabilitation of persons with traumatic brain injury. *JAMA* 282:974-983.
- Ndode-Ekane XE, Hayward N, Gröhn O, Pitkänen A (2010) Vascular changes in epilepsy: functional consequences and association with network plasticity in pilocarpine-induced experimental epilepsy. *Neuroscience* 166:312-332.
- Niogi SN, Mukherjee P (2010) Diffusion tensor imaging of mild traumatic brain injury. *J Head Trauma Rehabil* 25:241-255.
- Niogi SN, Mukherjee P, Ghajar J, Johnson C, Kolster RA, Sarkar R, Lee H, Meeker M, Zimmerman RD, Manley GT, McCandliss BD (2008a) Extent of microstructural white matter injury in post concussive syndrome correlates with impaired cognitive reaction time: a 3T diffusion tensor imaging study of mild traumatic brain injury. *AJNR Am J Neuroradiol* 29:967-973.
- Niogi SN, Mukherjee P, Ghajar J, Johnson CE, Kolster R, Lee H, Suh M, Zimmerman RD, Manley GT, McCandliss BD (2008b) Structural dissociation of attentional control and memory in adults with and without mild traumatic brain injury. *Brain* 131:3209-3221.
- Nishibe M, Barbay S, Guggenmos D, Nudo RJ (2010) Reorganization of motor cortex after controlled cortical impact in rats and implications for functional recovery. *J Neurotrauma* 27:2221-2232.
- Raison C, Capuron L, Miller AH (2006) Cytokines sing the blues: inflammation and the pathogenesis of depression. *Trends Immunol* 27:24-31.
- Ramlackhansingh AF, Brooks DJ, Greenwood RJ, Bose SK, Turkelman FE, Kinnunen KM, Gentleman S, Heckemann RA, Gunanayagam K, Gelosa G, Sharp DJ (2011) Inflammation after trauma: microglial activation and traumatic brain injury. *Ann Neurol* 70:374-383.
- Richter M, Miltner WH, Straube T (2008) Association between therapy outcome and right hemispheric activation in chronic aphasia. *Brain* 131:1391-1401.
- Sacco K, Cauda F, D'Agata F, Duca S, Zettin M, Virgilio R, Nascimbene A, Belforte G, Eula G, Gastaldi L, Appendino S, Geminiani G (2011) A combined robotic and cognitive training for locomotor rehabilitation: evidences of cerebral functional reorganization in two chronic traumatic brain injured patients. *Front Hum Neurosci* doi:10.3389/fnhum.2011.00146.
- Staudt M (2010) Brain plasticity following early life brain injury: insights from neuroimaging. *Semin Perinatol* 34:87-92.
- Stevens MC, Lovejoy D, Kim J, Oakes H, Kureshi I, Witt ST (2012) Multiple resting state network functional connectivity abnormalities in mild traumatic brain injury. *Brain Imaging Behav* 6:293-318.
- Takahashi CD, Der-Yeghaian L, Le V, Motiwala RR, Cramer SC (2008) Robot-based handmotor therapy after stroke. *Brain* 131:425-437.
- Teskey GC (2001) Using kindling to model the neuroplastic changes associated with learning and memory, neuropsychiatric disorders, and epilepsy. In: Shaw CA, McEachern J, eds. *Toward a Theory of Neuroplasticity*. Philadelphia, PA: Psychology Press.
- Tivarus ME, Starling SJ, Newport EL, Langfitt JT (2012) Homotopic language reorganization in the right hemisphere after early left hemisphere injury. *Brain Lang* 123:1-10.
- Ungerleider LG, Doyon J, Karni A (2002) Imaging brain plasticity during motor skill learning. *Neurobiol Learn Mem* 78:553-564.
- van Bregt DR, Thomas TC, Hinzman JM, Cao T, Liu M, Bing G, Gerhardt GA, Pauly JR, Lifshitz J (2012) Substantia nigra vulnerability after a single moderate diffuse brain injury in the rat. *Exp Neurol* 234:8-19.
- Voss HU, Schiff ND (2009) MRI of neuronal network structure, function, and plasticity. *Prog Brain Res* 175:483-496.
- Yan HQ, Ma X, Chen X, Li Y, Shao L, Dixon CE (2007) Delayed increase of tyrosinehydroxylase expression in rat nigrostriatal system after traumatic brain injury. *Brain Res* 1134:171-179.
- Yeatman JD, Feldman HM (2013) Neural plasticity after pre-linguistic injury to the arcuate and superior longitudinal fasciculi. *Cortex* 49:301-311.
- Yogarajah M, Focke NK, Bonelli SB, Thompson P, Vollmar C, McEvoy AW, Alexander DC, Symms MR, Koepf MJ, Duncan JS (2010) The structural plasticity of white matter networks following anterior temporal lobe resection. *Brain* 133:2348-2364.
- Yu X, Chung S, Chen DY, Wang S, Dodd SJ, Walters JR, Isaac JT, Kotretsky AP (2012) Thalamocortical inputs show post-critical-period plasticity. *Neuron* 74:731-742.
- Zhou IY, Liang YX, Chan RW, Gao PP, Cheng JS, Hu Y, So KF, Wu EX (2014) Brain resting state functional MRI connectivity: morphological foundation and plasticity. *Neuroimage* 84:1-10.
- Zhu D, Li K, Guo L, Jiang X, Zhang T, Zhang D, Chen H, Deng F, Faraco C, Jin C, Wee CY, Yuan Y, Lv P, Yin Y, Hu X, Duan L, Hu X, Han J, Wang L, Shen D, et al. (2013a) DICCCOL: dense individualized and common connectivity-based cortical landmarks. *Cereb Cortex* 23:786-800.
- Zhu D, Li K, Terry DP, Puente AN, Wang L, Shen D, Miller LS, Liu T (2013b) Connectome-scale assessments of structural and functional connectivity in MCI. *Hum Brain Mapp* doi:10.1002/hbm.22373.
- Zhuo J, Xu S, Proctor JL, Mullins RJ, Simon JZ, Fiskum G, Gullapalli RP (2012) Diffusion kurtosis as an in vivo imaging marker for reactive astrogliosis in traumatic brain injury. *Neuroimage* 59:467-477.

# Combining Biochemical and Imaging Markers to Improve Diagnosis and Characterization of Mild Traumatic Brain Injury in the Acute Setting: Results from a Pilot Study

Zhifeng Kou<sup>1,2\*</sup>, Ramtilak Gattu<sup>2</sup>, Firas Kobeissy<sup>3</sup>, Robert D. Welch<sup>4,5</sup>, Brian J. O'Neil<sup>4,5</sup>, John L. Woodard<sup>6</sup>, Syed Imran Ayaz<sup>4</sup>, Andrew Kulek<sup>4</sup>, Robert Kas-Shamoun<sup>4</sup>, Valerie Mika<sup>4</sup>, Conor Zuk<sup>2</sup>, Francesco Tomasello<sup>7</sup>, Stefania Mondello<sup>7</sup>

**1** Department of Biomedical Engineering, Wayne State University, Detroit, Michigan, United States of America, **2** Department of Radiology, School of Medicine, Wayne State University, Detroit, Michigan, United States of America, **3** Center for Neuroproteomics and Biomarkers Research, Department of Psychiatry, McKnight Brain Institute, University of Florida, Gainesville, Florida, United States of America, **4** Department of Emergency Medicine, School of Medicine, Wayne State University, Detroit, Michigan, United States of America, **5** The Cardiovascular Research Institute, School of Medicine, Wayne State University, Detroit, Michigan, United States of America, **6** Department of Psychology, Wayne State University, Detroit, Michigan, United States of America, **7** Department of Neurosciences, University of Messina, Messina, Italy

## Abstract

**Background:** Mild traumatic brain injury (mTBI) is a significant healthcare burden and its diagnosis remains a challenge in the emergency department. Serum biomarkers and advanced magnetic resonance imaging (MRI) techniques have already demonstrated their potential to improve the detection of brain injury even in patients with negative computed tomography (CT) findings. The objective of this study was to determine the clinical value of a combinational use of both blood biomarkers and MRI in mTBI detection and their characterization in the acute setting (within 24 hours after injury).

**Methods:** Nine patients with mTBI were prospectively recruited from the emergency department. Serum samples were collected at the time of hospital admission and every 6 hours up to 24 hours post injury. Neuronal (Ubiquitin C-terminal Hydrolase-L1 [UCH-L1]) and glial (glial fibrillary acidic protein [GFAP]) biomarker levels were analyzed. Advanced MRI data were acquired at  $9 \pm 6.91$  hours after injury. Patients' neurocognitive status was assessed by using the Standard Assessment of Concussion (SAC) instrument.

**Results:** The median serum levels of UCH-L1 and GFAP on admission were increased 4.9 folds and 10.6 folds, respectively, compared to reference values. Three patients were found to have intracranial hemorrhages on SWI, all of whom had very high GFAP levels. Total volume of brain white matter (WM) with abnormal fractional anisotropy (FA) measures of diffusion tensor imaging (DTI) were negatively correlated with patients' SAC scores, including delayed recall. Both increased and decreased DTI-FA values were observed in the same subjects. Serum biomarker level was not correlated with patients' DTI data nor SAC score.

**Conclusions:** Blood biomarkers and advanced MRI may correlate or complement each other in different aspects of mTBI detection and characterization. GFAP might have potential to serve as a clinical screening tool for intracranial bleeding. UCH-L1 complements MRI in injury detection. Impairment at WM tracts may account for the patients' neurocognitive symptoms.

**Citation:** Kou Z, Gattu R, Kobeissy F, Welch RD, O'Neil BJ, et al. (2013) Combining Biochemical and Imaging Markers to Improve Diagnosis and Characterization of Mild Traumatic Brain Injury in the Acute Setting: Results from a Pilot Study. PLoS ONE 8(11): e80296. doi:10.1371/journal.pone.0080296

**Editor:** Shaolin Yang, University of Illinois at Chicago, United States of America

**Received** June 20, 2013; **Accepted** October 2, 2013; **Published** November 19, 2013

**Copyright:** © 2013 Kou et al. This is an open-access article distributed under the terms of the Creative Commons Attribution License, which permits unrestricted use, distribution, and reproduction in any medium, provided the original author and source are credited.

**Funding:** This work was supported by a Seed Grant from the International Society for Magnetic Resonance in Medicine (PI: Zhifeng Kou) and a research grant from the Department of Defense. Drs. Mondello and Kobeissy were employees and received salaries from Banyan Biomarkers, Inc. Dr. Welch is a site PI of a clinical trial from Banyan Biomarkers, Inc., supported by the Department of Defense. Dr. O'Neil is a site PI for BrainScope Technologies. The funders had no role in study design, data collection and analysis, decision to publish, or preparation of the manuscript.

**Competing interests:** The authors have read the journal's policy and have the following conflicts: Drs. Mondello and Kobeissy were employees and received salaries from Banyan Biomarkers, Inc. Banyan Biomarkers Inc. assisted in bioassay analysis for this study. There are no further patents, products in development or marketed products to declare. This does not alter the authors' adherence to all the PLOS ONE policies on sharing data and materials.

\* E-mail: zhifeng\_kou@wayne.edu

## Introduction

Traumatic brain injury (TBI) is a significant public healthcare burden in the United States, accounting for 1.7 million incidents in the United States each year [1,2]. The majority of TBI patients belong to the mild TBI (mTBI) severity group due to the improvement of motor vehicle safety design in recent years [3]. mTBI leads to over 1 million emergency visits in the United States each year [4]. It causes a constellation of physical, cognitive, and emotional symptoms that significantly impact the patients' quality of life, and costs the nation \$16.7 billion each year [3,5,6]. Currently, most mTBI patients stay in the emergency department (ED) for only a few hours and then are discharged home without a concrete follow-up plan or an understanding of potential symptoms. Up to 50% of mTBI patients develop neurocognitive problems within the first month [7,8], and 5-15% of them continue to manifest neurocognitive sequelae at one year [7,9]. Often, their neurocognitive outcomes inconsistently correlate with clinical measures such as the Glasgow Coma Scale (GCS) score and post-traumatic amnesia. Most mTBI patients do not have abnormalities on computed tomography (CT) and conventional magnetic resonance imaging (MRI) [10,11] in the emergent setting. The immediate challenge for emergency physicians is to identify intracranial abnormalities in those CT-negative patients, who may have long-term neurocognitive symptoms [12].

Advanced MRI has demonstrated improved sensitivity in detecting TBI pathologies and functional impairments that underlie patients' cognitive symptoms [13,14]. Examples include diffusion tensor imaging (DTI) of axonal injury [15-24], susceptibility weighted imaging (SWI) of hemorrhagic lesions [25-27], and others. Advanced MRI offers anatomical and pathological information, reflecting brain damage with high spatial resolution [13,14]. The American College of Emergency Physicians and Center for Disease Control Joint Study Panel highly recommended examining the role of advanced MRI in the acute setting (within 24 hours after injury) [12]. However, to date, very few studies have scanned mTBI patients within 24 hours after injury when the patients are still in the ED. This is mainly due to, first the high cost of MRI making it prohibitive to scan all mTBI patients, and second the inability to access the MRI acutely 24/7. Consequently, in the majority of medical centers in North America, MRI is not a standard of care of mTBI patients in the acute setting.

In addition to patient's clinical characteristics and advanced neuroimaging studies, brain-specific proteins released into the bloodstream after brain injury, as a result of cellular damage and activation, have demonstrated the potential to serve as diagnostic and prognostic markers in mTBI [28,29]. Along with providing improved diagnostic capability and molecular characterization of subjects who sustained mTBI, appropriate biomarker screening may lead to a more selective strategy for neuroimaging, reducing the need for a substantial number of unnecessary imaging exams. With these aims in mind, several groups recently reported the application of neuroproteomics to identify and characterize biochemical markers of TBI [30]. Among the variety of biomarkers that have been used to investigate the neuronal marker, Ubiquitin C-terminal

Hydrolase-L1 (UCH-L1) [31-33] and the astrocyte-specific protein Glial Fibrillary Acidic Protein (GFAP) [34], and all-Spectrin Breakdown Products (SBDPs) for axonal injury [35,36] seem particularly promising.

UCH-L1 is a small (25 kDa), neuronal protease involved in either the addition or removal of ubiquitin from proteins that are destined for metabolism via the ATP-dependent proteasome pathway; it is highly enriched in the brain (1 - 5% of total soluble brain protein)[37,38]. Mutations and polymorphisms of UCH-L1 have been associated with familial Parkinson's Disease [39]. UCH-L1 is released into the extracellular space as a consequence of cell destruction under diverse pathological conditions affecting the brain. Previous clinical studies have demonstrated increased UCH-L1 levels in cerebral spinal fluid (CSF) and in serum in severe TBI patients and that the magnitude of this increase correlated with injury severity, CT finding and patient outcome [31,33]. Recently, a study was completed investigating UCH-L1 in adults with mild and moderate TBI showing increased UCH-L1 levels in mTBI patients compared to uninjured controls and that UCH-L1 was able to detect intracranial lesions on CT with an area under the curve (AUC) of 0.73 [40]. Based on these encouraging results and the fact that UCH-L1 is specific to neurons and its high specificity and abundance in the CNS, it appears to be an excellent candidate biomarker for the brain injury clinical studies.

Compared with UCH-L1, GFAP is a monomeric intermediate filament protein, a major constituent of the astroglial cytoskeleton, and highly brain-specific [41,42]. This glial protein represents an ideal complement of the neuronal UCH-L1, as demonstrated by a recent study showing that the correlations between these 2 markers reflect structural changes detected by neuroimaging and may be used as an indicator for differing intracranial pathologies after brain trauma [43]. Additionally, previous studies evaluating severe TBI patients demonstrated that GFAP concentrations were associated with injury severity and outcome [44,45]. Recently, in a prospective cohort study of 108 patients with mild or moderate TBI, GFAP was found to be elevated in the serum within 1 h after injury, discerning TBI patients from uninjured controls with an area under the curve (AUC) of 0.90 and discriminating patients with and without intracranial lesion as assessed by CT with an AUC of 0.79 [46]. The same study also reported a significant difference in GFAP levels between mild TBI (GCS 15) and general trauma controls [47], in suggestion of the CNS-specific nature of GFAP.

As a simple biofluid-based rapid diagnostic tool, serum biochemical markers offer great potential for rapid, accurate, and cost-effective diagnosis of brain injury, and a temporal profile of blood protein levels might be indicative of disease progression or resolution. Particularly, several biochemical markers, including UHC-L1 and GFAP, among others, are reported being CNS-specific, which makes them ideal for brain injury detection. On the other hand, emerging data suggest that MRI and especially advanced MRI techniques are very sensitive in detecting brain injury that are occult in clinical imaging by providing spatial and pathophysiological information. Although the combinational and complementary use of these tools is promising and might have important

implications for improving injury detection and outcome prediction, the correlation among injury pathologies at tissue level assessed by neuroimaging and at the protein level as assessed by blood biomarker profiles has not yet been elucidated.

We hypothesized that, in mTBI patients, elevated GFAP levels will be associated with intracranial abnormalities detected by baseline MRI and SWI, and elevated UCH-L1 will be associated with white matter damage indicated by DTI. Our objective in this study was to evaluate serum GFAP and UCH-L1 levels after mTBI and their correlation to the advanced MRI findings, including SWI and DTI, in a pilot cohort in an acute setting. In particular, we were interested in establishing a serum profile of these biomarkers that might serve as signatures for the presence of brain pathology as assessed by advanced MRI methods, and thus aid in the identification of patients who need an MRI scan in the acute setting.

## Materials and Methods

### Patient Recruitment

This study was approved by both the Human Investigation Committee of Wayne State University and the Institutional Review Board of Detroit Medical Center. Written informed consent was obtained from each subject before enrollment.

A total of 9 patients who sustained mTBI were prospectively recruited from the ED of Detroit Receiving Hospital (DRH), a Level-1 trauma center, which is an affiliated hospital of Detroit Medical Center (DMC). Patient eligibility was based on the mTBI definition by the American Congress of Rehabilitation Medicine [48] with the following inclusion criteria: Patients aged 18 or older with an initial Glasgow Coma Scale (GCS) score of 13-15 in ED with any period of loss of consciousness less than 30 minutes or any post traumatic amnesia less than 24 hours, or recorded change of mental status (confused, disoriented or dazed). Patients with a GCS of <15 were screened with the Conley test for the ability to consent. All patients required a CT scan as part of their clinical evaluation. All of them were able to speak English. The exclusion criteria included patients under the age of 18 years, pregnant woman, medically documented history of brain injury, neurological disorders or psychoactive medications, history of substance abuse, CT indication of any metal in the brain and body, known contraindication to MRI such as a pacemaker or other non-MR compatible implanted device as defined by metal screening procedure, or patients without a clear history of trauma as their primary event (e.g., seizure, epilepsy, etc.). In the acute stage, a patient might have mental status change or amnesia in which medical history may not be properly obtained, thus the patient's record was retrospectively screened as well to exclude any patient who does not fit our inclusion criteria. Additionally, we performed an imaging study of 18 healthy controls without history of head injury or antecedents of central nervous system disease.

### Neurocognitive Assessments

At the acute setting, once a patient was conscious and stable, they were administered neurocognitive tests and

surveyed about their post-concussion symptoms (PCS). Given the situation of emergency care, it is not feasible to perform a full battery of neuropsychological assessment. Instead, a short instrument called Standardized Assessment of Concussion (SAC) [49] was used to assess the patients' neurocognitive status. The SAC instrument was originally developed for onsite testing of subject's neurocognitive performance after sports concussion [50]. It has been reported that SAC is sensitive to the acute changes following concussion and it only requires limited training of an administrator [51]. The SAC assesses 4 cognitive domains including orientation, attention, immediate memory and delayed recall, and the resulting points give a patient score between 0 (indicating greater cognitive deficit) and 30. Previous results report its sensitivity to brain injury in the emergency setting, particularly in that delayed recall is more sensitive to brain injury [51]. The Emergency Room Edition of the SAC instrument also has a graded symptom checklist with all PCS symptoms listed. The patients were asked to grade each symptom from none, mild, moderate, to severe, (graded from a 0 to 3 respectively). The total points were the overall PCS score.

### Neuroimaging Protocol

In the ED, once a patient was cleared of any immediate life-threatening risk following a CT scan and was stable enough for an MRI, the patient was transported to the MRI center for imaging scan. All MRI data were collected on a 3-Tesla Siemens Verio scanner with a 32-channel radio frequency head coil. The subject's head was fixed by a foam pad to restrict motion. Imaging protocol included SWI, DTI, and resting state functional MRI, in addition to the baseline structural imaging (T1, T2 gradient recalled echo [GRE] and T2 fluid-attenuated inversion recovery [FLAIR]) sequences, with total data acquisition time of 39 min. Of the 9 patients, resting state fMRI data was collected in decent quality for only 4 of them. The rest of the patients either could not stay in the magnet any longer after baseline MRI and SWI and DTI sequences or did not cooperate for resting state data collection. Therefore, this paper focuses on the relationship between blood biomarkers and SWI and DTI data.

SWI is a 3-dimentional, T2\* based GRE sequence with long TE and 3-D flow compensation. The phase images were high-pass filtered (96x96 filter size) by using an in-line manufacturer-applied filter and then integrated with magnitude images to generate the processed SWI image to better delineate the spatial relation between microhemorrhages and veins [13,52]. SWI parameters include TR/TE of 30/20ms, flip angle of 15 degree, bandwidth of 100 Hz/Px, field of view (FOV) of 256x256 mm<sup>2</sup>, imaging matrix of 512x256, 25% oversampling, slice thickness of 2 mm, total 64 slices, 20% distance factor, GRAPPA iPat factor of 2, with resultant voxel size of 0.5x1x2 mm<sup>3</sup> and imaging acquisition time 4m and 18s.

DTI sequence is a standard echo planar imaging (EPI) 2D sequence provided as part of the Siemens package. The parameters include TR/TE of 13300/124 ms, EPI factor of 192, bandwidth of 1240 Hz/Px, FOV of 256x256 mm<sup>2</sup>, imaging matrix of 192x192, slice thickness of 2 mm, total 60 slices, no gap between slices, 30 gradient directions, 2 averages, B

values of 0/1000 s/mm<sup>2</sup>, anterior-posterior phase encoding, GRAPPA acceleration factor of 2, with resultant voxel size of 1.3x1.3x2 mm<sup>3</sup> and data acquisition time of 14m 26s.

### Image Processing and Interpretation

All SWI and DTI images were processed by a co-author who was blinded to the subjects' clinical conditions to avoid any bias. All SWI images were further processed by using our in-house software SPIN (signal processing for NMRI) (MRI Research Institute, Detroit, Michigan). All structural MRI images, including SWI images, were read by two board certified neuroradiologists to identify other conditions that may confound the findings. The neuroradiologists were blinded to the medical history and conditions of subjects to avoid any bias as well. We also graded the structural imaging findings based on their radiologic report for statistical analysis: 0 for negative finding; 1 for non-specific finding, including non-specific WM hyperintensities; and 2 for traumatic hemorrhage.

**DTI image processing.** Given the relatively long sequence in our DTI data collection (2 averages, total 14m 26s), several steps were taken to overcome the potential motion artifacts: 1) During every scan, each subject's head was tightly enclosed within the head coil with soft padding in a comfortable position; 2) Instead of inline averaging of two volumes of data, each volume was saved individually for later motion correction; 3) A motion correction and eddy current correction algorithm, automatic image registration (AIR) [53], was applied to correct all the diffusion-weighted images for each volume of data by using B0 image as the reference image; and, finally, 4) two volumes of motion-corrected images were averaged for further preprocessing.

Preprocessing of DTI images was carried out by using DTI Studio (<https://www.dtistudio.org>). Fractional Anisotropy (FA) maps were created from the tensor calculations by suppressing the background noise on B0 image in DTI Studio. Skull stripping of the B0 image was done by using the BET routine package in Mricro with a fractional intensity of 0.1. A binary mask of the skull-stripped B0 image was used on the FA map to preserve the pure brain parenchyma.

**Voxel based analysis (VBA).** VBA was performed after the skull stripped FA image was spatially normalized, by using a non-linear algorithm, to the standard FMRIB FA template for all the 27 subjects (9 mTBI patients and 18 healthy controls) in SPM8 software

(<http://www.fil.ion.ucl.ac.uk/spm/software/spm8/>). A mean FA map and a standard deviation of FA map were created for the controls. A Z-score map was created for each individual patient in a voxel-based approach: For each voxel, the FA difference between each individual patient and the mean of controls was divided by the standard deviation of the controls at the same voxel. Voxels with Z-score > 2 for increased FA and Z-score < -2 for decreased FA were selected for further consideration.

**Tract based spatial statistics (TBSS).** A similar approach was also used to evaluate the lesion load by using the TBSS method after registering each subject nonlinearly to the standard FMRIB FA template. The TBSS analytical approach was used to compare patient and control groups to evaluate the WM changes after TBI. All the processing steps were

performed according to the TBSS manual (<http://fsl.fmrib.ox.ac.uk/fsl/fslwiki/TBSS/UserGuide>). Briefly, every subject's FA image was spatially and non-linearly normalized to a standard FA FMRIB template and transformed into a standard space using FNIRT algorithm from FSL software package. Subsequently, a mean FA image was created from this set of non-linearly transformed images. A search algorithm then created a mean skeleton, looking for the local maxima perpendicular to the WM tract across the whole brain volume in all the transformed images, and then projected this skeleton across all the subjects in the group to extract the skeleton of individual subject. Next, a voxel-wise permutation-inference analysis was carried out between the skeletons of two groups, and a two tailed t-statistics was performed to extract the voxels that fall below or above a certain threshold. These voxels were converted to a p value based on the threshold set by the t-stat value and the cluster size. In TBSS analysis, a skeleton threshold of 0.3 was used to eliminate grey matter (GM) voxels or partial volume effects, and cluster forming threshold t of 4 was used.

**Masking out non-white matter voxels.** The selected abnormal voxels were further filtered to eliminate the GM and the non-WM voxels accounting for the partial volume effects arising from CSF and GM. This filtering was done by segmenting each non-linearly normalized FA map and the mean FA map from the controls into WM, GM and CSF in SPM8 and consequently creating a compound mask by applying a threshold ( $p>0.78$ ) on these two segmented WM FA images. In this way, we were able to get rid of the false positives arising on the edges of WM because of the misregistration, and voxels having FA < 0.3 were considered to be non WM voxels and discarded by using a mask. Spurious voxels that doesn't form a cluster size of at least 10 voxels were discarded as random noise in VBA and cluster size of less than 5 were discarded as random noise in TBSS. Clusters were extracted using the cluster tool in FSL. As a result, the total number of selected voxels was defined as the lesion load for each subject in both VBA and TBSS analyses.

### Blood Collection and Biomarker Analysis

All blood samples were collected within 6 hours after injury, beginning upon subject's arrival to ED and then every 6 hours thereafter, until discharge or up to 24 hours. Samples were immediately centrifuged at 4000 rpm for 10 min and frozen and stored at -80°C until the time of analysis. Blinded sample analysis was conducted in a central laboratory (Banyan Biomarkers, Alachua, FL) employing electro-chemiluminescent immunoassay method (ECL-IA) for quantitative analysis of UCH-L1 and GFAP in human serum samples using the MSD platform (MesoScale Discovery, Gaithersburg, MD). The UCH-L1 assay system utilizes a mouse monoclonal IgM anti-human UCH-L1 antibody for solid phase immobilization to capture UCH-L1 from samples. The UCH-L1 antigen in turn binds to a sulfo-tag labeled anti-mouse antibody. The GFAP ECL-IA utilizes a proprietary mouse monoclonal IgG anti-human GFAP antibody for solid phase immobilization and a proprietary polyclonal rabbit antibody for detection. The rabbit IgG polyclonal detection antibody in turn binds to a sulfo-tag labeled

anti-rabbit antibody. Detection signal can be measured when an electrical current is applied to the electrodes at the bottom of each well of the plate. The signal is measured at 620 nm. Quantitative determination of the biomarker concentration is achieved by comparing the unknown sample signal intensities to a standard curve, obtained from the calibrators run in the same assay. Target concentrations are reported in ng/ml. Each assay plate included 3 QC controls at high, medium and low concentrations of the assay range, each plated in duplicate. Calibrators were prepared in Pooled Human Serum (PHS) matrix. Specifically, a serial dilution of the calibrator protein is prepared and aliquots of that calibrator solution are assayed in the same assay volume and under the same conditions as the samples. The calibrator signal intensities were used to generate a dose-response curve and to calculate the sample concentrations using a weighted four-parameter logistic function (MSD software and MSD reader). The lower limit of detection of the UCH-L1 and GFAP assays was determined to be 0.10 and 0.008 ng/mL, respectively. Samples with undetectable levels of UCH-L1 or GFAP were assigned a value of 50% of the lower limit of detection (ie, 0.05 and 0.004 ng/mL, respectively). The median (IQR) serum UCH-L1 and GFAP concentrations determined in blood samples from 29 healthy volunteers recruited as part of an ongoing biomarker study were used as normal reference values. Healthy subjects were age and gender matched with TBI patients.

### Statistical analysis

Statistical analyses were performed by using SAS version 9.2 (Cary, NC, USA) and R software (<http://www.r-project.org>). Data normality was assessed by using the Kolmogorov-Smirnov test. Results for continuous variables are presented as mean (SD) or median (interquartile range) as appropriate. Frequencies and percentages are presented for categorical variables. Between-group differences were assessed by the Student's t-test (for normally distributed continuous variables) and the Mann-Whitney U test (non-normal continuous variables). Pearson's chi-squared test was used to explore the relationships between categorical variables. Pearson correlations were performed to determine the relationships among different parameters, including imaging, biomarkers and patients neurocognitive measurements. The relationship between biomarker concentration and parameters for TBI severity, neuroimaging and neurocognitive scores was assessed by bivariate correlations (Spearman's). Two sided tests were used and  $p < 0.05$  was considered significant.

## Results

### Characteristics of the Subjects

Individual patient demographic and clinical characteristics are presented in Table 1. In our mTBI cohort ( $n = 9$ ), with 8 (89%) male subjects and 1 (11%) female subject, the average patient age was  $41.22 \pm 14.37$  (mean  $\pm$  standard deviation) years, and all of their GCS scores were 15 upon ER admission. All patients had various length of loss of consciousness (LOC). Five (55%) patients were injured in assault and 4 (45%) were victims of motor vehicle accidents. The median SAC and PCS

scores were 23.5 and 15.5, respectively. Two patients presented positive findings in acute CT scan: one with epidural hematoma and cortical contusion in the parieto-temporal region and the other with a small subarachnoid hemorrhage (SAH). MRI scans were performed at  $9 \pm 6.91$  hours after injury. Three patients, including those two CT positive patients, presented hemorrhagic findings on structural MRI. One of these patients (Case 1) presented small hemorrhages that were completely missed by CT, and another patient was CT positive but missed the intraventricular hemorrhage by CT. In the control population ( $n=18$ ), 61% were male and 39% female, and the average patient age was  $34.83 \pm 14.30$  years. There was no age difference between patients and controls, but a significant gender difference was found between these two groups ( $p=0.002$ , Chi-square test).

### Patients' Neurocognitive Performance

The mean patients' SAC score was  $22.75 \pm SD 2.6$ . We compared this mean with published normative data of over 568 subjects [54] (mean  $\pm$  SD,  $26.3 \pm 2.2$ ). The patients' mean SAC score was significantly below this published mean score ( $t(8)=-4.180$ ,  $p=0.0041$ ). Among each subcategory of SAC test, patients' delayed recall and immediate memory were both significantly lower than published normalized data ( $p=0.042$  and  $p=0.021$ , respectively), and concentration had a trend of reduction towards significance ( $p=0.056$ ).

### MRI Findings

In structural MRI (T1, T2 FLAIR, and SWI) analysis, there was no group difference in SAC scores between patients with positive anatomical MRI findings and patients with negative anatomical MRI findings. In DTI analysis, both increased and decreased FA beyond the threshold ( $t \geq 4$ ) were found in all patients with variable number of clusters in different locations of the WM. By adding these clusters together, the volume of abnormal FA, called "lesion load", was used to correlate with patients' neurocognitive and biomarker data. DTI lesion load with pure increased FA was found significantly higher than that with pure decreased FA (student t-test,  $p=0.034$  for TBSS analysis; and  $p=0.017$  for VBA analysis). This suggests the increased FA as the main pathology.

Figure 1 presents the relationship between SAC scores and overall DTI lesion load, which contains total number of voxels with abnormal FA (either increased or decreased). Specifically, SAC scores were found to be inversely correlated with DTI-TBSS lesion load (Pearson  $r=-0.883$ ,  $p=0.004$ ) and DTI-VBA lesion load ( $r=-0.796$ ,  $p=0.018$ ) and had an almost significant correlation with age ( $r=-0.701$ ,  $p=0.053$ ). By looking at subcategories of SAC scores, both DTI-TBSS lesion load and DTI-VBA lesion load were correlated with SAC delayed recall ( $r=-0.834$ ,  $p=0.010$  and  $r=-0.796$ ,  $p=0.018$ , respectively). DTI-TBSS and DTI-VBA lesion loads were strongly correlated (Pearson  $r=0.881$ ,  $p=0.002$ ). There was also a partial correlation of SAC scores with DTI-TBSS and DTI-VBA lesion loads after controlling for age ( $r=-0.893$ ,  $p=0.0001$ ;  $r=-0.82$ ,  $p=0.0016$ , respectively) and a partial correlation of SAC delayed recall with patients' DTI-TBSS and VBA lesion loads, controlling for age ( $r=-0.858$ ,  $p=0.001$ ;  $r=-0.811$ ,  $p=0.002$ ,

**Table 1.** Individual demographic and clinical data of the 9 patients enrolled in the study.

Patient no.	Age/ Gender	Race	GCS	LOC	Mechanism of injury	SAC	CT	Structural MRI
P-001	56/M	Asian	15	1 min	MVA	Negative		Nonspecific WM hyperintensities, Small foci of intraventricular blood on the left. Small blood product in the left lingual gyrus
P-002	36/F	Black	15	10 min	MVA	23	Negative	Negative
P-003	19/M	Black	15	2 min	MVA	25	Negative	Nonspecific FLAIR hyperintensity in posterior cerebral WM
P-004	35/M	Arabic	15	30 min	Assault	26	Positive hemorrhagic contusion on left parieto-temporal lobe	Hemorrhagic contusion on left parieto-temporal lobe, left ventricular hemorrhage
P-005	52/M	Black	15	5 min	Assault	19	Negative	Non-specific, multiple scattered discrete foci in cerebral WM
P-006	53/M	Black	15	5 min	MVA	24	Negative	Non-specific: Two isolated punctate foci of blood in the right periratinal WM
P-007	39/M	Caucasian	15	2 min	Assault	22	Small SAH in right Sylvian Fissure	SAH in right Sylvian Fissure
P-008	58/M	Caucasian	15	2 min	Assault	19	Negative	Non-specific, super sella lesion, congenital cistern lesion in posterial fossa
P-009	23/M	Caucasian	15	30 min	Assault	24	Negative	Negative

doi:10.1371/journal.pone.0080296.t001

respectively). Similarly, after controlling for age, DTI-TBSS and DTI-VBA lesion loads remained significantly correlated (Pearson  $r=0.853$  and  $p=0.001$ ).

By further investigating the FA increase vs. FA decrease in association with patients' SAC score, the lesion load for pure FA increase was found to be significantly correlated with patients SAC scores (Pearson  $r=-0.87$ ,  $p=0.005$  for TBSS; and  $r=-0.86$ ,  $p=0.005$  for VBA) and delayed recall (Pearson  $r=-0.79$ ,  $p=0.018$  for TBSS and  $r=-0.770$ ,  $p=0.025$  for VBA). In contrast, the lesion volume for pure FA decrease was neither correlated with SAC nor delayed recall (all  $p>0.05$  for Pearson correlation).

The structural imaging finding, including SWI, was neither correlated with patients' SAC scores nor PCS scores (all  $p>0.05$ ).

Given the fact that over half of cases have non-specific findings on structural MRI, particularly WM hyperintensities, student T-tests were further performed to see its effect. No group difference was found between cases with non-specific findings and cases without non-specific findings (all with  $p>0.3$ ), in terms of their SAC score, DTI lesion loads (both TBSS and VBA data), or biomarker levels (both UCH-L1 and GFAP).

### Serum Concentrations of UCH-L1 and GFAP

Median serum concentrations taken at the time of hospital admission in the patients, within 6 hours after injury, were raised 4.9 folds for UCH-L1, and 10.6 folds for GFAP compared to the laboratory reference values in controls (see Table 2 and Figure 2). Serum UCH-L1 concentrations on admission did not correlate with GFAP ( $r=-0.24$ ,  $p=0.52$ ). Serum biomarker concentrations at the time of hospital admission did not correlate with age, time to sample withdrawal, GCS, duration of LOC, SAC or PCS score (all  $p>0.5$ ). Patients injured in assault had significantly higher UCH-L1 concentrations than patients injured in a MVA (median 0.35 vs 0.10 ng/ml,  $p=0.03$ ) (Figure 3) while GFAP concentrations were not associated with mechanism of injury.

Neither UCH-L1 nor GFAP concentrations were associated with structural MRI grading or DTI lesion load, as assessed by Pearson correlation ( $p>0.05$ ). However, patients with hemorrhages on structural MRI presented significantly higher levels of GFAP compared with the non- hemorrhagic group ( $p=0.002$ ) (see Table 2 and Figure 3).

Temporal profile of biomarker levels indicates that UCH-L1 tend to peak at the admission (within 6 hours after injury) and GFAP at 12 hours after injury. See supplement Figure S1 for details.

### Length of Loss of Consciousness

All patients had variable length of loss of consciousness (LOC). While length of LOC has often been considered as an injury severity measure, we did not find any correlation between LOC length and any other variables, including SAC, structural MRI, DTI lesion load, and blood biomarkers (Pearson correlation  $p>0.05$ ).

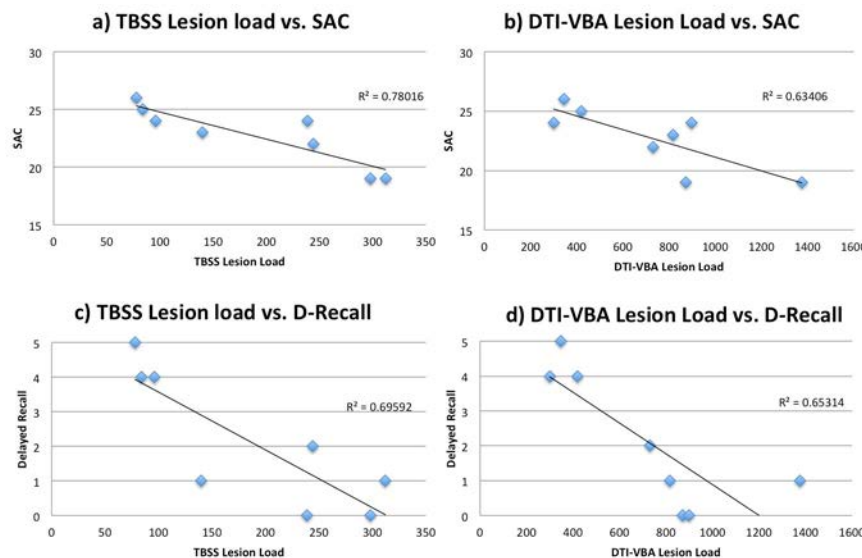


**Figure 1. Correlations between DTI lesion load and patients' neurocognitive data.** As demonstrated in the figures, DTI lesion load (both TBSS and VBA data) are significantly correlated with patients' overall SAC score and delayed recall. R squared values are shown on each figure for linear regression.

doi: 10.1371/journal.pone.0080296.g001

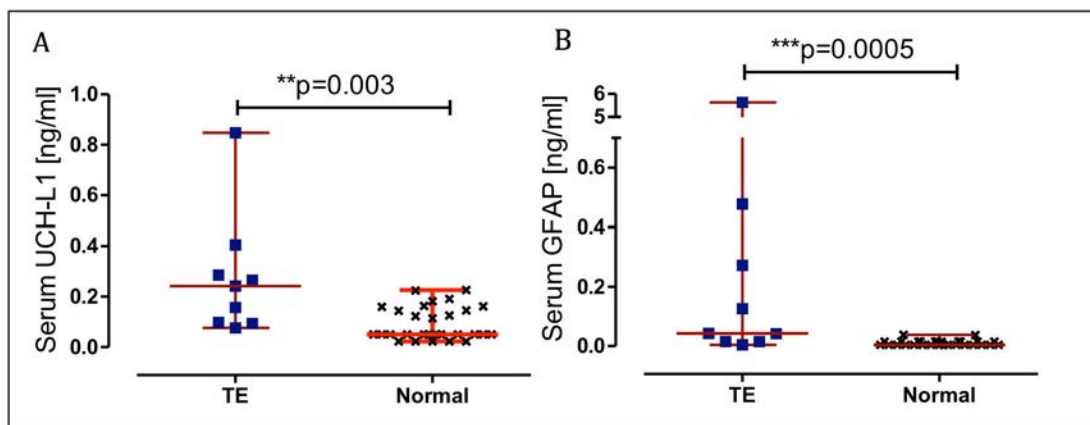


**Figure 2. Dot plots demonstrating UCH-L1 and GFAP concentrations.** Serum UCH-L1 (A) and GFAP (B) concentrations on admission in TBI patients and in controls. Error bars represent median and range. Significant differences are indicated with \*\* ( $P < 0.01$ ) or \*\*\* ( $P < 0.001$ ) (Mann–Whitney U-test).

doi: 10.1371/journal.pone.0080296.g002

### Illustrative Cases

**Case 1 - Intraventricular Hemorrhage Missed by CT.** A 56-year old male driver suffered mental status change after his car was rear-ended by another vehicle. He presented in the ED with a GCS score of 15 with abrasion and a small laceration on his left eyebrow without closure and left clavicle fracture. His major clinical symptoms were left shoulder pain and headache. Non-contrast CT scan showed no intracranial abnormalities. Initial MRI scanning performed at 20 hours after injury revealed small foci of intraventricular blood on the left side, small blood product in the left lingual gyrus seen on SWI images and

several nonspecific WM hyperintensities on FLAIR images (Figure 4). Graphs displaying time course of UCH-L1 and GFAP are shown in Figure 4. In the sample obtained on admission, GFAP levels were markedly high. GFAP elevation persisted throughout the monitoring time gradually decreasing at 24 hours post injury (median 4.610, range 3.241–6.475 ng/ml). In contrast, in the same blood samples, UCH-L1 levels were only slightly high compared to controls (median 0.098, range 0.055–0.1410 ng/ml).

**Case 2 – Traumatic axonal injury case with normal structural MRI and high UCH-L1 level.** This 64-year old male

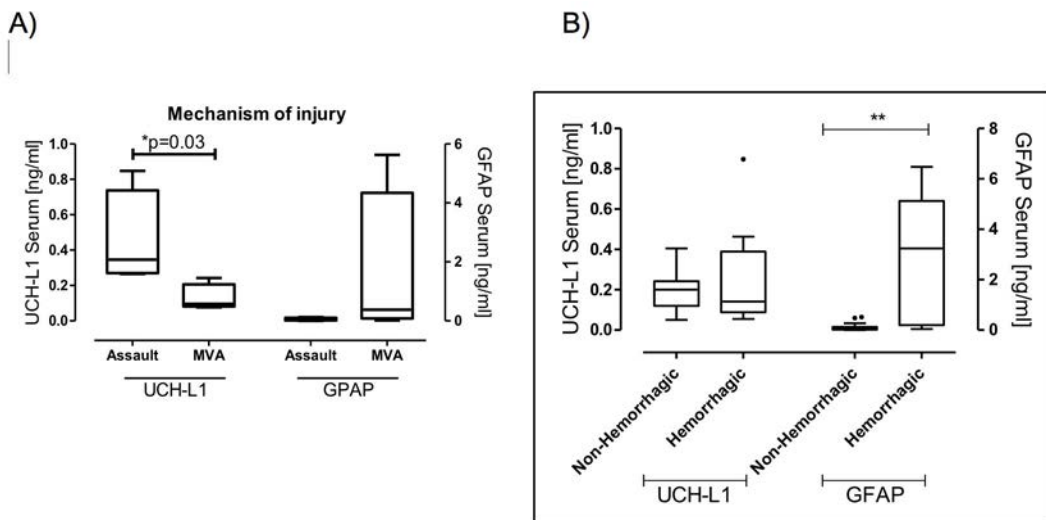


**Figure 3. Box-and-whisker plots demonstrating UCH-L1 and GFAP concentrations.** (A) Serum UCH-L1 and GFAP concentrations in patients who were victims of assault and in patients injured in a MVA. (B) Serum UCH-L1 and GFAP concentrations in patients with ventricular hemorrhages and hemorrhagic contusions and in patients with non-hemorrhagic lesions. The black horizontal line in each box represents the median, with the boxes representing the interquartile range. Significant differences are indicated \* ( $P < 0.05$ ) or \*\* ( $P < 0.01$ ) (Mann–Whitney U-test).

doi: 10.1371/journal.pone.0080296.g003

**Table 2.** Serum concentration of UCH-L1 and GFAP in patients with mTBI and in controls.

	Serum UCH-L1 (ng/mL)	Serum GFAP (ng/mL)
Admission	0.242 (0.096–0.336)*	0.043 (0.015–0.375)*
TBI Hemorrhagic	0.164(0.098–0.314)*	0.517(0.239–4.610)** †
Non-Hemorrhagic	0.171(0.107–0.248)**	0.015(0.015–0.06)**
Controls	0.05 (0.05–0.153)	0.004 (0.004–0.015)

Data are given as median (interquartile range).

\*  $p < .01$  and \*\*  $p < .001$  (p values of the Mann–Whitney test for differences between the groups [TBI versus Controls])

†.  $p < .01$  (p values of the Mann–Whitney test for differences between the groups [Hemorrhagic versus Non-Hemorrhagic])

doi: 10.1371/journal.pone.0080296.t002

patient was a victim of an assault and suffered brief loss of consciousness and femur fracture. He presented in the ED with a GCS score of 15 with symptoms of severe headache, dizziness, not feeling sharp, memory problems, poor concentration, fatigue/sluggish, sadness/depression, and irritability. His SAC score was 19 out of 30, and delayed recall 0 out of 5. Non-contrast CT scan showed no intracranial abnormalities. MRI scan performed at 7 hours after injury demonstrated multiple foci of non-specific WM hyper-intensities on FLAIR, but no intracranial bleeding on SWI. DTI data revealed multi-clusters with significantly decreased FA in the superior corona radiata and corticospinal tract (see Figure 5); these findings were suggestive of traumatic axonal injury at microstructural level. The results of neurochemical biomarker time course demonstrated UCH-L1 being

consistently elevated ( $>0.2\text{ng}/\text{ml}$ ) with high initial values that gradually decreased. GFAP was slightly increased with a peak at 12 hours post-injury (peak  $0.063\text{ ng}/\text{ml}$ ).

## Discussion

To our knowledge, this is the first effort to combine both blood biomarker and advanced MRI to improve the detection and characterization of mild TBI in the acute setting (within 24 hours after injury). We found that a) the biomarker levels were significantly higher in mTBI patients after injury; b) the levels of GFAP were highest in all subjects with intracranial bleeding on SWI, which is new finding in mTBI research; c) the total volume of WM voxels with abnormal DTI FA measures is correlated with patient's neurocognitive status, including memory; and d) DTI FA values could both increase and decrease in the acute setting, which is also a new finding in mTBI research. In the acute setting, the immediate challenge for emergency physicians is to identify those CT negative but symptomatic patients with intracranial abnormalities that may be predictive of long term neurocognitive sequelae [12]. Given the fact that most mTBI patients stay in the emergency department from only a few hours to 24 hours' observation, our comprehensive approach at this stage, while the patients are still in the emergency department, is more likely to help emergency physicians make decisions on patient management.

This study also ideally extends the previous work by our co-authors demonstrating the relationships between different pathways for UCH-L1 and GFAP and different types of brain injury pathophysiology after severe TBI as characterized by CT [55]. In addition to the previous findings, these pilot data suggest that the combined use of biochemical markers and

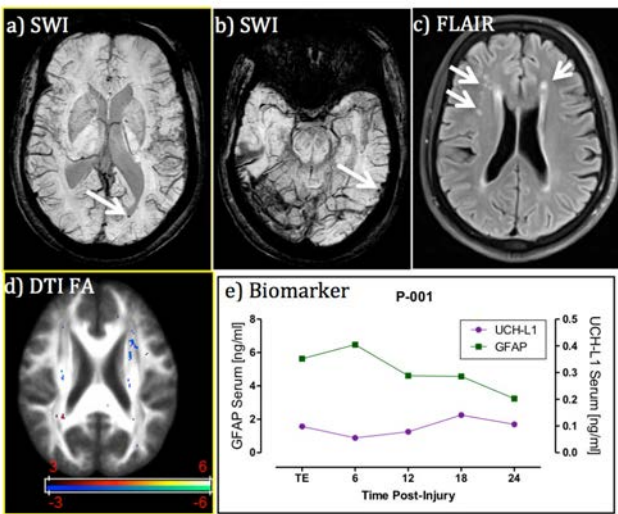


**Figure 4. Case 1. MRI and biomarker profile in a patient with intraventricular hemorrhage missed by CT.** Panels a) and b) are SWI images at different locations of the brain showing intra-ventricular blood and left lingual gyrus blood product (see arrows); panel c) is FLAIR image showing non-specific white matter hyper-intensities (see arrows); panel d) is DTI FA map showing the co-existence of voxels with increased and decreased FA measures (red color means FA decrease and blue color FA increase in comparison with controls,  $t>3$  for t-test); and panel e) is blood biomarker temporal profile, which exhibiting extraordinarily high GFAP levels over time in comparison with controls (median 0.004, interquartile range 0.004-0.015). Despite being missed by CT, the injury was still detected by both blood biomarker and MRI.

doi: 10.1371/journal.pone.0080296.g004

advanced MRI techniques may provide an important tool to evaluate and characterize mTBI patients, which is of importance for the understanding of the different pathophysiological mechanisms following TBI and for the development of effective therapies.

#### The heterogeneity of brain injury pathology

It is well recognized that brain injury pathology is heterogeneous and complex [56]. Each technique employed in this study brings unique aspects of brain injury pathology and contributes to the whole picture: intracranial bleeding, detected by SWI, manifests blood vessel damage [25]; DTI finding signifies the damage of WM integrity [13,14]; UCH-L1 for neuronal injury [44,57]; and GFAP for glial damage [55,58]. These different pathologies may be correlated with each other and, together, they can cover the spectrum of brain injury that contributes to impaired brain function. Our data demonstrated that intracranial bleeding was associated with elevated GFAP levels, which validated our first hypothesis regarding the association between GFAP and structural MRI. It also suggests an association between glial injury and vascular damage in mild TBI. Meanwhile, the non-association between UCH-L1 and MRI data goes against our second hypothesis on the

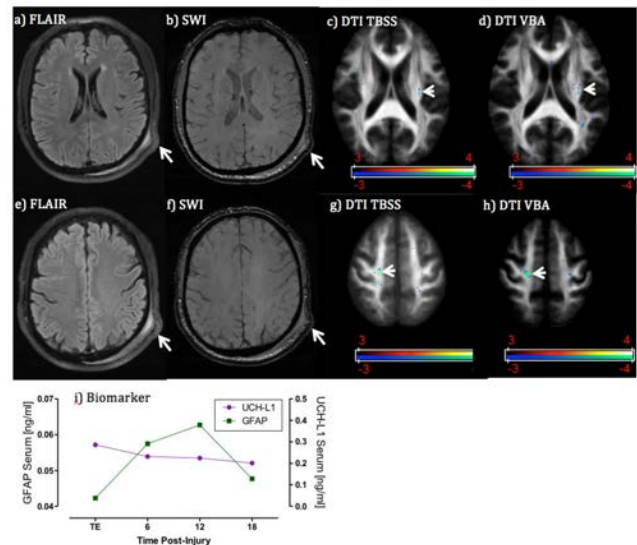


**Figure 5. Case 2. MRI and biomarker profile in a patient with traumatic axonal injury but normal-appearing structural MRI.** Panels a-d) are MRI images at the corpus callosum and fornix level. Panels e-h) are MRI images at the level of superior coronal radiata. Panel i) is blood biomarker profile. FLAIR and SWI images both indicate the scalp contusion at the parieto-occipital region (long arrows) but normal-appearing brain structure. However, both DTI TBSS and VBA analyses detected significantly reduced FA values at the ipsilateral side (corticospinal tract) and contralateral side (superior corona radiata) of brain white matter (arrow heads), in suggestion of coup and contra coup injury at the microstructure of white matter. Cold color indicates reduced FA values in comparison with controls ( $t>3$  for t-test). Blood biomarkers indicate slightly increased GFAP levels over time but significantly increased UCH-L1 at the admission.

doi: 10.1371/journal.pone.0080296.g005

relationship between UCH-L1 and DTI findings. As a matter of fact, both imaging and biochemical markers demonstrated abnormalities of mTBI in different aspects, suggesting that they are also complementary to each other for brain injury detection. This further confirms the heterogeneity of brain injury pathology.

#### Intracranial bleeding and elevated GFAP levels

Searching for intracranial bleeding is critically important in diagnostic radiology. Despite the fact that most mild TBI patients have negative CT findings, those mTBI patients (GCS 13-15) with positive CT findings are classified as "complicated mild TBI" [59]. As a subcategory of mTBI, their outcome tend to be worse than other mTBI patients with negative CT findings and even close to moderate level of TBI [59]. Regarding the role of structural MRI findings on mTBI classification, a recent study of 135 mTBI patients, scanned at 12 days after injury, demonstrated that one or more brain contusions on structural MRI, and  $\geq 4$  foci of hemorrhagic axonal injury on MRI, were

each independently associated with poorer 3-month outcome [60].

From pathophysiological perspective, GFAP is a structural protein of astroglial cells that are located in the intracellular space of astrocytes. The damage to astrocytes will cause the release of GFAP into extra-cellular space and that might leak into the blood stream through a compromised blood-brain barrier (BBB) [61]. Furthermore, the end processes of astrocytes surround the endothelial cells of vasculature system and make astrocytes an integral part of neural vascular unit [62]. The damage or temporal opening of the BBB will also likely further damage to the surrounding astrocytes as well. Supporting this, in stroke studies, considerable amount of data demonstrated significantly increases in GFAP in expanding intra-cerebral hemorrhage (ICH) than that in ischemic stroke [63,64]. Other studies reported a close correlation between GFAP serum concentration and ICH volume [65,66]. Even a multi-center clinical trial was conducted to use GFAP to differential ICH from ischemic stroke [65]. In addition to ICH, our data demonstrated that all intracranial hemorrhage cases, including both extra-axial and parenchymal hemorrhage, have significantly elevated GFAP levels. This implies that GFAP levels in blood serum have the potential to serve as a quick screening biomarker to triage mTBI patients for MRI confirmation of intracranial bleeding for prediction of an unfavorable outcome.

### The role of BBB

The elevated biomarker levels measured in our patients support the idea of a BBB breakdown that has often been documented in patients with TBI even after mild injuries [67]. Indeed, both UCH-L1 and GFAP are CNS-specific proteins with very low concentrations in blood in healthy people, almost below the threshold of detection by using current biomarker technology [40,46]. The elevated level of either one requires the same pathway to leak into the blood pool: the compromise or breakdown of the BBB. Given the much smaller size of UCH-L1 and GFAP than red blood cells, these proteins could more easily get into the blood stream through BBB temporal opening. Consequently, the elevated biomarker levels seem to detect a BBB compromise more relevant than the MRI-detectable bleeding. At a microscopic level, the BBB damage may not be severe enough or the temporal opening of BBB may not be long enough to allow enough red blood cells to pass through or cause sufficient amount of leakage that makes it visible as bleeding on neuroimaging at the macro-level [40]. However, this BBB compromise may be already big enough for sufficient amount of small protein biomarkers to leak into the blood stream and become detectable with modern biomarker detection techniques. Compared with detectable bleeding, which consists of only a small fraction of mTBI patients, the elevation of CNS-specific proteins in the blood pool might be able to serve as a more sensitive biomarker for the compromise of BBB in mTBI at the acute stage.

### Correlation with patients' neurocognitive performance

Our data showed that DTI lesion loads, measured as both TBSS FA and VBA FA lesion loads, are correlated with their

SAC score and delayed recall. More evidence reported that DTI FA values are correlated with mTBI patients' neurocognitive outcome [14,68]. Particularly, certain regions of DTI WM tract are correlated with patients' specific neurocognitive outcome [14,68]. As an example, Muhkerjee et al reported that DTI findings are correlated with patients' neurocognitive performance, but not hemorrhage [69,70]. Our DTI finding at the acute stage is in the same line as the published result at the sub-acute or chronic stage. This further confirms the hypothesis that there might be microstructural damages or changes in WM tracts that account for patients' neurocognitive deficits. However, this small-scale damage may not reach to the degree of vessel rupture that causes bleeding or hemorrhage.

### DTI FA increase or decrease

In this study, we also noticed the co-existence of both increased and decreased FA values in mTBI patients within 24 hours after injury and the dominance of increased FA lesions. All DTI studies of moderate to severe TBI patients [23,71-73] and subacute/chronic mTBI patients [22,69,74-76] report FA decreases which are correlated with clinical or neuropsychological measures. However, there are seemingly contradictory findings in mild TBI in the acute stage (within one week after injury) in the literature: Inglese [22] and Arfanakis[21] both reported FA decreases, while Wilde [77], Bazarian [78], and Mayer [79] reported FA increases and decreased radial diffusivity. Furthermore, Michael Lipton et al [80] reported bi-directional changes (both increase and decrease) of FA in chronic mTBI patients. Most recently, Bazarian et al [81] studied 9 high school athletes with diagnosed concussion or multiple sub-concussive blows and also reported bi-directional changes of FA at chronic stages. Of particular note, the terminology "acute stage" could mean quite different timing frames across the studies: some defined it as within 24 hours after injury and some even as within 7 days after injury. To date, only two studies reported MRI scan of mTBI patients within 24 hours after injury and they both have only a handful of patients [21,77]. The co-existence of both FA decrease and increase within 24 hours after injury is a relatively new in the field and needs further investigation in a relative large number of patients. It further demonstrates the heterogeneity of mTBI pathology at this stage. Meanwhile, lesion load with increased FA is significantly higher than the lesion load with decreased FA in our study. Increased FA lesion load, but not decreased FA lesion load, is correlated with patients' SAC and delayed recall scores in our data. It has been suggested that increased FA acutely may reflect cytotoxic edema [77], which would shunt extracellular fluid into swollen cells. This could have the effect of reducing inter-axonal free water and therefore reducing radial diffusivity and increasing overall fractional anisotropy. In contrast, a decreased FA could be due to several possible mechanisms: a) an impaired axonal transportation or axonal swelling, both of which cause decrease of longitudinal diffusivity along white matter tract; and b) vasogenic edema, which causes an enlarged extra-cellular space and an increased radial diffusivity. Our data of bi-directional changes of FA and the dominance of FA increase

demonstrates the heterogeneous pathology while cytotoxic edema might be a leading cause for patients' neurocognitive symptoms at hyper-acute stage (within 24 hours after injury).

### The need for an axonal injury biomarker

Our findings confirm that a panel of biomarkers rather than a single analyte seem to have the most utility for the diagnosis of mTBI patients, and improved characterization of the injury. Importantly, in the current study neither UCH-L1 nor GFAP was associated with WM injury identified by DTI. Because traumatic axonal injury is believed to be a major determinant of functional and neurocognitive symptoms following TBI as demonstrated by the correlation between DTI and patients' neurocognitive deficits, there might be a need for specific axonal injury biomarkers. Further work is needed to develop additional biomarker platforms, including axonal injury markers, in addition to the neuronal and glial damage proteins examined here, and to identify the relationships with advanced MRI techniques and patient outcomes that will help validate and confirm their clinical utilities in the acute setting [12].

### Limitations and future work

Despite its encouraging finding, this preliminary work has limitations, including a small sample size and the lack of long-term outcome data. It has been reported that DTI FA abnormality in certain WM tracts is correlated with patients' specific neurocognitive deficits in TBI [14,68]. This correlation between DTI lesion load and SAC score is consistent with the literature. However, the findings in our study with relative small sample size need further validation in a large number of patients. Further, it has been reported that orthopedic injury cases could also have slightly increased GFAP levels [47]. Though not significantly higher than controls, this could be another confounding factor which makes blood biomarker non-specific to brain injury. Therefore, a cohort of orthopedic injury controls is also needed for this study validation. Another confounding factor is that the mTBI patients and healthy controls are not age-matched. As demonstrated in our data, age is also correlated with patients' neurocognitive score. A demographically (included age, gender and education) matched study in future will be able to eliminate this confounding factor. In short, additional research will be required to validate our current findings in a large cohort of patients and demographically matched controls with longitudinal follow up and to further determine the relationships between neuroimaging and biomarker findings in the prediction of mTBI outcome.

### Conclusions

To summarize, this work represents the first effort of combining both blood protein biomarkers and advanced MRI to

improve the detection and characterization of brain injuries after mild TBI in the acute stage (within 24 hours after injury). Our data demonstrate elevated GFAP and UCH-L1 levels in mTBI patients at the acute stage in comparison with controls. Particularly, all cases with intra-cranial hemorrhage had significantly higher GFAP levels than those without hemorrhage. Patients' DTI measures were correlated with their neurocognitive status at this stage. This overlapping and complementary role of blood biomarkers and imaging in brain injury detection offers the promise that they might be used in conjunction in the management of patients with mTBI. Further studies with larger numbers of patients will be required to assess the reproducibility of these findings and to confirm the potential clinical utilities as diagnostic adjuncts in the acute setting.

### Supporting Information

**Figure S1. Serum biomarker levels over the first 24 hours after mTBI compared with controls.** Serum UCH-L1 (A) levels are maximal early after injury (on admission) (TE=0.24 [0.096-0.346]), while GFAP (B) concentrations peaked 12 hours after injury (0.35 [0.036-2.56]). Error bars represent median and IQR.  
(TIF)

### Acknowledgements

The authors acknowledge and appreciate the following members for their contributions: a) the research team (Patrick Medado, Talal Derani and others) of Emergency Medicine of Wayne State University for their screening and recruitment of patients, b) MRI research team (Zahid Latif, R.T., Yang Xuan, B.S., and Bo Wu, B.S.) for their assistance in MRI data acquisition, and c) Banyan Biomarkers Inc., particularly Drs. Ronald Hayes and Zhiqun Zhang, for their unselfish support in bioassay analysis. The authors also thank Ms. Natalie Wiseman for proof reading and particularly appreciate Dr. E Mark Haacke for his guidance and precious support for this project.

### Author Contributions

Conceived and designed the experiments: ZK RW BO JW FT SM. Performed the experiments: ZK SIA AK RKS VM CZ SM. Analyzed the data: ZK RG FK CZ SM. Contributed reagents/materials/analysis tools: ZK RW BO. Wrote the manuscript: ZK SM.

## References

- Kay T (1993) Neuropsychological treatment of mild traumatic brain injury. *Journal of Head Trauma Rehabilitation* 8: 74-85. doi: 10.1097/00001199-199309000-00009.
- National Institutes of Health (1999) NIH consensus development panel on rehabilitation of persons with traumatic brain injury. *Journal of the American Medical Association (JAMA)* 282: 974-983. doi:10.1001/jama.282.10.974.
- CDC (2003). Report to Congress on Mild Traumatic brain injury in the United States: Steps to Prevent a Serious Public Health Problem. Atlanta (GA): Centers for Disease Control and Prevention, National Center for Injury Prevention and Control.
- Bazarian JJ, McClung J, Cheng YT, Flesher W, Schneider SM (2005) Emergency department management of mild traumatic brain injury in the USA. *Emerg Med J* 22: 473-477. doi:10.1136/emj.2004.019273. PubMed: 15983080.
- Bazarian JJ, McClung J, Shah MN, Cheng YT, Flesher W et al. (2005) Mild traumatic brain injury in the United States, 1998-2000. *Brain Injury* 19: 85-91. doi:10.1080/02699050410001720158. PubMed: 15841752.
- Ruff R (2005) Two decades of advances in understanding of mild traumatic brain injury. *J Head Trauma Rehabil* 20: 5-18. doi: 10.1097/00001199-200511000-00009. PubMed: 15668567.
- Alves W, Macciocchi SN, Barth JT (1993) Postconcussive symptoms after uncomplicated mild head injury. *J Head Trauma Rehabil* 8: 48-59. doi:10.1097/00001199-199309000-00007.
- Bazarian JJ, Wong T, Harris M, Leahy N, Mookerjee S et al. (1999) Epidemiology and predictors of post-concussive syndrome after minor head injury in an emergency population. *Brain Inj* 13: 173-189. doi: 10.1080/026990599121692. PubMed: 10081599.
- Rimel RW, Giordani B, Barth JT, Boll TJ, Jane JA (1981) Disability caused by minor head injury. *Neurosurgery* 9: 221-228. doi: 10.1227/00006123-198109000-00001. PubMed: 7301062.
- Bellinger HG, Vanderploeg RD, Curtiss G, Warden DL (2007) Recent neuroimaging techniques in mild traumatic brain injury. *J Neuropsychiatry Clin Neurosci* 19: 5-20. doi:10.1176/appi.neuropsych.19.1.5. PubMed: 17308222.
- National Academy of Neuropsychology (2002). Mild Traumatic Brain Injury-an Online Course. Denver, Co: National Academy of Neuropsychology.
- Jagoda AS, Bazarian JJ, Bruns JJ Jr, Cantrill SV, Gean AD et al. (2008) Clinical policy: neuroimaging and decisionmaking in adult mild traumatic brain injury in the acute setting. *Ann Emerg Med* 52: 714-748. doi:10.1016/j.annemergmed.2008.08.021. PubMed: 19027497.
- Kou Z, Wu Z, Tong KA, Holshouser B, Benson RR et al. (2010) The role of advanced MR imaging findings as biomarkers of traumatic brain injury. *J Head Trauma Rehabil* 25: 267-282. doi:10.1097/HTR.0b013e3181e54793. PubMed: 20611045.
- Kou Z BR, Haacke EM (2012) Magnetic Resonance Imaging Biomarkers of Mild Traumatic Brain Injury. In: DS ea. Biomarkers for Traumatic Brain Injury. Royal Society of Chemistry.
- Shimony JS, McKinstry RC, Akbudak E, Aronovitz JA, Snyder AZ et al. (1999) Quantitative diffusion-tensor anisotropy brain MR imaging: normative human data and anatomic analysis. *Radiology* 212: 770-784. doi:10.1148/radiology.212.3.r9au51770. PubMed: 10478246.
- Conturo TE, McKinstry RC, Akbudak E, Robinson BH (1996) Encoding of anisotropic diffusion with tetrahedral gradients: a general mathematical diffusion formalism and experimental results. *Magn Reson Med* 35: 399-412. doi:10.1002/mrm.1910350319. PubMed: 8699953.
- Mac Donald CL, Dikranian K, Song SK, Bayly PV, Holtzman DM et al. (2007) Detection of traumatic axonal injury with diffusion tensor imaging in a mouse model of traumatic brain injury. *Exp Neurol* 205: 116-131. doi:10.1016/j.expneurol.2007.01.035. PubMed: 17368446.
- Kou Z, Shen Y, Zakaria N, Kallakuri S, Cavanaugh JM et al. (2007) Correlation of Fractional Anisotropy with Histology for Diffuse Axonal Injury in a Rat Model. Joint Annual Meeting ISMRM-ESMRMB. Berlin, Germany.
- Ptak T, Sheridan RL, Rhea JT, Gervasi AA, Yun JH et al. (2003) Cerebral fractional anisotropy score in trauma patients: a new indicator of white matter injury after trauma. *AJR Am J Roentgenol* 181: 1401-1407. doi:10.2214/ajr.181.5.1811401. PubMed: 14573445.
- Huisman TA, Schwamm LH, Schaefer PW, Koroshetz WJ, Shetty-Alva N et al. (2004) Diffusion Tensor Imaging as potential biomarker of white matter injury in diffuse axonal injury. *AJNR Am J Neuroradiol* 25: 370-376. PubMed: 15037457.
- Arfanakis K, Haughton VM, Carew JD, Rogers BP, Dempsey RJ et al. (2002) Diffusion tensor MR imaging in diffuse axonal injury. *AJNR Am J Neuroradiol* 23: 794-802. PubMed: 12006280.
- Inglese M, Makani S, Johnson G, Cohen BA, Silver JA et al. (2005) Diffuse axonal injury in mild traumatic brain injury: a diffusion tensor imaging study. *J Neurosurg* 103: 298-303. doi:10.3171/jns.2005.103.2.0298. PubMed: 16175860.
- Benson RR, Meda SA, Vasudevan S, Kou Z, Govindarajan KA et al. (2007) Global white matter analysis of diffusion tensor images is predictive of injury severity in TBI. *J Neurotrauma* 24: 446-459. doi: 10.1089/neu.2006.0153. PubMed: 17402851.
- Mac Donald CL, Johnson AM, Cooper D, Nelson EC, Werner NJ et al. (2011) Detection of blast-related traumatic brain injury in U.S. military personnel. *N Engl J Med* 364: 2091-2100. doi:10.1056/NEJMoa1008069. PubMed: 21631321.
- Kou Z, Benson RR, Haacke EM (2010) Susceptibility weighted imaging in traumatic brain injury. In: J GillardA WaldmanP Barker. *Clinical MR Neuroimaging*, 2nd Edition. Cambridge: Cambridge University.
- Paterakis K, Karantanas AH, Komnos A, Volikas Z (2000) Outcome of patients with diffuse axonal injury: the significance and prognostic value of MRI in the acute phase. *J Trauma* 49: 1071-1075. doi: 10.1097/00005373-200012000-00016. PubMed: 11130491.
- Reichenbach JR, Venkatesan R, Schilling DJ, Kido DK, Haacke EM (1997) Small vessels in the human brain: MR venography with deoxyhemoglobin as an intrinsic contrast agent. *Radiology* 204: 272-277. PubMed: 9205259.
- Dash PK, Zhao J, Hergenroeder G, Moore AN (2010) Biomarkers for the diagnosis, prognosis, and evaluation of treatment efficacy for traumatic brain injury. *Neurotherapeutics* 7: 100-114. doi:10.1016/j.nurt.2009.10.019. PubMed: 20129502.
- Kochanek PM, Berger RP, Bayir H, Wagner AK, Jenkins LW et al. (2008) Biomarkers of primary and evolving damage in traumatic and ischemic brain injury: diagnosis, prognosis, probing mechanisms, and therapeutic decision making. *Curr Opin Crit Care* 14: 135-141. doi: 10.1097/MCC.0b013e3282f57564. PubMed: 18388674.
- Mondello S, Muller U, Jeromin A, Streeter J, Hayes RL et al. (2011) Blood-based diagnostics of traumatic brain injuries. *Expert Rev Mol Diagn* 11: 65-78. doi:10.1586/erm.10.104. PubMed: 21171922.
- Mondello S, Akinyi L, Buki A, Robicsek S, Gabrielli A et al. ( Sept 202012) Clinical utility of serum levels of ubiquitin c-terminal hydrolase as a biomarker for severe traumatic brain injury. *Neurosurgery Sept* 20 [Epub ahead of print]. PubMed: 21937927.
- Papa L, Akinyi L, Liu MC, Pineda JA, Tepas JJ 3rd et al. (2010) Ubiquitin C-terminal hydrolase is a novel biomarker in humans for severe traumatic brain injury. *Crit Care Med* 38: 138-144. doi:10.1097/CCM.0b013e3181cbaff4. PubMed: 19726976.
- Mondello S, Papa L, Buki A, Bullock MR, Czeiter E et al. (2011) Neuronal and glial markers are differently associated with computed tomography findings and outcome in patients with severe traumatic brain injury: a case control study. *Crit Care* 15: R156. doi:10.1186/cc10115. PubMed: 21702960.
- Papa L, Lewis LM, Falk JL, Zhang Z, Silvestri S et al. ( Nov 2012) Elevated Levels of Serum Glial Fibrillary Acidic Protein Breakdown Products in Mild and Moderate Traumatic Brain Injury Are Associated With Intracranial Lesions and Neurosurgical Intervention. *Ann Emerg Med* Nov 8. PubMed: 22071014.
- Brophy GM, Pineda JA, Papa L, Lewis SB, Valadka AB et al. (2009) alphaH-Spectrin Breakdown Product Cerebrospinal Fluid Exposure Metrics Suggest Differences in Cellular Injury Mechanisms after Severe Traumatic Brain Injury - *J Neurotrauma* 26: 471-479. doi:10.1089/neu.2008.0657.
- Mondello S, Robicsek SA, Gabrielli A, Brophy GM, Papa L et al. (2010) alpha-spectrin breakdown products (SBDPs): diagnosis and outcome in severe traumatic brain injury patients. *J Neurotrauma* 27: 1203-1213. doi:10.1089/neu.2010.1278. PubMed: 20408766.
- Jackson P, Thompson RJ (1981) The demonstration of new human brain-specific proteins by high-resolution two-dimensional polyacrylamide gel electrophoresis. *J Neurol Sci* 49: 429-438. doi: 10.1016/0022-510X(81)90032-0. PubMed: 7217993.
- Saigoh K, Wang YL, Suh JG, Yamanishi T, Sakai Y et al. (1999) Intragenic deletion in the gene encoding ubiquitin carboxy-terminal hydrolase in gad mice. *Nat Genet* 23: 47-51. doi:10.1038/14314. PubMed: 10471497.
- Lincoln S, Vaughan J, Wood N, Baker M, Adamson J et al. (1999) Low frequency of pathogenic mutations in the ubiquitin carboxy-terminal hydrolase gene in familial Parkinson's disease. *Neuroreport* 10: 427-429. doi:10.1097/000011756-199902050-00040. PubMed: 10203348.
- Papa L, Lewis LM, Silvestri S, Falk JL, Giordano P et al. (2012) Serum levels of ubiquitin C-terminal hydrolase distinguish mild traumatic brain

- injury from trauma controls and are elevated in mild and moderate traumatic brain injury patients with intracranial lesions and neurosurgical intervention. *J Trauma Acute Care Surg* 72: 1335-1344. PubMed: 22673263.
41. Eng LF, Vanderhaeghen JJ, Bignami A, Gerstl B (1971) An acidic protein isolated from fibrous astrocytes. *Brain Res* 28: 351-354. doi: 10.1016/0006-8993(71)90668-8. PubMed: 5113526.
  42. Missler U, Wiesmann M, Wittmann G, Magerkurth O, Hagenström H (1999) Measurement of glial fibrillary acidic protein in human blood: Analytical method and preliminary clinical results. *Clin Chem* 45: 138-141. PubMed: 9895354.
  43. Mondello S, Jeromin A, Buki A, Bullock R, Czeiter E et al. (2012) Glial neuronal ratio: a novel index for differentiating injury type in patients with severe traumatic brain injury. *J Neurotrauma* 29: 1096-1104. doi: 10.1089/neu.2011.2092. PubMed: 22165978.
  44. Mondello S, Papa L, Buki A, Bullock MR, Czeiter E et al. (2011) Neuronal and glial markers are differently associated with computed tomography findings and outcome in patients with severe traumatic brain injury: a case control study. *Crit Care* 15: R156-. PubMed: 21702960.
  45. Vos PE, Jacobs B, Andriessen TM, Lamers KJ, Borm GF et al. (2010) GFAP and S100B are biomarkers of traumatic brain injury: an observational cohort study. *Neurology* 75: 1786-1793. doi: 10.1212/WNL.0b013e3181fd62d2. PubMed: 21079180.
  46. Papa L, Lewis LM, Falk JL, Zhang Z, Silvestri S et al. (2012) Elevated levels of serum glial fibrillary acidic protein breakdown products in mild and moderate traumatic brain injury are associated with intracranial lesions and neurosurgical intervention. *Ann Emerg Med* 59: 471-483. doi: 10.1016/j.annemergmed.2011.08.021. PubMed: 22071014.
  47. Papa L, Lewis LM, Falk JL, Zhang Z, Silvestri S et al. (2012) Elevated levels of serum glial fibrillary acidic protein breakdown products in mild and moderate traumatic brain injury are associated with intracranial lesions and neurosurgical intervention. *Ann Emerg Med* 59: 471-483. doi: 10.1016/j.annemergmed.2011.08.021. PubMed: 22071014.
  48. American Congress of Rehabilitation Medicine (1993) Definition of mild traumatic brain injury. *J Head Trauma Rehabil* 8: 86-88. doi: 10.1097/00001199-199309000-00010.
  49. McCrea M, Randolph C, Kelly JP (2000) Standardized Assessment of Concussion (SAC): Manual for Administration, Scoring and Interpretation, 2nd ed. Waukesha, WI: CNS Inc.
  50. McCrea M, Guskiewicz KM, Marshall SW, Barr W, Randolph C et al. (2003) Acute effects and recovery time following concussion in collegiate football players: the NCAA Concussion Study. *JAMA* 290: 2556-2563. doi: 10.1001/jama.290.19.2556. PubMed: 14625332.
  51. Naunheim RS, Matero D, Fucetola R (2008) Assessment of Patients with Mild Concussion in the Emergency Department. *J Head Trauma Rehabil* 23: 116-122. doi: 10.1097/01.HTR.0000314530.30401.70. PubMed: 18362765.
  52. Haacke EM, Xu Y, Cheng Y-CN, Reichenbach JR (2004) Susceptibility weighted imaging (SWI). *Magnetic Resonance in Medicine* 52: 612-618. doi: 10.1002/mrm.20198. PubMed: 15334582.
  53. Woods RP, Grafton ST, Watson JD, Sicotte NL, JC M (1998) Automated image registration: II. Intersubject validation of linear and nonlinear models. *J Comput Assist Tomogr* 22: 153-165. doi: 10.1097/00004728-199801000-00028. PubMed: 9448780.
  54. McCrea M, Kelly JP, Randolph C, Kluge J, Bartolic E et al. (1998) Standardized assessment of concussion (SAC): on-site mental status evaluation of the athlete. *J Head Trauma Rehabil* 13: 27-35. doi: 10.1097/00001199-199804000-00005. PubMed: 9575254.
  55. Mondello S, Papa L, Buki A, Bullock MR, Czeiter E et al. (2011) Neuronal and glial markers are differently associated with computed tomography findings and outcome in patients with severe traumatic brain injury: a case control study. *Crit Care* 15: R156. doi: 10.1186/cc10115. PubMed: 21702960.
  56. Saatman KE, Duhaime AC, Bullock Ross Maas AIR, Valadka A et al. (2008) Classification of traumatic brain injury for targeted therapies. *J Neurotrauma* 25: 719-738. doi: 10.1089/neu.2008.0586. PubMed: 18627252.
  57. Mondello S, Linnet A, Buki A, Robicsek S, Gabrielli A et al. (2012) Clinical utility of serum levels of ubiquitin C-terminal hydrolase as a biomarker for severe traumatic brain injury. *Neurosurgery* 70: 666-675. PubMed: 21937927.
  58. Vos PE, Lamers KJ, Hendriks JC, van Haaren M, Beems T et al. (2004) Glial and neuronal proteins in serum predict outcome after severe traumatic brain injury. *Neurology* 62: 1303-1310. doi: 10.1212/01.WNL.0000120550.00643.DC. PubMed: 15111666.
  59. Williams DH, Levin HS, Eisenberg HM (1990) Mild head injury classification. *Neurosurgery* 217: 442-448. PubMed: 2234336.
  60. Yuh EL, Mukherjee P, Lingsma HF, Yue JK, Ferguson AR et al. (2013) Magnetic resonance imaging improves 3-month outcome prediction in mild traumatic brain injury. *Ann Neurol* 73: 224-235. doi: 10.1002/ana.23783. PubMed: 23224915.
  61. Foerch C (2012) Astroglial proteins as biomarkers of intracerebral hemorrhage. In: S DambinovaRL HayesKKW WangDE ThurstonD Fox.Biomarkers for traumatic brain injury. Cambridge, UK: Royal Society of Chemistry.
  62. Neuwest EA, Bauer B, Fahlke C, Fricker G, Iadecola C et al. (2011) Engaging neuroscience to advance translational research in brain barrier biology. *Nature Reviews* 12: 169-182. doi: 10.1038/nrn2995. PubMed: 21331083.
  63. Foerch C, Curdt I, Yan B, Dvorak F, Hermans M et al. (2006) Serum glial fibrillary acidic protein as a biomarker for intracerebral haemorrhage in patients with acute stroke. *J Neurol Neurosurg Psychiatry* 77: 181-184. doi: 10.1136/jnnp.2005.074823. PubMed: 16174653.
  64. Undén J, Strandberg K, Malm J, Campbell E, Rosengren L et al. (2009) Explorative investigation of biomarkers of brain damage and coagulation system activation in clinical stroke differentiation. *J Neurol* 256: 72-77. doi: 10.1007/s00415-009-0054-8. PubMed: 19221847.
  65. Foerch C, Niessner M, Back T, Bauerle M, De Marchis GM et al. (2012) Diagnostic accuracy of plasma glial fibrillary acidic protein for differentiating intracerebral hemorrhage and cerebral ischemia in patients with symptoms of acute stroke. *Clin Chem* 58: 237-245. doi: 10.1373/clinchem.2011.172676. PubMed: 22125303.
  66. Foerch C, Curdt I, Yan B, Dvorak F, Hermans M et al. (2006) Serum glial fibrillary acidic protein as a biomarker for intracerebral haemorrhage in patients with acute stroke. *J Neurol Neurosurg Psychiatry* 77: 181-184. doi: 10.1136/jnnp.2005.074823. PubMed: 16174653.
  67. Korn A, Golani H, Melamed I, Pascual-Marqui R, Friedman A (2005) Focal cortical dysfunction and blood-brain barrier disruption in patients with Postconcussion syndrome. *J Clin Neurophysiol* 22: 1-9. doi: 10.1097/01.WNP.0000150973.24324.A7. PubMed: 15689708.
  68. Niogi SN, Mukherjee P (2010) Diffusion Tensor Imaging of Mild Traumatic Brain Injury - Journal of Head Trauma Rehabilitation 25: 241-255. doi: 10.1097/HTR.0b013e3181e52c2a.
  69. Niogi SN, Mukherjee P, Ghajar J, Johnson C, Kolster RA et al. (2008) Extent of microstructural white matter injury in postconcussive syndrome correlates with impaired cognitive reaction time: a DTI diffusion tensor imaging study of mild traumatic brain injury. *AJR Am J Neuroradiol* 29: 967-973. doi: 10.3174/ajnr.A0970. PubMed: 18272556.
  70. Niogi SN, Mukherjee P, Ghajar J, Johnson CE, Kolster R, Lee H, Suh M, Zimmerman RD, Manley GT, McCandless BD (2008) Structural dissociation of attentional control and memory in adults with and without mild traumatic brain injury. *Brain* 131: 3209-3221. doi: 10.1093/brain/awn247. PubMed: 18952679.
  71. Newcombe VF, Williams GB, Nortje J, Bradley PG, Harding SG et al. (2007) Analysis of acute traumatic axonal injury using diffusion tensor imaging. *Br J Neurosurg* 21: 340-348. doi: 10.1080/02688690701400882. PubMed: 17676452.
  72. Levin HS, Wilde EA, Chu Z, Yallampalli R, Hanten GR et al. (2008) Diffusion tensor imaging in relation to cognitive and functional outcome of traumatic brain injury in children. *J Head Trauma Rehabil* 23: 197-208. doi: 10.1097/01.HTR.0000327252.54128.7C. PubMed: 18650764.
  73. Kou Z, Gattu R, Benson RR, Raz N, Haacke EM (2008) Region of Interest Analysis of DTI FA Histogram Differentiates Mild Traumatic Brain Injury from Controls. Toronto, Canada.
  74. Wozniak JR, Krach L, Ward E, Mueller BA, Muetzel R et al. (2007) Neurocognitive and neuroimaging correlates of pediatric traumatic brain injury: a diffusion tensor imaging(DTI) study. *Arch Clin Neuropsychol* 22: 555-568. doi: 10.1016/j.acn.2007.03.004. PubMed: 17446039.
  75. Rutgers DR, Fillard P, Paradot G, Tadié M, Lasjaunias P et al. (2008) Diffusion tensor imaging characteristics of the corpus callosum in mild, moderate, and severe traumatic brain injury. *AJR Am J Neuroradiol* 29: 1730-1735. doi: 10.3174/ajnr.A1213. PubMed: 18617586.
  76. Kraus MF, Susmaras T, Cauglin BP, Walker CJ, Sweeney JA et al. (2007) White matter integrity and cognition in chronic traumatic brain injury: A diffusion tensor imaging study. *Brain* 130: 2508-2519. doi: 10.1093/brain/awm216. PubMed: 17872928.
  77. Wilde EA, McCauley SR, Hunter JV, Bigler ED, Chu Z et al. (2008) Diffusion tensor imaging of acute mild traumatic brain injury in adolescents. *Neurology* 70: 948-955. doi: 10.1212/01.wnl.0000305961.68029.54. PubMed: 18347317.
  78. Bazarian JJ, Zhong J, Blyth B, Zhu T, Kavcic V et al. (2007) Diffusion tensor imaging detects clinically important axonal damage after mild

- traumatic brain injury: a pilot study. *J Neurotrauma* 24: 1447-1459. doi: 10.1089/neu.2007.0241. PubMed: 17892407.
79. Mayer AR, Ling J, Mannell MV, Gasparovic C, Phillips JP et al. (2010) A prospective diffusion tensor imaging study in mild traumatic brain injury. *Neurology* 74: 643-650. doi:10.1212/WNL.0b013e3181d0ccdd. PubMed: 20089939.
80. Lipton ML, Kim N, Park YK, Hulkower MB, Gardin TM et al. (2012) Robust detection of traumatic axonal injury in individual mild traumatic brain injury patients: intersubject variation, change over time and bidirectional changes in anisotropy. *Brain Imaging Behav* 6: 329-342. PubMed: 22684769.
81. Bazarian JJ, Zhu T, Blyth B, Borrino A, J Z (2012) Subject-specific changes in brain white matter on diffusion tensor imaging after sports-related concussion. *Magn Reson Imaging* 30: 171-180. PubMed: 22079073.

# Quantitative Susceptibility Mapping of Small Objects Using Volume Constraints

Saifeng Liu,<sup>1</sup> Jaladhar Neelavalli,<sup>2\*</sup> Yu-Chung N. Cheng,<sup>2</sup> Jin Tang,<sup>1</sup> and E. Mark Haacke<sup>1–3</sup>

Microbleeds have been implicated to play a role in many neurovascular and neurodegenerative diseases. The diameter of each microbleed has been used previously as a possible quantitative measure for grading microbleeds. We propose that magnetic susceptibility provides a new quantitative measure of extravasated blood. Recently, a Fourier-based method has been used that allows susceptibility quantification from phase images for any arbitrarily shaped structures. However, when very small objects, such as microbleeds, are considered, the accuracy of this susceptibility mapping method still remains to be evaluated. In this article, air bubbles and glass beads are taken as microbleed surrogates to evaluate the quantitative accuracy of the susceptibility mapping method. We show that when an object occupies only a few voxels, an estimate of the true volume of the object is necessary for accurate susceptibility quantification. Remnant errors in the quantified susceptibilities and their sources are evaluated. We show that quantifying magnetic moment, rather than the susceptibility of these small structures, may be a better and more robust alternative. **Magn Reson Med** 69:716–723, 2013. © 2012 Wiley Periodicals, Inc.

**Key words:** susceptibility mapping; microbleeds; air bubbles; magnetic moment

The measurement of magnetic susceptibility offers an entirely new form of contrast in magnetic resonance imaging (1–6). More specifically, susceptibility quantification has already found applications in mapping out iron in the form of ferritin in brain tissues such as the basal ganglia (1,4,6) and in the form of deoxyhemoglobin for measuring the oxygen saturation in veins (1,4). This new form of imaging may provide a means for monitoring longitudinal changes in iron content in dementia, multiple sclerosis, traumatic brain injury, and Parkinson's disease. It may also be used to monitor microbleeds which have been implicated in the progression of vascular dementia (7), Alzheimer's, and other neurovascular disorders (8,9).

<sup>1</sup>School of Biomedical Engineering, McMaster University, Hamilton, Ontario, Canada.

<sup>2</sup>Department of Radiology, Wayne State University, Detroit, Michigan, USA.

<sup>3</sup>The MRI Institute for Biomedical Research, Detroit, Michigan, USA.

Grant sponsor: National Institutes of Health; Grant numbers: DOD W81XWH-11-1-0493, NHLBI R21 HL 108230-A2; Grant sponsor: The Wayne State University Perinatal Research Initiative.

\*Correspondence to: Jaladhar Neelavalli, Ph.D., Department of Radiology, Wayne State University, HUH-MR Research G030/Radiology, 3990 John R Street, Detroit, MI 48201. E-mail: jaladhar@wayne.edu

Received 25 November 2011; revised 29 March 2012; accepted 29 March 2012.

DOI 10.1002/mrm.24305

Published online 8 May 2012 in Wiley Online Library (wileyonlinelibrary.com).

© 2012 Wiley Periodicals, Inc.

One of the most recent susceptibility mapping methods is a Fourier-based method (2,3,5,10) which utilizes phase images. The accuracy of such a method depends on the volume measurement of the object. For example, to quantify the susceptibility of a given microbleed, usually the center and the radius of the microbleed have to be determined (10–13). Alternate volume estimations of the microbleed from high-resolution spin echo images may overcome these limitations. With a gradient echo sequence, the apparent volume of the object is increased owing to what is commonly referred to as the “blooming” effect, a signal loss around the object caused by  $T_2^*$  dephasing. This increased apparent volume may be used to obtain an estimate of susceptibility while the product of the apparent volume and the estimated susceptibility is much more robust and should still provide a good estimate of the magnetic moment of the object.

The goal of this article is to evaluate the quantitative accuracy of a Fourier-based susceptibility mapping method when it is applied to small structures, and to show that: (1) an accurate estimate of the magnetic moment is possible using multiecho gradient echo imaging; and (2) the accuracy of the effective susceptibility can be improved using the magnetic moment when an estimate of the true volume is available. For validation, we used a gel phantom with air bubbles and glass beads to mimic the clinical situation of microbleeds. The method illustrated here does not depend on the susceptibility value or the size of the object.

## THEORY

Current susceptibility mapping methods are based on the relationship between the susceptibility distribution and the magnetic field variation in the Fourier domain (1–6,10):

$$\Delta B(k) = G(k)\Delta\chi(k) \quad [1]$$

where  $\Delta B(k)$  is the Fourier transform of the magnetic field variation  $\Delta B(r)$ ,  $\Delta\chi(k)$  is the Fourier transform of the susceptibility distribution  $\Delta\chi(r)$ , and  $G(k)$  is the Green's function

$$G(k) = 1/3 - k_z^2/(k_x^2 + k_y^2 + k_z^2) \quad [2]$$

assuming that the main field direction is in the  $z$ -direction. Susceptibility quantification is an ill-posed inverse problem, owing to zeros in the Green's function  $G(k)$  along the magic angle in the  $k$ -space domain. As a result, regularization is required, as  $G(k)^{-1}$  is needed in the evaluation of susceptibility. In this study, we applied the regularization procedure described in a previous study (1) in which the intensity of  $G(k)^{-1}$  is reasonably attenuated when the absolute value of  $G(k)$  is below a

threshold value. The selection of this threshold is a trade-off between the susceptibility-to-noise ratio of the reconstructed susceptibility map and the accuracy in susceptibility quantification (1,6). The threshold value was chosen to be 0.1 in this study.

Although ideally  $\Delta\chi$  is the sought after parameter, when reduced resolution or  $T_2^*$  effects confound a clean measurement of the object's volume, it is more appropriate to investigate the associated magnetic moment (or, equivalently, the total or integrated susceptibility weighted by the voxel volume (12)). To see why this is the case, consider a sphere with a susceptibility difference  $\Delta\chi$ , the induced magnetic field at point  $P(r, \theta)$  outside the sphere is given by (14):

$$\Delta B_{\text{out}}(r) = \frac{\Delta\chi r_0^3 (3\cos^2\theta - 1)B_0}{3r^3} \quad [3]$$

where  $\Delta\chi = \chi_{\text{in}} - \chi_{\text{out}}$ ,  $\chi_{\text{in}}$  is the susceptibility inside the object,  $\chi_{\text{out}}$  is the susceptibility outside the object,  $r_0$  is the radius of the sphere,  $r$  is the distance from the point  $P(r, \theta)$  to the center of the sphere, and  $\theta$  is the angle between the point  $P$  and the main field direction. For simplicity, the meaning of susceptibility in this article will be taken to be  $\Delta\chi$  rather than  $\chi_{\text{in}}$  or  $\chi_{\text{out}}$ . Equation 3 also indicates that the product  $\Delta\chi V$  is independent of echo time (TE), where  $V = 4\pi r_0^3/3$  is the true volume of the sphere. The magnetic dipole moment of the spherical object is given as (14):

$$\mu = \frac{4\pi r_0^3 M}{3} \approx \frac{4\pi r_0^3 \Delta\chi B_0}{(3\mu_0)} \quad [4]$$

when  $\Delta\chi$  is much smaller than 1. Here  $\mu_0$  is the permeability of free space and  $M$  is the induced magnetization. The product of  $\Delta\chi$  and volume  $V$  is the effective magnetic moment term ( $\Delta\chi V$ ) and is simply referred to as magnetic moment hereafter in this paper. The phase value at a particular TE is given in a right-handed system by:

$$\Delta\phi(r) = -\gamma\Delta B_{\text{out}}(r)TE \quad [5]$$

The susceptibility  $\Delta\chi$  may be quantified using the phase information if the true volume ( $V$ ) of the object is known. Otherwise, the magnetic moment ( $\Delta\chi V$ ) may be found. As gradient echo images lead to a dephasing artifact and the object appears larger than its actual size, we defined an apparent volume  $V'$  and assuming that the susceptibility of this larger object can be accurately quantified, the magnetic moment could still be accurately calculated. An estimated susceptibility value  $\Delta\chi'$  can be calculated from the Fourier-based method using Eqs. 1–5. The quantity  $\Delta\chi'V'$  provides an estimate of the magnetic moment. Finally, the true susceptibility  $\Delta\chi$  can be calculated using the following equation:

$$\Delta\chi = \Delta\chi'V'/V \quad [6]$$

In this study, we use three volume definitions. The first one is the true volume  $V$ . The second one is the apparent volume  $V'$ , which is used in estimating the

magnetic moment. The apparent volume is related to the signal loss owing to  $T_2^*$  dephasing and is determined from gradient echo magnitude images, as described later. The last one is the spin echo volume  $V_{\text{se}}$ , which is measured from the spin echo images. This volume is used as an MR-based estimate of the true volume. We used simulations and multiecho gradient echo images of a gel phantom containing air bubbles and glass beads of varying sizes to test Eq. 6. Although glass beads can be considered as almost perfect spheres, air bubbles are closer to the clinical situation of variable-shaped microbleeds.

## METHODS

### Simulations

To evaluate the validity of Eq. 6 for susceptibility calculation of small objects, we simulated magnitude and phase images of four spheres with different radii at 21 different TEs (from 0 to 20 ms, with a step size of 1 ms). In each simulation, the sphere was placed in the center of a  $1024^3$  matrix with complex elements. The radii of four spheres tested, within this  $1024^3$  matrix, were 32, 48, 64, and 96 pixels, respectively. The magnitude inside each sphere was set to 0, whereas the background magnitude was set to 300 to simulate intensities in the experimental data from the gel phantom. The phase images of the spheres were generated according to Eqs. 3 and 5 with  $\Delta\chi = 9.4$  ppm. To simulate Gibbs ringing as well as partial volume effects seen in actual MR data, a process simulating the MR data sampling was used. Complex images generated in each  $1024^3$  matrix were Fourier transformed into  $k$ -space. The central  $32^3$  region was selected from  $k$ -space and was inverse Fourier transformed back to the imaging domain generating low-resolution data containing both Gibbs ringing and partial-volume effects. The radii of the four spheres became 1, 1.5, 2, and 3 pixels, respectively, in this final  $32^3$  volume. White gaussian noise was then added to the real and imaginary channels of the complex data in the image domain such that the signal-to-noise ratio in resultant magnitude images was 10:1. Susceptibility and the magnetic moment values were quantified for each of the spheres at all TEs and errors associated with these measurements were evaluated.

### Phantom Experiments

A gel phantom, containing 14 small air bubbles and 9 glass beads of varying sizes, was imaged at 3T (Siemens VERIO, Erlangen, Germany) using a five-echo 3D gradient echo sequence. The TEs were 3.93, 9.60, 15.27, 20.94, and 26.61 ms, respectively. Other imaging parameters for the gradient echo sequence were repetition time 33 ms, flip angle 11°, read bandwidth 465 Hz/pixel, voxel size  $0.5 \times 0.5 \times 0.5\text{mm}^3$ , and matrix size  $512 \times 304 \times 176$ . A multislice 2D spin echo data set was also collected with flip angle of 90°, repetition time of 5000 ms, and TE = 15 ms and with the same field of view, bandwidth, resolution, and matrix size as in the gradient echo data set. This is to maintain a one-to-one correspondence of the spin echo with the gradient echo images of

the phantom. To ensure that the field perturbation measured in the phase images is the actual perturbation profile from the gel phantom, we first performed shimming using a spherical phantom immediately before performing the imaging experiment. Manual shimming was performed on the spherical phantom, to a spectral full-width at half-maximum of 13 Hz and the shim coefficients were noted. The same shim settings were used while imaging the gel phantom to ensure that field perturbation profile owing to the presence of the phantom in the magnet is not influenced by any additional shimming.

For the construction of the phantom, an agarose gel solution was prepared with an 8% concentration by weight and poured into a cylindrical container. In the lower portion of the container, the gel was first filled to one-third the height of the cylinder and nine glass beads of various sizes were embedded in the gel. The true diameter of the glass beads was roughly measured using calipers before the glass beads were put into the gel solution. Specifically, four glass beads were 2 mm in diameter, three glass beads were 3 mm in diameter, one glass bead was 5 mm in diameter, and the largest glass bead was 6 mm in diameter. The phantom was allowed to cool so that the gel solidified and properly engulfed the glass beads. The rest of the prepared gel solution was then poured into the cylindrical container and variable-sized bubbles were injected by pumping various amount of air into the gel using an empty syringe (two smallest air bubbles were excluded from this study, owing to the limitation in volume estimation of small objects; details are provided in later sections). The theoretical susceptibility difference between air and water is known to be 9.4 ppm and will be used to compare with the measurements from our method. For glass beads, the susceptibility values were measured independently in a former study to be  $-1.8 \pm 0.3$  ppm relative to water (15).

First, to identify air bubbles and glass beads in the collected MR data, binary masks from magnitude data were used. The intensity variation in the magnitude images caused by the RF field inhomogeneity was first removed using a 2D quadratic fitting, before the binary masks were created. A reasonably uniform magnitude intensity profile across the phantom was obtained after this intensity correction. The binary masks were created by local thresholding of the corrected magnitude images (11). First, a relatively strict threshold was used to pick only the voxels where the signal was <50% of the signal in the gel away from the air bubbles or glass beads, as both air bubbles and glass beads have much lower intensities than the intensity of the surrounding gel. Next, the mean ( $\alpha_{\text{mag-gel}}$ ) and standard deviation ( $\sigma_{\text{mag-gel}}$ ) were calculated for a cubic  $21 \times 21 \times 21$  voxels volume of interest for each bubble or glass bead. A voxel roughly at the center of the bubble or glass bead was first chosen to center this  $21^3$  voxel window. The voxels picked up in the first step were excluded in the mean and standard deviation calculation. If a neighboring voxel has intensity lower than  $\alpha_{\text{mag-gel}} - \beta\sigma_{\text{mag-gel}}$ , it was regarded as a voxel belonging to air or glass bead. For the high signal-to-noise ratio data used here,  $\beta$  was empirically chosen to be 4 to separate air bubbles and glass beads from gel.

### Susceptibility Quantification

To reduce the background field or phase variation, a forward modeling approach was used to estimate air/gel-phantom interface effects (16). The phase processing steps were as follows:

- i. The original phase images were first unwrapped using the phase unwrapping tool, PRELUDE, in FMRIB Software Library (FSL) (17). With the geometry of the gel phantom extracted from the magnitude images at the shortest TE (3.93 ms in this study), the background field effects were reduced by fitting the predicted phase to the unwrapped phase by a least squares method. An additional 2D quadratic fitting was added to remove the induced phase owing to eddy currents.
- ii. The phase value inside a particular air bubble/glass bead (where the binary mask is 1) was set to the mean phase (essentially 0) from the local  $21 \times 21 \times 21$  window excluding the voxels which belong to the air bubble or glass bead. This is owing to the fact that the phase inside a sphere is theoretically zero and the nonzero phase is induced by the remnant background field variation as well as Gibbs ringing. This step also determines the apparent volume ( $V$ ) from magnitude images.
- iii. At each TE, a  $160 \times 160 \times 87$  voxel volume was cropped from the original phase images. This volume was selected because it covers most of the air bubbles and glass beads, whereas voxels near the edge of the gel phantom were excluded. The selected volume was then zero-filled to a  $512 \times 512 \times 256$  matrix.
- iv. Susceptibility maps were generated using a threshold-based approach described previously in Ref. (1). The mean ( $\alpha_{x\text{-air}}$  or  $\alpha_{x\text{-glass}}$ ) and standard deviation ( $\sigma_{x\text{-air}}$  or  $\sigma_{x\text{-glass}}$ ) of the susceptibility values of air bubble (or glass bead) were measured, taking into account the background susceptibility of the gel. Measurements were obtained in the following manner: the background mean ( $\alpha_{x\text{-gel}}$ ) and standard deviation ( $\sigma_{x\text{-gel}}$ ) of the local gel susceptibility value around each bubble or glass bead was first calculated from the  $21^3$  voxel region centered around each of the bubble/bead. Within this  $21^3$  volume, the voxels belonging to the bubble or glass bead, as determined by the binary mask, were excluded for this background mean and standard deviation calculation. Once these measures were obtained, for susceptibility of air bubbles, only voxels with susceptibility values higher than  $\alpha_{x\text{-gel}} + 3\cdot\sigma_{x\text{-gel}}$  were used for calculation purposes; whereas for glass beads, only voxels with a susceptibility value lower than  $\alpha_{x\text{-gel}} - 3\cdot\sigma_{x\text{-gel}}$  were used. This process assumes that the noise in the susceptibility maps follows a gaussian distribution, and the susceptibility of a voxel consisting of air or glass is statistically different from a voxel consisting of gel. The change in sign is owing to the fact that the air bubbles are paramagnetic relative to the gel, whereas glass beads are diamagnetic. To account for the baseline shift caused by

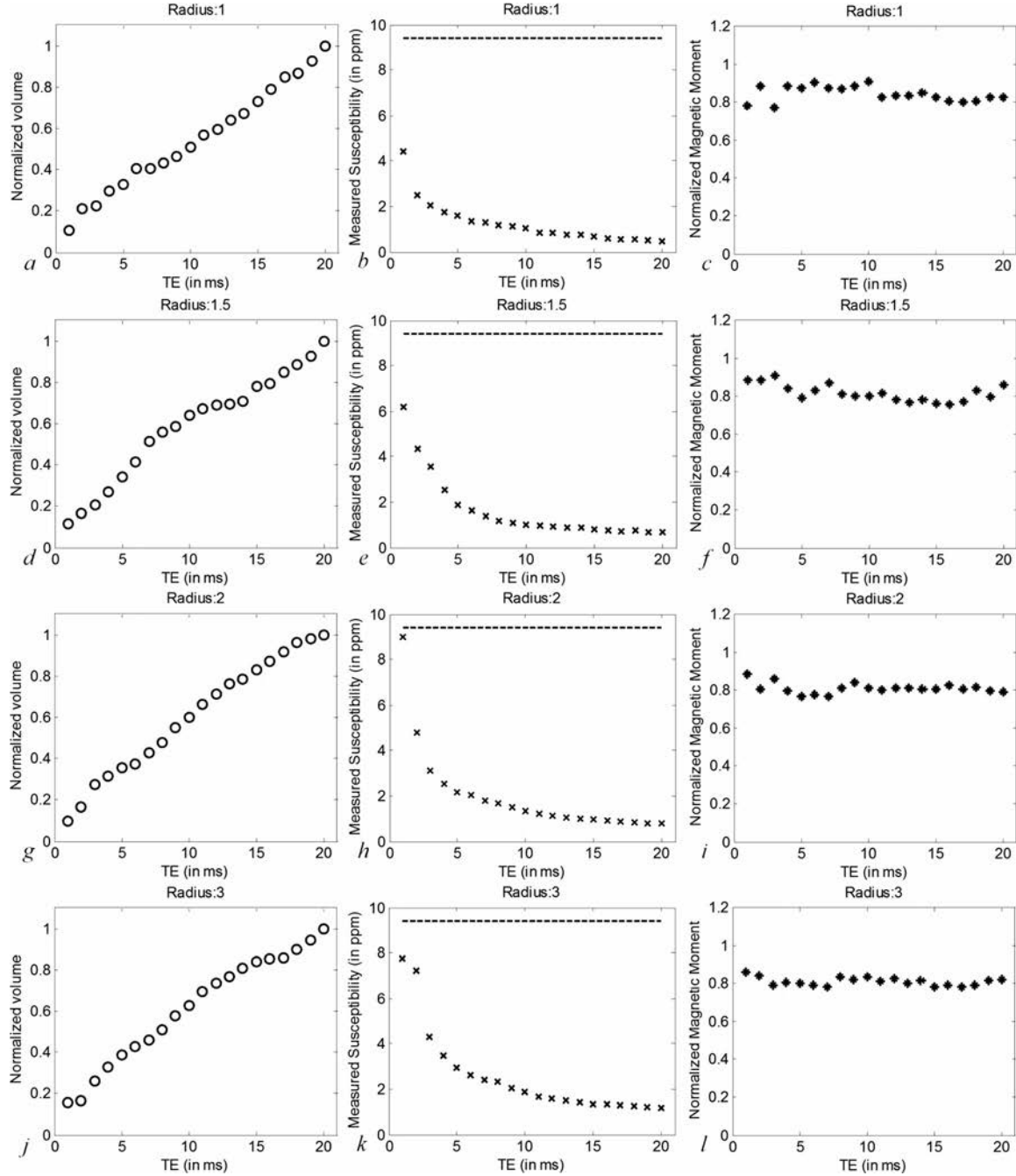


FIG. 1. Apparent volume normalized to the volume at TE = 20 ms (first column), measured susceptibility (second column), and normalized magnetic moments (third column) measured at different TEs of four different spheres. The dashed lines in the second column (**b**, **e**, **h**, and **k**) indicate the true susceptibility 9.4 ppm. For each sphere, the effective magnetic moments were normalized to the true effective magnetic moment.

remnant field variation, the susceptibility of the air bubble (or glass bead) was taken as  $\alpha_{\text{X-air}} - \alpha_{\text{X-gel}}$  (or  $\alpha_{\text{X-glass}} - \alpha_{\text{X-gel}}$ ).

#### Volume Measurement

The apparent volume of the air bubble or glass bead was determined from the binary masks directly, i.e., by counting the number of voxels inside the air bubble or glass bead. On the other hand, the spin echo volume is

measured utilizing the “object strength” notion proposed by Tofts et al. (18), in which the total intensity is measured for a particular volume of interest. For a volume composed of two types of tissues, a and b, the total intensity can be expressed as

$$I = I_a \cdot n_a + I_b \cdot (N - n_a) = (I_a - I_b) \cdot n_a + I_b \cdot N \quad [7]$$

where  $I$  is the total intensity, “ $I_a$ ” and “ $I_b$ ” are the intensities of the voxels containing purely tissue “a” or tissue “b,” respectively. The total number of voxels in this

**Table 1**  
Spin Echo Volume (in Voxels) and the Diameter (in mm) Calculated from Spin Echo Volume for Each Glass Bead

Bead	1	2	3	4	5	6	7	8	9
<b>Measure</b>									
Spin echo volume	35.4	37.5	38.2	39.1	96.5	103.8	113.6	516.6	912.1
Spin echo diameter	2.0	2.1	2.1	2.1	2.9	2.9	3.0	5.0	6.0
Actual diameter	2.0	2.0	2.0	2.0	3.0	3.0	3.0	5.0	6.0

volume of interest is denoted by “N,” and the number of voxels occupied by tissue “a” is denoted by “ $n_a$ .” Consequently, the number of voxels occupied by tissue “b” can be expressed as  $N - n_a$ .

By varying the size of the volume of interest, the total intensity is linearly dependent on the number of voxels in the volume of interest. Although “ $I_b$ ” can be determined as the slope in the fit to Eq. 7,  $n_a$  can be calculated from the intercept if “ $I_a$ ” is given ( $n_a$  may not be an integer as partial volume is included). In this study, “ $I_b$ ” corresponds to the intensity of a voxel composed purely of gel, whereas “ $I_a$ ” corresponds to the intensity of a voxel composed purely of air or glass. For a relatively large air bubble or glass bead, “ $I_a$ ” is dominated by the thermal noise, which can be approximated as  $1.25 \times \sigma_{\text{mag-gel}}$ , where  $\sigma_{\text{mag-gel}}$  is the measured standard deviation of the gel region in the magnitude images (19). For an air bubble or glass bead with a radius generally  $< 3$  pixels, “ $I_a$ ” is a combination of thermal noise and Gibbs ringing. To best account for these fluctuations, “ $I_a$ ” is calculated from:

$$I_a = \begin{cases} w_1 \cdot \alpha_{\text{mag-air}} + w_2 \cdot 1.25 \cdot \sigma_{\text{mag-gel}}, & \text{for air bubble} \\ w_1 \cdot \alpha_{\text{mag-glass}} + w_2 \cdot 1.25 \cdot \sigma_{\text{mag-gel}}, & \text{for glass bead} \end{cases} \quad [8]$$

where  $\alpha_{\text{mag-air}}$  and  $\alpha_{\text{mag-glass}}$  are the measured mean values inside the bubble and glass bead, respectively;  $w_1$  and  $w_2$  are two weighting factors. Based on our simulations (explained below),  $w_1$  and  $w_2$  were empirically determined from simulations to be 0.4 and 0.6, respectively, to minimize the error in estimation of the true volume.

#### Error in Volume Measurement

Although a regression method is used to measure the spin echo volume, it is still affected by partial volume effects, Gibbs ringing, as well as random noise. The simulated magnitude images at  $\text{TE} = 0$  were used to mimic spin echo magnitude images and to study the error in spin echo volume estimation. In addition, to examine the stability of this method relative to thermal noise, the volume measurement evaluation was performed 10 times for each simulated sphere, with inde-

pendently generated random noise for each of these simulations. The errors were determined by comparing the measured volume with the true volume. Note that this error estimation does not apply for the apparent volume which is determined directly from the binary masks.

## RESULTS

### Simulations

Magnetic moments for simulated spheres were calculated with the measured susceptibilities and the apparent volume for each sphere at a given TE. The results across different TEs are shown in Fig. 1. The measured volumes at different TEs were normalized to the volume at the longest TE, whereas the measured magnetic moments were normalized to the true magnetic moment, which is the product of input volume (i.e., the true volume) of the sphere and the input susceptibility (true susceptibility) 9.4 ppm. The normalized magnetic moment is roughly a constant for all spheres. However, for the sphere with a radius  $< 2$  pixels, the magnetic moments measured in the short TE range have more fluctuations than those measured at longer TEs. In addition, the magnetic moments are under-estimated for all spheres. The mean normalized magnetic moments were measured as:  $0.85 \pm 0.04$  (radius = 1 pixel),  $0.82 \pm 0.05$  (radius = 1.5 pixels),  $0.81 \pm 0.03$  (radius = 2 pixels), and  $0.81 \pm 0.02$  (radius = 3 pixels).

After the magnetic moments were obtained, the susceptibility values were corrected using the actual known volume (i.e., true volume) using Eq. 6. Specifically, the corrected susceptibilities are  $7.95 \pm 0.38$  ppm (radius = 1 pixel),  $7.70 \pm 0.43$  ppm (radius = 1.5 pixels),  $7.62 \pm 0.27$  ppm (radius = 2 pixels), and  $7.63 \pm 0.21$  ppm (radius = 3 pixels). There is still a 15–19% underestimation in the averaged susceptibility after attempting to correct the volume of the sphere.

To evaluate the stability of the volume measuring method, we carried out 10 simulations for each sphere at  $\text{TE} = 0$ . The means and standard deviations of the percentage errors relative to true volume for each sphere are  $18.02 \pm 27.26\%$  (radius = 1 pixel),  $1.89 \pm 12.18\%$  (radius = 1.5 pixels),  $3.67 \pm 8.91\%$  (radius = 2 pixels), and  $2.09 \pm 2.54\%$  (radius = 3 pixels). The algorithm failed to

**Table 2**  
Spin Echo Volume (in Voxel) of the 14 Air Bubbles

Bubble	1	2	3	4	5	6	7
Volume	3.3	15.1	28.7	42.2	43.9	82.8	87.7
Bubble	8	9	10	11	12	13	14
Volume	92.7	118.2	170.5	238.6	288.7	322.7	897.2

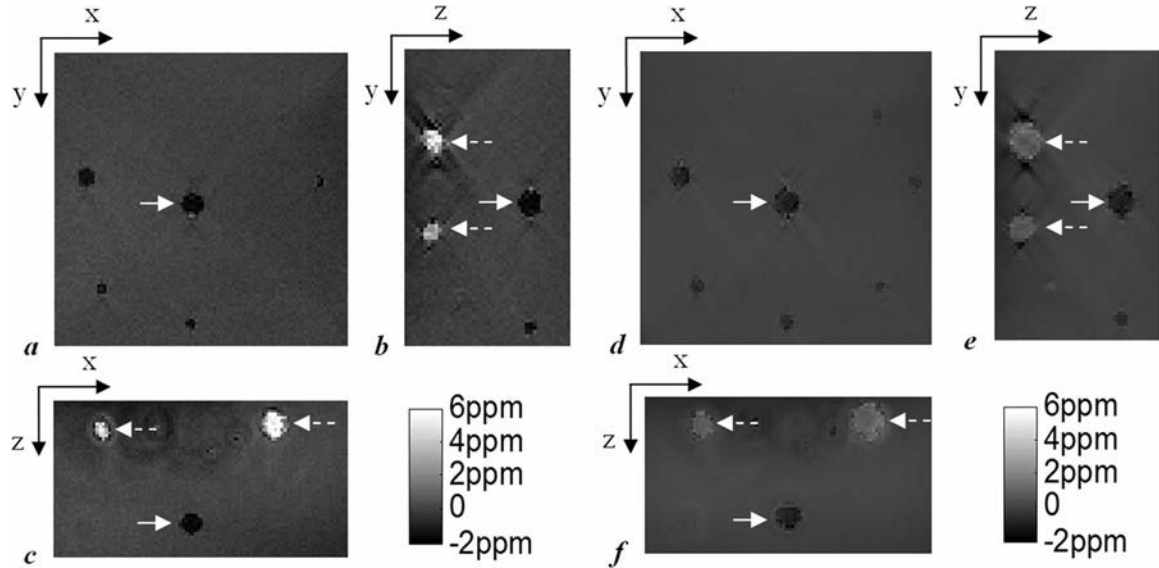


FIG. 2. Axial, sagittal, and coronal views of the susceptibility maps with TE = 3.93 ms (**a**, **b**, and **c**) and TE = 26.61 ms (**d**, **e**, and **f**). The main field direction is in "y" direction. Glass bead No. 9 in Table 1 is pointed by the white arrows. The air bubbles are indicated by the white dashed arrows.

quantify, in two of the 10 simulations for sphere with radius of 1 pixel. Larger errors and more variations of the volume measurements were seen in spheres with radii  $<2$  pixels. For the sphere with a radius of 3 pixels, the error in the volume estimation appears to be within 5% using the proposed method. As can be expected, when the object radius is only 1 pixel, the volume measurement becomes unstable.

#### Phantom Experiments

A total of 14 air bubbles and 9 glass beads were examined in the phantom data. The measured spin echo volumes of the glass beads and air bubbles are summarized in Tables 1 and 2. In these two tables, the glass beads as well as air bubbles are sorted based on their spin echo volumes, from small to large objects. The diameters of these glass beads calculated from their spin echo volumes agree reasonably well with their physically measured diameters, as summarized in Table 1. Also note that the error in volume measurement is unreliable for spherical objects with radii  $<1.5$  pixels (14.13 voxels for the volume). The error is generally larger than 20%, as shown in the simulations. Thus, the first two smallest air bubbles were excluded from the analysis.

Figure 2 shows three orthogonal views of the susceptibility map of the largest glass bead for the shortest TE

and the longest TE. Using Eq. 6, the measured susceptibilities can be corrected with the volume estimated from the spin echo images. These results are summarized in Table 3. The mean of the corrected susceptibility values of the glass beads averaged over all the TEs is  $-1.82 \pm 0.17$  ppm, which is within the range of the measured values in the previous study (15). The mean of the corrected susceptibility values of the air bubbles is  $6.66 \pm 0.85$  ppm. This is to be compared to the actual susceptibility of 9.4 ppm.

#### DISCUSSION

The susceptibility mapping technique using the regularized Fourier-based method has certain advantages over other methods, especially in terms of time efficiency and simplicity. However, it suffers from problems caused by the intrinsic singularities in the inverse of the Green's function, as well as partial volume effects which disrupt the true phase behavior. For small objects, susceptibility quantification using the inverse method (1) yields a significant underestimation of the susceptibility. The increased apparent volume at long TE can be utilized to create a larger virtual object for which the actual susceptibility can be more accurately measured and thus the Fourier-based susceptibility quantification gives a relatively smaller error for the magnetic moment. At this point, the

Table 3

Mean Measured and Corrected Susceptibilities (in ppm) of the Glass Beads and Air Bubbles at Different TEs

TE/ms	Glass Bead		Air bubble	
	Measured	Corrected	Measured	Corrected
3.93	$-1.50 \pm 0.07$	$-1.79 \pm 0.13$	$3.15 \pm 1.16$	$6.13 \pm 0.77$
9.60	$-1.07 \pm 0.32$	$-1.76 \pm 0.13$	$1.70 \pm 0.61$	$6.44 \pm 0.90$
15.27	$-0.86 \pm 0.32$	$-1.82 \pm 0.19$	$1.30 \pm 0.45$	$6.64 \pm 0.76$
20.94	$-0.68 \pm 0.28$	$-1.82 \pm 0.18$	$1.07 \pm 0.36$	$6.88 \pm 0.77$
26.61	$-0.59 \pm 0.25$	$-1.88 \pm 0.21$	$0.93 \pm 0.34$	$7.22 \pm 0.74$

susceptibility close to the actual value can be extracted from the estimated magnetic moment with an estimation of the true volume, either if it is known ahead of time, or it can be estimated from a high-resolution spin echo data set.

Based on the discussions above, the error  $\delta\Delta\chi$  in the corrected susceptibility  $\Delta\chi$  comes from the estimated magnetic moment  $\mu_a = \Delta\chi'V'$  and estimated volume ( $V$ ). Through error propagation, the error in the corrected susceptibility is given by:

$$\frac{\delta\Delta\chi}{|\Delta\chi|} = \sqrt{\left(\frac{\delta\mu_a}{\mu_a}\right)^2 + \left(\frac{\delta V}{V}\right)^2} \quad [9]$$

As we can see, the smaller the error in the estimated volume, the smaller the error in the corrected susceptibility. This equation explains the error seen in the corrected susceptibility of the air bubbles as well as glass beads.

In simulations, where the true volume is known, the remnant underestimation in the averaged corrected susceptibility ranges from 15 to 19%. As there is no error in the true volume, this error must be owing to the error in the apparent volume measurement and  $\Delta\chi'$  quantification owing to the regularization process. The level of underestimation is related to the threshold value in the inverse of the Green's function. A smaller threshold leads to less underestimation, but more streaking artifacts in the susceptibility maps. The regularized Fourier-based method, with threshold value of 0.1, can lead to an underestimation of around 13% for objects with radii larger than 3 pixels and even worse for smaller objects (1,6). This can be viewed as a systematic error.

In phantom studies, after using the volume estimated from the spin echo data, the corrected susceptibility values of the air bubbles have a maximum underestimation close to 44%, compared to the theoretical value 9.4 ppm. This is essentially a consequence of error in the spin echo volume measurement and the underestimation of  $\Delta\chi'$  quantified using the Fourier-based method. To overcome these limitations, one has to go to high-resolution images that can minimize volume quantification error and to relatively longer TEs that can improve accuracy in the magnetic moment quantification. However, the decreased signal-to-noise ratio in high-resolution spin echo images may introduce additional variation/noise in the final volume results.

There are a number of limitations to this study. Although a forward calculation was carried out to reduce the geometry induced field variation, remnant background field variation still exists. To best account for it, the phase inside the spherical objects was set to the local average phase. This also helps to reduce the large variation in susceptibility estimate induced by Gibbs ringing and thermal noise. However, this phase correction process is based on the assumption that the object of interest is a sphere. For nonspherical objects, this phase correction process may lead to variations of magnetic moment at different TEs. In addition, phase correction also creates a virtually larger object. It is possible that the center of the created object deviates from the true center of the original object of interest. This leads to additional errors even for spherical objects, as

seen from simulations. Thus, the phase inside the spherical object has significant effects to this method. Theoretically, only when the center of a simulated large sphere coincides with the original center of the sphere, and when the background phase value is 0, we can obtain a constant magnetic moment across different TEs. Hence, slight variations in object definition from a binary mask, which is used for phase substitution, can introduce variations in magnetic moment values. This is the essential source of shape dependence of the proposed method.

Although the estimated magnetic moments of the glass beads are almost a constant over different TEs, as indicated by the corrected susceptibilities, the estimated magnetic moments of the air bubbles are usually larger at a longer TE than at a shorter TE. This can be understood by the fact that the air bubbles are not perfect spherical objects compared to the glass beads. In fact, most of the air bubbles have ellipsoidal shapes, and any attempt of phase correction inside the bubble based on the assumption of the spherical shape will cause errors in the susceptibility measurement and thus lead to errors in the measurement of the magnetic moments.

Generally speaking, for small objects which can be well approximated as spheres, the theoretically expected errors in the estimated magnetic moment measurements are within 20% of the expected values and can be further reduced by adjusting the regularization thresholds in the susceptibility mapping method. Practically, the errors might be larger owing to the limited knowledge of the true volume. Although most small microbleeds can be well approximated as spheres, the use of more accurate volume estimation methods has the potential to reduce the error in susceptibility quantification of microbleeds.

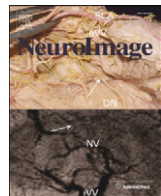
## CONCLUSIONS

In conclusion, we have shown that for very small structures, obtaining accurate magnetic susceptibility values is limited by the errors in the volume estimations of these structures and in the Fourier-based method itself. Despite this inability to estimate the actual volume of a small object accurately (whether it is an air bubble or microbleed), the estimated magnetic moment is almost a constant over different TEs. This demonstrates that it is possible to measure the magnetic moment at a longer TE when the apparent volume is increased owing to  $T_2^*$  dephasing. By measuring or knowing *a priori* the actual volume of an object, it is possible to obtain a reasonable estimate of the susceptibility.

## REFERENCES

- Haacke EM, Tang J, Neelavalli J, Cheng YC. Susceptibility mapping as a means to visualize veins and quantify oxygen saturation. *J Magn Reson Imaging* 2010;32:663–676.
- Liu T, Spincemaille P, de Rochefort L, Kressler B, Wang Y. Calculation of susceptibility through multiple orientation sampling (COS-MOS): a method for conditioning the inverse problem from measured magnetic field map to susceptibility source image in MRI. *Magn Reson Med* 2009;61:196–204.
- de Rochefort L, Brown R, Prince MR, Wang Y. Quantitative MR susceptibility mapping using piece-wise constant regularized inversion of the magnetic field. *Magn Reson Med* 2008;60:1003–1009.

4. Schweser F, Deistung A, Lehr BW, Reichenbach JR. Quantitative imaging of intrinsic magnetic tissue properties using MRI signal phase: an approach to *in vivo* brain iron metabolism? *NeuroImage* 2011;54:2789–2807.
5. Wharton S, Schäfer A, Bowtell R. Susceptibility mapping in the human brain using threshold-based k-space division. *Magn Reson Med* 2010;63:1292–1304.
6. Shmueli K, de Zwart JA, van Gelderen P, Li T, Dodd SJ, Duyn JH. Magnetic susceptibility mapping of brain tissue *in vivo* using MRI phase data. *Magn Reson Med* 2009;62:1510–1522.
7. Ayaz M, Boikov AS, Haacke EM, Kido DK, Kirsch WM. Imaging cerebral microbleeds using susceptibility weighted imaging: one step toward detecting vascular dementia. *J Magn Reson Imaging* 2010;31:142–148.
8. Greenberg SM, Vernooij MW, Cordonnier C, Viswanathan A, Al-Shahi Salman R, Warach S, Launer LJ, Van Buchem MA, Breteler MM. Cerebral microbleeds: a guide to detection and interpretation. *Lancet Neurol* 2009;8:165–174.
9. Yates PA, Sirisriro R, Villemagne VL, Farquharson S, Masters CL, Rowe CC, For the AIBL Research Group. Cerebral microhemorrhage and brain  $\beta$ -amyloid in aging and Alzheimer disease. *Neurology* 2011;77:48–54.
10. Cheng Y-CN, Neelavalli J, Haacke EM. Limitations of calculating field distributions and magnetic susceptibilities in MRI using a Fourier based method. *Phys Med Biol* 2009;54:1169–1189.
11. McAuley G, Schrag M, Barnes S, Obenaus A, Dickson A, Holshouser B, Kirsch W. Iron quantification of microbleeds in postmortem brain. *Magn Reson Med* 2011;65:1592–1601.
12. Liu T, Surapaneni K, Lou M, Cheng L, Spincemaille P, Wang Y. Cerebral microbleeds: burden assessment by using quantitative susceptibility mapping. *Radiology* 2012;262:269–278.
13. Cheng Y-C, Hsieh C-Y, Neelavalli J, Haacke EM. Quantifying effective magnetic moments of narrow cylindrical objects in MRI. *Phys Med Biol* 2009;54:7025–7044.
14. Haacke EM, Brown RW, Thompson MR, Venkatesan R. Magnetic resonance imaging: physical principles and sequence design, 1st ed. New York: Wiley-Liss; 1999.
15. Hsieh C, Cheng Y, Tackett R, Kumar R, Lawes G, Haacke E. TH-D-304A-02: quantifying magnetic moments and susceptibilities of small spherical objects in MRI. *Med Phys* 2009;36:2816.
16. Neelavalli J, Cheng YN, Jiang J, Haacke EM. Removing background phase variations in susceptibility-weighted imaging using a fast, forward-field calculation. *J Magn Reson Imaging* 2009;29:937–948.
17. Jenkinson M. Fast, automated, N-dimensional phase-unwrapping algorithm. *Magn Reson Med* 2003;49:193–197.
18. Tofts PS, Silver NC, Barker GJ, Gass A. Object strength—an accurate measure for small objects that is insensitive to partial volume effects. *MAGMA* 2005;18:162–169.
19. Gudbjartsson H, Patz S. The Rician distribution of noisy MRI data. *Magn Reson Med* 1995;34:910–914.



## Measuring iron in the brain using quantitative susceptibility mapping and X-ray fluorescence imaging

Weili Zheng <sup>a</sup>, Helen Nichol <sup>b</sup>, Saifeng Liu <sup>c</sup>, Yu-Chung N. Cheng <sup>a</sup>, E. Mark Haacke <sup>a,c,\*</sup>

<sup>a</sup> HUH-MR Research/Radiology, Wayne State University, Detroit, MI, USA

<sup>b</sup> Department of Anatomy & Cell Biology, University of Saskatchewan, Saskatoon, SK, Canada

<sup>c</sup> School of Biomedical Engineering, McMaster University, Hamilton, Ontario, Canada

### ARTICLE INFO

#### Article history:

Accepted 3 April 2013

Available online 13 April 2013

#### Keywords:

Brain iron

Ferritin

Quantitative susceptibility mapping (QSM)

X-ray fluorescence imaging (XRF)

### ABSTRACT

Measuring iron content in the brain has important implications for a number of neurodegenerative diseases. Quantitative susceptibility mapping (QSM), derived from magnetic resonance images, has been used to measure total iron content *in vivo* and in post mortem brain. In this paper, we show how magnetic susceptibility from QSM correlates with total iron content measured by X-ray fluorescence (XRF) imaging and by inductively coupled plasma mass spectrometry (ICPMS). The relationship between susceptibility and ferritin iron was estimated at  $1.10 \pm 0.08$  ppb susceptibility per  $\mu\text{g}$  iron/g wet tissue, similar to that of iron in fixed (frozen/thawed) cadaveric brain and previously published data from unfixed brains. We conclude that magnetic susceptibility can provide a direct and reliable quantitative measurement of iron content and that it can be used clinically at least in regions with high iron content.

© 2013 Elsevier Inc. All rights reserved.

### Introduction

Iron is an important endogenous biomarker for many neurological diseases and normal aging (Haacke et al., 2005; Schenck and Zimmerman, 2004). Previous histological work has shown that focally elevated iron deposition is associated with various neurological and psychiatric disorders, including multiple sclerosis (MS) (LeVine, 1997), Alzheimer's disease (Bouras et al., 1997; Hallgren and Sourander, 1960; LeVine, 1997), Huntington's disease (Chen et al., 1993; Dexter et al., 1991) and Parkinson's disease (Chen et al., 1993; Dexter et al., 1991). Increased iron accumulation has been detected in chronic hemorrhage, MS lesions, cerebral infarction, anemia, thalassemia, hemochromatosis, and NBIA (neurodegeneration with brain iron accumulation) (Haacke et al., 2005). An *in vivo* non-invasive and quantitative estimation of non-heme iron deposition (predominantly ferritin) is essential to understand the cause of iron accumulation and its distribution patterns as well as its physiological role in any given disease (Bartzokis et al., 2007; Gerlach et al., 1994; Ke and Qian, 2003).

A variety of methods have been used in the past to quantify iron using magnetic resonance imaging (MRI) (Haacke et al., 2005). The standard workhorses in this area are T2 (House et al., 2007; Jensen et al., 2010; Mitsumori et al., 2012) and T2\* (or R2\* = 1/T2\*) imaging methods that create T2\* or R2\* maps derived from multi-echo gradient (recalled) echo magnitude images. The latter are particularly useful since gradient echo sequences are very sensitive to the local susceptibility induced

magnetic field inhomogeneity due to iron (Bartzokis et al., 1993; Haacke et al., 1989, 2005; Ordidge et al., 1994; Peters et al., 2007; Reichenbach et al., 1997). Further, T2\* or R2\* maps provide an important contrast mechanism to investigate brain tissue microstructure and to detect abnormal levels of brain iron (Bartzokis et al., 2007; Bouras et al., 1997; Chen et al., 1993; Dexter et al., 1991; Haacke et al., 2005, 2009; Hallgren and Sourander, 1960; LeVine, 1997; Wallis et al., 2008).

In this paper, we focus on susceptibility measurements from phase images. Phase has been used as a means to measure iron content (Haacke et al., 2007). However, phase is dependent on the geometry of the object and so it can be misinterpreted. The solution lies in using a susceptibility map reconstructed from the phase information. In theory, this approach is independent of field strength, echo time, the object's relative orientation to the main field and the object's shape (Cheng et al., 2009b; de Rochefort et al., 2010; Haacke et al., 2010; Kressler et al., 2010; Li et al., 2011; Liu et al., 2009; Marques and Bowtell, 2005; Schweser et al., 2011; Shmueli et al., 2009; Wharton and Bowtell, 2010; Yao et al., 2009). Recent work has suggested that susceptibility changes in the basal ganglia, thalamus and other deep gray matter nuclei have better correlation with iron concentration than phase information (Bilgic et al., 2012; Fukunaga et al., 2010; Langkammer et al., 2012b; Schweser et al., 2011, 2012; Shmueli et al., 2009; Wharton and Bowtell, 2010; Yao et al., 2009) and, therefore, quantitative susceptibility mapping (QSM) may provide a good means to study tissue iron content.

Currently, the neuroscience community relies upon the 50 year old data on iron in cadaveric brains published by Hallgren and Sourander (Hallgren and Sourander, 1958). Total iron in cadaveric brain has been measured using synchrotron X-ray fluorescence (XRF) iron mapping

\* Corresponding author at: HUH-MR Research/Radiology, Wayne State University, 3990 John R Street, Detroit, MI 48201, USA. Fax: +1 313 745 9182.

E-mail address: nmrimaging@aol.com (E.M. Haacke).

**Table 1**  
Methodology and data processing.

	ICPMS	XRF	SWI	
	Background phase removal			QSM
Ferritin samples	✓	✓	Quadratic fitting	Forward fitting
Cadaveric brain		✓	SHARP	Truncated k-space division (Haacke et al., 2010)

(Hopp et al., 2010; Zheng et al., 2012), proton-induced X-ray emission mapping (Butz et al., 2000), inductively coupled plasma mass spectrometry (ICPMS) measurements (Langkammer et al., 2010, 2012a) and atomic absorption spectrometry measurements (House et al., 2007). Among these, the first two techniques can provide a voxel by voxel quantification of iron content which can then be compared with MR iron quantification.

In this paper, our goal is to develop an absolute quantification scale by separating the iron induced susceptibility change from other potential sources by comparing ferritin-gelatin phantoms with quantified XRF iron maps of basal ganglia from cadaver brains and ICPMS iron values.

## Materials and methods

### Preparation of ferritin phantoms

Horse spleen ferritin (Ref. F4503, Sigma-Aldrich, USA) was used to prepare ferritin-gelatin phantoms. The iron concentration as determined by the supplier using ICPMS was  $7.13 \pm 0.15$  mg/ml. The ferritin solution was first diluted by adding 4 ml of original solution with 16ml warm 7% gelatin resulting in a stock solution with iron concentration of about  $1426 \pm 30$   $\mu$ g/ml. This stock solution was serially diluted six times in warm gelatin by a factor of 2 each time. The ferritin-doped gelatin solutions as well as pure gelatin were loaded into straws and then embedded in a pure gelatin matrix. Total iron was measured in aliquots of the ferritin-doped gelatin by XRF and ICPMS. See the detailed scheme of the experiment in Table 1.

### Rapid scanning X-ray fluorescence (RS-XRF)

All XRF measurements were conducted at the Stanford Synchrotron Radiation Lightsource (SSRL). RS-XRF images of ferritin phantoms and cadaveric brain were acquired at wiggler beam line 10-2 at SSRL. The samples were mounted onto a set of motorized stages oriented at  $45^\circ$  to the incident beam. The incident beam (12 keV) passing through a tantalum aperture produced a  $100 \mu\text{m} \times 100 \mu\text{m}$  spot on the sample which was raster-scanned in the beam using a dwell time of 15 ms/point. Fluorescent energy windows were centered for Fe (6.21–6.70 keV) as well as all other biologically interesting elements, scatter and total incoming counts. Elements were quantified in  $\mu\text{g}$  iron/g wet tissue by comparison of signal strength with XRF calibration standards ( $\pm 5\%$  uncertainty) (Micromatter, Vancouver, BC, Canada) according to Hopp and colleagues (Hopp et al., 2010) using Sam's Microanalysis kit (Webb, 2010). An area of the ferritin-doped gelatin block was mapped and average counts were compared with XRF calibration standards.

### Inductively coupled plasma mass spectrometry

To confirm the total iron content of the ferritin phantoms, 5 ml samples were taken from the straws after MR imaging and the iron content was determined by ICPMS using an ELAN 9000 system (PerkinElmer, Waltham, MA, USA) (American Environmental Testing



**Fig. 1.** Photograph of the cadaveric brain sample in gelatin.

Laboratory Inc., California). The samples were diluted to the range acceptable for ICPMS via serial dilutions.

### Preparation of the cadaveric brain sample

One frozen coronal section (96 mm long  $\times$  132 mm wide  $\times$  5 mm thick) of human cadaveric multiple sclerosis (MS) brain (MS 3852) (see Fig. 1) was obtained from the Human Brain and Spinal Fluid Resource Center, Los Angeles, CA, under the University of Saskatchewan ethics approval BioREB 06-250. Coronal sections showed extensive irregular demyelination throughout the brainstem. There were also a few small scattered demyelinating periventricular foci (bilateral). The surface of the sample (a 5 mm thick section) showed patchy areas of slight rarefaction without significant axonal loss or change in oligodendrocyte density. There were varying degrees of associated gliosis. The areas of rarefaction were associated with extensive demyelination. To reduce storage artifacts such as leaching of metals, fresh autopsy brain was flash frozen and the slices were shipped on dry ice and stored frozen until they were thawed by immersion in buffered formalin. After 6 h of fixation, the brain slice was drained and sealed in plastic prior to initial synchrotron imaging of the surface of the slice. To resolve regions of interest, the slices were embedded in gelatin for MR imaging. The brain hemispheres were sectioned to expose the region of interest and then the slice was sealed in metal-free thin polypropylene film. RS-XRF images were acquired and quantified at SSRL (see the detailed scheme of the experiment in Table 1).

### MR imaging and image processing

#### Imaging and phase processing of ferritin samples

MR data of ferritin samples were collected on a 3 T Siemens Verio system using a multi-echo susceptibility weighted imaging (SWI) sequence with 11 echoes (TR = 40 ms, FA =  $15^\circ$ ). The resolution was 1 mm  $\times$  1 mm  $\times$  1 mm with a matrix of  $256 \times 256 \times 128$ . The shortest echo time was 5 ms with a 2.39 ms increment for the other 10 echoes. Magnitude and phase images were reconstructed from the raw data for each individual and combined channel. The geometry of the ferritin samples was segmented from multi-echo spin echo images (TR = 2000 ms, resolution 0.22 mm  $\times$  0.22 mm  $\times$  3 mm).

In order to reconstruct a susceptibility map, a pristine phase map was required. That is, the phase was unwrapped and all spurious phase information was removed. Phase images (TE = 21.73 ms) were unwrapped using Prelude in FSL (Jenkinson, 2003). To remove

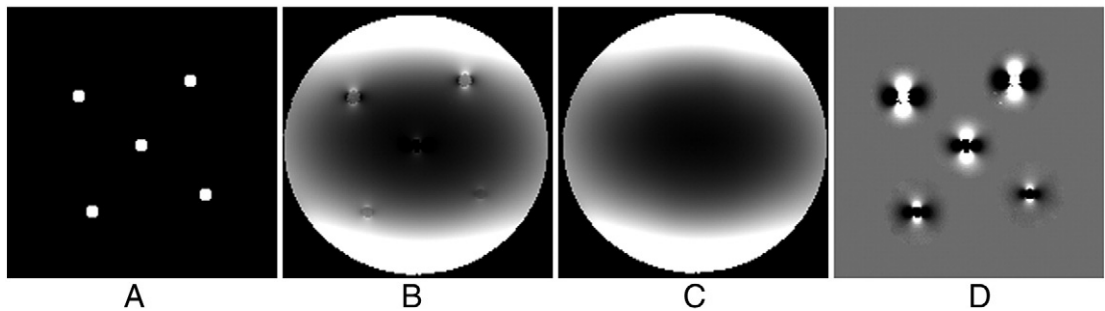


**Fig. 2.** Removing the background phase ( $TE = 21.73$  ms). A) Geometry of the straws segmented from the spin echo images. B) Original phase. C) Background phase after extrapolation of magnetic fields into the straw regions. D) Subtraction of C from B to reveal pristine dipole effects due to the iron in the straws.

the low spatial frequency background field effects, phase from regions outside the straws were chosen, where there were minimal remnant dipole effects. First, a circular mask with a radius three times that of the straw was defined and centered on each straw and all the information inside this mask was removed from the images. The remaining signal was fit with a quadratic function and extrapolated back into the masked region. Then the estimated dipole phase was obtained by subtracting this modified background phase from the original phase. The susceptibility inside each of the ferritin straws was assumed to be uniform and was estimated using a least squares fitting of the forward simulated dipole phase with the estimated phase (Neelavalli et al., 2009). All the steps were performed in MATLAB R2009a. The results of each step are shown in Fig. 2.

#### Imaging and image processing of cadaveric brain

MR images were collected on a 3 T Siemens Verio system using the same 11 echo SWI sequence but with different imaging parameters. The coronal images were acquired with a resolution  $0.5\text{ mm} \times 0.5\text{ mm}$  in phase encoding and readout direction and  $0.7\text{ mm}$  in the slice select direction with a readout bandwidth of  $465\text{ Hz/pixel}$ , a field-of-view of  $256\text{ mm} \times 192\text{ mm}$  with  $N_x = 512$ ,  $N_y = 384$  and  $N_z = 40$ . The shortest echo time was  $5.68\text{ ms}$  with a  $2.57\text{ ms}$  increment for the other 10 echoes. MR phase images ( $TE = 8.25\text{ ms}$ ) were first unwrapped using Prelude in FSL (Jenkinson, 2003) and then the background phase was removed using TSVD-SHARP (Schweser et al., 2011) with a kernel size of  $5\text{ mm}$ . An initial estimation of the susceptibility distribution was obtained using truncated k-space division, with a threshold value of 0.1. Due to the presence of some air bubbles near the brain tissue, the streaking artifacts would mask several important regions in the susceptibility map. Thus, the air bubbles were first extracted from the susceptibility map by setting a threshold, since air has a much higher susceptibility relative to water than that of brain tissue. The extracted susceptibility maps of the air bubbles were used to predict their induced field variation through a forward field calculation. Finally, the predicted fields induced by the air bubbles were removed from the SHARP (Schweser et al., 2012) processed field map. The central region of these air bubbles in phase images was set to be zero, in order to reduce the streaking artifacts caused by the noise inside the bubble. This newly processed field map was used to generate the

final susceptibility maps, using a truncated k-space division with a threshold of 0.1 (Haacke et al., 2010) via SPIN (Signal Processing in NMR, Detroit, MI, USA) software.

## Results

#### Correlation between susceptibility and ferritin iron content

The susceptibilities ( $TE = 21.73\text{ ms}$ ) of the five empty straws embedded in gelatin were estimated at  $(9.46 \pm 0.015; 9.64 \pm 0.015; 9.46 \pm 0.016; 9.65 \pm 0.013; 9.46 \pm 0.015)$  ppm. Assuming that the susceptibility difference between the air and gel is  $9.4\text{ ppm}$  (Cheng et al., 2009a), the total susceptibility measurement including the background removal, straw geometry segmentation error and least squares fitting had a bias of  $1.42\%$ .

The measured susceptibilities ( $TE = 21.73\text{ ms}$ ) and iron concentrations of the six ferritin samples are listed in Table 2. The dipolar phase pattern outside the straw from the sample with the lowest iron concentration ( $39 \pm 6\text{ }\mu\text{g Fe/ml}$ ) had its sign reversed compared with other samples. This sample shows a negative susceptibility of  $-14\text{ ppb}$  when using the forward fitting approach. One possible explanation for this could be a small baseline shift coming from an imperfect background removal. Since the iron concentration range that can be measured with XRF is broad, there was no need for dilution. In contrast, ICPMS requires dilution of samples to make iron concentration in the proper range for analysis. The results in Table 2 show that the iron content measured by two approaches (XRF and ICPMS) was essentially the same. The correlation slopes in Fig. 3 obtained from ICPMS ( $1.11 \pm 0.06\text{ ppb per }\mu\text{g iron/ml}$ ) and XRF imaging ( $1.10 \pm 0.08\text{ ppb per }\mu\text{g iron/ml}$ ) were close and both were less than the theoretical estimation of  $1.27\text{ ppb per }\mu\text{g iron/ml}$  from Schenck (1992).

#### Correlation between susceptibility and iron in cadaveric brain

In order to correlate the susceptibility and XRF iron maps, images from both methods were co-registered (Fig. 4). ROIs marked in each image were used for a voxel by voxel comparison of susceptibility and iron measurements (Table 3). At  $TE = 8.25\text{ ms}$ , the correlation equations were found to be  $Y = 0.80(\pm 0.01)$  (ppb susceptibility

**Table 2**

Susceptibilities of ferritin phantoms as quantified from SWI phase data ( $TE = 21.73\text{ ms}$ ) and iron concentrations measured by XRF and ICPMS. Data are shown as mean  $\pm$  one standard deviation.

	Sample no. 1	Sample no. 2	Sample no. 3	Sample no. 4	Sample no. 5	Sample no. 6	Gelatin solution (7%)
Susceptibility (ppb) ( $N = 19,205$ )	$840 \pm 2.4$	$428 \pm 1.3$	$271 \pm 0.9$	$101 \pm 0.4$	$39 \pm 0.3$	$-14 \pm 0.2$	N.A. for forward fitting
XRF iron concentration ( $\mu\text{g/ml}$ ) ( $N = 961$ )	$790 \pm 94$	$395 \pm 44$	$229 \pm 32$	$110 \pm 27$	$77 \pm 16$	(Not available)	(Not available)
ICPMS iron concentration ( $\mu\text{g/ml}$ )	$772 \pm 115$	$448 \pm 67$	$240 \pm 36$	$127 \pm 19$	$66 \pm 10$	$39 \pm 6$	$0.23 \pm 0.11$

Standard deviation includes the spatial distribution variation in the straws.

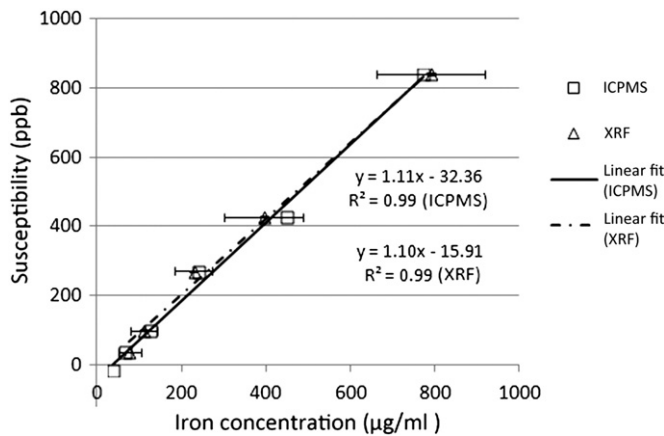


**Fig. 3.** Correlation between susceptibility measured by MRI and total iron measured by ICPMS and XRF for ferritin phantoms.

per  $\mu\text{g iron/g wet tissue}$ ) \*  $X$  ( $\mu\text{g iron/g wet tissue}$ ) + 10.87( $\pm 2.9$ ) (ppb susceptibility) and  $Y = 0.79(\pm 0.02) * X - 3.66(\pm 4.2)$  (ppb suscep-

rowsep="1"tibility) for left and right hemisphere, respectively. The phase images at  $TE = 21.1$  ms were also processed, the fitted equations were  $Y = 0.78(\pm 0.02) * X - 4.36(\pm 4)$  (ppb susceptibility) and  $Y = 0.79(\pm 0.01) * X - 5.22(\pm 2.8)$  (ppb suscep-

## Discussion

Using ferritin phantoms and a cadaveric brain sample, we have found that the susceptibility correlates reasonably well with the iron measured by XRF and/or ICPMS (Fig. 3). The cadaveric brain used in the study was from a person with multiple sclerosis. It is commonly assumed that the iron in normal and pathological MS brains is predominantly stored in the form of ferritin. As long as this assumption holds, the MS pathology will not affect the susceptibility/iron correlation slope. Our correlation of iron content with susceptibility for cadaveric brains (Fig. 5) was comparable with that obtained by Langkammer et al. (2012b). This is expected since we used SHARP with the same

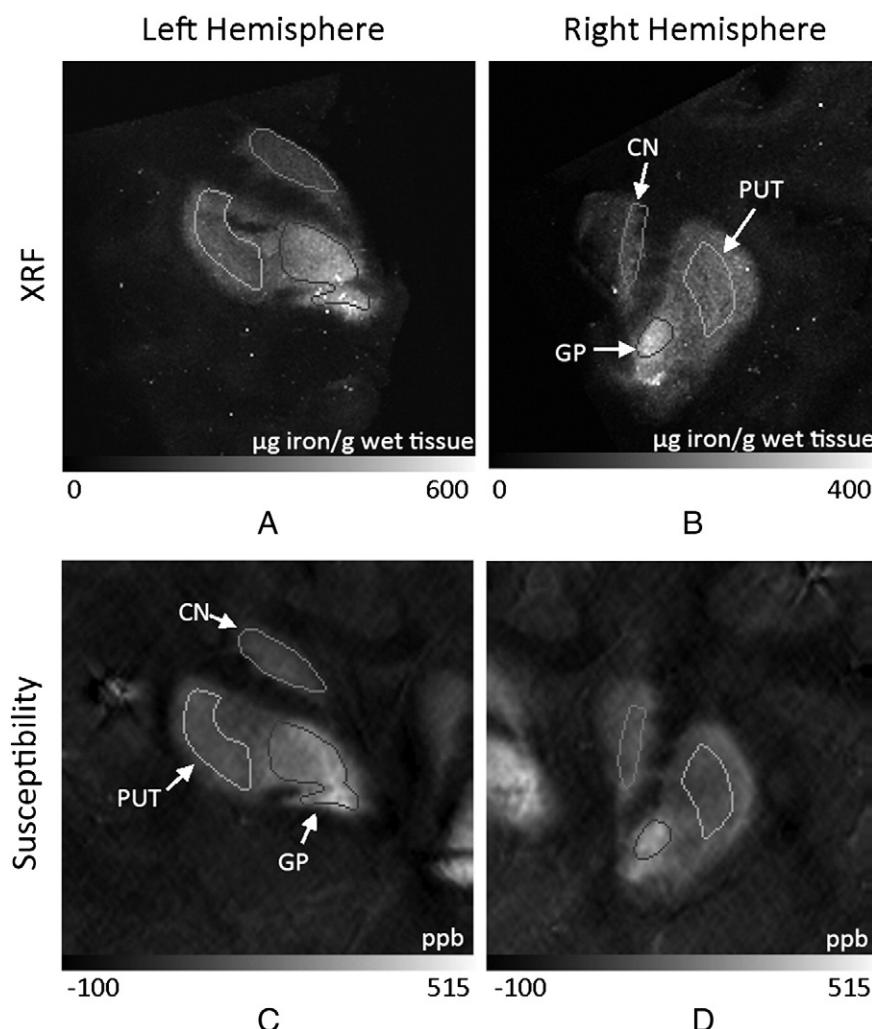


**Fig. 4.** Iron quantified from XRF Fe mapping (A, B) for left and right hemispheres; putative iron quantified as susceptibility ( $TE = 8.25$  ms) (C, D). Images are co-registered and the ROIs used for a pixel by pixel correlation are outlined in both images. CN: caudate nucleus. PUT: putamen. GP: globus pallidus. ROIs were defined by excluding the edges in the map for each structure.

**Table 3**

Average susceptibility of a cadaveric brain as quantified from SWI phase data ( $TE = 8.25$  ms) and Fe measured using XRF imaging. ROIs are defined in Fig. 4. Data are shown as mean  $\pm$  one standard deviation.

	CN (left)	PUT (left)	GP (left)	CN (right)	PUT (right)	GP (right)
Susceptibility (ppb)	111 $\pm$ 25	152 $\pm$ 18	273 $\pm$ 73	105 $\pm$ 31	121 $\pm$ 24	242 $\pm$ 40
Iron estimated by XRF ( $\mu\text{g/g}$ wet tissue)	153 $\pm$ 28	210 $\pm$ 35	338 $\pm$ 73	135 $\pm$ 28	179 $\pm$ 26	277 $\pm$ 40

Mean is estimated as the average within the ROI. Standard deviation includes the spatial distribution variation within the ROI.

parameters to remove the background fields. The SWIM approach used in this paper underestimates the susceptibility by 14% for deep gray matter structures according to our simulations. The homogeneity-enabled incremental dipole inversion (HEIDI) method used by Langkammer et al. (2012b) underestimates the susceptibility by about 7% (Langkammer et al., 2012b; Schweser et al., 2012). Our slope ( $0.8 / (1-14\%) \cong 0.93$ ) is close to that in Langkammer et al. (2012b) ( $0.89 / (1-7\%) \cong 0.957$ ) for deep gray matter when these biases are accounted for. Since the cadaveric brain in our experiment was formalin fixed and those in Langkammer et al. (2012b) were unfixed, this suggests that fixation may not change tissue susceptibility in deep gray matter.

However, the slope of 0.59 ppb susceptibility per  $\mu\text{g}$  iron/g wet tissue obtained from our in vivo data (Haacke, 2012) and other single orientation results that used Hallgren and Sourander's equation as the iron baseline (Shmueli et al., 2009; Wharton and Bowtell, 2010) was smaller than the 0.8 ppb susceptibility per  $\mu\text{g}$  iron/g wet tissue obtained from our cadaveric brain data, even though they were processed with the same methods. Thus, there appears to be a difference between in vivo and ex vivo susceptibilities and their correlation with iron. The reason for this is unclear but could be due to the freezing and fixation process which could affect local susceptibilities of the tissue.

Formalin fixation might change MR signal but previous work on myelin susceptibility (Lee et al., 2012; Liu et al., 2011) demonstrated that the effect of formalin fixation on the susceptibility changes due to myelin was subtle. The similar iron/susceptibility slopes of fixed brain in our work and of the unfixed brains in the work of Langkammer and colleagues (Langkammer et al., 2012b) further supports the view that formalin fixation has negligible effect on susceptibility. The effects of fixation on R2 and thus R2\* values, however, are known to be substantial (Dawe et al., 2009; Lee et al., 2012; Pfefferbaum et al., 2004; Schmierer et al., 2008) and are beyond the scope of this paper.

The susceptibility/iron correlation slopes obtained from cadaveric and in vivo brains in Table 4 are generally smaller than the theoretical slope of 1.32 ppb susceptibility per  $\mu\text{g}$  iron/g wet tissue except for the slope obtained with myelin correction in Schweser et al. (2011). One possible reason for the smaller slope from the in vivo human brains is that there are still some forms of iron that are MR invisible although these may be in other species that are known to be present at low levels (Hopp et al., 2010). A second explanation for smaller slopes seen in our work (Haacke, 2012) and other work (Shmueli et al., 2009; Wharton and Bowtell, 2010) is that Hallgren and Sourander's measurements of total iron (Hallgren and Sourander, 1958) may not be accurate. Third, susceptibility mapping is known to have a bias and leads to a smaller slope, but this bias can be potentially corrected (J. Liu et al., 2012; T. Liu et al., 2012; Schweser et al., 2012; Wharton and Bowtell, 2010). Other possible factors that have been explored include contributions of myelin (Duyn et al., 2007; Liu et al., 2011; Ogg et al., 1999), chemical exchange between water and macromolecular protons (Luo et al., 2010; Shmueli et al., 2011; Zhong et al., 2008) and microstructure orientation (He and Yablonskiy, 2009; Lee et al., 2010; Liu, 2010). Indeed, it could well be a combination of all these sources that lead to different measurements of iron in vivo and ex vivo. Despite these imperfections, the slopes for susceptibility versus iron content are generally consistent between both ex vivo studies (this paper and Langkammer et al., 2012b) and in vivo studies using similar susceptibility mapping methods (see Table 4) (Haacke, 2012; Shmueli et al., 2009; Wharton and Bowtell, 2010).

## Conclusion

Our results suggest that susceptibility changes from iron measured in ex vivo studies reasonably reflect iron content even for in vivo studies, although the predicted values may be underestimated. Our study further demonstrates that the correlation of susceptibility with iron is consistent with other results in the literature and is independent of echo time and orientation. Thus, susceptibility would appear to be a direct and reliable quantitative indication of iron, especially for brain

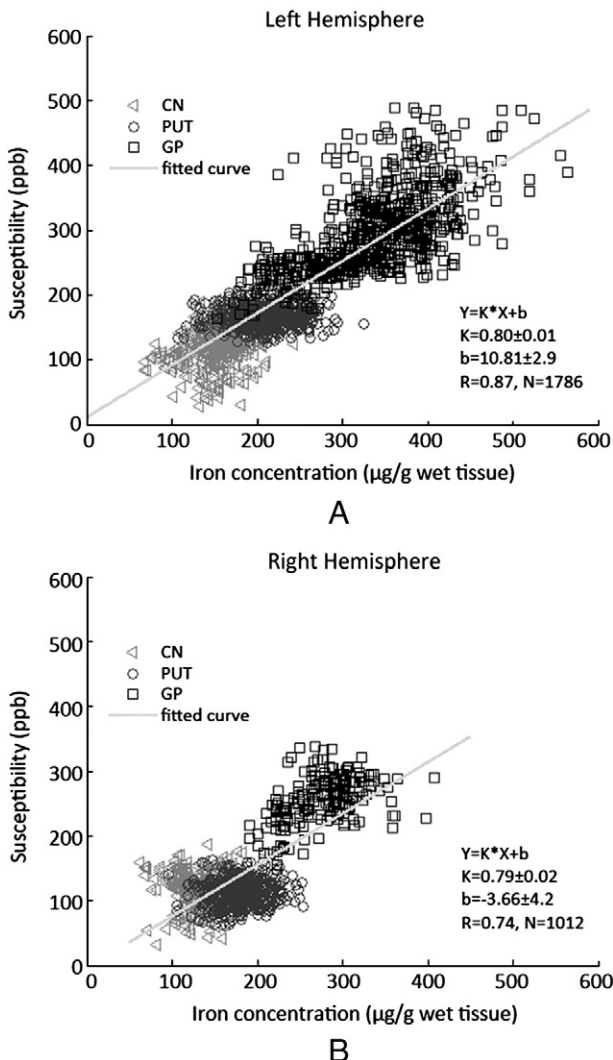


**Fig. 5.** Correlation between susceptibility and XRF iron measurements for all data points taken from each of the regions demarcated in Fig. 4. A: fitting for left hemisphere; B: fitting for right hemisphere.

**Table 4**

Correlation between susceptibility mapping and iron concentration.

Authors	Correlation slope <sup>a</sup>	Structures	Background removal	QSM method <sup>b</sup>	Myelin correction	Field (Tesla)	Sample	Iron
This paper	1.11	N.A.	Quadratic fitting	Forward fitting	N.A.	3 T	Ferritin	ICPMS
This paper	1.10	N.A.	Quadratic fitting	Forward fitting	N.A.	3 T	Ferritin	XRF
This paper	0.80	GP, PUT, CN	SHARP	TKD <sup>1</sup> (SO)	No	3 T	MS cadaveric brain (fixed)	XRF
Haacke (2012)	0.59	GP, PUT, CN	SHARP	TKD <sup>1</sup> (SO)	No	3 T	In vivo brains	H&S <sup>c</sup>
Shmueli et al. (2009)	0.56	PUT, RN, SN	Polynomial fitting	TKD <sup>2</sup> (SO)	No	7 T	In vivo brain	H&S
Wharton and Bowtell (2010)	0.75/0.6	GP, SN, RN, PUT, CN, TH, GM	Simulated geometric effect + fitting	TKD <sup>3</sup> (MO/SO)	No	7 T	In vivo brains	H&S
Langkammer et al. (2012a)	0.89	GP, PUT, CN, TH	SHARP	HEIDI (SO)	No	3 T	Unfixed cadaveric brains	ICPMS
Schweser et al. (2011)	1.30	GP, SN, DN, PUT, CN, TH, WM, GM	SHARP	MO regularization	Yes	3 T	In vivo brains	H&S

<sup>a</sup> The unit of the slope for human brain is susceptibility/ $\mu\text{g}$  iron/g wet tissue ( $\rho = 1.04\text{g/ml}$  at  $36.5^\circ\text{C}$ ); the unit of the slope for the ferritin solution is ppb susceptibility/ $\mu\text{g}$  iron/ml and the corresponding theoretical value is 1.27.

<sup>b</sup> SO: single orientation; MO: multiple orientation; TKD: thresholded k-space division. TKD<sup>1</sup>: Haacke et al., 2010; TKD<sup>2</sup>: Shmueli et al., 2009; TKD<sup>3</sup>: (Wharton and Bowtell, 2010).

<sup>c</sup> H&S: (Hallgren and Sourander, 1958).

regions with high iron content. Susceptibility mapping provides a reliable tool for clinical investigations of iron that could be used to study changes in iron over time or within a given age-matched population.

## Acknowledgments

This work is supported by the Canadian Institutes of Health Research (CIHR)/Heart and Stroke Foundation of Canada (HSFC) Synchrotron Medical Imaging Team Grant #CIF 99472.

This work was supported in part by the Telemedicine and Advanced Technology Research Center (TATRC) at the U.S. Army Medical Research and Materiel Command (USAMRMC) through award W81XWH-12-1-0522. The views, opinions and/or findings contained in this report are those of the author(s) and should not be construed as an official government position, policy or decision unless so designated by other documentation.

Portions of this research were carried out at the Stanford Synchrotron Radiation Lightsource, a Directorate of SLAC National Accelerator Laboratory and an Office of Science User Facility operated for the U.S. Department of Energy Office of Science by Stanford University. The SSRL Structural Molecular Biology Program is supported by the DOE Office of Biological and Environmental Research, and by the National Institutes of Health, National Center for Research Resources, Biomedical Technology Program (P41RR001209).

The authors would like to thank Sam Webb at the Stanford Synchrotron Radiation Lightsource and Angela Auriat at the Dept. of Neurosurgery, Stanford University for their help in collecting XRF data. We thank Zahid Latif, Yang Xuan, Yimin Shen for their assistance with the MR protocols, and Dr. Wei Feng and Dr. Jaladhar Neelavalli for their help on susceptibility mapping. The authors would also like to thank Dr. Karin Shmueli at NINDS, National Institute of Health for her valuable discussions of the literature.

## Conflict of interest

The authors have no conflicts of interest.

## References

- Bartzokis, G., Aravagiri, M., Oldendorf, W.H., Mintz, J., Marder, S.R., 1993. Field dependent transverse relaxation rate increase may be a specific measure of tissue iron stores. *Magn. Reson. Med.* 29, 459–464.
- Bartzokis, G., Tishler, T.A., Lu, P.H., Villablanca, P., Altshuler, L.L., Carter, M., Huang, D., Edwards, N., Mintz, J., 2007. Brain ferritin iron may influence age- and gender-related risks of neurodegeneration. *Neurobiol. Aging* 28, 414–423.
- Bilgic, B., Pfefferbaum, A., Rohlfing, T., Sullivan, E.V., Adalsteinsson, E., 2012. MRI estimates of brain iron concentration in normal aging using quantitative susceptibility mapping. *Neuroimage* 59, 2625–2635.
- Bouras, C., Giannopoulos, P., Good, P.F., Hsu, A., Hof, P.R., Perl, D.P., 1997. A laser microprobe mass analysis of brain aluminum and iron in dementia pugilistica: comparison with Alzheimer's disease. *Eur. Neurol.* 38, 53–58.
- Butz, T., Flagmeyer, R.-H., Heitmann, J., Jamieson, D.N., Legge, G.J.F., Lehmann, D., Reibetanz, U., Reinert, T., Saint, A., Spemann, D., Szymanski, R., Tröger, W., Vogt, J., Zhu, J., 2000. The Leipzig high-energy ion nanoprobe: a report on first results. *Nucl. Instrum. Methods Phys. Res. B* 161–163, 323–327.
- Chen, J.C., Hardy, P.A., Kucharczyk, W., Clauber, M., Joshi, J.G., Vourlas, A., Dhar, M., Henkelman, R.M., 1993. MR of human postmortem brain tissue: correlative study between T2 and assays of iron and ferritin in Parkinson and Huntington disease. *Am. J. Neuroradiol.* 14, 275–281.
- Cheng, Y.C.N., Hsieh, C.Y., Neelavalli, J., Haacke, E.M., 2009a. Quantifying effective magnetic moments of narrow cylindrical objects in MRI. *Phys. Med. Biol.* 54, 7025–7044.
- Cheng, Y.C.N., Neelavalli, J., Haacke, E.M., 2009b. Limitations of calculating field distributions and magnetic susceptibilities in MRI using a Fourier based method. *Phys. Med. Biol.* 54, 1169–1189.
- Dawe, R.J., Bennett, D.A., Schneider, J.A., Vasireddi, S.K., Arfanakis, K., 2009. Postmortem MRI of human brain hemispheres: T2 relaxation times during formaldehyde fixation. *Magn. Reson. Med.* 61, 810–818.
- de Rochefort, L., Liu, T., Kressler, B., Liu, J., Spincemaille, P., Lebon, V., Wu, J.L., Wang, Y., 2010. Quantitative susceptibility map reconstruction from MR phase data using Bayesian regularization: validation and application to brain imaging. *Magn. Reson. Med.* 63, 194–206.
- Dexter, D.T., Carayon, A., Jayov-Agid, F., Agid, Y., Wells, F.R., Daniel, S.E., Lees, A.J., Jenner, P., Marsden, C.D., 1991. Alterations in the levels of iron, ferritin and other trace metals in Parkinson's disease and other neurodegenerative diseases affecting the basal ganglia. *Brain* 114, 1953–1975.
- Duyn, J.H., van Gelderen, P., Li, T.Q., de Zwart, J.A., Koretsky, A.P., Fukunaga, M., Li, T.Q., 2007. High-field MRI of brain cortical substructure based on signal phase. *Proc. Natl. Acad. Sci. U. S. A.* 104, 11796–11801.
- Fukunaga, M., Li, T.Q., van Gelderen, P., de Zwart, J.A., Shmueli, K., Yao, B., Lee, J., Maric, D., Aronova, M.A., Zhang, G., 2010. Layer-specific variation of iron content in cerebral cortex as a source of MRI contrast. *Proc. Natl. Acad. Sci. U. S. A.* 107 (8), 3834–3839.
- Gerlach, M., Ben-Shachar, D., Riederer, P., Youdim, M.B., 1994. Altered brain metabolism of iron as a cause of neurodegenerative diseases? *J. Neurochem.* 63, 793–807.
- Haacke, E.M., 2012. Quantitative measurements of iron. Clinical Intensive Course, Advanced Neuroimaging 1.: Intl Soc Mag Reson Med, 20 (Melbourne, Australia, [http://www.ismrm.org/12/WK\\_Neuro1.htm](http://www.ismrm.org/12/WK_Neuro1.htm)).
- Haacke, E., Tkach, J., Parrish, T., 1989. Reducing T<sup>2</sup> dephasing in gradient field-echo imaging. *Radiology* 170, 457–462.
- Haacke, E.M., Cheng, N.Y., House, M.J., Liu, Q., Neelavalli, J., Ogg, R.J., Khan, A., Ayaz, M., Kirsch, W., Obenauer, A., 2005. Imaging iron stores in the brain using magnetic resonance imaging. *Magn. Reson. Imaging* 23, 1–25.
- Haacke, E.M., Ayaz, M., Khan, A., Manova, E.S., Krishnamurthy, B., Gollapalli, L., Ciulla, C., Kim, I., Petersen, F., Kirsch, W., 2007. Establishing a baseline phase behavior in magnetic resonance imaging to determine normal vs. abnormal iron content in the brain. *J. Magn. Reson. Imaging* 26, 256–264.
- Haacke, E.M., Makki, M., Ge, Y., Maheshwari, M., Sehgal, V., Hu, J., Selvan, M., Wu, Z., Latif, Z., Xuan, Y., Khan, O., Garber, J., Grossman, R.I., 2009. Characterizing iron deposition in multiple sclerosis lesions using susceptibility weighted imaging. *J. Magn. Reson. Imaging* 29, 537–544.
- Haacke, E.M., Tang, J., Neelavalli, J., Cheng, Y.C.N., 2010. Susceptibility mapping as a means to visualize veins and quantify oxygen saturation. *J. Magn. Reson. Imaging* 32, 663–676.
- Hallgren, B., Sourander, P., 1958. The effect of age on the non-haemin iron in the human brain. *J. Neurochem.* 3, 41–51.
- Hallgren, B., Sourander, P., 1960. The non-haemin iron in the cerebral cortex in Alzheimer's disease. *J. Neurochem.* 5, 307–310.
- He, X., Yablonskiy, D.A., 2009. Biophysical mechanisms of phase contrast in gradient echo MRI. *Proc. Natl. Acad. Sci. U. S. A.* 106, 13558–13563.

- Hopp, K., Gh Popescu, B.F., McCrea, R.P.E., Harder, S.L., Robinson, C.A., Haacke, E.M., Rajput, A.H., Rajput, A., Nichol, H., 2010. Brain iron detected by SWI high pass filtered phase calibrated with synchrotron X-ray fluorescence. *J. Magn. Reson. Imaging* 31, 1346–1354.
- House, M.J., Pierre, T.G.S., Kowdley, K.V., Montine, T., Connor, J., Beard, J., Berger, J., Siddaiah, N., Shankland, E., Jin, L.W., 2007. Correlation of proton transverse relaxation rates ( $R_2$ ) with iron concentrations in postmortem brain tissue from Alzheimer's disease patients. *Magn. Reson. Med.* 57, 172–180.
- Jenkinson, M., 2003. A fast, automated, n-dimensional phase unwrapping algorithm. *Magn. Reson. Med.* 49, 193–197.
- Jensen, J.H., Tang, H., Tosti, C.L., Swaminathan, S.V., Nunez, A., Hultman, K., Szulc, K.U., Wu, E.X., Kim, D., Sheth, S., Brown, T.R., Brittenham, G.M., 2010. Separate MRI quantification of dispersed (ferritin-like) and aggregated ( hemosiderin-like) storage iron. *Magn. Reson. Med.* 63, 1201–1209.
- Ke, Y., Qian, Z.M., 2003. Iron misregulation in the brain: a primary cause of neurodegenerative disorders. *Lancet Neurol.* 2, 246–253.
- Kressler, B., de Rochefort, L., Liu, T., Spincemaille, P., Jiang, Q., Wang, Y., 2010. Nonlinear regularization for per voxel estimation of magnetic susceptibility distributions from MRI field maps. *IEEE Trans. Med. Imaging* 29, 273–281.
- Langkammer, C., Krebs, N., Goessler, W., Scheurer, E., Ebner, F., Yen, K., Fazekas, F., Ropele, S., 2010. Quantitative MR imaging of brain iron: a postmortem validation study. *Radiology* 257, 455–462.
- Langkammer, C., Krebs, N., Goessler, W., Scheurer, E., Yen, K., Fazekas, F., Ropele, S., 2012a. Susceptibility induced gray-white matter MRI contrast in the human brain. *Neuroimage* 59, 1413–1419.
- Langkammer, C., Schweser, F., Krebs, N., Deistung, A., Goessler, W., Scheurer, E., Sommer, K., Reishofer, G., Yen, K., Fazekas, F., Ropele, S., Reichenbach, J.R., 2012b. Quantitative susceptibility mapping (QSM) as a means to measure brain iron? A post mortem validation study. *Neuroimage* 62, 1593–1599.
- Lee, J., Shmueli, K., Fukunaga, M., van Gelderen, P., Merkle, H., Silva, A.C., Duyn, J.H., 2010. Sensitivity of MRI resonance frequency to the orientation of brain tissue microstructure. *Proc. Natl. Acad. Sci. U. S. A.* 107, 5130–5135.
- Lee, J., Shmueli, K., Kang, B.-T., Yao, B., Fukunaga, M., Gelderen, P.v., Palumbo, S., Bosetti, F., Silva, A.C., Duyn, J.H., 2012. The contribution of myelin to magnetic susceptibility-weighted contrasts in high-field MRI of the brain. *Neuroimage* 59, 3967–3975.
- LeVine, S.M., 1997. Iron deposits in multiple sclerosis and Alzheimer's disease brains. *Brain Res.* 760, 298–303.
- Li, W., Wu, B., Liu, C., 2011. Quantitative susceptibility mapping of human brain reflects spatial variation in tissue composition. *Neuroimage* 55, 1645–1656.
- Liu, C., 2010. Susceptibility tensor imaging. *Magn. Reson. Med.* 63, 1471–1477.
- Liu, T., Spincemaille, P., de Rochefort, L., Kressler, B., Wang, Y., 2009. Calculation of susceptibility through multiple orientation sampling (COSMOS): a method for conditioning the inverse problem from measured magnetic field map to susceptibility source image in MRI. *Magn. Reson. Med.* 61, 196–204.
- Liu, C., Li, W., Johnson, G.A., Wu, B., 2011. High-field (9.4 T) MRI of brain dysmyelination by quantitative mapping of magnetic susceptibility. *Neuroimage* 56, 930–938.
- Liu, T., Xu, W., Spincemaille, P., Avestimehr, A.S., Wang, Y., 2012a. Accuracy of the morphology enabled dipole inversion (MEDI) algorithm for quantitative susceptibility mapping in MRI. *IEEE Trans. Med. Imaging* 31, 816–824.
- Liu, J., Liu, T., Rochefort, Ld, Ledoux, J., Khalidov, I., Chen, W., Tsouris, A.J., Wisniew, C., Spincemaille, P., Prince, M.R., Wang, Y., 2012b. Morphology enabled dipole inversion for quantitative susceptibility mapping using structural consistency between the magnitude image and the susceptibility map. *Neuroimage* 59, 2560–2568.
- Luo, J., He, X., d'Avignon, D.A., Ackerman, J.J.H., Yablonskiy, D.A., 2010. Protein induced water  $^1\text{H}$  MR frequency shifts: contributions from magnetic susceptibility and exchange effects. *J. Magn. Reson.* 202, 102–108.
- Marques, J.P., Bowtell, R., 2005. Application of Fourier-based method for rapid calculation of field inhomogeneity due to spatial variation of magnetic susceptibility. *Concepts Magn. Reson. B Magn. Reson. Eng.* 25, 65–78.
- Mitsumori, F., Watanabe, H., Takay, N., Garwood, M., Auerbac, E.J., Michaeli, S., Mangia, S., 2012. Toward understanding transverse relaxation in human brain through its field dependence. *Magn. Reson. Med.* 68, 947–953.
- Neelavalli, J., Cheng, Y.-C.N., Jiang, J., Haacke, E.M., 2009. Removing background phase variations in susceptibility weighted imaging using a fast, forward-field calculation. *J. Magn. Reson. Imaging* 29, 937–948.
- Ogg, R.J., Langston, J.W., Haacke, E.M., Steen, R.G., Taylor, J.S., 1999. The correlation between phase shifts in gradient-echo MR images and regional brain iron concentration. *Magn. Reson. Imaging* 17, 1141–1148.
- Ordidge, R., Gorell, J., Deniau, J., Knight, R., Helpern, J., 1994. Assessment of relative brain iron concentrations using  $T_2$ -weighted and  $T_2^*$ -weighted MRI at 3 Tesla. *Magn. Reson. Med.* 32, 335–341.
- Peters, A.M., Brookes, M.J., Hoogenraad, F.G., Gowland, P.A., Francis, S.T., Morris, P.G., Bowtell, R., 2007.  $T_2^*$  measurements in human brain at 1.5, 3 and 7 T. *Magn. Reson. Imaging* 25, 748–753.
- Pfefferbaum, A., Sullivan, E.V., Adalsteinsson, E., Garrick, T., Harper, C., 2004. Postmortem MR imaging of formalin-fixed human brain. *Neuroimage* 21, 1585–1595.
- Reichenbach, J., Venkatesan, R., Yablonskiy, D., Thompson, M., Lai, S., Haacke, E., 1997. Theory and application of static field inhomogeneity effects in gradient-echo imaging. *Magn. Reson. Imaging* 7, 266–279.
- Schenck, J.F., 1992. Health and physiological effects of human exposure to whole-body four-Tesla magnetic fields during MRI. *Ann. N. Y. Acad. Sci.* 649, 285–301.
- Schenck, J.F., Zimmerman, E.A., 2004. High-field magnetic resonance imaging of brain iron: birth of a biomarker? *NMR Biomed.* 17, 433–445.
- Schmieler, K., Wheeler-Kingshott, C.A.M., Tozer, D.J., Boulby, P.A., Parkes, H.G., Yousry, T.A., Scaravilli, F., Barker, G.J., Tofts, P.S., Miller, D.H., 2008. Quantitative magnetic resonance of postmortem multiple sclerosis brain before and after fixation. *Magn. Reson. Med.* 59, 268–277.
- Schweser, F., Deistung, A., Lehr, B.W., Reichenbach, J.R., 2011. Quantitative imaging of intrinsic magnetic tissue properties using MRI signal phase: an approach to in vivo brain iron metabolism? *Neuroimage* 54, 2789–2807.
- Schweser, F., Sommer, K., Deistung, A., Reichenbach, J.R., 2012. Quantitative susceptibility mapping for investigating subtle susceptibility variations in the human brain. *Neuroimage* 62, 2083–2100.
- Shmueli, K., de Zwart, J.A., van Gelderen, P., Li, T.Q., Dodd, S.J., Duyn, J.H., 2009. Magnetic susceptibility mapping of brain tissue in vivo using MRI phase data. *Magn. Reson. Med.* 62, 1510–1522.
- Shmueli, K., Dodd, S.J., Li, T.Q., Duyn, J.H., 2011. The contribution of chemical exchange to MRI frequency shifts in brain tissue. *Magn. Reson. Med.* 65, 35–43.
- Wallis, I.W., Paley, M.N.J., Graham, J.M., Grunewald, R.A., Wignall, E.L., Joy, H.M., Griffiths, P.D., 2008. MRI assessment of basal ganglia iron deposition in Parkinson's disease. *J. Magn. Reson. Imaging* 28, 1061–1067.
- Web, S.M., 2010. AIP Conf. Proc. 1365, 196–199. <http://dx.doi.org/10.1063/1.3625338>.
- Wharton, S., Bowtell, R., 2010. Whole-brain susceptibility mapping at high field: a comparison of multiple- and single-orientation methods. *Neuroimage* 53, 515–525.
- Yao, B., Li, T.Q., Gelderen, P.V., Shmueli, K., de Zwart, J.A., Duyn, J.H., 2009. Susceptibility contrast in high field MRI of human brain as a function of tissue iron content. *Neuroimage* 44, 1259–1266.
- Zheng, W., Haacke, E.M., Webb, S., Nichol, H., 2012. Imaging of stroke: a comparison between X-ray fluorescence and magnetic resonance imaging methods. *Magn. Reson. Imaging* 30, 1416–1423.
- Zhong, K., Leupold, J., von Elverfeldt, D., Speck, O., 2008. The molecular basis for gray and white matter contrast in phase imaging. *Neuroimage* 40, 1561–1566.

## Original Research

# Noncontrast-Enhanced Magnetic Resonance Angiography and Venography Imaging With Enhanced Angiography

Yongquan Ye, PhD,<sup>1\*</sup> Jiani Hu, PhD,<sup>1</sup> Dongmei Wu, MS,<sup>2</sup> and E. Mark Haacke, PhD<sup>1,3</sup>

**Purpose:** To achieve simultaneous high-resolution magnetic resonance angiography and venography (MRAV) imaging in terms of enhanced time-of-flight (TOF) angiography and susceptibility-weighted imaging (SWI), with a clear separation of arteries and veins.

**Materials and Methods:** A new flow rephase/dephase interleaved double-echo sequence was introduced that facilitates multiple types of imaging contrast, i.e., TOF, SWI, and dark blood, in a single acquisition. A nonlinear subtraction (NLS) method is proposed and assessed to maximally enhance angiography contrast with minimum venous contamination.

**Results:** Fully flow rephased TOF MRA and SWI MRV data were acquired simultaneously, along with an extra flow dephased dark blood image for angiography enhancement calculation. Compared to linear subtraction methods, the proposed NLS method was able to enhance angiography contrast while effectively eliminating vein-tissue contrast. The NLS method even outperformed low-dose contrast-enhanced MRA for a clean, enhanced angiography map.

**Conclusion:** Using the proposed interleaved double-echo sequence along with the NLS postprocessing method, one can simultaneously obtain both high-quality SWI and significantly enhanced TOF MRA with clear separation of arterial and venous maps.

**Key Words:** TOF MRA; SWI; MRAV; nonlinear processing

**J. Magn. Reson. Imaging** 2013;38:1539–1548

© 2013 Wiley Periodicals, Inc.

UNDERSTANDING THE CEREBRAL vascular system morphologically and functionally is very important for both neuroscientific studies and clinical applications. Numerous clinical problems such as arteriovenous malformation (AVM) (1), tumor evaluation (2–3), and traumatic brain injury (TBI) (4,5) require detailed vascular information for best diagnostic interpretation. Due to the vast differences in hemodynamic characteristics, pathological behavior, and the underlying magnetic resonance imaging (MRI) principles of vessel-tissue contrast, arteries and veins are usually imaged with separate protocols, leading to increased scanning time and motion-related misregistrations. Recently, there has been a focus on single-scan magnetic resonance angiography and venography (MRAV) imaging (6–9) in order to obtain a more complete perspective of the vasculature. Collecting MRA and MRV in a single acquisition gets rid of any potential registration problems and enables a precise review and a complete picture of the relationship between the two vasculature networks.

However, further applications of these MRAV methods are hindered by two major, yet conflicting, objectives: enhancing vessel-tissue contrast and distinguishing arteries and veins. In MRA, bright-blood (BB) strategies such as time-of-flight (TOF) and contrast-enhanced MRA (CE MRA) are used to obtain high blood signal while reducing tissue signal as much as possible. MRV, on the other hand, can be most reliably done with dark-blood (DB) methods such as susceptibility-weighted imaging (SWI) (10–12) to selectively suppress venous signal while maintaining high tissue signal for better vein-tissue contrast or arterial saturation. Since the tissue signal is unwanted in MRA scan but is required for optimal venous contrast in SWI, obtaining both simultaneously is a challenge, regardless of whether using single-echo (7), double-echo (6), or multiecho (9) strategies. Gadolinium (Gd)-based contrast agents can be used as either a BB or DB (13) method that can enhance both arteries and veins at the same time due to the global vascular T<sub>1</sub> or T<sub>2</sub> shortening effects; thus, its use will make it more difficult to separate arteries and veins in CE MRA.

Currently the gold standard of angiography is intra-arterial digital subtraction angiography (IADSA) (14,15). The basic principle is to create two different levels of blood signal while keeping tissue signal the same by

<sup>1</sup>Department of Radiology, Wayne State University, Detroit, Michigan, USA.

<sup>2</sup>Shanghai Key Laboratory of Magnetic Resonance, East China Normal University, Shanghai, China.

<sup>3</sup>Department of Biomedical Engineering, Wayne State University, Detroit, Michigan, USA.

Contract grant sponsor: Department of Defense; Contract grant number: DOD W81XWH-11-1-0493; Contract grant sponsor: Wayne State University; Contract grant number: WSU OVPR 177310.

\*Address reprint requests to: Y.Y., MR Research Facility, Department of Radiology, Wayne State University, DRH 5E-13, 3990 John R Road, Detroit, MI 48201. E-mail: mqyeah@gmail.com

Received April 20, 2012; Accepted February 20, 2013.

DOI 10.1002/jmri.24128

View this article online at [wileyonlinelibrary.com](http://wileyonlinelibrary.com).

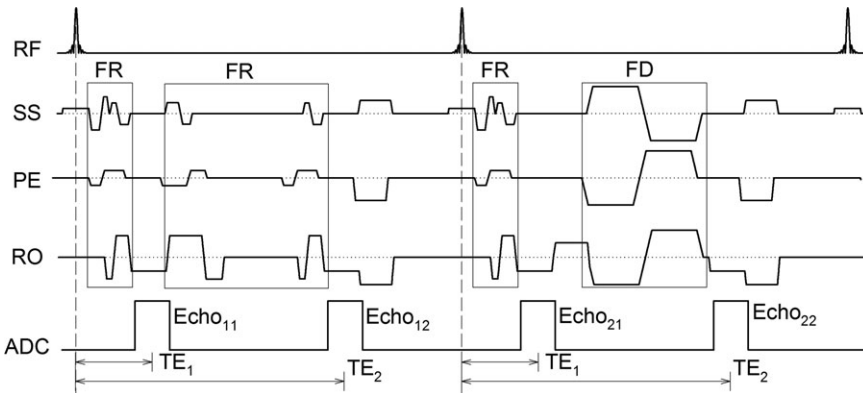


**Figure 1.** Diagram of the FR/FD interleaved double-echo sequence. Echo<sub>11</sub>, Echo<sub>12</sub>, and Echo<sub>21</sub> are flow rephased (FR) using first-order moment nulling gradients dynamically calculated with the phase encoding gradients and TEs taken into account, and Echo<sub>12</sub> is flow dephased (FD) by bipolar gradients with a low VENC value.

administering an iodinated contrast agent into the intravascular space, and generate a pure vessel map simply using subtraction. Similar attempts have been made to enhance MRA contrast by using a rephase/dephase strategy to create high/low blood signals while maintaining the tissue signal (16–20). In the recent work by Kimura et al (16), a double-echo sequence collecting flow rephased/dephased images, called hybrid of opposite contrast MRA (HOP-MRA), was developed and a linearly weighted subtraction was proposed to increase the vessel-background contrast by minimizing the subtracted tissue signals. Although capable of enhancing arteries, the major issue of linear subtraction, weighted or not, is that it will introduce heavy venous contamination such that veins also appear bright in the subtracted images. As a result, it is difficult to distinguish between arteries and veins, especially for smaller vessels. The venous contamination can be possibly reduced if both flow rephased and dephased images are acquired with long (preferably equal) TEs, so that veins are already suppressed because of T<sub>2</sub><sup>\*</sup> decay. With equal TE, the rephase/dephase subtraction can reduce the tissue signal-to-noise level, and can better reveal the arteries after processing such as maximum intensity projection (MIP) or vessel tracking. However, flow compensation at long TE will be less efficient, especially for fast flows, leading to artifacts and signal non-uniformity in large arteries such as carotid arteries (21).

To tackle this challenge, we propose using a flow rephase/dephase interleaved double-echo gradient recalled echo (GRE) sequence capable of MRAV imaging and at the same time acquiring both flow rephased and dephased images. A nonlinear subtraction processing method is then proposed for selective MRA enhancement utilizing the flow rephased and dephased images. The performance of both nonlinear and linear subtraction methods will be analyzed and compared for the artery-tissue contrast theoretically and experimentally.

## MATERIALS AND METHODS

### Sequence Design

In order to acquire MRAV data as well as flow dephased data for MRA enhancement (16), we developed a flow rephase/dephase interleaved dual-echo GRE sequence as shown in Fig. 1. In the first TR,

both echoes were fully flow rephased (FR, or flow compensated) on all three axes, while in the second TR the second echo was flow dephased (FD) by a series of bipolar gradient pairs.

Unlike Du and Jin's (6) method in which flow rephasing for the second echo was achieved with a fly-back gradient in the readout direction, we implemented an active scheme for flow rephasing to the second echo on all three axes by dynamically calculating the gradients for first-order moment nulling on each axis, taking into account TE as well as phase encoding or readout gradients (22). In this way, one can independently set the two echoes for their TE, bandwidth, and asymmetry without affecting the flow rephasing performance. Flow dephasing for the second echo was done by using bipolar gradients of very low velocity encoding (VENC) value.

With this sequence, four images will be generated with a single scan: two FR images with a short TE<sub>1</sub> for normal TOF-MRA (Echo<sub>11</sub> and Echo<sub>21</sub>), one FR image with a long TE<sub>2</sub> for SWI (Echo<sub>12</sub>), and one FD image (Echo<sub>22</sub>) also with TE<sub>2</sub>. Since excellent SWI results can be reliably generated from the Echo<sub>12</sub> data (6,10), the following analysis will focus on enhancing MRA contrast and separating venous and arterial signal by assessing and comparing nonlinear subtraction and linear subtraction methods.

### Linear Subtraction (LS) vs. Nonlinear Subtraction (NLS)

Since the contrast characteristics of linear subtraction have been extensively discussed in previous studies, interested readers are referred to Kimura et al's article for details (16). Here, we will further assess the effect of different weighting factors in the subtraction and their effects on vessel-tissue contrast.

Denoting the signal intensity under two different imaging conditions (eg, FR and FD) as S and S', and assuming the same noise standard deviation (SD)  $\sigma$  for both signal levels, one can calculate the signal-to-noise ratio (SNR) of the LS image as:

$$\text{SNR}_{\text{ls}} = \frac{\Delta S_{\text{ls}}}{\sigma\sqrt{1+\alpha^2}} = \frac{S - \alpha S'}{\sigma\sqrt{1+\alpha^2}} = \frac{S(1-\alpha\beta)}{\sigma\sqrt{1+\alpha^2}} \quad [1]$$

where  $\alpha$  is the weighting factor for the subtraction, and  $\beta = S'/S$  is defined as the ratio between the two

**Table 1**  
Estimated Signal Ranges of Arteries, Veins, and Tissue in FR and FD Images

	Artery	Vein	Tissue
S (FR)	High	Medium	Medium
S' (FD)	Low	Low	Medium but S' < S

signal levels. The CNR between artery and tissue, i.e.,  $CNR_{at,ls}$ , can be written as:

$$CNR_{at,ls} = \frac{(S_a - S'_a) - \alpha(S_t - S'_t)}{\sigma\sqrt{1 + \alpha^2}} \quad [2]$$

The subscripts "a" and "t" denote artery and tissue, respectively. The vein-tissue  $CNR_{vt,ls}$  can be written in the same form. On the other hand, if the signal is nonlinearly weighted in a self-weighted manner (i.e., squared on a voxelwise basis) prior to subtraction so that  $\Delta S_{nls} = S^2 - \alpha S'^2$ , the noise after NLS can be approximated by:

$$\sigma_{nls} = 2\sqrt{(S^2 + \alpha^2 S'^2)\sigma} \quad [3]$$

and  $SNR_{nls}$  can be written as:

$$SNR_{nls} = \frac{S^2 - \alpha S'^2}{\sigma_{nls}} = \frac{S(1 - \alpha\beta^2)}{2\sigma\sqrt{1 + \alpha^2\beta^2}} \quad [4]$$

Comparing with Eq. [1], the  $\beta$  factor now appearing in the denominator in Eq. [4] is the major difference between LS and NLS. The value of  $\beta$  depends on the type of tissue, i.e., whether they are arteries, veins, or parenchymal tissues, and it varies according to their respective rephase/dephase signals and partial volume effects.

The expression for  $CNR_{nls}$  between vessels and tissues is much more complicated than the LS version shown in Eq. [2]. From a qualitative point of view,  $S'_a$  and  $S'_v$  will be very low or even nulled as a combined result of low VENC gradients along with high flow velocity (for arteries) or  $T_2^*$  decay (for veins), while  $S_a$  will be higher than  $S_v$  thanks to greater TOF inflow. For static parenchymal tissues, on the other hand, the dephasing gradients will not significantly change the signal as its equivalent diffusion weighting effects are negligible (see next session). However, since in our sequence  $S'$  is collected with longer TE so that it will decay (relative to  $S$  collected at short TE) by  $\sim 20\%$  with a typical  $\Delta TE$  of 15 msec and a tissue  $T_2^*$  of 80 msec at 3T, so that  $\beta < 1$  remains true for tissues. The summary of the above analysis is listed in Table 1. Generally speaking,  $\beta$  will be of low value for both arteries and veins (especially for arteries due to the high  $S_a$ ), but is expected to be around 0.8 for tissues mainly due to  $T_2^*$  decay.

To confirm this, we performed Monte Carlo simulations according to Eqs. [1–4] to evaluate the signal change  $\Delta S_{ls}$  and  $\Delta S_{nls}$ , noise SD, and SNR for all  $S > S'$  (i.e.,  $\beta < 1$ ) combinations.  $S$  and  $S'$  ranged from 1 to 300 and were added with Gaussian noise ( $\sigma = 10$ ), yielding a maximum SNR of about 30 in the original

signals. Also, simulation on the effect of weighting factor  $\alpha$  to  $\Delta S_{ls}$  and  $\Delta S_{nls}$  are also performed to estimate and predict its optimal value.

### Data Acquisition and Processing

Six healthy volunteers (two males and four females, age  $27 \pm 4$  years) were recruited for the study and written consents approved by the local Institutional Review Board were obtained from each volunteer prior to the scans. All scans were performed on a Siemens 3T Verio system (Siemens Healthcare, Erlangen, Germany) with a product 32-channel head coil. The scanning parameters of the FR/FD interleaved double-echo GRE sequence were:  $TE_1/TE_2/TR = 6.2/22/28$  msec, flip angle (FA) =  $15^\circ$ , bandwidth = 260 Hz/pixel, voxel size =  $0.5 \times 0.5 \times 1.0$  mm $^3$ , slice number = 48, and total scan time was 6 minutes 40 seconds. The bipolar gradients for flow dephasing were 4 msec in duration and 24 mT/m in amplitude, leading to a VENC value of about 1.46 cm/s. As a side note, previous literature on similar studies used the b value (16) rather than the VENC value for describing the dephasing effects. However, the b values are actually too small to introduce significant difference observed in the vessels (eg,  $b = 2$  s/mm $^2$  reported previously (16) and  $b = 1.8$  s/mm $^2$  in our case), thus the blood signal loss in the FD image is primarily due to flow dephasing effects. One of the subjects also additionally underwent low-dose contrast-enhanced MRA scans with an injection of 5 cc Magnevist (gadopentate dimeglumine), and single echo flow rephased GRE sequence was scanned using a matching protocol (with  $TE/TR = 6.2/28$  msec and FA =  $15^\circ$ ) to collect CE TOF MRA images as comparison to the subtraction results. GRAPPA with an acceleration factor of 2 was used for all scans.

SWI results were calculated from the flow rephased Echo<sub>12</sub> data, using a highpass filter of  $64 \times 64$  on the phase image and a four-time phase mask multiplication (i.e.,  $m = 4$ ) (10). mIP images over a 12-mm slab were created to better visualize the veins as continuous structures.

For both LS and NLS calculations, the two identical short TE FR images (i.e., Echo<sub>11</sub> and Echo<sub>21</sub>) were averaged to improve SNR especially for arteries, and the averaged image was used as  $S$ . Taking the FD image as  $S'$ , LS and NLS results were then calculated with  $\alpha = 0.75, 1.00$ , and  $1.25$ , respectively. MIP images over a 12-mm slab were also created for all final results to display the arteries. The skull signal was removed for better visualization using SPIN (Signal Processing In NMR, Detroit, Michigan), and a brain-only binary mask was obtained and applied to all processed data described above (but prior to intensity projections) to remove the skull.

The artery-tissue CNR of different artery sizes was also determined to evaluate the artery enhancing performance on various vessel sizes. The contrast was determined by subtracting the mean signal intensity of the surrounding tissue from the signal maxima of the artery segment, and noise was taken as the SD of the tissue signal. The artery diameter was estimated as the

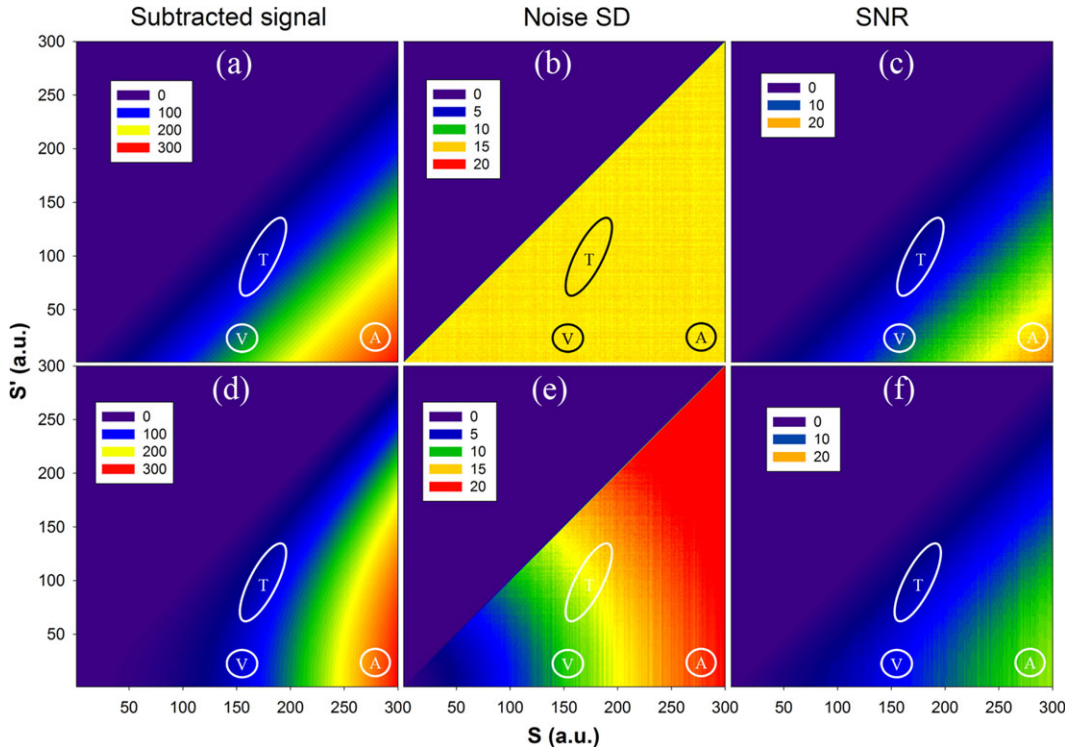


**Figure 2.** Simulation results of the subtraction signal ( $\Delta S_{ls}$  in **(a)** and  $\Delta S_{nls}$  in **(d)**), noise SD **(b,e)**, and the resulting SNR **(c,f)** of LS **(a–c)** and NLS **(d–f)**. The simulation was performed for all  $S > S'$  (i.e.,  $\beta < 1$ ) combinations, and  $\alpha = 1$  and  $\sigma = 10$  was used for calculations here. Higher temperature color corresponds to higher subtraction signal **(a,d)**, or higher noise SD **(b,e)**, or higher SNR of the subtracted image **(c,f)**. The three ROIs indicate the estimated regions for arteries ("A"), veins ("V") and tissues ("T") signals. The color scales of NLS were scaled to match the range of LS for the columns of subtracted signal and noise SD.

half-width-maximum-height of its profile and was sorted into several groups: less than 1 mm, 1–1.5 mm, 1.5–2 mm, and 2–2.5 mm. For each group, five vessels were selected and the mean and SD of CNR were evaluated.

## RESULTS

The simulation comparing LS and NLS are shown in Fig. 2, where the estimated signal regions for arteries, veins, and tissues are indicated according to Table 1. The simulation confirmed that the introduction of factor  $\beta$  into the denominator in Eq. [4] modifies the nonlinear subtraction outcomes between rephased and dephased signals. Specifically, the gradient of  $\Delta S_{nls}$  is shifted towards high  $S'$  when  $S'$  values are low, but the shift is much less significant for medium to high  $S'$  values (Fig. 2d). For LS,  $\Delta S_{ls}$  of the veins is higher than that of the tissues, thus showing a positive vein-tissue contrast (Fig. 2a). However, venous  $\Delta S_{nls}$  is located at the same gradient level with the tissues, effectively reducing or even eliminating the vein-tissue contrast. Meanwhile, both  $\Delta S_{ls}$  and  $\Delta S_{nls}$  of the arteries remain very high (hot colors), maintaining a high contrast to the tissues (Fig. 2d). In light of the above results, it is predicted that both veins and arteries will be shown in the LS approach, while predominantly only arteries will be visible in the NLS approach.

The weighting factor  $\alpha$  was introduced in order to best null the subtracted tissue signal (16). The effect

of  $\alpha$  is to "tilt" the gradient of  $\Delta S_{ls}$  or  $\Delta S_{nls}$ , as demonstrated in Fig. 3, where simulations using  $\alpha = 0.5$ , 1.0, and 1.5 were compared. When a higher  $\alpha$  value is used,  $\Delta S_{ls}$  will reduce more at high  $S'$  values. For practical considerations, since  $S'$  of tissues is higher than both arteries and veins in the dephased images, one can expect to see a more decreased tissue signal in the LS images with higher  $\alpha$  value. This is consistent with the suggested optimal value of 1.5 for  $\alpha$  (16). However, the difference in  $\Delta S_{ls}$  between veins and arteries will also become greater with high  $\alpha$  value due to the reduced tissue signal (Fig. 3a–c), suggesting an even increased vein-tissue contrast in the LS results. For the nonlinear approach,  $\Delta S_{nls}$  of both veins and tissues only vary slightly between  $\alpha$  values, and the vein-tissue contrast in the NLS results is minimal and insensitive to the weighting factor (Fig. 3e,f).

The single slice images of the unprocessed FR and FD data along with the LS/NLS processed data of one representative subject are shown in Fig. 4, while the corresponding MIP or mIP results are shown in Fig. 5. These images show several representative arteries and veins that can be used as a demonstration of our approach. The profiles of a pair of neighboring artery and vein, normalized by the respective maximum signal, were extracted as indicated by the thin black line in Fig. 4a and shown in Fig. 6, and the vessel-tissue contrast and CNR value of these vessels are shown in Table 2. The contrast was calculated as the signal difference between vessel center and surrounding

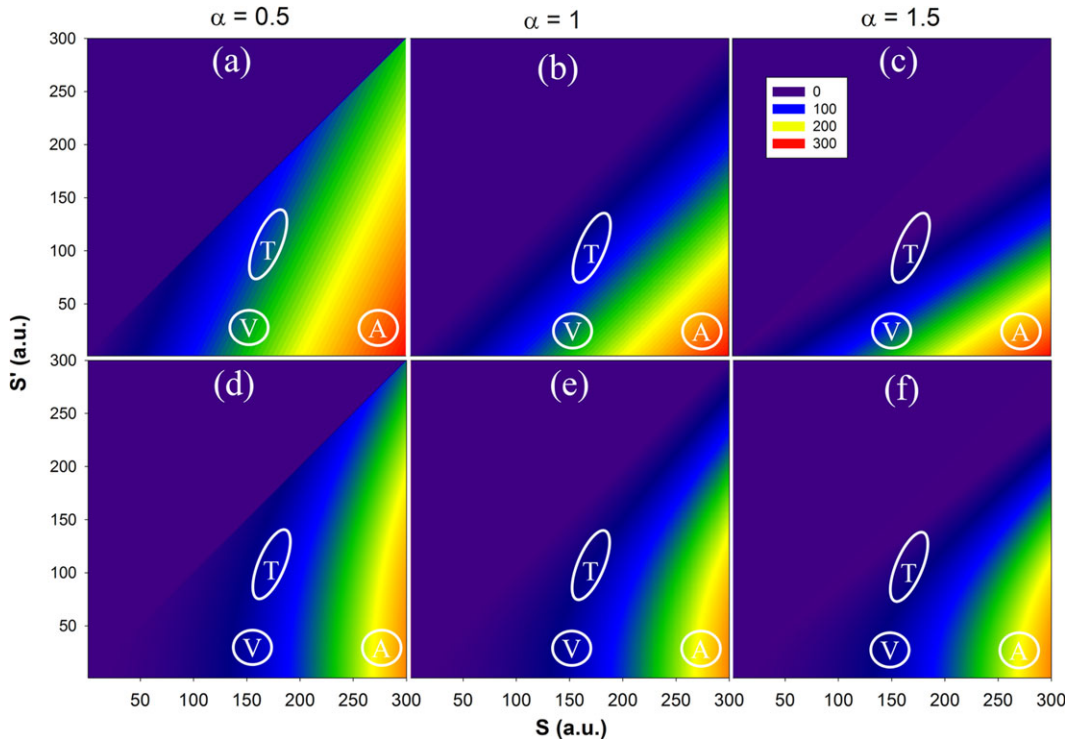


**Figure 3.** Simulation results of the subtraction signal  $\Delta S_{ls}$  (a–c) and  $\Delta S_{nls}$  (d–f), with  $\alpha = 0.5$  (a,d), 1 (b,e), and 1.5 (c,f), respectively. The color gradients of NLS were scaled to match the range of LS.

tissues divided by the tissue signal mean, and the CNR was calculated as the signal difference between vessel center and surrounding tissues divided by the standard deviation of tissue signal. The  $\beta$  value was about 0.07 and 0.27 for the artery and the vein (calculated at the vessel profile center), respectively, and was about 0.79 for the surrounding tissues, which is in agreement with the above theoretical analysis. The comparison between LS, NLS, and low-dose CE TOF MRA are similarly shown in Fig. 7, and the artery-tissue CNR of different artery sizes are shown in Fig. 8.

## DISCUSSION

In this study we proposed an MRAV imaging method with selective MRA enhancement. Specifically, we designed an FR/FD interleaved double-echo GRE sequence which, for the first time, offers the capacity of obtaining both fully flow rephased SWI data for venography and TOF MRA with selectively enhanced angiography and minimal venous contamination. Specifically, a dynamic full flow compensation scheme and a nonlinear subtraction method were proposed to achieve the above objectives.

For noncontrast-enhanced MRA, the 3D TOF method is most widely used for clinical exams for its potential to image small, tortuous arteries noninvasively. TOF MRA creates a positive artery-tissue contrast as a result of the in-flowing arterial blood being much less saturated than the static tissues. However, the in-flowing blood will gradually become saturated as it passes through the imaging slab, losing the

contrast especially for smaller vessels with slow flow. There are several means to increase the contrast for small arteries, including using magnetization transfer contrast (MTC) radiofrequency (RF) pulse to suppress tissue signal (23,24), multiple thinner slabs to reduce saturation effect (25), TONE pulse for spatially varying flip angle excitation (26), or acquiring an additional flow dephased image and then subtract it from the flow rephased image (16–20). The subtraction method is of particular interest as it can greatly reduce or even null the background tissue signal while retaining high vessel signal. Furthermore, a common dilemma for existing MRAV methods is the conflicting requirement on tissue signal, that TOF MRA requires low tissue signal while SWI-based MRV requires high tissue signal. This now can be perfectly addressed with our interleaved double-echo MRAV sequence, as one can have sufficient tissue signal for SWI using a proper flip angle and have reduced tissue signal for MRA after subtraction.

The major drawback of the LS method is that as the venous blood is also suppressed by the dephasing gradients, vein-tissue contrast will become positive and confounds the interpretation of the MRA results. Previous studies mainly focused on maximizing the artery-tissue contrast, but failed to address such venous contamination issue (16,17). Compared to LS methods, the proposed NLS method is proven to be able to enhance the artery-tissue contrast while suppressing the venous-tissue contrast (Figs. 4–7). Self-weighted NLS reduces the vein-tissue contrast by additionally taking into account the signal intensity of both rephased and dephased states, i.e., tissues have low

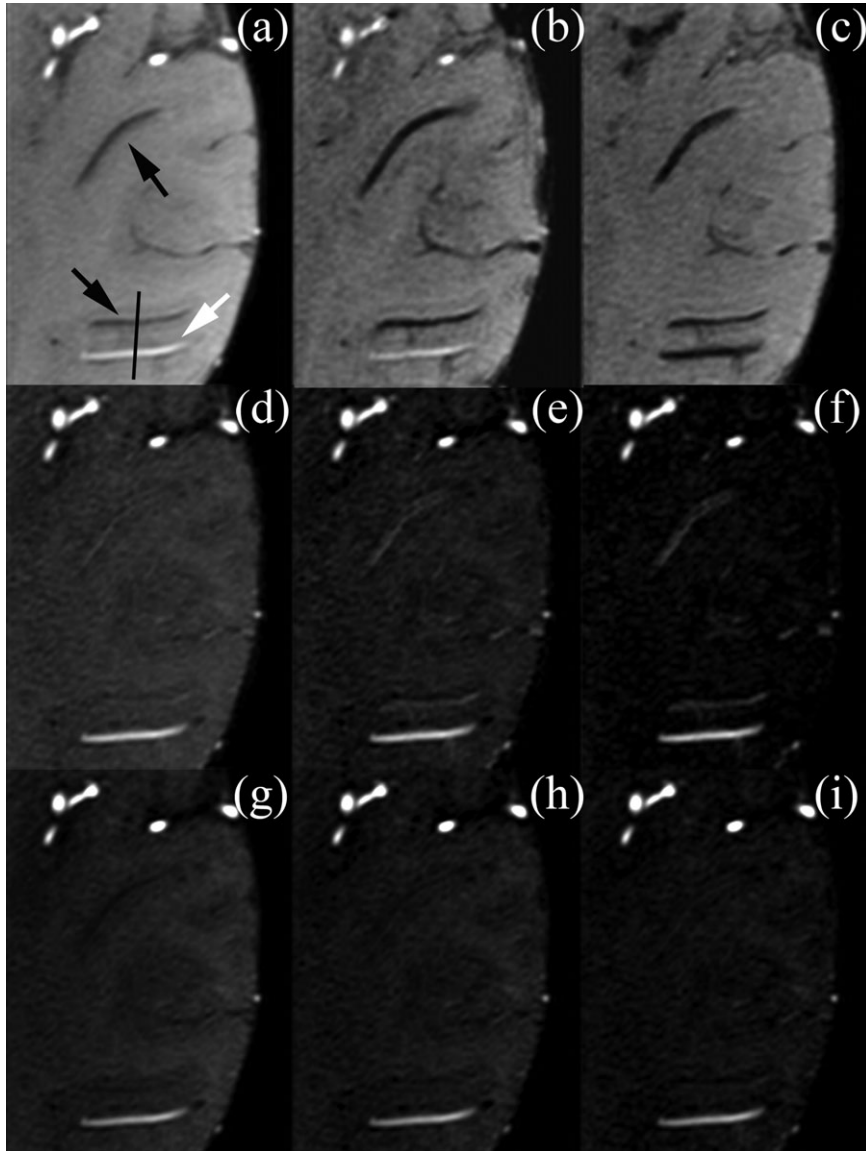


**Figure 4.** Top row: single slice images of (a) TOF images from the averaged FR echoes, (b) SWI from Echo<sub>12</sub>, (c) FD dark blood data from Echo<sub>22</sub>. Middle row: LS results using (d)  $\alpha = 0.75$ , (e)  $\alpha = 1.00$ , and (f)  $\alpha = 1.25$ . Bottom row: NLS results using (g)  $\alpha = 0.75$ , (h)  $\alpha = 1.00$ , and (i)  $\alpha = 1.25$ . Black and white arrows indicate two veins and one artery of interest; the thin black line indicates the location at which the vessel profiles are drawn for Fig. 6. The display window was the same among each row, except for the SWI image, which was individually adjusted.

$S - S'$  but high  $S + S'$  while veins have high  $S - S'$  but low  $S + S'$ , and therefore both have similar  $S^2 - S'^2$ .

Apart from the linearity or nonlinearity, the weighting factor  $\alpha$  in the subtraction also alters the vessel-tissue contrast by changing the  $\Delta S$  distribution, as demonstrated in Fig. 3. With a greater  $\alpha$  factor, the LS method indeed was able to enhance artery-tissue contrast by reducing tissue signal, but also further enhanced the vein-tissue contrast (Fig. 6b). These enhanced veins may be misinterpreted as small arteries (Fig. 5) that have medium to low contrast due to partial volume effects or steady-state saturation effects. The vein-tissue contrast is minimized in NLS due to the fact that both veins and tissues are of similar  $\Delta S_{nls}$  level, and the slight variation of tissue signal between different  $\alpha$  values does not significantly change their contrast. Although using  $\alpha = 0.75$  in LS can also lead to minimal vein-tissue contrast, the artery-tissue CNR is reduced by over 23% compared to  $\alpha = 1.25$  (Fig. 6b and Table 2). Note that there was a large increase in CNR of LS with  $\alpha = 1.25$ . This was because the tissue signal was completely subtracted

out since  $\alpha \approx 1$ , thus the noise distribution changed from Gaussian to Raleigh and resulted in a smaller standard deviation. For NLS, in contrast, such variation in CNR is less than 3% between all  $\alpha$  values, and  $\alpha$  around 1 is seen to sufficiently eliminate the vein-tissue contrast (Fig. 6c and Table 2). We observed such insensitivity of  $\alpha$  in NLS results in all subjects. This means that one simply needs to square the rephased/dephased images and subtract them in order to obtain clean, enhanced angiography.

To better demonstrate the MRA enhancing effects of LS and NLS, we also collected low-dose CE TOF MRA data for comparison. By using low-dose contrast agent (5 cc), low flip angle (15°), and long TR (28 msec), the  $T_1$  shortening effect of the contrast agent is mainly utilized to minimize saturation of the blood signal so as to maximize TOF effects, rather than using the steady-state  $T_1$  enhancement, as in full-dose CE MRA. Although  $T_1$  weightings may still contribute more or less to the enhanced blood signal, such an effect is not strong, as evidenced by the lack of most slow-flowing veins in Fig. 7d and the identical

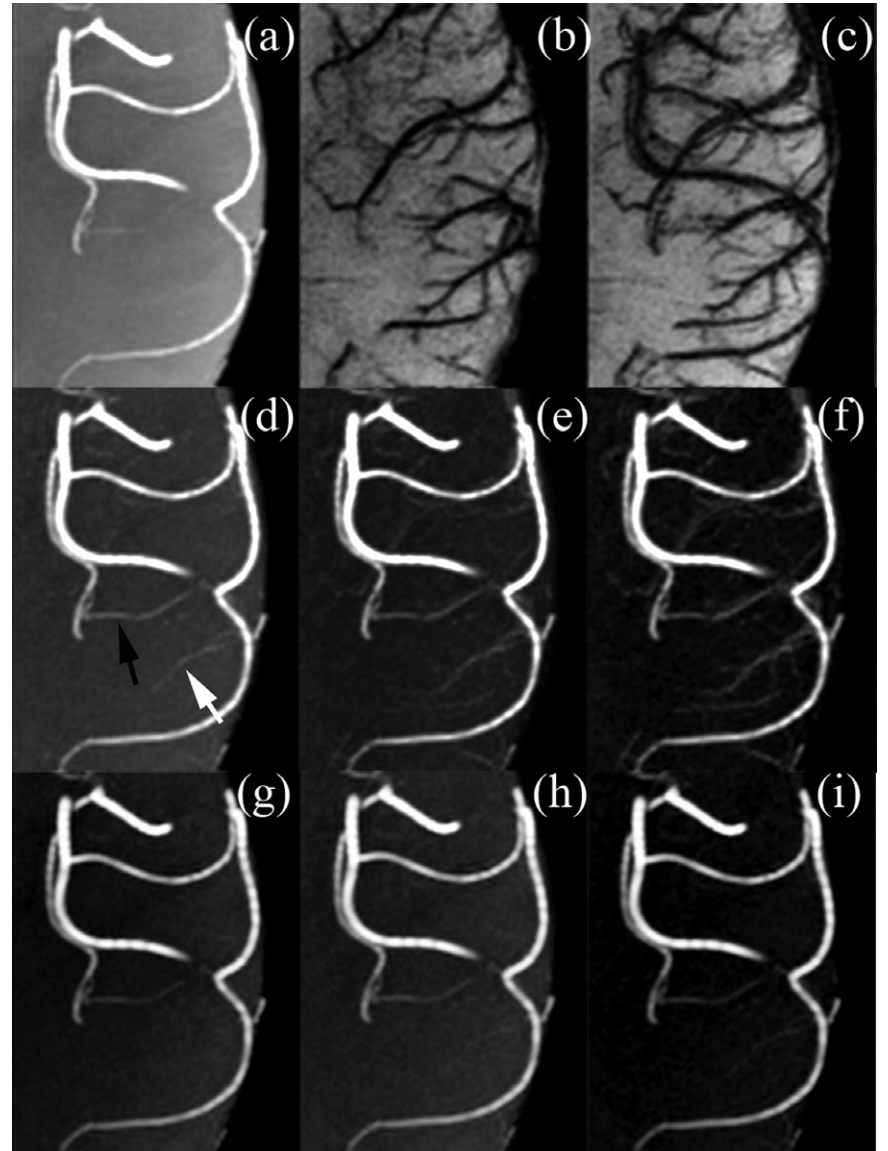


**Figure 5.** Corresponding MIP (or mIP) images of Fig. 4. The white and black arrows in (d) indicate an artery and a vein, respectively. All results shown were projected over a 1–2-mm slab.

artery-tissue contrast between normal TOF and 5 cc data in Fig. 7e. Were the  $T_1$  shortening effect strong, veins would also have become visible and artery-tissue contrast would be higher. By this means, one can establish an upper baseline for maximal TOF effects in arteries to compare the performance of LS and NLS

with. As shown in Fig. 7, arteries are enhanced in all three results being compared. Most noticeably, NLS seems to even outperform the CE TOF data by its higher artery-tissue contrast (Figs. 7e, 8), extra revelation of some small arteries (e.g., near the frontal part), uniform background signal, and the lack of

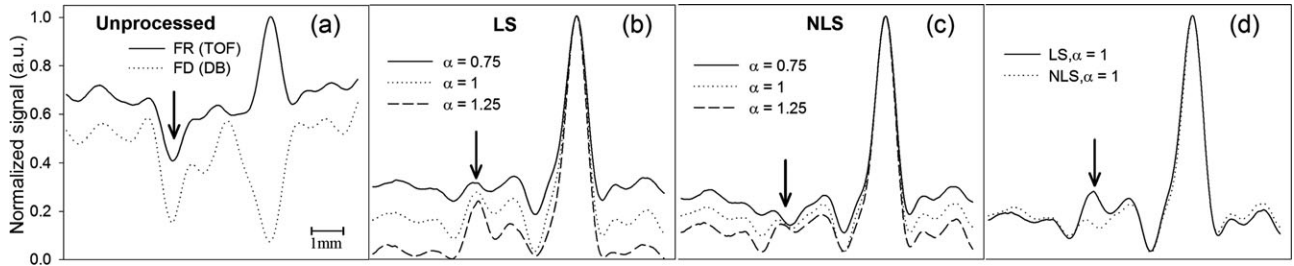


**Figure 6.** Normalized vessel profiles of a vein and an artery from (a) unprocessed FR (TOF) and FD (dark blood) data, (b) LS processed data, (c) NLS processed data, and (d) comparison between LS and NLS. The arrows indicate the center of the vein, which will not be seen in some cases due to reduced contrast with surrounding tissues. Quantification of contrast and CNR are shown in Table 2. The diameter of this artery was ~2 mm.

Table 2

Vessel-Tissue Contrast of the Artery and the Vein Whose Profile Was Indicated by the Black Line in Fig. 4a

	Artery		Vein	
	Contrast (%)	CNR	Contrast (%)	CNR
TOF(FR)	28.3	5.5	-37.2	-7.2
LS ( $\alpha=0.75/1.00/1.25$ )	206.1/453.8/2493.3	17.8/17.8/23.2	-3.5/37.4/366.4	-0.3/1.5/3.4
NLS ( $\alpha=0.75/1.00/1.25$ )	255.4/389.4/680.8	15.5/15.6/15.2	-35.2/-20.0/12.6	-2.1/-0.8/0.3

veins or the contrast-enhanced choroid plexus. LS offers similar artery-tissue contrast with NLS but also lots of venous signal, making it very much like the routine full-dose CE MRA data (data not shown). The comparison confirms that the proposed self-weighted NLS method is potentially capable of revealing the

maximal arterial TOF effect without the use of contrast agent. One thing worth mentioning is that due to its fast flow, the superior sagittal sinus would also appear bright in all methods compared (Fig. 7), albeit it can be easily distinguished. Inferior sagittal sinus, however, is only seen with contrast agent (Fig. 7d) but not in TOF, LS, or NLS results.

Due to partial volume effects and blood flow velocity, it is expected that the CNR<sub>at</sub> may vary according to artery sizes. Moreover, because squaring the image in NLS will amplify the noise by twice the original signal intensity, SNR<sub>nls</sub> will have lower value than SNR<sub>ls</sub> (Fig. 2f vs. 2c) on a voxelwise basis. According to Fig. 8, CNR<sub>at</sub> becomes greater for larger vessels with all methods, which is expected. Paired *t*-test results indicate that CNR<sub>at</sub> of NLS is significantly greater than LS for arteries larger than 1.5 mm (two-tailed *P* = 0.046 and 0.035 for 1.5–2.0 mm and 2.0–2.5 mm groups, respectively), while both have similar CNR<sub>at</sub> for those smaller than 1.5 mm (*P* = 0.126 and 0.395 for <1 mm and 1.0–1.5 mm groups, respectively). This indicates that NLS results are similar to LS for small arteries, but will significantly outperform LS for larger arteries (Figs. 7, 8).

On the other hand, since veins have very low signal while arteries still have high signal (provided competent flow rephasing) in SWI processed images, multiplying with the SWI processed magnitude mask may also help suppress the veins in the LS results (10,27), and we have also tested this method using the same data we collected (results not shown). For large

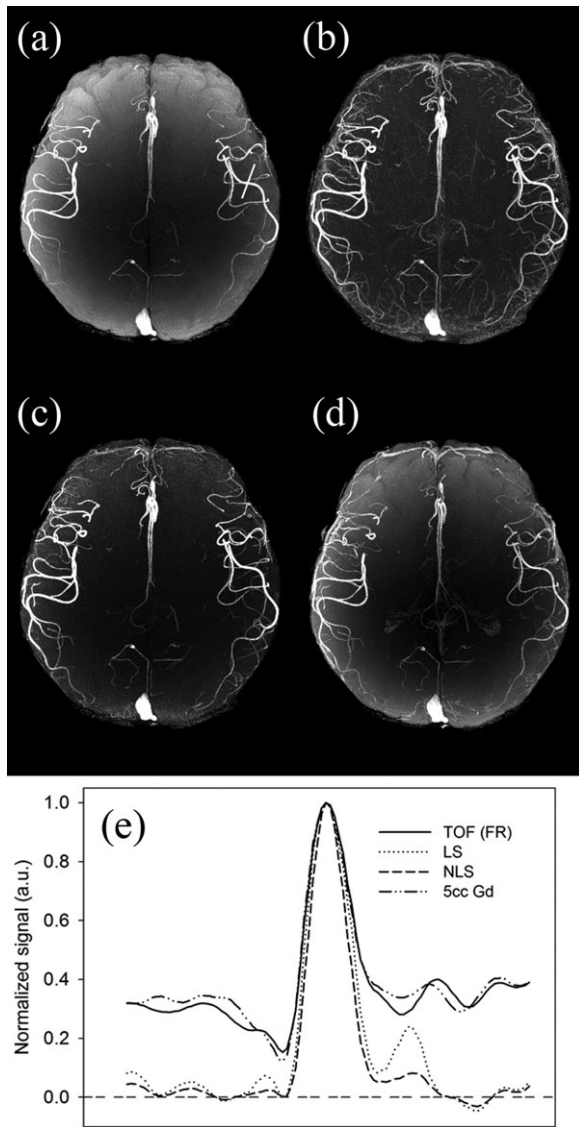


**Figure 7.** MIP images of (a) TOF MRA, (b) LS, (c) NLS, and (d) low-dose CE MRA with 5 cc gadopentetate dimegllumine. (a–c) Collected with a single scan of the FR/FD interleaved double-echo sequence before the use of contrast agent, and  $\alpha$  was 1 for both LS and NLS calculation. (e) Comparison of the normalized profiles of one representative artery as shown in (a), extracted from the corresponding single slice images.

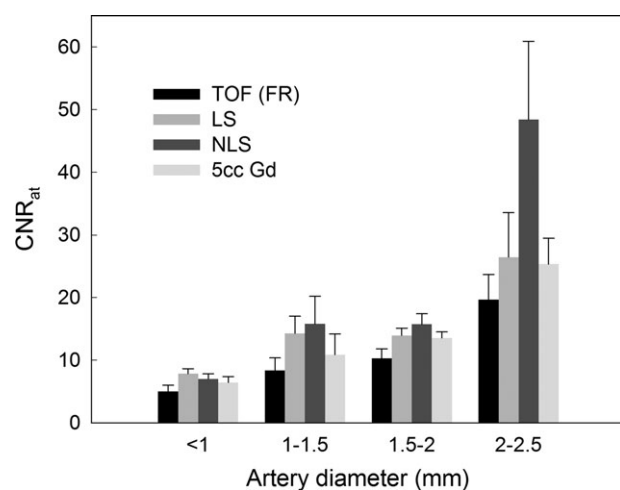


**Figure 8.** Artery-tissue CNR of different artery size groups. Two-tailed paired *t*-test results between LS and NLS are: *P* = 0.126 for <1 mm, *P* = 0.395 for 1–1.5 mm, *P* = 0.046 for 1.5–2 mm and *P* = 0.035 for 2–2.5 mm.

arteries, masking with SWI images also yielded very high artery-tissue contrast and negative vein-tissue contrast. Smaller arteries, on the other hand, were not as equally enhanced as in LS or NLS, probably due to the local signal variations and increased noise caused by phase masking process. Another potential drawback of this SWI masking method would be the introduction of susceptibility artifacts commonly seen in SWI images (11), which may suppress nearby arteries due to signal dropout especially at the edge of the brain. The SWI masking method may find itself useful in full-dose CE MRA scans, in which both arteries and veins display high values in the original images, rendering both subtraction methods less effective in reducing venous signals. By integrating phase information, the SWI masking method may have the potential to selectively suppress the veins even with the presence of contrast agent.

The major drawback of the interleaved design of the sequence is that it still requires approximately the same total scan time as the separate acquisition of both MRA and SWI data. However, compared to separate acquisition of both MRA and SWI, our MRAV method offers strictly aligned images for direct and accurate comparison between the two vascular networks, and a selectively enhanced MRA map that surpasses any existing noncontrast-enhanced MRA or MRAV methods. Also with proper adjustment in scanning parameters, this method may have the potential for MRAV imaging of proximal vessels such as the carotid arteries and the jugular veins in the neck.

In conclusion, we have proposed an FR/FD interleaved double-echo MRAV sequence which for the first time can provide both fully flow-compensated SWI results and selective MRA enhancement in a single scan, while maintaining a good balance between the two contrast sets. Three different types of images, i.e., TOF MRA, SWI, and flow dephased, could be obtained simultaneously with perfect alignment to each other so that no realignment process is necessary. In conjunction with NLS, one can obtain high-resolution SWI and enhanced TOF MRA without the need for contrast agent, and the process can be easily automated with minimal additional computational power. NLS offers a clean TOF angiography free of venous contamination as if acquired with minimal saturation effects. For future works, the acquisition time may be further reduced to provide whole brain coverage using a segmented echo planar imaging (EPI) readout approach (28) or compress sensing (29–31) since the subtracted images contain highly sparse information of arteries. Also, a TONE pulse may be implemented with proper flip angle range to further improve the enhanced MRA results while maintaining high SWI contrast.

## REFERENCES

- Marchal G, Bosmans H, Van Fraeyenhoven L, et al. Intracranial vascular lesions: optimization and clinical evaluation of three-dimensional time-of-flight MR angiography. *Radiology* 1990;175:443–448.
- van den Berg R, Verbist BM, Mertens BJ, van der Mey AG, van Buchem MA. Head and neck paragangliomas: improved tumor detection using contrast-enhanced 3D time-of-flight MR angiography as compared with fat-suppressed MR imaging techniques. *AJNR Am J Neuroradiol* 2004;25:863–870.
- Sehgal V, Delproposto Z, Haddar D, et al. Susceptibility-weighted imaging to visualize blood products and improve tumor contrast in the study of brain masses. *J Magn Reson Imaging* 2006;24:41–51.
- Kohler R, Vargas MI, Masterson K, Lovblad KO, Pereira VM, Becker M. CT and MR angiography features of traumatic vascular injuries of the neck. *Am J Radiol* 2011;196:W800–809.
- Shen Y, Kou Z, Kreipke CW, Petrov T, Hu J, Haacke EM. In vivo measurement of tissue damage, oxygen saturation changes and blood flow changes after experimental traumatic brain injury in rats using susceptibility weighted imaging. *Magn Reson Imaging* 2007;25:219–227.
- Du YP, Jin Z. Simultaneous acquisition of MR angiography and venography (MRAV). *Magn Reson Med* 2008;59:954–958.
- Barnes S, Haacke E. Single echo simultaneous angiography and venography (MRAV) techniques at 3T. In: Proc 17th Annual Meeting ISMRM, Honolulu; 2009. p 1861.
- Park SH, Moon CH, Bae KT. Compatible dual-echo arteriovenography (CODEA) using an echo-specific K-space reordering scheme. *Magn Reson Med* 2009;61:767–774.
- Du YP, Jin Z, Hu Y, Tanabe J. Multi-echo acquisition of MR angiography and venography of the brain at 3 Tesla. *J Magn Reson Imaging* 2009;30:449–454.
- Haacke EM, Xu Y, Cheng YC, Reichenbach JR. Susceptibility weighted imaging (SWI). *Magn Reson Med* 2004;52:612–618.
- Haacke EM, Mittal S, Wu Z, Neelavalli J, Cheng YC. Susceptibility-weighted imaging: technical aspects and clinical applications, Part 1. *AJNR Am J Neuroradiol* 2009;30:19–30.
- Mittal S, Wu Z, Neelavalli J, Haacke EM. Susceptibility-weighted imaging: technical aspects and clinical applications, Part 2. *AJNR Am J Neuroradiol* 2009;30:232–252.
- Lin W, Mukherjee P, An H, et al. Improving high-resolution MR bold venographic imaging using a T1 reducing contrast agent. *J Magn Reson Imaging* 1999;10:118–123.
- Brown BG, Bolson E, Frimer M, Dodge HT. Quantitative coronary arteriography: estimation of dimensions, hemodynamic resistance, and atherosoma mass of coronary artery lesions using the arteriogram and digital computation. *Circulation* 1977;55:329–337.
- Coatrieux JL, Garreau M, Collorec R, Roux C. Computer vision approaches for the three-dimensional reconstruction of coronary arteries: review and prospects. *Crit Rev Biomed Eng* 1994;22:1–38.
- Kimura T, Ikeda M, Takemoto S. Hybrid of opposite-contrast MR angiography (HOP-MRA) combining time-of-flight and flow-sensitive black-blood contrasts. *Magn Reson Med* 2009;62:450–458.
- Axel L, Morton D. MR flow imaging by velocity-compensated/uncompensated difference images. *J Comput Assist Tomogr* 1987;11:31–34.
- James E, Potchen MD, Haacke EM. Magnetic resonance angiography: concepts & applications: St. Louis: Mosby YearBook; 1993. p 169–170.
- Wedein VJ, Meuli RA, Edelman RR, et al. Projective imaging of pulsatile flow with magnetic resonance. *Science* 1985;230:946–948.
- Laub GA, Kaiser WA. MR angiography with gradient motion refocusing. *J Comput Assist Tomogr* 1988;12:377–382.
- Jeong EK, Parker DL, Tsuruda JS, Won JY. Reduction of flow-related signal loss in flow-compensated 3D TOF MR angiography, using variable echo time (3D TOF-VTE). *Magn Reson Med* 2002;48:667–676.
- Haacke EM, Brown R, Thompson M, Venkatesan R. Magnetic resonance imaging. Physical principles and sequence design. New York: Wiley-Liss; 1999. p 670–697.
- Edelman RR, Ahn SS, Chien D, et al. Improved time-of-flight MR angiography of the brain with magnetization transfer contrast. *Radiology* 1992;184:395–399.
- Atkinson D, Brant-Zawadzki M, Gillan G, Purdy D, Laub G. Improved MR angiography: magnetization transfer suppression with variable flip angle excitation and increased resolution. *Radiology* 1994;190:890–894.
- Parker DL, Yuan C, Blatter DD. MR angiography by multiple thin slab 3D acquisition. *Magn Reson Med* 1991;17:434–451.

26. Tkach J, Masaryk T, Ruggieri P. Use of tilted optimized nonsaturating excitation. SMRM. Vol. 2. Berlin: 1992. p 3095.
27. Ishimori Y, Monma M, Kohno Y. Artifact reduction of susceptibility-weighted imaging using a short-echo phase mask. *Acta Radiol* 2009;50:1027–1034.
28. Xu Y, Haacke EM. An iterative reconstruction technique for geometric distortion-corrected segmented echo-planar imaging. *Magn Reson Imaging* 2008;26:1406–1414.
29. Lustig M, Donoho D, Pauly JM. Sparse MRI: the application of compressed sensing for rapid MR imaging. *Magn Reson Med* 2007;58:1182–1195.
30. Wu B, Li W, Guidon A, Liu C. Whole brain susceptibility mapping using compressed sensing. *Magn Reson Med* 2012;67:137–147.
31. Cukur T, Lustig M, Saritas EU, Nishimura DG. Signal compensation and compressed sensing for magnetization-prepared MR angiography. *IEEE Trans Med Imaging* 2011;30:1017–1027.

## Original Research

# Robust Selective Signal Suppression Using Binomial Off-Resonant Rectangular (BORR) Pulses

Yongquan Ye, PhD,<sup>1\*</sup> Jiani Hu, PhD,<sup>1</sup> and E. Mark Haacke, PhD<sup>1,2</sup>

**Purpose:** To study the selective signal suppression capability of a binomial off-resonant rectangular (BORR) radiofrequency pulse method.

**Materials and Methods:** The BORR pulse consists of two consecutive rectangular pulses with a phase difference of  $\pi$ . The exact solution of the Bloch equations was used to simulate its frequency response. The BORR pulse was implemented in a gradient echo sequence and tested on phantoms, the knee, and the breast.

**Results:** The frequency response of the BORR pulse acquired on the phantom confirmed the theory. Broad suppression bands ensured high suppression efficiency and robustness in both *in vitro* and *in vivo* scans compared with other saturation pulses.

**Conclusion:** The BORR pulse method provides a simple, efficient, and robust selective signal suppression alternative for three-dimensional short TR (repetition time) imaging.

**Key Words:** binomial RF pulse; chemical shift imaging; selective suppression; off-resonance

**J. Magn. Reson. Imaging** 2014;39:195–202.

© 2013 Wiley Periodicals, Inc.

SEPARATING WATER AND fat signal is very important for several MR clinical applications, such as the evaluation of traumatic or degenerative cartilaginous lesions (1–3), detection and characterization of breast cancer (4–6), and imaging the optic nerve especially in the presence of a contrast agent (7,8). Apart from the well-known methods of inversion recovery (9–12), phase difference (13–15) and selective saturation radiofrequency (RF) pulses (16–18), using the

frequency response of rectangular pulses (19) can also have the potential for selective signal suppression. Joseph (20) analyzed the Fourier transform (FT) of a rectangular refocusing pulse in a spin echo sequence for its off-resonance frequency response profile (FRP) and used it to suppress water or fat signal, and Morrell (21) proposed a binomial hard pulse scheme to suppress on-resonant spins. Because the function of selective signal suppression is carried out by the refocusing pulse (20) or the excitation pulse (21), such methods are potentially beneficial for short repetition time (TR) fast imaging. However, the bandwidth of the suppression band is rather narrow in both approaches, posing several practical limitations, including reduced suppression efficiency (20,21) especially for fat signal with multiple resonance peaks (22–24), and reduced robustness against field inhomogeneity and/or frequency drift. This is the major reason for the residual fat signal seen in both studies by Josephs (20) and Morrell (21), and such residual signal cannot be reduced by means of optimizing scanning parameters.

In this study, we analyze the FRP of a pair of binomial rectangular pulses with opposing phase (25) using the rotation matrix representation. By properly configuring the duration and frequency offset for the RF pulses, it will be shown that one can obtain much broader suppression bands and, as a result, very efficient and robust signal suppression for water or fat. We will refer to this method as the binomial off-resonant rectangular (BORR) RF pulse. By integrating the BORR pulse into a gradient refocused echo (GRE) sequence, the theoretical FRP will be validated on phantoms, and water-fat separated images will be acquired on the knee and the breast to demonstrate the feasibility and robustness of the method.

<sup>1</sup>Department of Radiology, Wayne State University, Detroit, Michigan, USA

<sup>2</sup>Department of Biomedical Engineering, Wayne State University, Detroit, Michigan, USA

Contract grant sponsor: Department of Defense; Contract grant number: W81XWH-11-1-0493.

Contract grant sponsor: Wayne State University; Contract grant number: OVPR 177310.

\*Address reprint requests to: Y.Y., MR Research Facility, Department of Radiology, Wayne State University, DRH 5E-13, 3990 John R Road, Detroit, MI 48201. E-mail: mqyeah@gmail.com

Received October 29, 2012; Accepted March 1, 2013

DOI 10.1002/jmri.24149

View this article online at [wileyonlinelibrary.com](http://wileyonlinelibrary.com).

## MATERIALS AND METHODS

### Theory

Consider a rotating frame in a right handed system. Figure 1 illustrates the spin precession model when two rectangular pulses are applied consecutively along +y and -y axis, each with duration  $\tau$  and frequency offset  $\Delta f$ . Assuming the initial magnetization  $M(0)$  is in the equilibrium state along z-axis, it will then precess around  $B_{eff-1}$  during the first pulse, with

the precession cone passing through the z-axis and precession angle the same as the angle  $\theta$  between  $B_{\text{eff}-1}$  and z-axis. The magnetization  $M(\tau)$  by the end of the first pulse can be determined as demonstrated in the work by Gregory and Bain (19). During the second pulse, however, the situation becomes more complicated as the precession angle is no longer equal to  $\theta$  and is dependent on the status of  $M(\tau)$ . The full expression of  $M(2\tau)$  will be given next. But for now with a gedanken approach, one can come up with two specific scenarios that can be of particular interest. First, in the case of on-resonance, i.e.,  $\Delta B' = 0$ ,  $B_{\text{eff}}$  of the two rectangular pulses will lie along the y-axis but in opposite directions, and the magnetization will be returned back to the z-axis after both pulses at  $2\tau$ . This means on-resonance spins will always contribute null signal. This is the underlying principle in Morrell's work (21). Another scenario will be that  $M$  precesses around  $B_{\text{eff}}$  one or multiple full cycles during each sub-pulse and returns to z-axis at  $2\tau$ . The second scenario, as will be demonstrated below, is capable of offering much broader suppression bands.

To set the stage for this analysis, we denote the normalized equilibrium magnetization as  $M_0 = [M_x, M_y, M_z] = [0, 0, 1]$ . During the application of each RF pulse, which has the same frequency offset  $\Delta f$  (in Hz), the magnetization sees a  $B_{\text{eff}}$  of:

$$B_{\text{eff}} = \sqrt{(\Delta f/\gamma + \Delta B)^2 + B_1^2} \quad (1)$$

where  $\Delta B$  is the local field inhomogeneity and  $B_1$  is the RF field strength. Substituting  $\Delta f/\gamma + \Delta B$  with  $\Delta B'$ ,  $B_{\text{eff}}$  can be simplified as:

$$B_{\text{eff}} = \sqrt{\Delta B'^2 + B_1^2} \quad (2)$$

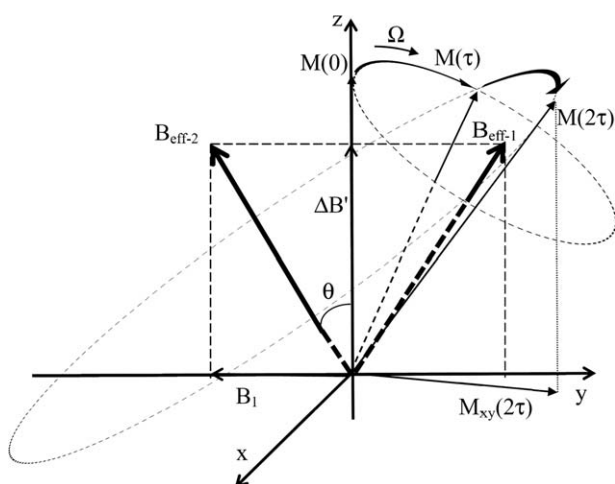


**Figure 1.** Spin precession model during BORR pulse in a right handed reference frame rotating at Larmor frequency. The sub-pulses are applied along +y and -y axis consecutively, both with the same amplitude of  $B_1$  and duration  $\tau$ . Thus both  $B_{\text{eff}}$  have the same amplitude and angle  $\theta$  relative to z-axis.  $\Omega$  is the angular precession rate, while  $\Delta B'$  is the total field variance as the sum of field inhomogeneity  $\Delta B$  and the RF frequency offset  $\Delta f$ .

The angle  $\theta$  between  $B_{\text{eff}}$  and the z-axis is:

$$\theta = \begin{cases} \tan^{-1}(B_1/\Delta B'), & \Delta B' > 0 \\ \pi/2, & \Delta B' = 0 \\ \tan^{-1}(B_1/\Delta B') + \pi, & \Delta B' < 0 \end{cases} \quad (3)$$

The frequency at which  $M$  precesses around  $B_{\text{eff}}$  is:

$$\Omega = -\gamma B_{\text{eff}} = -\gamma \sqrt{\Delta B'^2 + B_1^2} \quad (4)$$

The precession in Figure 1 can be written in the form of a rotation matrix (26) as:

$$M(2\tau) = R_x(-\theta)R_z(-\Omega)\bar{R}_x(\theta)R_x(\theta)R_z(-\Omega\tau)R_x(-\theta)M(0) \quad (5)$$

where  $R_x$  and  $R_z$  are the rotation matrices around the x- and z-axes (19,26), respectively. Ignoring relaxation effects, the expanded expression for Eq. (5) can be written as:

$$\begin{aligned} M_x(2\tau) &= 2\sin(\Omega\tau)[1 - \cos(\Omega\tau)]\sin\theta\cos^2\theta \\ M_y(2\tau) &= \sin^2(\Omega\tau)\sin(2\theta)/2 - [1 - \cos(\Omega\tau)]^2\sin(4\theta)/4 \\ M_z(2\tau) &= 1 - [1 - \cos(\Omega\tau)]^2\sin^2(2\theta)/2 \end{aligned} \quad (6)$$

Compared with the FRP expression of the single rectangular pulse (19), the FRP of the BORR pulse is much more complicated as it is highly nonlinearly dependent on  $B_1$  and  $\Delta B'$  in terms of  $\theta$  and  $\Omega$ . Therefore, numerical simulation will be performed to directly evaluate the FRP.

## Simulation

Numerical simulation was performed based on Eqs. (2–6) using Matlab (Mathworks, Natick, MA) to visualize the FRP of the BORR pulse directly. Both water's and fat's FRPs were simulated by setting the frequency offset  $\Delta f$  of the BORR pulse to the respective on-resonance frequency at 3 Tesla (T) (i.e., 0 and  $-460$  Hz). The simulation assumed  $\tau = 1.28$  ms and  $B_1 = 3.06$   $\mu$ T/m (equivalent to an on-resonance  $60^\circ$  flip angle for each sub-pulse), with relaxation and steady state effects neglected.

## MR Sequence

The MR sequence was developed on the basis of a three-dimensional (3D) GRE sequence by replacing the original excitation pulse with the BORR pulse (Fig. 2), and was tested on a 3T Verio scanner (Siemens Medical Solutions, Erlangen, Germany). Variables include: the duration  $\tau$ ,  $B_1$  field strength (determined by choosing a nominal flip angle  $\alpha$ ) and frequency offset  $\Delta f$ . TE (echo time) is defined as the interval between the end of the BORR pulse and the echo center, because the magnetization is manipulated continuously throughout the BORR pulse and the total tipping effect can only be determined after both sub-pulses have been fully applied. We will denote this

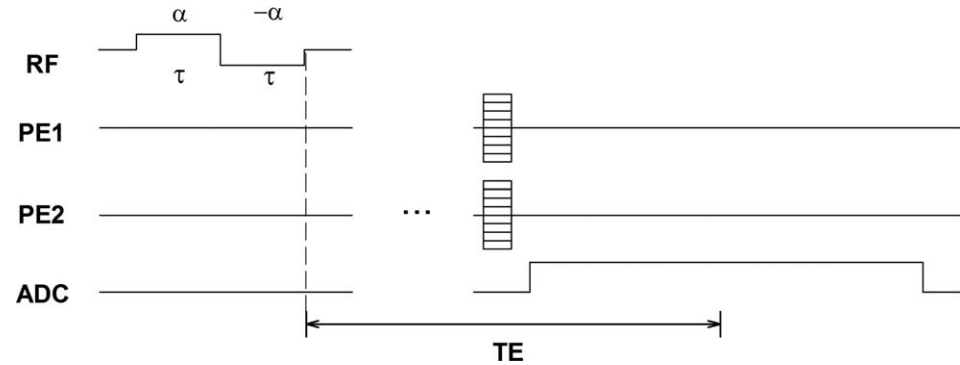


**Figure 2.** Diagram of the BORR-GRE sequence. Both rectangular sub-pulses have the same flip angle  $\alpha$ , frequency offset  $\Delta f$  and duration  $\tau$  but opposite phase. TE was defined as the interval between the end of the second RF pulse and the center of the echo.

sequence as BORR-GRE to differentiate it from other GRE sequences being tested.

### Experimental

For phantom data, three vials containing 0.2% Gadolinium (Gd)-doped water, 3% agar gel, and vegetable oil were scanned. Corresponding  $T_1$  values were estimated by determining the nulling TI with inversion recovery and dividing it by 0.69 and were found to be approximately 80 ms, 780 ms, and 110 ms, respectively. The BORR-GRE protocol for the phantom scans was: TR/TE = 30/3 ms, field of view (FOV) =  $120 \times 67$  mm $^2$ , voxel size =  $0.6 \times 0.6 \times 3$  mm $^3$ ,  $\tau$  = 1.28 ms,  $\alpha$  =  $8^\circ$ , and  $\Delta f$  = [-1000, 1000 Hz]. 101 volumes of data at 20-Hz intervals were collected to produce an outline of the FRP. For comparison, several routinely used spectrally selective methods were also tested with the normal 3D GRE sequence, including water/fat saturation pulses (WS and FS) and water/fat excitation pulses (WE and FE). The WS and FS pulses were 5.12-ms Gaussian pulses on-resonant to water and fat respectively, while WE and FE used a 2.56-ms 1-2-1 binomial spectral-spatial (SPSP) pulse with RF phase cycling (27). All GRE scans used an excitation flip angle of  $2\alpha$ , i.e.,  $16^\circ$ , so as to match the total RF power of the two  $8^\circ$  sub-pulses in BORR, but otherwise the same scanning parameters as the BORR-GRE sequence.

For the knee scans, four healthy volunteers (three males; 25–31 years old) were imaged. Optimization of the BORR-GRE sequence was first performed on two volunteers to determine the optimal value for  $\Delta f$  and  $\tau$ . The other two volunteers then underwent BORR-GRE scans using following parameters: TR/TE = 30/4 ms, FOV =  $160 \times 130$  mm $^2$ , voxel size =  $0.6 \times 0.6 \times 2$  mm $^3$ ,  $\tau$  = 1.5 ms,  $\alpha$  =  $8^\circ$ ,  $\Delta f$  = 160 Hz for fat suppression and -760 Hz for water suppression. The 3D GRE images with FS/WS/FE/WE preparatory pulses or without preparatory pulses were acquired on the other two volunteers using identical parameters to BORR-GRE but with excitation flip angle of  $16^\circ$ .

For breast DCE imaging scans, three healthy volunteers (35–52 years old) underwent the scans, and one of them had a benign fibroadenoma lesion in the right breast. A dynamic scan with eight measurements of the BORR-GRE sequence was performed, during

which gadopentetate dimeglumine (Magnevist, Schering, Germany) was injected at the beginning of the second measurement with a 0.2 mmol/kg dosage. The injection was performed with a power injector at a rate of 2 mL/s and was followed by a 15-mL saline flush. This dynamic BORR-GRE protocol used  $FOV = 324 \times 384$  mm $^2$  and a spatial resolution of  $1 \times 1 \times 1.5$  mm $^3$ , leading to a scanning time of 75 s per measurement. Other parameters were the same as in the knee scan. Also, dynamic FLASH data using the Quick-Fatsat method (i.e., applying fat saturation pulse every 10–20 TRs to shorten the scanning time) to suppress fat signal were also acquired precontrast for comparison.

All subjects provided written consents approved by local Internal Review Board. The phantom and the knee data were obtained using the product eight-channel knee coil, and the breast DCE imaging data were obtained using the product eight-channel breast coil. The knee data were acquired sagittally with read-out along the head-foot direction, whereas the breast scans were collected using transverse imaging planes. For all GRE and BORR-GRE scans, RF spoiling through phase cycling (28) and GRAPPA (29) with  $2 \times$  acceleration factor was used.

### RESULTS

The FRPs of the BORR pulse from both simulation and phantom data are compared in Figure 3. With the same  $\tau$  value, the FRPs from both simulation and phantom data agreed with each other in terms of the pattern of outline, on-resonance nulling frequency, pass band, and suppression band center frequency and bandwidth (see Table 1).

Figure 4 shows representative images to compare the suppression performance between the BORR pulse and those selective saturation/excitation methods. The BORR-GRE images were selected with RF frequency offset  $\Delta f$  = -820 Hz to suppress water and agar, or 340 Hz to suppress fat according to Table 1, and it can be seen that only noise remained in the suppressed samples. In comparison, residual signals are seen in WE, WS, and FE images.

The knee data are similarly shown in Figure 5. According to test scans on the first two volunteers, the center frequency of suppression band was found

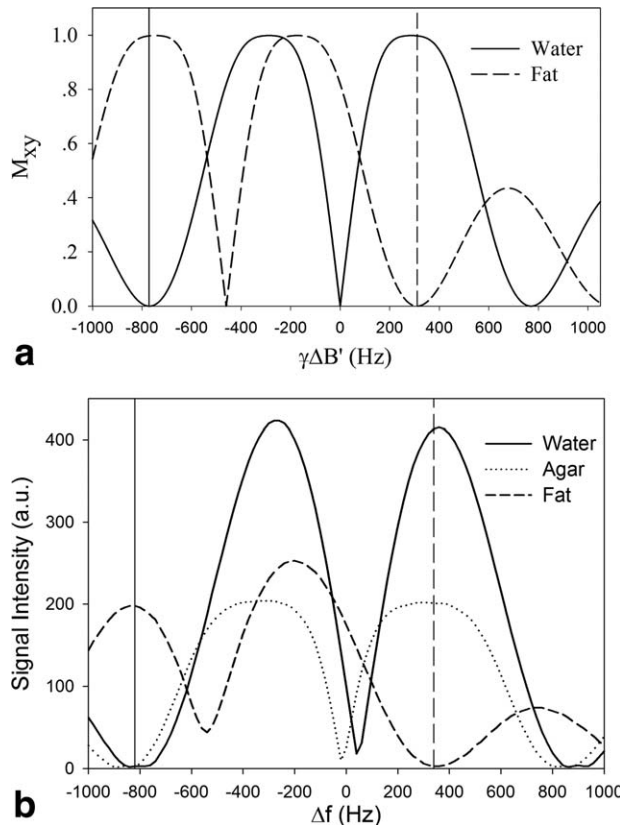


**Figure 3.** a: Simulated FRPs of water (solid line) and fat (dashed line) for 3T, with corresponding on-resonance frequency of 0 and  $-460$  Hz, respectively. b: FRPs of water (solid line), agar gel (dotted line), and fat (dash line) from the phantom data acquired at 3T. The flip angle  $\alpha$  of each RF pulse was  $8^\circ$ . The vertical lines indicate the center of the suppression bands of water (solid) and fat (dash), which were  $-770$  Hz and  $310$  Hz in (a), or  $-820$  Hz and  $340$  Hz in (b), respectively.  $\tau$  was  $1.28$  ms for both simulation and phantom scans. The residual signals at the nulling points are 18, 10, and 45 for water, agar gel and oil, respectively, while the signals at the suppression band centers are all suppressed to noise level.

to be slightly different from the phantom data, and was  $160$  Hz for fat and  $-760$  Hz for muscle. This can be due to the fact that a large part of the body was inside the magnet affecting the field distribution, and/or the tissues have much more complicated micro chemical and susceptibility environments than phantom samples.

The breast DCE images are shown in Figure 6. The signal time curves extracted from the lesion, normal

breast tissue, and fatty tissue (Fig. 6d) are very similar to those obtained using dynamic FLASH methods (4). This is expected because BORR-GRE is essentially a  $T_1$ -weighted sequence. Compared with the FLASH image with Quick-Fatsat (Fig. 6c), the BORR-GRE images showed better suppressed fat signal, with the fat-breast tissue signal ratio being only  $\sim 13\%$  versus the  $\sim 28\%$  in the Quick-Fatsat image. With sufficiently suppressed fat signal, it is not necessary to perform subtraction between the post- and precontrast images to visualize the lesion (4,30), which can be affected by motion-induced errors.

## DISCUSSION

By using binomial off-resonant rectangular pulses with opposing phase, we have demonstrated a robust and efficient method, namely the BORR pulse, for selective signal excitation. Thanks to the much broader off-resonant suppression bands, the BORR pulse is capable of addressing the two major limitations in water-fat separation, i.e., susceptibility to field inhomogeneity and insufficient suppression (or partial excitation) for unwanted signals.

Intuitively, by using two consecutive RF pulses with opposing phase, one would expect that the two pulses would negate each other. For the BORR pulse, this is true and only true for on-resonant spins, as shown by the central nulling point in the simulation (Fig. 3a) and phantom data (Fig. 3b). On-resonant here means the Larmor frequency of the spin being exactly the same as the RF pulse frequency, thus the signal will rapidly increase for spins with as little as  $\sim 10$  Hz shift away from on-resonance (Fig. 3). Actually, this nulling point has been proposed for fat suppression (21), albeit very short duration ( $160\ \mu s$ ) was used on the binomial hard pulses to make this nulling point into a slightly broader nulling “band.” Nevertheless, using this nulling point for fat suppression has several major limitations. First, the narrow suppression bandwidth makes the suppression highly susceptible to field inhomogeneity (21). Second, it is not possible to suppress fat signal effectively due to its multi-peak signal contribution, as discussed in (22–24) and also confirmed in Figure 3b, where the residual signal at fat’s nulling point is very high (approximately 17.8% of its maximal signal). Another important limitation of their method (21) was that water signal was very low regardless of the fact that they used a  $60^\circ$  flip angle

**Table 1**  
On-Resonance Nulling Point Frequency, Pass band/Suppression band Bandwidth and Center Frequency From the Simulation and Phantom Data in Figure 3

	Nulling point frequency (Hz)		Pass/suppression band bandwidth (Hz)		Pass/suppression band center frequency (Hz)	
	Simulation	Phantom	Simulation	Phantom	Simulation	Phantom
Water	0	40	210/140	120/200	290/-770	360/-800
Fat	-460	-540	210/140	140/160	-750/310	-830/340
Agar	N/A	-20	N/A	260/150	N/A	300/-860

<sup>a</sup>The bandpass is defined as that region within which the signal is maintained above 95% of the maximum while for the suppression band the signal is below 5%.

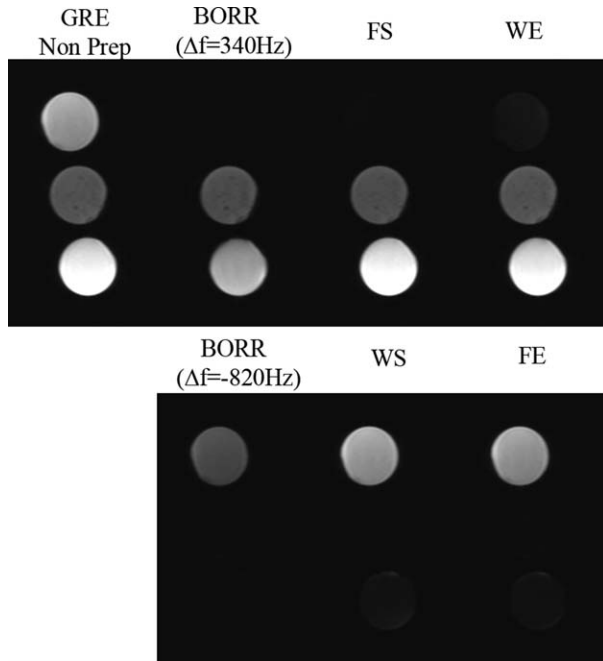


**Figure 4.** Phantom images acquired using BORR-GRE and GRE using FS/WE/WS/FE methods or without (“Non Prep”). The three vials contained vegetable oil (upper), 3% agar gel (middle) and Gd doped water (lower). All images are displayed with the same window settings.

(only equivalent to  $13^\circ$  of on-resonance excitation) (21). It was because the water frequency was located at the transition band (i.e. the rising portion to the right of the nulling point) rather than the passband of the FRP. As a result, the high RF energy applied was inefficiently used, and may lead to high specific absorption rate (SAR) of RF power for fast imaging especially at high fields.

The proposed BORR pulse is not subject to such problems because it uses off-resonant suppression bands that are much broader. The condition for forming this suppression band is that the magnetization precesses about  $B_{\text{eff}}$  for one cycle (or multiple cycles for those suppression bands further off-resonant) during each of the rectangular sub-pulses. As a result, the magnetization is returned to the z-axis at the end of BORR pulse as if not excited at all. This reinstallation to the equilibrium state ensures the highest level of suppression. Better yet, an exact  $2\pi$  precession around  $B_{\text{eff}}$  is not required to maintain high suppression efficiency. As demonstrated in Figure 7, the magnetization precesses in opposite directions with the same angular speed (determined by Eq. (4) during each RF pulse). As a result, a precession moderately under (Fig. 7b) or over  $2\pi$  (Fig. 7c) during the first pulse will be largely compensated by a similar amount of opposite precession during the second pulse, returning the final magnetization  $M(2\pi)$  close to z-axis. According to simulation, a  $\pm 50$  Hz variation relative to the suppression band center results in a highest residual signal of merely 3.2% (Fig. 7). This is the underlying mechanism for forming the broad suppression bands, which facilitate the method’s robustness against frequency variations from

various sources. One good example can be found by looking at the FRPs of water and agar gel. Mixed with Gd contrast agent, the water sample has a frequency difference of approximately 60 Hz relative to the agar gel (Table 1). High suppression rate cannot be achieved for both samples with the routine FE and WS methods (Fig. 4). However, the BORR pulse successfully suppressed both samples down to noise level (Fig. 4), as a large portion of their off-resonant suppression bands overlap with each other (Fig. 3b). With the advanced shimming techniques available in modern scanners, the frequency variation induced by field inhomogeneity across the object (31) usually falls within the suppression bandwidth range of the BORR pulse and thus will not affect the signal suppression efficiency.

The suppression is also rather insensitive to  $B_1$  variations. Because the  $|\gamma\Delta B'|$  value at the suppression band center is greater than 300 Hz at 3T (Table 1) while  $\gamma B_1$  is usually less than 65 Hz (i.e.,  $30^\circ$ ) for small flip angles, small variations in  $B_1$  field will not significantly change  $\Omega$  and  $\theta$ , and the suppression band’s center frequency and bandwidth will remain largely unchanged.

Another major issue of fat signal suppression is the signal contribution from fat’s multiple resonance peaks. At 3T, the chemical shift between the nearest two peaks located on either side of the main  $\text{CH}_2$  peak is approximately 150 Hz (23). A narrow suppression band such as that used in (20,21) can only suppress the main  $\text{CH}_2$  peak, as evidenced by the high residual signal of vegetable oil compared with water and agar gel (Fig. 3b). With a suppression band that has 150–200 Hz bandwidth, the main  $\text{CH}_2$  peak along with the two neighboring peaks can be adequately suppressed. This is confirmed by the completely nulled vegetable oil signal at the suppression band center (Figs. 3 and

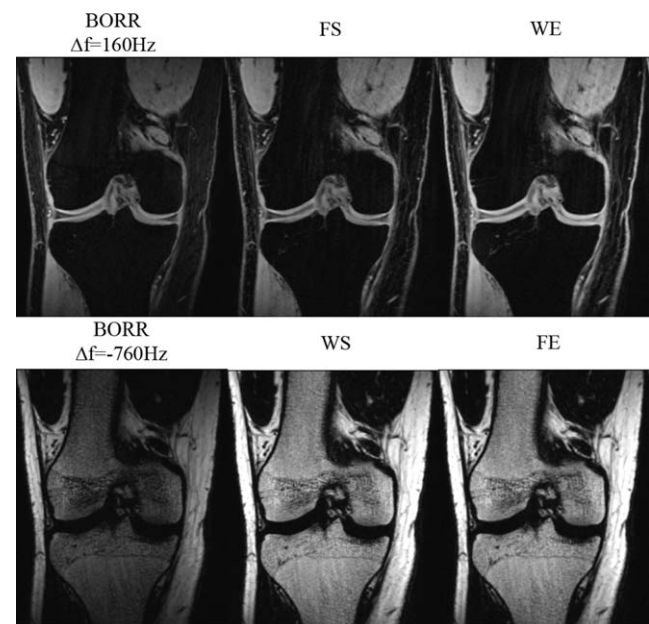


**Figure 5.** Knee images acquired using BORR-GRE and GRE with FS/WE/WS/FE methods. All images are displayed with the same window settings.

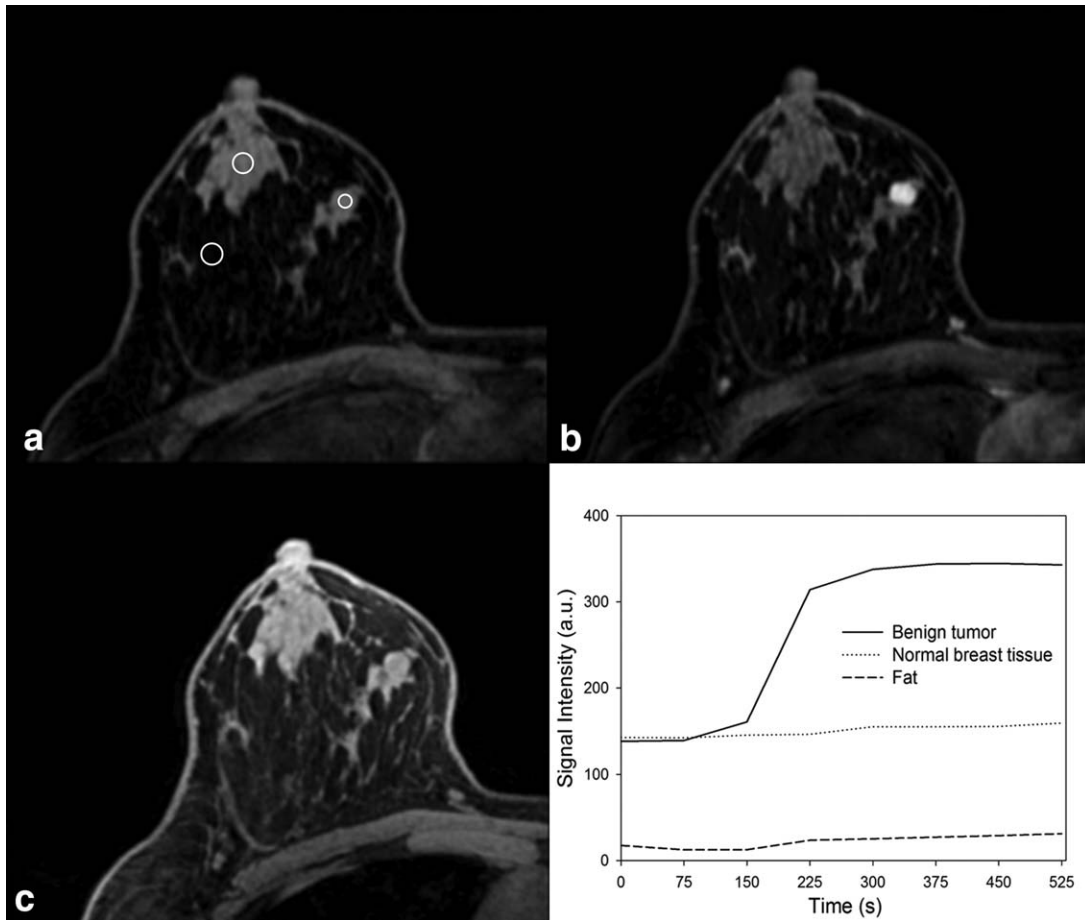


**Figure 6.** Fat suppressed BORR-GRE breast DCE images acquired before (a) and after (b) contrast agent injection. c: Precontrast image of a dynamic FLASH sequence for comparison. d: Signal uptake curves at the lesion, normal breast tissue and fatty tissue extracted from ROIs shown in (a). The signal ratio between fat and breast tissue (precontrast) is approximately 13% in (a) and 28% in (c).

4). Also this very high suppression efficiency suggests that, although the other three fatty peaks farther away may not be suppressed, such as the olefinic fatty acid peak located near the water's resonance frequency (23), their contribution can be considered negligible.

For the pass band signal, on the other hand, it is possible to achieve maximal signal which is only limited by steady state  $T_1$  saturation effects. Because the

spin precession during each sub-pulse is not in the same direction, the tipping effects may not fully add up for off-resonant spins; therefore, the BORR pulse with two  $\alpha$  sub-pulses yields slightly reduced signal than a normal  $2\alpha$  excitation pulse, as can be seen by comparing the BORR-GRE images and other GRE images in Figures 4 and 5. To estimate the effective flip angle at the pass band center, one can consider the maximal signal takes place when  $\Omega\tau = \pi$ .

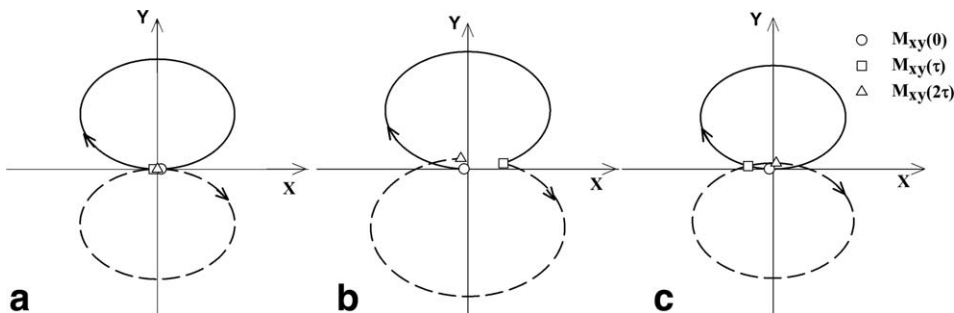


**Figure 7.** Simulation of  $M_{xy}$  trajectories during the first (solid line) and second (dash line) RF pulse with  $\gamma\Delta B'$  of 760 Hz (a), 710 Hz (b), and 810 Hz (c) when  $\tau = 1.28$  ms. a: Shows the case of an exact  $2\pi$  precession around  $B_{eff}$  during both pulses, while (b) and (c) simulate precession slightly under or over  $2\pi$  during each pulse. The final magnitude of  $M_{xy}$  (position indicated with the triangles) is 0, 3.2% and 1.6% of the maximum, respectively. Arrows indicate the trajectory of  $M_{xy}$ .

According to Eq. (6),  $M_{xy}(2\tau)$  will then lie along  $-y$  axis and have the magnitude of  $\sin(4\theta)$ , thus having an effective flip angle as  $4\theta$  instead of  $2\alpha$ . Take for example the parameter from the phantom experiment where  $\tau = 1.28$  ms and  $\alpha = 8^\circ$ , then  $\gamma B_1$  and  $\gamma \Delta B'$  are 17.36 Hz and 390 Hz, respectively, and  $\theta$  equals  $2.55^\circ$ . Therefore, the effective flip angle at the pass band center is  $4\theta = 10.2^\circ$ , or  $1.28\alpha$ , which is less than  $16^\circ$ , or  $2\alpha$ , with a reduction of  $\sim 36\%$ . Based on the signal intensity observed in the phantom and the knee, and comparing with the corresponding GRE images with nominal flip angle  $2\alpha$  (which may not necessarily be  $16^\circ$  due to steady state effects), the effective flip angle of the pass band signal of the BORR pulse are then determined to be  $1.48\alpha$ ,  $1.88\alpha$ , and  $1.12\alpha$  for water, agar gel, and vegetable oil in the phantom, and  $1.58\alpha$  for muscle and  $1.02\alpha$  for trabecular marrow in the knee. Apart from the long  $T_1$  agar gel in which steady state saturation effect is significant in both BORR-GRE and GRE data, this result matches the estimated pass band signal relative to the nominal flip angle. However, such signal reduction is much less than that in Morrell's method (21), which was approximately 74%. The high effective flip angle in agar gel suggests the RF power efficiency is higher when near steady state; thus, it is best to set  $2\alpha$  near the Ernst angle of the tissue to be imaged. Therefore, the BORR pulse can offer sufficient SNR without significantly increased SAR level.

Due to the nonselective nature of the rectangular RF pulse, currently the BORR pulse method only supports 3D imaging. However, this is not a major drawback for knee and breast imaging, because  $T_1$ -weighted imaging is most efficiently done in a 3D mode for these body parts. With a properly selected readout direction as we had used, the images can be free from aliasing artifacts. Nevertheless, with the capability of simultaneous excitation and, the BORR pulse can find itself compatible to most short TR fast imaging sequences such as GRE, FLASH, and SSFP to achieve excellent selective imaging of water or fat at similar or even faster scanning speeds. The BORR pulse can be more appreciated at very high fields such as 7T, where water/fat chemical shift is higher and thus shorter  $\tau$  is required, which in turn facilitates broader suppression bands and faster scanning speeds. On the other hand, our preliminary simulation using Sinc pulse has suggested similar patterns of off-resonant stopbands and passbands, and will be the focus of our further study to improve the BORR method to become spatially selective.

Finally, we will compare the working principle between the BORR pulse and the SPSP pulse. An SPSP pulse may comprise of 2 (32), 3 (27), or more (33–35) RF pulses, and differs from our BORR pulse in the following three aspects: (i) RF pulses can be spatially selective; (ii) the tipping effect of the sub-pulses is considered instantaneous; and (iii) the magnetization precesses freely around the  $z$ -axis between RF pulses and different amounts of phase are developed according to the chemical shift property. Although both methods are similar in that the suppression is done by restoring the magnetization to  $z$ -

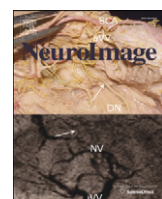
axis, the SPSP pulse uses the phase difference developed during the interval between RF pulses, while the BORR pulse continuously modulates the magnetization during the RF pulses. The phase and interval between the SPSP sub-pulses must be carefully adjusted to correctly tip the magnetization (35), otherwise the suppression and excitation efficiency will be reduced. Also, to achieve a broad suppression band, more sub-pulses are needed for the SPSP method, which in turn not only increases the duration of the SPSP pulse, but also reduces the pass band signal (27). In comparison, the simple implementation, high suppression efficiency, and robustness of the BORR pulse merit it free of such problems, except that only 3D image acquisition is supported due to its nonselective nature.

In conclusion, we have developed a simple and robust binomial rectangular RF pulse method for highly effective and selective water/fat suppression. Both phantom and *in vivo* data (on the knee and the breast) were collected and were found to conform to theoretical prediction and simulation. By properly setting the duration and frequency offset of the RF sub-pulses, water or fat signal can be well suppressed down to noise levels, and the suppression is robust and spatially homogeneous thanks to the broad bandwidth of the suppression band. Our binomial rectangular RF pulse method may find itself useful in short TR 3D fast imaging techniques, where good water or fat suppression is difficult to achieve. The drawback of the method is the slightly reduced pass band signal and the nonselectiveness of the rectangular sub-pulses. However, the effects of such limitations are not significant when the BORR pulse is implemented in short TR 3D fast imaging sequences such as GRE, FLASH and SSFP.

## REFERENCES

1. Crema MD, Roemer FW, Marra MD, et al. Articular cartilage in the knee: current MR imaging techniques and applications in clinical practice and research. Radiographics 2011;31:37–61.
2. Lee SY, Jee WH, Kim SK, Kim JM. Proton density-weighted MR imaging of the knee: fat suppression versus without fat suppression. Skeletal Radiol 2011;40:189–195.
3. Mohr A, Priebe M, Taouli B, Grimm J, Heller M, Broermann J. Selective water excitation for faster MR imaging of articular cartilage defects: initial clinical results. Eur Radiol 2003;13:686–689.
4. Kuhl CK, Mielcarek P, Klaschik S, et al. Dynamic breast MR imaging: are signal intensity time course data useful for differential diagnosis of enhancing lesions? Radiology 1999;211:101–110.
5. Nunes LW, Schnall MD, Orel SG, et al. Breast MR imaging: interpretation model. Radiology 1997;202:833–841.
6. Nunes LW, Schnall MD, Orel SG. Update of breast MR imaging architectural interpretation model. Radiology 2001;219:484–494.
7. Hendrix LE, Kneeland JB, Haughton VM, et al. MR imaging of optic nerve lesions: value of gadopentetate dimeglumine and fat-suppression technique. AJNR Am J Neuroradiol 1990;11:749–754.
8. Miller DH, Mac Manus DG, Bartlett PA, Kapoor R, Morrissey SP, Moseley IF. Detection of optic nerve lesions in optic neuritis using frequency-selective fat-saturation sequences. Neuroradiology 1993;35:156–158.
9. Bydder GM, Young IR. MR imaging: clinical use of the inversion recovery sequence. J Comput Assist Tomogr 1985;9:659–675.
10. Smith RC, Constable RT, Reinhold C, McCauley T, Lange RC, McCarthy S. Fast spin echo STIR imaging. J Comput Assist Tomogr 1994;18:209–213.

11. Balchandani P, Spielman D. Fat suppression for 1H MRSI at 7T using spectrally selective adiabatic inversion recovery. *Magn Reson Med* 2008;59:980–988.
12. Albert S. Water Fat Separation by Inversion Recovery Imaging. *Med Phys* 1986;13:572–572.
13. Ma J. Breath-hold water and fat imaging using a dual-echo two-point Dixon technique with an efficient and robust phase-correction algorithm. *Magn Reson Med* 2004;52:415–419.
14. Dixon WT. Simple proton spectroscopic imaging. *Radiology* 1984;153:189–194.
15. Reeder SB, Hargreaves BA, Yu H, Brittain JH. Homodyne reconstruction and IDEAL water-fat decomposition. *Magn Reson Med* 2005;54:586–593.
16. Keller PJ, Hunter WW Jr, Schmalbrock P. Multisection fat-water imaging with chemical shift selective presaturation. *Radiology* 1987;164:539–541.
17. Disler DG, McCauley TR, Wirth CR, Fuchs MD. Detection of knee hyaline cartilage defects using fat-suppressed three-dimensional spoiled gradient-echo MR imaging: comparison with standard MR imaging and correlation with arthroscopy. *AJR Am J Roentgenol* 1995;165:377–382.
18. Peterfy CG, van Dijke CF, Janzen DL, et al. Quantification of articular cartilage in the knee with pulsed saturation transfer subtraction and fat-suppressed MR imaging: optimization and validation. *Radiology* 1994;192:485–491.
19. Gregory RM, Bain AD. The effects of finite rectangular pulses in NMR: phase and intensity distortions for a spin-1/2. *Concept Magn Reson A* 2009;34:305–314.
20. Joseph PM. A spin echo chemical shift MR imaging technique. *J Comput Assist Tomogr* 1985;9:651–658.
21. Morrell GR. Rapid fat suppression in MRI of the breast with short binomial pulses. *J Magn Reson Imaging* 2006;24:1172–1176.
22. Mao J, Yan H, Brey WW, Bidgood WD Jr, Steinbach JJ, Mancuso A. Fat tissue and fat suppression. *Magn Reson Imaging* 1993;11:385–393.
23. Yu H, Shimakawa A, McKenzie CA, Brodsky E, Brittain JH, Reeder SB. Multiecho water-fat separation and simultaneous R2\* estimation with multifrequency fat spectrum modeling. *Magn Reson Med* 2008;60:1122–1134.
24. Brix G, Heiland S, Bellemann ME, Koch T, Lorenz WJ. MR imaging of fat-containing tissues: valuation of two quantitative imaging techniques in comparison with localized proton spectroscopy. *Magn Reson Imaging* 1993;11:977–991.
25. Ye Y, Hu J, Haacke EM. Robust water-fat separation using binomial rectangular pulses. Proceedings of the 20th Scientific Meeting, ISMRM, Melbourne, Australia, 2012. (abstract 954).
26. Haacke EM, Brown R, Thompson M, Venkatesan R. Magnetic resonance imaging. Physical principles and sequence design. New York: Wiley-Liss; 1999. p 32–45.
27. Hardy PA, Recht MP, Piraino DW. Fat suppressed MRI of articular cartilage with a spatial-spectral excitation pulse. *J Magn Reson Imaging* 1998;8:1279–1287.
28. Zur Y, Wood ML, Neuringer LJ. Spoiling of transverse magnetization in steady-state sequences. *Magn Reson Med* 1991;21:251–263.
29. Griswold MA, Jakob PM, Heidemann RM, et al. Generalized auto-calibrating partially parallel acquisitions (GRAPPA). *Magn Reson Med* 2002;47:1202–1210.
30. Lipnick S, Liu X, Sayre J, Bassett LW, Debruyl N, Thomas MA. Combined DCE-MRI and single-voxel 2D MRS for differentiation between benign and malignant breast lesions. *NMR Biomed* 2010;23:922–930.
31. Truong TK, Clymer BD, Chakeres DW, Schmalbrock P. Three-dimensional numerical simulations of susceptibility-induced magnetic field inhomogeneities in the human head. *Magnetic resonance imaging* 2002;20:759–770.
32. Thomasson D, Purdy D, Finn JP. Phase-modulated binomial RF pulses for fast spectrally-selective musculoskeletal imaging. *Magn Reson Med* 1996;35:563–568.
33. Schick F. Simultaneous highly selective MR water and fat imaging using a simple new type of spectral-spatial excitation. *Magn Reson Med* 1998;40:194–202.
34. Bernstein MA, King KF, Zhou XJ. Handbook of MRI pulse sequence. New York: Academic Press; 2004. p 96–103.
35. Zur Y. Design of improved spectral-spatial pulses for routine clinical use. *Magn Reson Med* 2000;43:410–420.



## Review

## The role of susceptibility weighted imaging in functional MRI

E. Mark Haacke <sup>a,\*</sup>, Yongquan Ye <sup>b,1</sup><sup>a</sup> MR Research Facility, Department of Radiology, Wayne State University, HUH-MR Research G030/Radiology, 3990 John R Road, Detroit, MI 48201, USA<sup>b</sup> MR Research Facility, Department of Radiology, Wayne State University, DRH 5E-13, 3990 John R Road, Detroit, MI 48201, USA

## ARTICLE INFO

## Article history:

Accepted 1 January 2012

Available online 8 January 2012

## Keywords:

fMRI

SWI

High resolution

Blood oxygenation level

## ABSTRACT

The development of functional brain magnetic resonance imaging (fMRI) has been a boon for neuroscientists and radiologists alike. It provides for fundamental information on brain function and better diagnostic tools to study disease. In this paper, we will review some of the early concepts in high resolution gradient echo imaging with a particular emphasis on susceptibility weighted imaging (SWI) and MR angiography (MRA). We begin with the history of our own experience in this area, followed by a discussion of the role of high resolution in studying the vasculature of the brain and how this relates to the BOLD (blood oxygenation level dependent) signal. We introduce the role of SWI and susceptibility mapping (SWIM) in fMRI and close with recommendations for future high resolution experiments.

© 2012 Elsevier Inc. All rights reserved.

## Contents

Introduction . . . . .	923
The role of high resolution . . . . .	924
High resolution MR angiography: the role of saturation and dephasing . . . . .	926
Susceptibility weighted imaging (SWI) . . . . .	927
Susceptibility weighted imaging and mapping (SWIM) and oxygen saturation maps . . . . .	927
Summary and conclusions . . . . .	928
Acknowledgement . . . . .	928
References . . . . .	928

## Introduction

In the early 1990s, our research interests were in developing and understanding 3D gradient echo imaging methods to study neurological diseases. It would be no surprise to the reader that we were delighted to see the early work from Seiji Ogawa at Bell Labs (Ogawa et al., 1993) and Jack Belliveau and colleagues at MGH (Belliveau et al., 1991) regarding the use of magnetic resonance imaging (MRI) for functional MRI (fMRI) of the brain. The news came to our attention quickly, as we were then focusing on the effects of changes in local fields in gradient echo imaging at Case Western Reserve University (CWRU) more as artifacts than as a useful tool. At that time, we had interests in O<sup>17</sup> imaging (Hopkins et al., 1988; Kwong et al., 1991)

using gradient echo imaging for brain function and Amos Hopkins, the major instigator in this direction, became interested immediately in collaborating with people at MGH on the concept of fMRI with O<sup>17</sup> imaging. Some of the experiments done in this area showed that we could see major changes in the pial veins between activation and resting state (Frahm et al., 1993; Haacke et al., 1994; Lai et al., 1993), and that the early explanation of diffusion as the source of signal change in fMRI was likely not correct. This began what was then known as the brain/vein debate.

It took some years later and a number of key papers to show that the intravascular and extravascular effects, at least at 1.5 T, were the major sources of signal change in fMRI. To demonstrate this, researchers applied strong dephasing gradients and/or saturation pulses to basically remove the arterial signal from the images and then evaluated the fMRI response (Duong et al., 2003). After suppressing blood flow, there was little fMRI response remaining, implicating a major intravascular source. An example of the effect of saturation pulses applied outside the slices of interest for a 3 T fMRI experiment

\* Corresponding author. Fax: +1 313 745 9182.

E-mail addresses: [nmrimage@aol.com](mailto:nmrimage@aol.com) (E.M. Haacke), [mqyeah@gmail.com](mailto:mqyeah@gmail.com) (Y. Ye).<sup>1</sup> Fax: +1 313 745 9182.

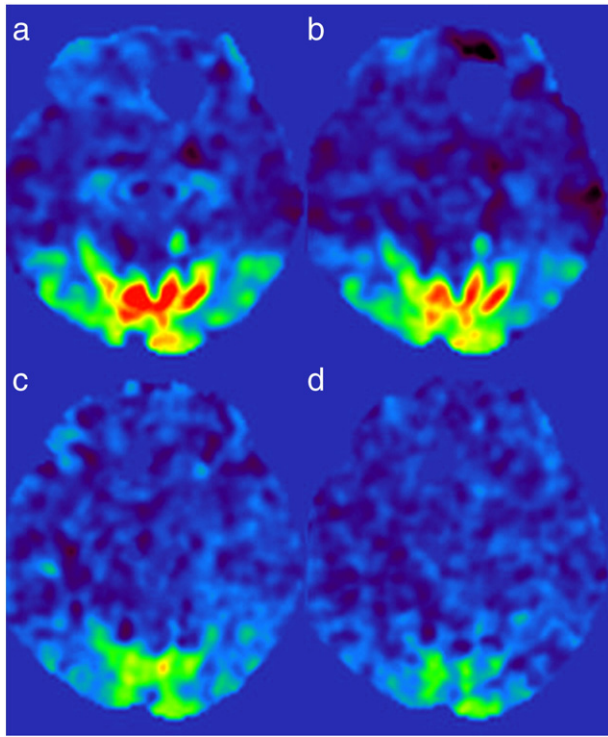


**Fig. 1.** GE- (a, b) and SE-EPI (c, d) t-maps obtained without (a, c) and with (b, d) blood saturation, showing a reduced BOLD response when blood signal is saturated. TE of GE- and SE-EPI was 24 ms and 96 ms respectively. The blood saturation was done by placing two saturation bands above and below the imaging slab, and the visual stimulation was 8 Hz flashing checkerboard with 30 s/30 s on/off block design.

in the visual cortex is shown in Fig. 1. Clearly, there is a decrease in the signal even for the gradient echo EPI sequence. It should be noted that for the long TR experiments used for whole brain multi-slice EPI, there is a strong inflow of fresh blood, which is referred to

as “inflow BOLD enhancement” (Duong et al., 2003; Duyn et al., 1994). By suppressing the signal from blood, the inflow BOLD enhancement effects are also suppressed, leaving only the extravascular effects. During the last 20 years, many papers have been written studying the role of intravascular and extravascular BOLD effects, even up to today, especially since higher and higher field strengths have become available and more and more signal is generated from extravascular effects (Baudendistel et al., 1998; Boxerman et al., 1995; Casciaro et al., 2008; Song et al., 2007; Ugurbil et al., 2000).

### The role of high resolution

One of our goals has been to look for methods to increase resolution and yet keep imaging time reasonable. One early example of this was partial Fourier imaging (Haacke et al., 1999; Xu and Haacke, 2001). This approach allowed us (and still does) to take an asymmetric echo, keep flow compensation for short echoes, and collect many points after the echo to maintain high resolution in the read direction. We also focused on segmented EPI to improve speed for high resolution imaging (Haacke et al., 1986; Xu and Haacke, 2008). We believed that new information awaited us structurally and functionally if we could push resolution down to 100  $\mu$ m. Today, high-field and parallel imaging are re-opening the door to that goal. The group in Minnesota pioneered this direction in the visual cortex by studying ocular dominance columns with high resolution fMRI (Menon et al., 1997; Yacoub et al., 2008). Of course, the most interesting approach would be to create high resolution functional imaging with anatomical qualities, whether it be vascular, metabolic, or brain function. No doubt researchers in this field will continue to fine tune the MR microscope to push these limits further and further in the future thanks to the continued technical developments that lead to higher signal-to-noise, faster imaging and better resolution.

*Why high resolution?* Evidently the workhorse for fMRI today remains a low resolution scan with roughly 3 mm resolution in each direction. The argument for this is that the signal-to-noise (SNR) has to be high enough that one can detect changes in signal as small as 1%. However, it depends on whether or not there is a scale invariant

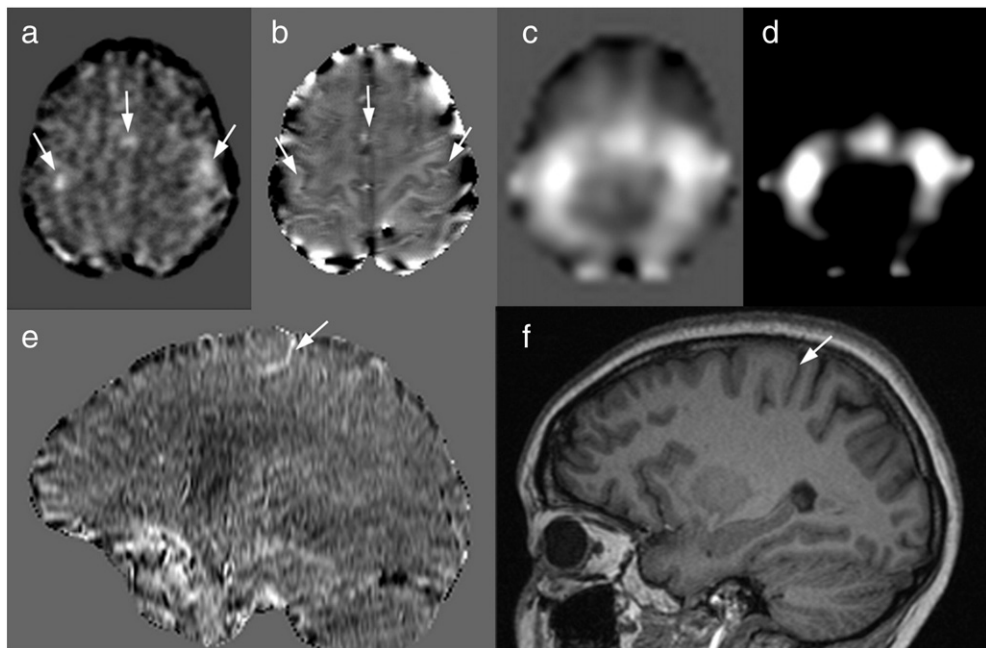


**Fig. 2.** Activations in the primary motor cortex using a block design finger tapping paradigm. (a) Filtered 3D GRE images of single subtraction between activation and resting state, with voxel size of  $1.75 \times 1.75 \times 2$  mm $^3$ ; (b) phase image from the same slice showing the motor cortex; (c) t-value map calculated from the GE-EPI data acquired using 3.5 mm isotropic voxels and a TE of 30 ms; (d) same as in (c) but with modified window level settings; (e) sagittal reformat of the 3D GE subtraction; and (f) sagittal MP-RAGE image. Imaging parameters for the 3D GRE sequence were: TR/TE = 30/20 ms, flip angle = 15°, BW = 80 Hz/pixel, 2 × GRAPPA, resolution =  $0.875 \times 0.875 \times 2$  mm $^3$ , N $_z$  = 64, acquisition time for each block was 96 s. The average signal change in GE-EPI activation (d) is about 0.8% with maximum of 3.5%, and the signal change in the 3D GRE data (e) is about 14%.

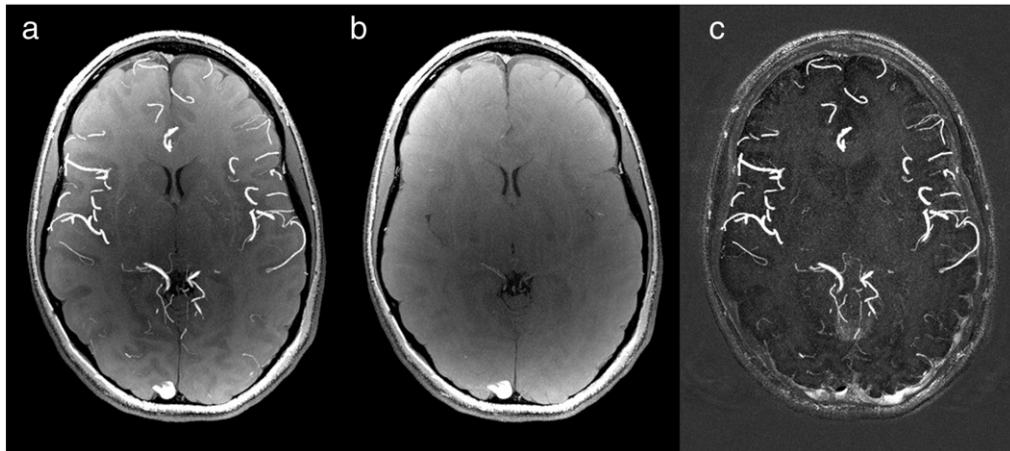


**Fig. 3.** (a) MaxIP images of a normal TOF; (b) TOF with a fixed arterial saturation pulse; and (c) their subtraction image. The imaging parameters were:  $0.5 \times 0.5 \times 0.5 \text{ mm}^3$  isotropic voxels, TR/TE = 20/11 ms, flip angle = 15°, and fully flow compensated. All MaxIP was done over 16 slices. Although most major vessels are suppressed, one can see some remnant arterial/venous signal even with saturation. The reduced signal from the veins in this case actually leads to a poorer signal cancellation in the usual SWI data (not shown here) which relies on having a strong intravascular component.

response. For capillary structures, resolution is probably not important. But what are we really seeing in current low resolution EPI fMRI results? In 1999, Hoogenraad et al. (1999) showed that a very high resolution gradient echo scan could be used to collect fMRI data (albeit much more slowly than EPI) and then collapsed back to the same low resolution as EPI and that the results were basically the same. This suggests that the signal from the major veins still plays a key role in the fMRI response even for low resolution imaging (see Fig. 2).

As mentioned earlier, the only way to really remove the intravascular effects is by saturation or dephasing or both, and in this way one can be sure that the response being imaged is predominantly extra-vascular. But saturation alone may not explain the fact that there remains some signal from what appears to be the same location as before in Fig. 1 but just reduced in amplitude. Consider the high resolution angiogram in Fig. 3. The role of saturation can be appreciated in this figure and its effect is demonstrated by subtraction of the saturated data from the unsaturated data (Fig. 3c). The second image (Fig. 3b) shows that the signal from the arteries and veins is almost iso-intense to the surrounding tissue but certainly not completely nulled either due to T<sub>1</sub> recovery. To remove any remnant effects from the venous blood, one could then apply dephasing gradients. This should null any remaining intravascular contribution to the signal (see also (Song et al., 1996) and Fig. 4). This was indeed the argument in the early brain/vein debate.

The results in Fig. 2 however are very suggestive. They are identical in nature to the earlier results from Frahm et al. (1993), Haacke et al. (1994), Lai et al. (1993), only acquired faster at 3 T. The unfiltered EPI acquired with lower resolution show pretty much the same areas of activation. The filtered EPI activation t-maps have lost the ability for good spatial localization and show activation badly blurred over that portion of the brain. Perhaps one of the best clinical applications for these high resolution fMRI methods would be in the study of eloquent cortex when the neurosurgeon must operate on a tumor (Baudelot et al., 2006; Hou et al., 2006; Sherman et al., 2011). Given the results seen in the 3D data with complete visualization of the brain, one wonders why this method has not been used more in the last 20 years. Can we use high resolution gradient echo methods practically? To understand when this is possible, we need to first address the role of vessel size.

The work by Cheng and Haacke (2001) tried to address this question of scale variance more carefully, showing that the expected fMRI response is scale invariant when the voxels are larger than the largest veins, hence making EPI the method of choice after that point ( $2 \times 2 \times 2 \text{ mm}^3$  is probably large enough to meet that limit and would provide far better spatial delineation than what people are using today which is often just a broadly spread out inflow enhanced vascular response). However, Haacke et al. (1994) and Cheng and Haacke (2001) also showed that when the scale becomes on the order of the vessel size and smaller, there will be a dramatic increase

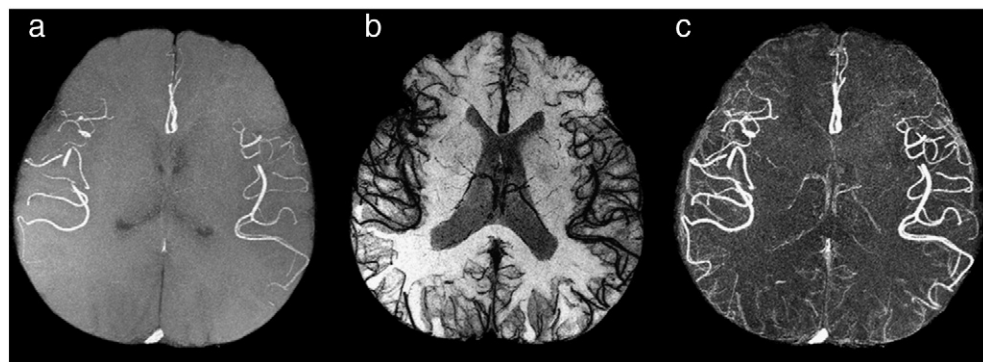


**Fig. 4.** (a) MRA MaxIP images acquired without dephasing gradients, and (b) MinIP images acquired with dephasing gradients, with a VENC value of 0.94 cm/s. Both arteries and even medullary veins are well suppressed. (c) is the result of subtracting (b) from (a), removing most of the background tissues while accentuating the vessels. All MaxIP was done over 16 slices of 0.5 mm thickness. In this subtraction both arteries and veins are evident although the venous structures are not as bright as the arterial structures in part because the signal from the veins is already suppressed because of their low T<sub>2\*</sub> value.

in signal response. In fact, in Lai et al. (1993), the authors showed an image from Duvernoy et al. (1981) showing the pial vein, venules and capillaries, and commented that as resolution improves so will the ability to localize the fMRI signal once the resolution is on the order of the size of the vessel (vein) of interest. The general argument against this has been that there is not enough SNR or temporal resolution to collect the data at such high resolution (and Cheng and Haacke's paper even suggests this to a point). However, this has all changed with the advent of high fields such as 3 T and even more so with 7 T, where very high SNR and very high resolution fMRI has become viable. It is a testament to the progress made in MRI that the picture from Duvernoy showing the pial veins, venules and capillaries has basically been replicated now with SWI filtered phase (Haacke et al., 1995; Haacke and Reichenbach, 2011) and gradient echo images at 7 T (Ge et al., 2008; Lee et al., 2010) and is beginning to be seen at 3 T (Haacke and Reichenbach, 2011).

In the early days, much work went into suppressing the signal from the veins (Duong et al., 2003; Glover et al., 1996). But now it is possible to do what was alluded to in the work of Haacke et al. (1994), image the small draining veins adjacent to the activated tissue, especially if the goal is to do the neuroscience to understand the sources of the local neural activity involved in activation. With these high SNR, high resolution, rapid scanning methods, it should be possible to begin to see local changes in venous oxygen saturation (which is the underlying mechanism of BOLD effect) at the level of medullary veins (several hundred microns) to perhaps even local changes in venules ( $50\text{ }\mu\text{m}$ ). It turns out that the optimal resolution according to Cheng and Haacke is about four times larger than the vessel volume. So a vein that is  $250\text{ }\mu\text{m}$  could be seen and imaged with a resolution of  $500\text{ }\mu\text{m}$  (as it is now with SWI for example (Belliveau et al., 1992; Haacke et al., 1997, 2004, 2009; Mittal et al., 2009) or a vessel that is  $50\text{ }\mu\text{m}$  could be seen with a resolution of  $100\text{ }\mu\text{m}$ . Practically, the results are better than Cheng and Haacke had anticipated. The 7 T data of today can already reveal venules with a resolution of  $0.2 \times 0.2 \times 1\text{ mm}^3$  (Ge et al., 2008; Lee et al., 2010). We can expect to see many more publications in the future on high resolution functional MRI using 3D gradient echo imaging techniques.

There are some practical issues that need to be dealt with to make imaging with high resolution more attractive. One of these is scanning time and the other is SNR. To cover the entire brain at 3 T with 64 2 mm thick slices and an in-plane resolution of  $0.5\text{ mm} \times 0.5\text{ mm}$  will take about 5 min. Keeping a single activation task running for 5 min is not easy and then of course another 5 min to obtain the resting state images. However, with the marriage of parallel imaging and segmented echo-planar imaging, we anticipate this time being reduced to one and a half minutes. Reducing the resolution slightly to  $1\text{ mm} \times 1\text{ mm} \times 2\text{ mm}$  would further reduce the time by about 30 s. Now this allows for a more conventional block design of 30 s activation and 30 s resting for five cycles, allowing the entire 3D scan to take place in just 5 min. This is similar to current imaging times in most fMRI experiments.

### **High resolution MR angiography: the role of saturation and dephasing**

Before we address the practical issue of high resolution fMRI with 3D gradient echo imaging and SWI, it is important to understand what is possible on the MR angiography side from the perspective of collecting high resolution data, enhancing contrast, and nulling signal from blood. In fMRI with EPI, one gets excellent intravascular signal contributions thanks to the inflow enhancement from the arterial side and hence venous signal. But with gradient echo imaging, blood signal will be suppressed with respect to gray matter due to blood's longer  $T_1$ . One can do MRA both with and without contrast agent to best enhance the vascular signal and more importantly, the contrast between vessels and surrounding tissue. Recall that if the vascular signal is too low, the enhancement from the intravascular BOLD effect

will be minimized. Fig. 3 and particularly Fig. 4 show the capability of high resolution imaging in mapping out not just the major arteries but also, most importantly, smaller branches that are the basic source of blood supply to the tissue.

These images can be further improved by using a magnetization transfer contrast (MTC) pulse, using a saturation band, dephasing the signal from the moving spins, or other means to suppress the background. Consider the use of MTC as a first approach. The problem with MTC is that it lengthens the scan time and increases the specific absorption rate (SAR) making it less desirable to use at high magnetic fields. A second approach is to perform two scans: one with high vessel signal and the other with low signal and subtract them. One can use saturation bands to suppress the arterial signal or venous signal by saturating the inflowing blood, or use a strong set of bipolar gradients to dephase moving spins in both arteries and veins. The advantage of the bipolar gradients over saturation bands is that it suppresses fast flowing blood, requires no SAR increases and can be acquired in an interleaved TR manner (i.e., one TR with dephasing and the next TR without) without interfering with equilibrium of the magnetization and without suffering from misregistration artifacts. The VENC concept in flow quantification methods (Haacke et al., 1999) can be used to describe the dephasing effects, that flowing blood with a velocity higher than the VENC value will be dephased. Setting the VENC values to about  $1\text{ cm/s}$  or less should do a reasonably good job dephasing laminar flow even for small vessels ( $250$  to  $500\text{ }\mu\text{m}$  sized arteries and veins). The disadvantage is that it still requires twice the time (except in some special double or triple echo sequence designs (Kimura et al., 2009)), and both arteries and veins will be shown in the subtracted images. Fig. 4a shows an example of the usual arterial inflow effects, Fig. 4b a MinIP image showing that most vessels are dephased, and Fig. 4c the subtraction of Fig. 4b from 4a. As a side note, those in the fMRI field often quote a b-value rather than the VENC value. However, the bipolar gradients are not being used as diffusion gradients, nor is the diffusion effect the underlying mechanism for signal suppression here. Therefore, we have used the more conventional nomenclature from MR angiography of VENC value above which aliasing occurs. With a pair of bipolar rectangular gradients, for simplicity, one can relate the VENC value to the b-value via  $\text{VENC} = \pi/(6bt)^{1/2}$  (since  $\text{VENC} = \pi/(2\gamma G\tau^2)$  and  $b = 2\gamma^2 G^2 \tau^3/3$ ), where  $\tau$  is the duration of one gradient lobe. So, for example, if the applied gradient is  $25\text{ mT/m}$  with  $5\text{ ms}$  duration, then  $b = 3.73\text{ s/mm}^2$  and  $\text{VENC} = 0.94\text{ cm/s}$ . Since the peak flows in pial veins is on the order of  $1\text{--}4\text{ cm/s}$ , one can expect their signal to be fully suppressed with a VENC of  $0.94\text{ cm/s}$ .

As a fourth approach, a contrast agent can be used to enhance vessel signal throughout the brain without being concerned about saturation effects even for slower flowing blood in small vessels. The challenge in imaging the vessels *in vivo* is to strive to mimic the example of the arteries from Salomon (1971) as shown in Fig. 5a. In this sagittal view, one can see the radial branching of the arteries into the brain. Many of the major arteries that are a few millimeters in size bifurcate into arteries that are perhaps only  $100$  to  $200\text{ }\mu\text{m}$  in size. These in turn branch into vessels only a few dozen microns in size and these finally to the capillaries. Using the high resolution MRA approach with contrast agent injection yields the comparative results shown in Fig. 5b. Although no dephasing example has been used to subtract away the remaining background tissue, there is still clear evidence of small arteries in these images that are approaching  $100$  to  $200\text{ }\mu\text{m}$  in size. A key component in understanding the role of the vasculature in BOLD imaging is to be able to map out the arteries and veins separately. Further, since a major component of the BOLD signal comes from intravascular effects, the use of a  $T_1$  reducing contrast agent to increase the venous signal should in principle lead to an improvement in the BOLD response.

The thrust for high resolution MR angiographic approaches is not just to better understand the vascular structure and source of vascular

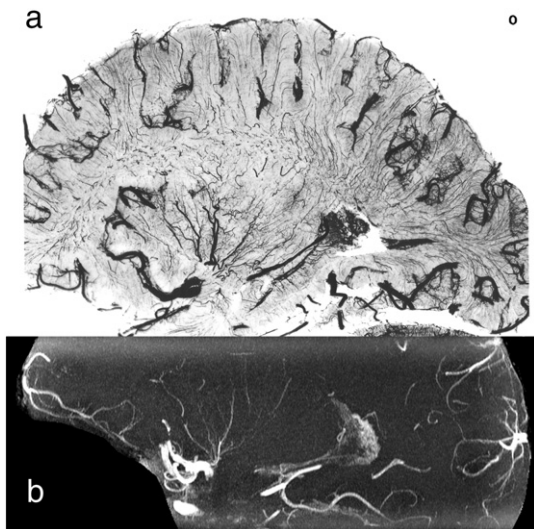


**Fig. 5.** (a) High resolution radiographic image of the arteries obtained by injecting radio-opaque dye in a cadaver brain within a few hours after death (Salamon, 1971). (b) A representative sagittal MaxIP image from a high resolution MRA dataset acquired in a transverse plane post-contrast with a voxel size of  $0.25 \times 0.5 \times 0.5 \text{ mm}^3$  and then reformatted to match this sagittal view. Note the radial pattern of the arteries into the thalamus and surrounding regions. Many very small vessels can be seen on the order of only a few hundred microns. No subtraction was performed here.

signal, but also to consider the novel approach of using the arterial signal as a means to study inflow changes induced by the activation state. This has been considered in the past for arterial spin labeling applications in fMRI (Detre and Wang, 2002; Obata et al., 2004) and more recently for task induced arterial inflow changes (Kang et al., 2010). Being able to analyze the inflow as well as cerebral blood reserve (such as CBV and CBF) may serve as a bridge to connect arterial input and venous BOLD effects, as well as to understand the underlying vasculature basis for the significant inter-individual variation commonly seen in BOLD fMRI.

#### Susceptibility weighted imaging (SWI)

Throughout this early period our interest was to understand BOLD imaging by studying the veins. This focus eventually led to pushing the resolution limits until, in 1997 (Reichenbach et al., 1997), we came up with the concept of susceptibility weighted imaging (SWI). One of the key participants in this work was Jürgen Reichenbach, then a post-doctoral fellow in St. Louis, Missouri at the Mallinckrodt Institute of Radiology (he is now a full Professor running his own imaging laboratory at the Friedrich-Schiller Universität in Jena, Germany). Other researchers who were involved at this time included Song Lai (Lai et al., 1993) and Frank Hoogenraad (Hoogenraad et al., 1999). Although the precursor to this had been a paper in 1995 studying the susceptibility effects that could be visualized with phase (Haacke et al., 1995), the potential clinical applications started first with SWI. During the next ten years, we saw SWI show its value in a wide-ranging set of conditions such as aging, multiple sclerosis, stroke, trauma and tumors (Mittal et al., 2009). In 1997, we used phase for both flow and susceptibility to study changes in oxygen saturation in fMRI experiments using a method we referred to as SAIF for susceptibility and interleaved flow imaging (Haacke et al., 1997).

In the late 1990s, we proposed that multi-echo fMRI (Barth et al., 1999) would be of interest and would serve as a new tool to investigate the echo time dependence of the BOLD response and how it led to different spatial response patterns. In that work, we also evaluated phase data showing that phase could serve as a good marker for susceptibility (oxygen saturation) changes in fMRI. In 1995 (Haacke et al., 1995), 1997 (Haacke et al., 1997; Reichenbach et al., 1997), and

in 2004 (Haacke et al., 2004), we published again with an effort to push the SWI filtered phase as a useful tool in itself. We have also used the phase as a means to map the primary motor cortex as the iron content in the gray matter is quite high in this region and the phase images give excellent gray matter/white matter contrast there (Ogg et al., 1999). More recently, there has been increased interest and attention paid to phase in fMRI (Rowe and Haacke, 2009; Rowe and Logan, 2004). The final thrust in this direction is an interesting return to quantifying oxygen saturation using susceptibility mapping (de Rochefort et al., 2008; Haacke et al., 2010) or it has also been called susceptometry (Fernandez-Seara et al., 2006). Perhaps one day direct measurements of changes in oxygen saturation at the level of the smallest veins will be a viable means to study local neural responses.

Practically, SWI has been used to create exquisite images of the veins without contrast agent. The standard clinical approaches use a resolution of  $0.5 \times 1.0 \times 2 \text{ mm}^3$  or when there is time  $0.5 \times 0.5 \times 2 \text{ mm}^3$ . The usual TE, TR and flip angle values at 3 T are 20 ms, 30 ms and  $15^\circ$ . Bandwidth is kept low at around 100 Hz/pixel to keep signal-to-noise high. With parallel imaging, whole brain coverage for the lower resolution of  $0.5 \times 1.0 \times 2 \text{ mm}^3$  takes only 3 to 4 min. An example of a processed MRA/SWI data set at 3 T is shown in Fig. 6. Until recently, only one echo was used with SWI scans, but there are now a number of papers extolling the virtues of multiple echo SWI with the idea that the first echo can be used for MRA (Barnes and Haacke, 2009b; Deistung et al., 2009; Du and Jin, 2008; Haacke and Reichenbach, 2011), the second for SWI and the combination for  $T_2^*$ . Here the small medullary veins are clearly seen in the MinIP images for SWI. With sufficient resolution, phase can be measured in the small veins and is, of course, proportional to the susceptibility, which, in turn, is proportional to the deoxyhemoglobin content. Phase itself has been used to measure changes in flow indirectly through changes in oxygen saturation in traumatic brain injury studies (Shen et al., 2007) and more recently in stroke (Li et al., 2011b). But because phase is non-local and depends on the geometry of the source and the location of the object relative to the main field, a direct measure of the venous susceptibility would be more appropriate. Hence, our closing section will be about the use of susceptibility mapping to measure oxygen saturation (Barnes and Haacke, 2009a; Li et al., 2011a; Reichenbach et al., 1997).

#### Susceptibility weighted imaging and mapping (SWIM) and oxygen saturation maps

The ability to map oxygen saturation may help develop the potential of high resolution SWI as a means to detect local BOLD changes, especially

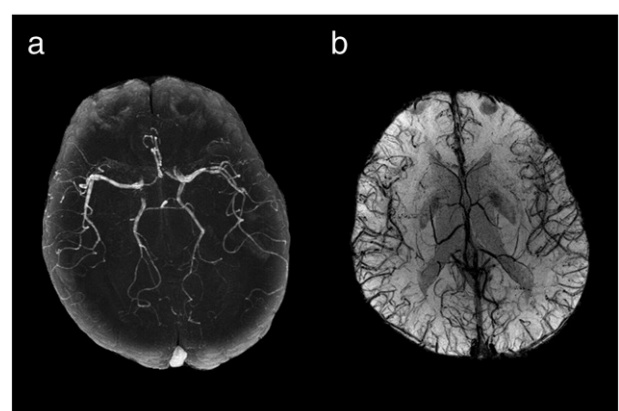


**Fig. 6.** An MRA MaxIP image (a) and SWI MinIP image (b) from the same data set with a  $0.5 \times 0.5 \times 1 \text{ mm}^3$  voxel size. The original data was acquired using a single echo GRE sequence with  $\text{TR/TE} = 30/20 \text{ ms}$ . Prior to the SWI MinIP processing, a two-slice sliding window averaging along the slice direction was done to enhance the phase effect.

at high fields. The presence of local changes in susceptibility causes a local change in magnetic field inside the object and a non-local change outside the object of interest. The phase inside the object is a constant while the change outside decays as  $1/r^2$  for a cylinder and  $1/r^3$  for a sphere. These non-local phases are generally unwelcomed. SWI usually emphasizes phase of one sign and uses this to enhance the magnitude image (Reichenbach et al., 1997; Xu and Haacke, 2006).

As alluded to earlier, the phase itself is of great interest. It has been used for contrast between white matter and gray matter (Haacke et al., 1995, 1999; Ogg et al., 1999; Shmueli et al., 2009) and today for contrast between a variety of structures in the brain and throughout the body. It offers the potential to study everything from vessel wall to even imaging nerves (Haacke et al., 1999). The problem with phase is that it is a non-local manifestation of the magnetic field. However, this very non-local behavior contains everything we need to predict the inherent local susceptibility source (Deville et al., 1979; Haacke et al., 2010; Salomir et al., 2003). This has garnered great interest in the last few years to create a quantitative susceptibility map (QSM) of the tissue (de Rochebort et al., 2008; Liu et al., 2009; Marques and Bowtell, 2008; Salomir et al., 2003) for the study of brain iron and oxygen saturation. The latter is possible because the resulting field inside the veins is directly related to the hematocrit and the local oxygen saturation. Therefore, a QSM (or as we refer to it, SWIM) analysis can provide, in practice, a relative oxygen saturation map of the major veins in the body. When the hematocrit is known, the absolute oxygen saturation can be found (Barnes and Haacke, 2009b; Haacke and Reichenbach, 2011). With such a map, one could, in principle, open a new means to study fMRI by directly monitoring changes in oxygen saturation.

As a means to demonstrate a systemic BOLD effect, we scanned a subject with and without caffeine. The patient ingested a 200 mg NoDoze pill and then was scanned over a 30 min period. The SWI MinIP images are shown in Figs. 7a and b, and the SWIM MaxIP images are shown in Figs. 7c and d, both before and after caffeine intake.

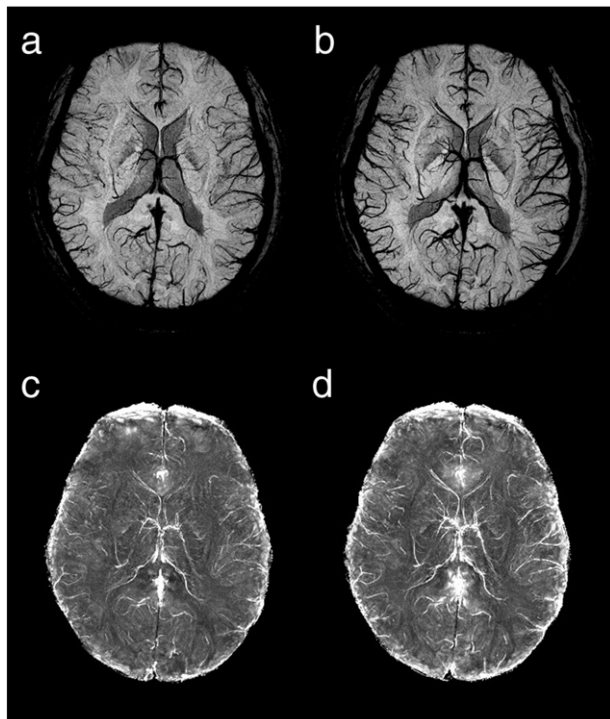


**Fig. 7.** Using susceptibility to monitor system changes in oxygen saturation. The SWI/SWIM results before (a, c) and after (b, d) 200 mg caffeine intake (one NoDoz pill) show significant systemic susceptibility changes in the veins, suggesting a corresponding change in oxygenation saturation. In the future, these types of SWIM images may provide a source of monitoring activation in high resolution, high field fMRI studies.

Although the SWI projections are qualitatively exquisite images, the QSM or SWIM projections are quantitative in nature. Despite the fact that the hematocrit is not known, a measurement of the venous signal changes normalized to the pre-caffeine data provides an accurate measure of the percent change in oxygen saturation and is independent of the hematocrit. It is very difficult to measure BOLD changes in the parenchyma since the blood volume fraction is so small and the BOLD changes are small, but this is not a problem in the major veins (Sedlacik et al., 2008). Even changes in the medullary veins are visible in Figs. 7c and d. Perhaps this new approach will open the door to using the veins as the major source of functional activity in the future rather than trying to discard the venous information.

## Summary and conclusions

With the advent of high fields, it is now possible to image the vasculature of the brain with high resolution rapidly. Having the ability do to so provide a means to understand better the flow and function of the vasculature system and to model the vascular system for any individual. In return, modeling the system can predict what we expect to see from an activated to resting state (Marques and Bowtell, 2008). This will surely lead to a better understanding of why different individuals respond differently to specific stimuli, and certainly to separating out structural effects from real functional effects. Along these lines, we would recommend that all fMRI experiments that collect T<sub>1</sub> weighted images for anatomical information also collect a high resolution SWI scan to monitor the venous vasculature in the activated regions of interest.

Further, imaging with high resolution may herald the day when complicated statistical analysis will no longer be needed as rapid 3D scanning during a single activated and resting state may allow for simple subtractions to be used to monitor changes in the vascular system. When resolution becomes so high that individual local veins draining the activated region can be discerned, the percent change in fMRI experiments can jump to as high as 30% (Cheng and Haacke, 2001; Haacke et al., 1994; Lai et al., 1993).

## Acknowledgement

The authors would like to acknowledge the Telemedicine and Advanced Technology Research Center for the support of this work through Award No: W81XWH-11-1-0493.

## References

- Barnes, S., Haacke, E.M., 2009a. Settling properties of venous blood demonstrated in the peripheral vasculature using susceptibility-weighted imaging (SWI). *J. Magn. Reson. Imaging* 29, 1465–1470.
- Barnes, S.R., Haacke, E.M., 2009b. Susceptibility-weighted imaging: clinical angiographic applications. *Magn. Reson. Imaging Clin. N. Am.* 17, 47–61.
- Barth, M., Reichenbach, J.R., Venkatesan, R., Moser, E., Haacke, E.M., 1999. High-resolution, multiple gradient-echo functional MRI at 1.5 T. *Magn. Reson. Imaging* 17, 321–329.
- Baudelot, C., Cron, G.O., Gallez, B., 2006. Determination of the maturity and functionality of tumor vasculature by MRI: correlation between BOLD-MRI and DCE-MRI using P792 in experimental fibrosarcoma tumors. *Magn. Reson. Med.* 56, 1041–1049.
- Baudindistel, K.T., Reichenbach, J.R., Metzner, R., Schroeder, J., Schad, L.R., 1998. Comparison of functional MR-venography and EPI-BOLD fMRI at 1.5 T. *Magn. Reson. Imaging* 16, 989–991.
- Belliveau, J.W., Kennedy Jr., D.N., McKinstry, R.C., Buchbinder, B.R., Weisskoff, R.M., Cohen, M.S., Vevea, J.M., Brady, T.J., Rosen, B.R., 1991. Functional mapping of the human visual cortex by magnetic resonance imaging. *Science* 254, 716–719.
- Belliveau, J.W., Kwong, K.K., Kennedy, D.N., Baker, J.R., Stern, C.E., Benson, R., Chesler, D.A., Weisskoff, R.M., Cohen, M.S., Tootell, R.B., et al., 1992. Magnetic resonance imaging mapping of brain function. Human visual cortex. *Invest. Radiol.* 27 (Suppl 2), S59–S65.
- Boxerman, J.L., Hamberg, L.M., Rosen, B.R., Weisskoff, R.M., 1995. MR contrast due to intravascular magnetic susceptibility perturbations. *Magn. Reson. Med.* 34, 555–566.
- Casciaro, S., Bianco, R., Distante, A., 2008. Quantification of venous blood signal contribution to BOLD functional activation in the auditory cortex at 3 T. *Magn. Reson. Imaging* 26, 1221–1231.
- Cheng, Y.C., Haacke, E.M., 2001. Predicting BOLD signal changes as a function of blood volume fraction and resolution. *NMR Biomed.* 14, 468–477.

- de Rochefort, L., Brown, R., Prince, M.R., Wang, Y., 2008. Quantitative MR susceptibility mapping using piece-wise constant regularized inversion of the magnetic field. *Magn. Reson. Med.* 60, 1003–1009.
- Deistung, A., Dittrich, E., Sedlacik, J., Rauscher, A., Reichenbach, J.R., 2009. ToF-SWI: simultaneous time of flight and fully flow compensated susceptibility weighted imaging. *J. Magn. Reson. Imaging* 29, 1478–1484.
- Detre, J.A., Wang, J., 2002. Technical aspects and utility of fMRI using BOLD and ASL. *Clin. Neurophysiol.* 113, 621–634.
- Deville, G., Bernier, M., Delrieux, J., 1979. NMR multiple echoes observed in solid 3He. *Phys. Rev. B* 19, 5666–5688.
- Du, Y.P., Jin, Z., 2008. Simultaneous acquisition of MR angiography and venography (MRAV). *Magn. Reson. Med.* 59, 954–958.
- Duong, T.Q., Yacoub, E., Adriany, G., Hu, X., Ugurbil, K., Kim, S.G., 2003. Microvascular BOLD contribution at 4 and 7 T in the human brain: gradient-echo and spin-echo fMRI with suppression of blood effects. *Magn. Reson. Med.* 49, 1019–1027.
- Duvernoy, H.M., Delon, S., Vannson, J.L., 1981. Cortical blood vessels of the human brain. *Brain Res. Bull.* 7, 519–579.
- Duyn, J.H., Moonen, C.T., van Yperen, G.H., de Boer, R.W., Luyten, P.R., 1994. Inflow versus deoxyhemoglobin effects in BOLD functional MRI using gradient echoes at 1.5 T. *NMR Biomed.* 7, 83–88.
- Fernandez-Seara, M.A., Techawiboonwong, A., Detre, J.A., Wehrli, F.W., 2006. MR susceptibility for measuring global brain oxygen extraction. *Magn. Reson. Med.* 55, 967–973.
- Frahm, J., Merboldt, K.D., Hanicke, W., 1993. Functional MRI of human brain activation at high spatial resolution. *Magn. Reson. Med.* 29, 139–144.
- Ge, Y., Barnes, S., Heller, S., Xu, Y., Chen, Q., Haacke, E.M., Grossman, R.J., 2008. 3D high resolution susceptibility weighted imaging (SWI) venography at 3T and 7T. *Proc. Int'l. Soc. Magn. Reson. Med.* 17th Meeting, Honolulu, US.
- Glover, G.H., Lemieux, S.K., Drangova, M., Pauly, J.M., 1996. Decomposition of inflow and blood oxygen level-dependent (BOLD) effects with dual-echo spiral gradient-recalled echo (GRE) fMRI. *Magn. Reson. Med.* 35, 299–308.
- Haacke, E.M., Reichenbach, J.R., 2011. Susceptibility Weighted Imaging in MRI: Basic Concepts and Clinical Applications. Wiley-Blackwell, Hoboken, NJ.
- Haacke, E.M., Bearden, F.H., Clayton, J.R., Linga, N.R., 1986. Reduction of MR imaging time by the hybrid fast-scan technique. *Radiology* 158, 521–529.
- Haacke, E.M., Hopkins, A., Lai, S., Buckley, P., Friedman, L., Meltzer, H., Hedera, P., Friedland, R., Klein, S., Thompson, L., et al., 1994. 2D and 3D high resolution gradient echo functional imaging of the brain: venous contributions to signal in motor cortex studies. *NMR Biomed.* 7, 54–62.
- Haacke, E.M., Lai, S., Yablonskiy, D.A., Lin, W., 1995. In vivo validation of the BOLD mechanism: a review of signal changes in gradient echo functional MRI in the presence of flow. *Int. J. Imaging Syst. Technol.* 6, 153–163.
- Haacke, E.M., Lai, S., Reichenbach, J.R., Kuppusamy, K., Hoogenraad, F.G.C., Takeichi, H., Un!, W., 1997. In vivo measurement of blood oxygen saturation using magnetic resonance imaging: a direct validation of the blood oxygen level-dependent concept in functional brain imaging. *Hum. Brain Mapp.* 5, 341–346.
- Haacke, E.M., Brown, R., Thompson, M., Venkatesan, R., 1999. Magnetic Resonance Imaging. Physical Principles and Sequence Design. Wiley-Liss, New York.
- Haacke, E.M., Xu, Y., Cheng, Y.C., Reichenbach, J.R., 2004. Susceptibility weighted imaging (SWI). *Magn. Reson. Med.* 52, 612–618.
- Haacke, E.M., Mittal, S., Wu, Z., Neelavalli, J., Cheng, Y.C., 2009. Susceptibility-weighted imaging: technical aspects and clinical applications, part 1. *AJR Am. J. Neuroradiol.* 30, 19–30.
- Haacke, E.M., Tang, J., Neelavalli, J., Cheng, Y.C., 2010. Susceptibility mapping as a means to visualize veins and quantify oxygen saturation. *J. Magn. Reson. Imaging* 32, 663–676.
- Hoogenraad, F.G., Hofman, M.B., Pouwels, P.J., Reichenbach, J.R., Rombouts, S.A., Haacke, E.M., 1999. Sub-millimeter fMRI at 1.5 Tesla: correlation of high resolution with low resolution measurements. *J. Magn. Reson. Imaging* 9, 475–482.
- Hopkins, A.L., Haacke, E.M., Tkach, J., Barr, R.G., Bratton, C.B., 1988. Improved sensitivity of proton MR to oxygen-17 as a contrast agent using fast imaging: detection in brain. *Magn. Reson. Med.* 7, 222–229.
- Hou, B.L., Bradbury, M., Peck, K.K., Petrovich, N.M., Gutin, P.H., Holodny, A.I., 2006. Effect of brain tumor neovasculature defined by rCBV on BOLD fMRI activation volume in the primary motor cortex. *Neuroimage* 32, 489–497.
- Kang, C.K., Kim, S.H., Lee, H., Park, C.A., Kim, Y.B., Cho, Z.H., 2010. Functional MR angiography using phase contrast imaging technique at 3T MRI. *Neuroimage* 50, 1036–1043.
- Kimura, T., Ikeda, M., Takemoto, S., 2009. Hybrid of opposite-contrast MR angiography (HOP-MRA) combining time-of-flight and flow-sensitive black-blood contrasts. *Magn. Reson. Med.* 62, 450–458.
- Kwong, K.K., Hopkins, A.L., Belliveau, J.W., Chesler, D.A., Porkka, L.M., McKinstry, R.C., Finelli, D.A., Hunter, G.J., Moore, J.B., Barr, R.G., et al., 1991. Proton NMR imaging of cerebral blood flow using H<sub>2</sub>(<sup>17</sup>O). *Magn. Reson. Med.* 22, 154–158.
- Lai, S., Hopkins, A.L., Haacke, E.M., Li, D., Wasserman, B.A., Buckley, P., Friedman, L., Meltzer, H., Hedera, P., Friedland, R., 1993. Identification of vascular structures as a major source of signal contrast in high resolution 2D and 3D functional activation imaging of the motor cortex at 1.5T: preliminary results. *Magn. Reson. Med.* 30, 387–392.
- Lee, J., Hirano, Y., Fukunaga, M., Silva, A.C., Duyn, J.H., 2010. On the contribution of deoxy-hemoglobin to MRI gray-white matter phase contrast at high field. *Neuroimage* 49, 193–198.
- Li, C., Langham, M.C., Epstein, C.L., Magland, J.F., Wu, J., Gee, J., Wehrli, F.W., 2011a. Accuracy of the cylinder approximation for susceptrometric measurement of intravascular oxygen saturation. *Magn. Reson. Med.* doi:10.1002/mrm.23034.
- Li, M., Wu, J., Miao, Y., Yang, Z., Raza, W., Wang, Y., Haacke, E.M., Hu, J., 2011b. In vivo measurement of oxygenation changes after stroke using susceptibility weighted imaging. *Proc. Int'l. Soc. Magn. Reson. Med.* 19th Meeting, Montreal, Quebec, Canada, p. 4062.
- Liu, T., Spincemaille, P., de Rochefort, L., Kressler, B., Wang, Y., 2009. Calculation of susceptibility through multiple orientation sampling (COSMOS): a method for conditioning the inverse problem from measured magnetic field map to susceptibility source image in MRI. *Magn. Reson. Med.* 61, 196–204.
- Marques, J.P., Bowtell, R.W., 2008. Using forward calculations of the magnetic field perturbation due to a realistic vascular model to explore the BOLD effect. *NMR Biomed.* 21, 553–565.
- Menon, R.S., Ogawa, S., Strupp, J.P., Ugurbil, K., 1997. Ocular dominance in human V1 demonstrated by functional magnetic resonance imaging. *J. Neurophysiol.* 77, 2780–2787.
- Mittal, S., Wu, Z., Neelavalli, J., Haacke, E.M., 2009. Susceptibility-weighted imaging: technical aspects and clinical applications, part 2. *AJR Am. J. Neuroradiol.* 30, 232–252.
- Obata, T., Liu, T.T., Miller, K.L., Luh, W.M., Wong, E.C., Frank, L.R., Buxton, R.B., 2004. Discrepancies between BOLD and flow dynamics in primary and supplementary motor areas: application of the balloon model to the interpretation of BOLD transients. *Neuroimage* 21, 144–153.
- Ogawa, S., Menon, R.S., Tank, D.W., Kim, S.G., Merkle, H., Ellermann, J.M., Ugurbil, K., 1993. Functional brain mapping by blood oxygenation level-dependent contrast magnetic resonance imaging. A comparison of signal characteristics with a biophysical model. *Biophys. J.* 64, 803–812.
- Ogg, R.J., Langston, J.W., Haacke, E.M., Steen, R.G., Taylor, J.S., 1999. The correlation between phase shifts in gradient-echo MR images and regional brain iron concentration. *Magn. Reson. Imaging* 17, 1141–1148.
- Reichenbach, J.R., Venkatesan, R., Schillinger, D.J., Kido, D.K., Haacke, E.M., 1997. Small vessels in the human brain: MR venography with deoxyhemoglobin as an intrinsic contrast agent. *Radiology* 204, 272–277.
- Rowe, D.B., Haacke, E.M., 2009. MAgnitude and PHase Thresholding (MAPHT) of noisy complex-valued magnetic resonance images. *Magn. Reson. Imaging* 27, 1271–1280.
- Rowe, D.B., Logan, B.R., 2004. A complex way to compute fMRI activation. *Neuroimage* 23, 1078–1092.
- Salamon, G., 1971. Atlas of the arteries of the human brain. Sandoz, Paris.
- Salomir, R., de Senneville, B.D., Moonen, C.T.W., 2003. A fast calculation method for magnetic field inhomogeneity due to an arbitrary distribution of bulk susceptibility. *Concepts Magn. Reson.* 19B, 26–34.
- Sedlacik, J., Helm, K., Rauscher, A., Stadler, J., Mentzel, H.J., Reichenbach, J.R., 2008. Investigations on the effect of caffeine on cerebral venous vessel contrast by using susceptibility-weighted imaging (SWI) at 1.5, 3 and 7 T. *Neuroimage* 40, 11–18.
- Shen, Y., Kou, Z., Kreipke, C.W., Petrov, T., Hu, J., Haacke, E.M., 2007. In vivo measurement of tissue damage, oxygen saturation changes and blood flow changes after experimental traumatic brain injury in rats using susceptibility weighted imaging. *Magn. Reson. Imaging* 25, 219–227.
- Sherman, J.H., Hoes, K., Marcus, J., Komotar, R.J., Brennan, C.W., Gutin, P.H., 2011. Neurosurgery for brain tumors: update on recent technical advances. *Curr. Neurol. Neurosci. Rep.* 11, 313–319.
- Shmueli, K., de Zwart, J.A., van Gelderen, P., Li, T.Q., Dodd, S.J., Duyn, J.H., 2009. Magnetic susceptibility mapping of brain tissue in vivo using MRI phase data. *Magn. Reson. Med.* 62, 1510–1522.
- Song, A.W., Wong, E.C., Tan, S.G., Hyde, J.S., 1996. Diffusion weighted fMRI at 1.5 T. *Magn. Reson. Med.* 35, 155–158.
- Song, A.W., Guo, H., Truong, T.K., 2007. Single-shot ADC imaging for fMRI. *Magn. Reson. Med.* 57, 417–422.
- Ugurbil, K., Adriany, G., Andersen, P., Chen, W., Gruetter, R., Hu, X., Merkle, H., Kim, D.S., Kim, S.G., Strupp, J., Zhu, X.H., Ogawa, S., 2000. Magnetic resonance studies of brain function and neurochemistry. *Annu. Rev. Biomed. Eng.* 2, 633–660.
- Xu, Y., Haacke, E.M., 2001. Partial Fourier imaging in multi-dimensions: a means to save a full factor of two in time. *J. Magn. Reson. Imaging* 14, 628–635.
- Xu, Y., Haacke, E.M., 2006. The role of voxel aspect ratio in determining apparent vascular phase behavior in susceptibility weighted imaging. *Magn. Reson. Imaging* 24, 155–160.
- Xu, Y., Haacke, E.M., 2008. An iterative reconstruction technique for geometric distortion-corrected segmented echo-planar imaging. *Magn. Reson. Imaging* 26, 1406–1414.
- Yacoub, E., Harel, N., Ugurbil, K., 2008. High-field fMRI unveils orientation columns in humans. *Proc. Natl. Acad. Sci. U. S. A.* 105, 10607–10612.